# Spatio-temporal characterization of femtosecond laser pulses using self-referenced Fourier transform spectroscopy

Antoine Jeandet

## To cite this version:

Antoine Jeandet. Spatio-temporal characterization of femtosecond laser pulses using self-referenced Fourier transform spectroscopy. Optics [physics.optics]. Université Paris-Saclay, 2020. English. NNT : 2020UPASS089 . tel-03018886

HAL Id: tel-03018886
https://theses.hal.science/tel-03018886

Submitted on 23 Nov 2020

**HAL** is a multi-disciplinary open access archive for the deposit and dissemination of scientific research documents, whether they are published or not. The documents may come from teaching and research institutions in France or abroad, or from public or private research centers.

L'archive ouverte pluridisciplinaire **HAL**, est destinée au dépôt et à la diffusion de documents scientifiques de niveau recherche, publiés ou non, émanant des établissements d'enseignement et de recherche français ou étrangers, des laboratoires publics ou privés.

# Spatio-Temporal Characterization of Femtosecond Laser Pulses Using Self-Referenced Imaging Fourier Transform Spectroscopy

**Thèse de doctorat de l'Université Paris-Saclay**

École doctorale n° 572, Ondes et Matière (EDOM)
Spécialité de doctorat: Optique & Photonique
Unité de recherche: Université Paris-Saclay, CEA, CNRS, LIDYL, 91191, Gif-sur-Yvette, France.
Référent: Faculté des sciences d'Orsay

**Thèse présentée et soutenue à Orsay le 9 juillet 2020 par**

## Antoine JEANDET

**Composition du jury:**

| | |
|---|---|
| **Sophie Kazamias**<br>Professeur des Universités, LPGP (Université Paris-Saclay) | Présidente |
| **François Courvoisier**<br>Chargé de recherche, Femto-ST (CNRS) | Rapporteur & Examinateur |
| **Sylvain Gigan**<br>Professeur des Universités, LKB (ENS Paris) | Rapporteur & Examinateur |
| **Aurélie Jullien**<br>Chargée de recherche, INPHYNI (CNRS) | Examinatrice |
| **Dimitris Papadopoulos**<br>Ingénieur de Recherche, LULI (Ecole Polytechnique) | Examinateur |
| **Fabien Quéré**<br>Directeur de Recherche, LIDYL (CEA) | Directeur de thèse |
| **Benoît Bussière**<br>Ingénieur-Docteur, Amplitude Laser Group | Invité |

**Thèse de doctorat**

NNT: 2020UPASS089

# Remerciements

En écrivant la première page de ce manuscrit, je tourne (soulagé) l'ultime page de ma thèse ! J'éprouve une profonde reconnaissance en pensant aux personnes qui m'ont épaulé pendant ces quelques années. Puisque ce travail a aussi représenté un sérieux défi personnel, la fameuse tradition des remerciements de thèse me semble aujourd'hui absolument essentielle. Je débuterai donc par quelques mots de gratitude pour les personnes qui ont permis de rendre cette expérience moins difficile et vraiment passionnante.

Rien n'aurait débuté sans la détermination de Fabien Quéré, qui a lancé ce projet de caractérisation spatio-temporelle dans le laboratoire, et qui a été mon directeur de thèse pendant ces trois années. Exemple d'énergie et d'enthousiasme dès le début, Fabien a su me faire confiance avant que je n'y arrive moi-même, et il m'a confronté aux projets dont j'avais besoin pour apprendre et m'améliorer. Fabien a grandement contribué à ce travail par ses explications patientes et son pragmatisme, et je lui en suis infiniment reconnaissant. Il me semble qu'au démarrage d'une thèse, il subsiste souvent une part d'inconnue sur l'affinité que l'on pourra avoir avec son directeur de thèse, et que j'ai bénéficié d'une chance considérable en tombant sur un sujet proposé par Fabien. Immense merci.

Je remercie le LIDYL et son directeur Philippe Martin pour son accueil chaleureux dans le laboratoire. Mille mercis à Véronique Gereczy et Caroline Lebe pour m'avoir sauvé de nombreux pétrins administratifs avec calme et sang-froid. Je remercie également Amplitude Technologies et Gilles Riboulet pour avoir financé ce travail de thèse et pour m'avoir accueilli dans l'entreprise.

Je remercie aussi Gustave Pariente pour m'avoir confié son bébé hexapode à la fin de sa thèse et pour avoir passé du temps à m'en expliquer toutes les subtilités. J'ai découvert récemment la vraie valeur du temps dans les derniers mois d'une thèse ! Mille mercis à Olivier Gobert pour son support indispensable au cours de plusieurs expériences sur notre laser UHI–100. Les explications qu'Olivier a pris le temps de m'apporter ainsi que la justesse de ses conseils ont été décisifs pour le succès et la qualité des mesures. J'ai spécialement apprécié les moments que nous avons passé ensemble autour d'un schéma ou d'un montage optique. Je remercie aussi l'équipe de laseristes, Fabrice Réau, David Garzella, Jean-François Hergott et Delphine Jourdain pour avoir produit tous ces photons et pour m'avoir rendu plein de services au labo. Merci également à Gabriel Mennerat d'avoir pris le temps d'assister à mes répétitions de soutenance !

Je veux remercier spécialement Spencer W. Jolly pour sa présence et son aide pendant la deuxième partie de ma thèse. Je n'oublierai pas les bons moments que nous avons passé ensemble en labo, ni les multiples occasions où Spencer m'a débloqué de situations qui me paraissaient impossibles grâce à sa sérénité et à ses explications limpides.

Merci à tout le couloir de l'équipe PHI pour les longues discussions passionnantes autour de notre machine à café. Je pense particulièrement à Luca Fedeli, Haithem Kallala, Antonin Sainte-Marie, Guillaume Bouchard, Ludovic Chopineau, Antonin Borot, Pierre Schumacher, Henri Vincenti, Noé Tiger, et Neïl Zaim. Merci à Roman Yurchak, *pythonista* chevronné, pour les moment passés ensemble à programmer. Remerciements spéciaux à mon collègue de bureau Guillaume Blaclard, avec qui j'ai beaucoup aimé partager ces quelques mois de malheur consacrés à l'écriture simultanée de nos manuscrits.

Puisque mon temps de travail a été partagé entre Saclay et Lisses, j'aimerais aussi remercier ici mes collègues d'Amplitude. Malgré mes passages souvent furtifs dans le bureau R&D, j'ai beaucoup apprécié de pouvoir passer du temps avec Mathieu Paurisse, Helise Stabile, Alexandre Thai, Aura Gonzalez, Florian Mollica, Anna Golinelli, et Hermance Jacqmin. Je suis particulièrement reconnaissant envers Xiaowei Chen, Emilien Gontier, Aurélien Ricci et Pierre-Mary Paul qui ont encadré mon projet dans l'entreprise, et Benoît Bussière qui m'a beaucoup aidé lors des manips sur nos chaines lasers.

Comme vous le lirez au chapitre 8, une partie importante de ma thèse a consisté à me rendre dans d'autres laboratoires avec notre prototype et d'y réaliser des mesures. Je souhaiterais donc remercier ici les chercheuses et chercheurs qui m'ont accueilli et qui ont consacré du temps de faisceau à nos essais. Merci à Moana Pittman pour son accueil chaleureux sur LASERIX, ainsi qu'à Fabrice Sanson, Elsa Baynard, Alok-Kumar Pandey et Julien Demailly pour leur aide pendant les mesures. Je remercie aussi Marc Hanna, Frédéric Druon et Nour Daher pour le temps qu'ils ont alloué à Spencer et à moi-même pendant des mesures au Laboratoire Charles Fabry. Merci à Rodrigo Lopez-Martens pour son accueil en *Salle Noire* au Laboratoire d'optique Appliquée, et à Marie Ouillé pour son aide sympathique pendant la manip. *Last but not least*, mille mercis à toute l'équipe du laser BELLA au Berkeley Lab, qui nous a prêté son faisceau petawatt pendant deux semaines complètes. Je remercie particulièrement Wim Leemans et Kei Nakamura avec qui nous avons eu le privilège de travailler pour écrire l'article.

Grand merci aux amis du podcast Impact Factor 1000, Marion et Benjamin, pour ces fous rires partagés autour de nos micros. Je remercie également Lucas, Fabrice, Cassie, Raphaël, Gina et Hamadoun pour les bons moments que nous avons passé ensemble une bière à la main ou devant un bon (mais souvent mauvais) film.

Mille mercis à toute ma famille. À mes frères Théo et Lucas, mes grands-parents, mes oncles, tantes, cousines et cousins qui par leur présence et leur soutien m'ont aussi permis de passer de bons moments et de sortir la tête de ma thèse. Je veux remercier particulièrement mes parents qui, en plus de m'avoir tout appris et tout apporté depuis vingt-huit ans, ont aussi *prouvé* à mes frères et moi l'importance cruciale des projets et de l'ambition.

Comment finir cette page sans remercier Juliette, qui en plus d'avoir supporté mes humeurs de thésard fatigué, a su me faire rire et me motiver comme personne ? Alors même qu'elle était embarquée dans sa propre thèse, Juliette m'a conseillé (et relu !) avec patience et intelligence tout en se chargeant de rendre ces quelques années vraiment plus belles. Je suis heureux de pouvoir continuer à rouler sur notre petite route ensemble. Je pense aussi à la famille de Juliette et les remercie infiniment pour ces quelques moments de vacances ou de week-end partagées avec eux. Mille mercis à mes *melhores amigos* Paul et Lou pour nous avoir fait visiter un petit bout de leur pays.

Et puisque nous allons maintenant rentrer dans le vif du sujet, j'aimerais évidemment terminer en remerciant très sincèrement Sophie Kazamias, François Courvoisier, Sylvain Gigan, Aurélie Jullien, et Dimitris Papadopoulos qui ont accepté de lire ce manuscrit et de participer à la soutenance, alors même qu'une pandémie bouleversait le fonctionnement de leurs laboratoires respectifs et qu'ils avaient très certainement d'autres priorités en tête. Je les remercie également pour leurs questions pendant la soutenance, qui ont participé à rendre cette journée particulièrement agréable et intéressante.

*À la mémoire de mon grand-père,*
*À mes parents et à mes frères,*
*Pour Juliette.*

# Table of Contents

**List of Physical Quantities** xi

**List of Abbreviations** xiii

**Introduction** 1

**I. Structure & Metrology of High-Power Femtosecond Pulses** 7

**1. High-Power Femtosecond Laser Systems** 9

- 1.1. Generation of High-Power Femtosecond Pulses . . . . . . 10
  - 1.1.1. Chirped Pulse Amplification . . . . . . 10
  - 1.1.2. Post-compression . . . . . . 11
- 1.2. Description of the Generated Electric Field . . . . . . 12
  - 1.2.1. Spatial Description . . . . . . 12
  - 1.2.2. Temporal & Spectral Description . . . . . . 12
- 1.3. Spatial & Temporal Metrology of High-Power Laser Systems . . . . . . 14
  - 1.3.1. Purely-Spatial Metrology . . . . . . 14
  - 1.3.2. Purely-Temporal Metrology . . . . . . 16

**2. Spatio-Temporal Couplings in High-Power Lasers** 21

- 2.1. Spatio-Temporal Description of the Electric Field . . . . . . 22
- 2.2. Definition & Examples of Space-Time Couplings . . . . . . 23
  - 2.2.1. Spatially Linear Spatio-Temporal Couplings . . . . . . 24
  - 2.2.2. Spatially Quadratic Spatio-Temporal Couplings . . . . . . 26
  - 2.2.3. Spatio-Spectral Streak . . . . . . 28
- 2.3. Spatio-Temporal & Spatio-Spectral Characterization . . . . . . 30
  - 2.3.1. Spatially Resolved Spectral Measurement . . . . . . 31
  - 2.3.2. Spectrally Resolved Spatial Measurement . . . . . . 33
- 2.4. Interpretation of Spatio-Temporal Measurements . . . . . . 36
  - 2.4.1. Spectrally-Resolved Zernike Polynomials . . . . . . 36
  - 2.4.2. Spatio-Temporal Strehl Ratio . . . . . . 37

**II. TERMITES: Technique Principles & Optimization of the Design 41**

**3. Fundamentals of the Technique 43**
- 3.1. Experimental Setup: Concepts & Legacy . . . 44
  - 3.1.1. Imaging Fourier Transform Spectroscopy . . . 44
  - 3.1.2. From IFTS to TERMITES . . . 45
- 3.2. Numerical Retrieval of the Pulse Structure . . . 48
  - 3.2.1. Going Back to the Spectral Domain . . . 49
  - 3.2.2. Curvature Removal & Data Resampling . . . 52
  - 3.2.3. Reference Compensation . . . 55
  - 3.2.4. Retropropagation . . . 59
  - 3.2.5. Spectral Phase Stitching . . . 60

**4. Specifications & Performance 63**
- 4.1. Design Parameters and their Constraints . . . 64
  - 4.1.1. Hard Constraints . . . 64
  - 4.1.2. Soft Constraints . . . 68
- 4.2. Settling for an Optimal Set of Parameters . . . 71
  - 4.2.1. Optimization Procedure . . . 71
  - 4.2.2. Two Input Requirements, Leading to Two TERMITES Designs . . . 73

**5. Numerical Study of Potential Error Sources 77**
- 5.1. Numerical study of TERMITES measurements . . . 78
  - 5.1.1. Simulating TERMITES measurements . . . 78
  - 5.1.2. Interpreting the Generated Results . . . 79
- 5.2. Errors Linked to Instrument Properties . . . 80
  - 5.2.1. Delay Fluctuations . . . 80
  - 5.2.2. Reference Pointing Errors . . . 83
- 5.3. Errors Linked to Beam Properties . . . 84
  - 5.3.1. Energy Fluctuations . . . 84
  - 5.3.2. Pointing Fluctuations . . . 85

**6. Experimental Validation of TERMITES 89**
- 6.1. Measurement of Interferometer Delay Stability . . . 90
- 6.2. Comparison with Simpler Measurement Devices . . . 91
  - 6.2.1. Spectrally Averaged Profiles . . . 91
  - 6.2.2. Spatially-Resolved Spectrum . . . 92
- 6.3. Characterization of Calibrated Defects . . . 94
  - 6.3.1. Calibrated Pulse Front Curvature . . . 94
  - 6.3.2. Calibrated Streak from a Square-shaped Phase Defect . . . 96

**III. Characterization of Laser Systems** **101**

**7. Experimental Protocol for Successful TERMITES Measurements** **103**
- 7.1. Positioning TERMITES in the Laser Chain . . . 104
- 7.2. Input Beam Size Reduction . . . 104
- 7.3. Input Energy Requirements & Appropriate Attenuation . . . 106
  - 7.3.1. Maximal Input Pulse Energy . . . 106
  - 7.3.2. Attenuation Methods . . . 107

**8. Survey of Spatio-Temporal Couplings Measured in Ultra-Intense Lasers** **111**
- 8.1. Effects of Pulse Stretching . . . 112
  - 8.1.1. Spatial Chirp Created from a Misaligned Offner Stretcher . . . 112
- 8.2. Effects of Pulse Amplification . . . 113
  - 8.2.1. Spatio-spectral Filtering by Amplification . . . 113
  - 8.2.2. Gain Depletion in Chirped Pulse Amplifiers . . . 114
- 8.3. Effects of Beam Imaging . . . 116
  - 8.3.1. Telescope-induced Pulse Front Curvature . . . 116
- 8.4. Effects of Pulse Compression . . . 119
  - 8.4.1. Pulse Front Tilt . . . 119
  - 8.4.2. Distortions Caused by Surface Defects of Compressor Optics . . . 120
  - 8.4.3. Spatio-spectral Profile Masking . . . 122
- 8.5. Effects of Hollow-Core Fiber Compression . . . 124
  - 8.5.1. Spatially Resolved Spectral Broadening . . . 125
  - 8.5.2. Effect of Spatial Chirp on Fiber Coupling . . . 126

**Conclusion & Perspectives** **129**

**Appendices** **137**

**A. Supplementary Demonstrations** **137**

**B. Summary in French** **141**

**C. List of Publications** **143**

**Bibliography** **153**

# List of Physical Quantities

| Quantity | Description | Unit |
|---|---|---|
| $E_s$ | Complex spectral electric field, of which the phase has been locally *stitched* | – |
| $\hat{E}$ | Complex temporal electric field | – |
| $E$ | Complex spectral electric field | – |
| $SR$ | Strehl ratio | – |
| $W_0$ | Cross-Power Spectral Density from which the reference curvature is removed | – |
| $W$ | Cross-Power Spectral Density | – |
| $\beta$ | TERMITES Reference size ratio (expression on p. 46) | – |
| $\eta_{\mathrm{Si}}$ | Quantum efficiency ratio of Silicon | – |
| $\hat{W}$ | Raw signal acquired by IFTS (p. 44) or TERMITES (p. 47) | – |
| $N_s$ | Saturation capacity (or well depth) of a camera pixel | $e^-$ |
| $\xi_{\mathrm{PFC}}$ | Radial Group Delay caused by PFC | fs/mm$^2$ |
| $\xi^m_{\mathrm{curv}}$ | Curvature Group Delay of TERMITES reference at measurement plane | fs/mm$^2$ |
| $\Delta\tau_{\mathrm{curv}}$ | Delay range due to curvature of the TERMITES reference beam | fs |
| $\Delta\tau_c$ | Delay range due to temporal coherence of the TERMITES input beam | fs |
| $\Delta\tau$ | TERMITES delay range | fs |
| $\delta\tau$ | TERMITES delay step size | fs |
| $T$ | Group delay | fs |
| $\tau_c$ | Coherence time | fs |
| $\tau$ | Interferometer delay difference | fs |
| $\varepsilon$ | Spectral Fluence *or* Spatially-resolved spectrum (p. 22) | J/cm$^2$/nm |
| $F$ | Fluence | J/cm$^2$ |
| $S$ | Spectrum (energy spectral density) | J/nm |
| $\varepsilon^T$ | Total pulse energy | J |
| $\delta_x$ | Spatial sampling step size (camera pixel size) | µm |
| $L_R$ | Propagation distance between reference plane and measurement plane | mm |
| $f_R$ | Focal length of TERMITES convex mirror | mm |
| $\boldsymbol{r}$ | Radial position in the beam | mm |
| OPD | Optical Path Difference | nm |
| $\lambda_0$ | Central wavelength of a broadband laser field. | nm |
| $\omega_{\mathrm{max}}$ | Nyquist angular frequency | rad/fs |
| $\omega_0$ | Central angular frequency | rad/fs |
| $\varphi_{\mathrm{PFC}}$ | Phase generated by a curved pulse front | rad |
| $\varphi^m_{\mathrm{curv}}$ | Curvature phase of the reference of TERMITES, at measurement plane | rad |
| $\varphi^r_{\mathrm{curv}}$ | Curvature phase of the reference of TERMITES, at reference plane | rad |
| $\varphi_{\mathrm{curv}}$ | Phase generated by a curved wavefront | rad |
| $\hat{\varphi}$ | Temporal phase | rad |
| $\varphi$ | Spectral phase | rad |
| $I_0$ | Peak intensity in the far-field | W/cm$^2$ |
| $I$ | Irradiance (oftentimes written *intensity*) | W/cm$^2$ |

# List of Abbreviations

| Name | Description | First occurrence |
|---|---|---|
| **TERMITES** | Total E-field Reconstruction using a Michelson Interferometer TEmporal Scan | p. 4 |
| **CCD** | Charge Coupled Device | p. 14 |
| **CMOS** | Complementary Metal–Oxide–Semiconductor | p. 14 |
| **CPA** | Chirped Pulse Amplification | p. 2 |
| **CPLC** | Chirped Pulses with Longitudinal Chromatism | p. 3 |
| **CPSD** | Cross Power Spectral Density | p. 45 |
| **FFT** | Fast Fourier Transform | p. 51 |
| **FROG** | Frequency-Resolved Optical Gating | p. 17 |
| **FTS** | Fourier Transform Spectroscopy | p. 44 |
| **FWHM** | Full Width at Half Maximum | p. 11 |
| **GDD** | Group Delay Dispersion | p. 13 |
| **HCF** | Hollow-Core Fiber | p. 11 |
| **IFTS** | Imaging Fourier Transform Spectroscopy | p. 44 |
| **PDI** | Point Diffraction Interferometry | p. 45 |
| **PFC** | Pulse Front Curvature | p. 26 |
| **PFT** | Pulse Front Tilt | p. 24 |
| **PIC** | Particle-in-cell | p. 36 |
| **QWLSI** | Quadri-Wave Lateral Shearing Interferometry | p. 15 |
| **RGD** | Radial Group Delay | p. 105 |
| **RSI** | Radial Shearing Interferometry | p. 55 |
| **SHG** | Second Harmonic Generation | p. 17 |
| **SPIDER** | Spectral Phase Interferometry for Direct Electric-field Reconstruction | p. 18 |
| **SPM** | Self Phase Modulation | p. 11 |
| **SRSI** | Self-Referenced Spectral Interferometry | p. 60 |
| **TOD** | Third Order Dispersion | p. 13 |
| **WFS** | WaveFront Sensor | p. 33 |

# Introduction

---

Since the 1970s, the fast-paced development of ultrafast laser systems has revolutionized multiple scientific and industrial fields [1]. Such devices are capable of producing short pulses of coherent light lasting typically less than one picosecond. Today, most ultrashort lasers provide pulses of a few tens of femtoseconds using mode-locked Ti:Sapphire oscillators, and are used routinely in many different applications. For instance, the brevity of femtosecond laser pulses is employed in femtochemistry to capture ultrafast events in so-called pump-probe experiments [2]. Femtosecond pulses are also often used whenever fine material processing is needed, for instance in laser micro-machining [3] or laser eye surgery [4]. In such applications, the electric field of femtosecond pulses is used to locally generate a plasma on the target surface without transferring too much energy—and heat—to the surrounding material.

The key-idea behind *ultra-intense* laser experiments is to concentrate as much optical energy as possible in an ultrashort femtosecond pulse, before focusing it in a micrometer-scale area. The peak intensity $I_0$ (or peak irradiance, in $\mathrm{W/cm^2}$) achieved at focus is used to immediately ionize the target material and accelerate its particles to tremendous speeds. The exact nature of the subsequently emitted radiation depends on the actual peak intensity, but also on the target composition and on its state (solid, gas, plasma) before ionization. Starting from $I_0 = 10^{14}\,\mathrm{W/cm^2}$, attosecond XUV pulses can be generated from the non-linear response of atoms, molecules or even solids to the ultra-intense pulse [5–7]. Such extremely short pulses are typically used in highly resolved pump-probe experiments to study the attosecond-timescale dynamics of electrons [8]. From $I_0 = 10^{18}\,\mathrm{W/cm^2}$, electrons and ions are accelerated by the pulse electric field to relativistic speeds. Laser wakefield acceleration [9–11] is used to produce mono-energetic electron beams which recently reached an energy of 8 GeV [12]. Ions, for their part, can also be accelerated up to a few tens of MeV [13–15]. Today, one of the most challenging goals resides in reaching the *Schwinger limit* of $I_0 = 10^{29}\,\mathrm{W/cm^2}$. This intensity value constitutes the theoretical frontier to new quantum electrodynamics (QED) regimes, where vacuum is ripped apart and electron-positron pairs are produced in the strong electric field [16, 17].

In order to achieve these objectives, high-power laser systems [18] are used to generate amplified femtosecond pulses which are then focused in experimental chambers. Many different facilities are spread over the world and combine various technologies with the objective of achieving the highest peak powers to explore new regimes of physics [19]. At CEA, UHI–100 delivers 25 fs pulses and reaches the peak-power of 100 TW. The Apollon laser, for its part, is planned to provide 150 J pulses of 15 fs duration, which should therefore generate peak powers of 10 PW in 2020 [20].

Despite the complexity of high-power femtosecond systems, the maximum peak intensity is ultimately limited by only a few fundamental obstacles. One of the most challenging limit has been the damaging of optics in the laser itself, before pulses had any chance of reaching the experimental target. Very high peak powers were experienced along the laser chain, which caused non-linear self-focusing and laser-induced breakdown in amplifying crystals, mirrors and lenses. *Chirped Pulse Amplification* (CPA) was applied to high-power lasers in 1985 [21–23] in order to overcome this major difficulty. The principle of CPA can be understood quite intuitively: low-power femtosecond pulses produced by the Ti:Sapphire mode-locked oscillator are stretched in time at the very beginning of the laser chain. This enables their amplification to high energy while keeping the instantaneous power sufficiently low. In this situation, laser optics are preserved even though the pulse energy is considerably amplified. At the very end of the amplification chain, the energy contained in individual pulses typically reaches the joule level and is spread over hundreds of picoseconds. One last step is required to generate high-power pulses: re-compressing the amplified pulses back to durations of a few femtoseconds. This is possible because a particular effort is made all along amplification to keep the spectrum of generated pulses broadband, which is a necessary condition to achieve ultrashort durations.

Let us focus on the subject of interest for this work: ultrafast metrology. Similarly to any other large-scale instrument like particle accelerators or gravitational-wave observatories, the good working order of high-power lasers is subject to numerous critical parameters that have to be monitored closely. Well before the advent of lasers, Lord Kelvin delivered a lecture about electrical measurement [24, p. 73], and started his presentation by a very universal statement:

> When you can measure what you are speaking about, and express it in numbers, you know something about it; but when you cannot measure it, when you cannot express it in numbers, your knowledge is of a meagre and unsatisfactory kind: it may be the beginning of knowledge, but you have scarcely, in your thoughts, advanced to the stage of science.

This quote remains truthful when speaking about high-power lasers : *advancing to the stage of science* would not have been possible without careful measurement and interpretation of pulse properties. For this purpose, measurement of the temporal intensity profile has historically played a decisive role. Temporal characterization became challenging since pulse durations got lower than a few picoseconds because shorter time-scales are not resolved by photodiodes or streak cameras. This fundamental limitation of electronic response times led to the development of several measurement techniques in order to follow the successive improvements in pulse duration up to the attosecond-scale [25, 26]. Among the different temporal measurement techniques, some of them—such as FROG or SPIDER—are actually standard metrology tools in the field, and are used routinely to obtain reliable pulse duration measurements.

Because of their very large output diameters—sometimes up to tens of centimeters—high-power laser beams must also be characterized in the spatial dimension. It is indeed necessary to properly measure and control the wavefront of pulses in order to focus them as tightly as possible on target, and obtain higher intensities. Corrections of laser wavefront is generally done using deformable mirrors, and its measurement can be performed using different well-established measurement device such as Shack-Hartmann sensors [27, 28] or multiple-wave lateral shearing interferometers [29, 30].

Despite the continuous metrology improvements made in the last decades, chromatic effects (also called *spatio-spectral couplings*) is often overlooked in high-power systems. This is a major issue in high-intensity experiments, because when a chromatic beam gets focused by a perfect optic, the different frequency components are all focused differently on target, which spreads the pulse energy over a larger area and decreases the peak intensity. For the moment, this kind of aberrations cannot be measured quantitatively in a simple way using the previously mentioned techniques. Chromatism is well-known in various fields—like opthalmology or optical astronomy—but has a specific consequence when it affects ultrashort pulses. Since temporal and spectral properties of ultrashort pulses are related by a Fourier transform, the spectral dependence of pulse spatial properties is equivalent to a spatial dependence of its temporal properties—which is also called *spatio-temporal couplings*. It means that in addition to the spatial energy spread at focus caused by chromatism, the pulse energy is also spread in time. Numerous sources of chromatism coexist in a CPA laser chain. Some of its constitutive components such are stretchers and compressors are literally based on the introduction of controlled amounts of chromatism in ultrashort pulses. In some cases, it can be improperly compensated, which is the most common reason for residual spatio-spectral and spatio-temporal couplings in the laser beam. More complex effects can also be generated in amplifiers or in simple telescopes that are used to resize the beam between each stage of the laser chain.

Nonetheless, spatio-temporal couplings can also be beneficial if introduced in a controlled way. The *ultrafast lighthouse effect* is notably employed in high-harmonic generation to isolate attosecond pulses using wavefront rotation [31, 32]. Recently, *Chirped Pulses with Longitudinal Chromatism* (CPLC)—also called *Flying focus*—have been extensively studied and enabled the fine control of intensity peak velocity at focus [33–37]. In more remote fields, transversally accelerating pulses are for example employed for precise glass nano-machining [38]. *Simultaneous spatial and temporal focusing*—which is used in biology for tissue ablation and microscopy—is also based on femtosecond pulses which are shaped spatio-temporally [39].

To sum up, spatio-temporal couplings are detrimental for effective intensity on target, but can also be beneficial if controlled accurately. In either case, experimentalists need to have reliable spatio-temporal measurement devices at their disposal. Many different techniques have been developed to provide quantitative information about the spatio-temporal profile of measured pulses [40]. However, none of them are widely adopted or considered as a metrology standard. This is partly due to the fact that most of existing techniques are complex to implement and provide results that prove to be difficult to interpret rigorously. However, the main obstacle to standardization of spatio-temporal measurements—and to global awareness about spatio-temporal couplings—is the absence of any commercial measurement device on the market. This implies that each published spatio-temporal measurement is carried out using different homemade techniques which all have varying weaknesses and precision. In this situation, fixing spatio-temporal couplings in ultra-intense lasers is impossible, and estimating the actual peak intensity on target is highly speculative.

TERMITES is a spatio-spectral characterization technique that has been developed since 2014 at the CEA LIDYL laboratory. This device, based on Fourier Transform Spectroscopy (FTS), has the advantage of providing full 3D information about the measured pulse while remaining simple in terms of optical set-up. Previous PhD theses were conducted on this subject. V. Gallet notably worked on the technique principles and contributed to develop a first prototype of the instrument at the end of his thesis [41]. G. Pariente continued the development of TERMITES [42] and vastly optimized the instrument. He chiefly worked on improving the design so that the full aperture of the UHI–100 laser could be characterized [43]. This work also led to a patent for the instrument [44], and to the discovery of a major unanticipated spatio-spectral coupling on the UHI–100 laser chain.

At this stage of the project, both TERMITES and the associated numerical processing of measured data were proof-of-concepts. In order to become a standard spatio-temporal characterization technique, TERMITES had to be extensively tested and improved. It had to be used in various realistic conditions in order to validate its good adaptability to characterize various types of systems. Then, a new prototype had to be manufactured in order to facilitate the use of TERMITES in a wide range of high-power broadband laser facilities. This first work package—oriented towards industrial development of the technique—was the first reason why Amplitude Laser Group and CEA LIDYL proposed a new joint thesis on this subject (in a french CIFRE contract).

Moreover, despite the recent increasing interest for spatio-temporal couplings in high-power lasers, chromatic aberrations generated in the various components of such systems are still largely unknown. The fact that TERMITES has the ability to retrieve highly-resolved 3D electric fields instead of solely quantifying specific couplings is crucial. This constitutes a powerful tool by enabling general spatio-temporal surveys without any assumption. For that reason, spatio-temporal characterization of various laser systems was the second main objective of my thesis, which was more oriented towards experimental research.

## Outline

This manuscript describes the results that we obtained in order to achieve the two main objectives of the thesis. In the first part, I briefly remind the general principles about the generation of high-power femtosecond pulses. Purely-temporal and purely-spectral measurement techniques are then quickly reviewed. Following this introduction, we get to the heart of the matter by introducing spatio-temporal couplings and their sources. The main spatio-temporal characterization techniques are finally presented. This part provides—I hope—a clear view of the spatio-temporal metrology landscape before starting the more detailed study about TERMITES.

The second part of this manuscript is dedicated to the first objective: improving the design of TERMITES, and studying both theoretically and experimentally its abilities and limitations. The influence of a few different design parameters is decisive for the good working order of TERMITES; we explain why in a dedicated chapter. Then, measurement perturbations are studied numerically and their effects on the retrieved electric field are quantified. The end of this second part is dedicated to extensive experimental tests that we carried out to validate the technique in practice.

Finally, the last part relates to the measurements that were conducted with TERMITES in order to establish the spatio-temporal quality of various laser systems—our second goal. We decided to firstly present a few crucial experimental aspects that can significantly improve the quality of measurement with TERMITES. All characterization measurements done during this thesis are then assembled in a last chapter, wherein the source of each measured spatio-temporal coupling is investigated. We decided to sort this last chapter in a logical order and to illustrate the discovered couplings for each of the standard CPA components, starting by the stretcher. We notably elaborate on the measurement done at the output of the petawatt laser BELLA, and describe the spatio-spectral couplings that have been observed on this system.

# Part I.

# Structure & Metrology of High-Power Femtosecond Pulses

Chapter 1.

# High-Power Femtosecond Laser Systems

This first chapter introduces essential concepts relative to high-power femtosecond lasers. We open the chapter by a brief description of their main building blocks, which will be particularly useful later in the manuscript to understand chromatic aberrations that are specific to CPA and post-compression. Then, ultrashort pulses are described analytically. We first express them in the temporal and spectral dimensions, and then in the spatial domain. Finally, well-established metrology techniques are addressed. We chiefly explain the working principles of devices which are usually used to measure purely-spatial and purely-temporal properties of the ultrashort pulses.

## Contents

**1.1. Generation of High-Power Femtosecond Pulses** . . . . . . . . . . . . . . . . . . . . . . . . . . . . 10
  1.1.1 Chirped Pulse Amplification
  1.1.2 Post-compression
**1.2. Description of the Generated Electric Field** . . . . . . . . . . . . . . . . . . . . . . . . . . . . . . . 12
  1.2.1 Spatial Description
  1.2.2 Temporal & Spectral Description
**1.3. Spatial & Temporal Metrology of High-Power Laser Systems** . . . . . . . . . . . . . . . . 14
  1.3.1 Purely-Spatial Metrology
  1.3.2 Purely-Temporal Metrology

## 1.1. Generation of High-Power Femtosecond Pulses

### 1.1.1. Chirped Pulse Amplification

During early design of high-power lasers, peak power was limited by optical damage and nonlinear phase distortion caused by the very high optical powers that were experienced by laser system components. Nowadays, the most intense laser systems are nearly all based on the Chirped Pulse Amplification (CPA) technique which lifted these obstacles in 1985 [21]. As illustrated by panel (a) in figure 1.1, the idea of CPA consists of stretching ultrashort pulses in time—from tens of femtoseconds to hundreds of picoseconds—before amplifying them. This lowers the peak power while enabling the amplification of pulses to tens of joules. At the very end of the amplification chain, the pulse is compressed temporally to its initial duration in order to achieve very large peak powers. This idea was originally filed in a patent at the end of World War II [45], with the goal of improving the range of radar systems which were also limited by instantaneous power at the time [46]. Forty years later, the concept was applied to high-power lasers by Strickland and Mourou [21] and then implemented and tested more extensively [22, 23].

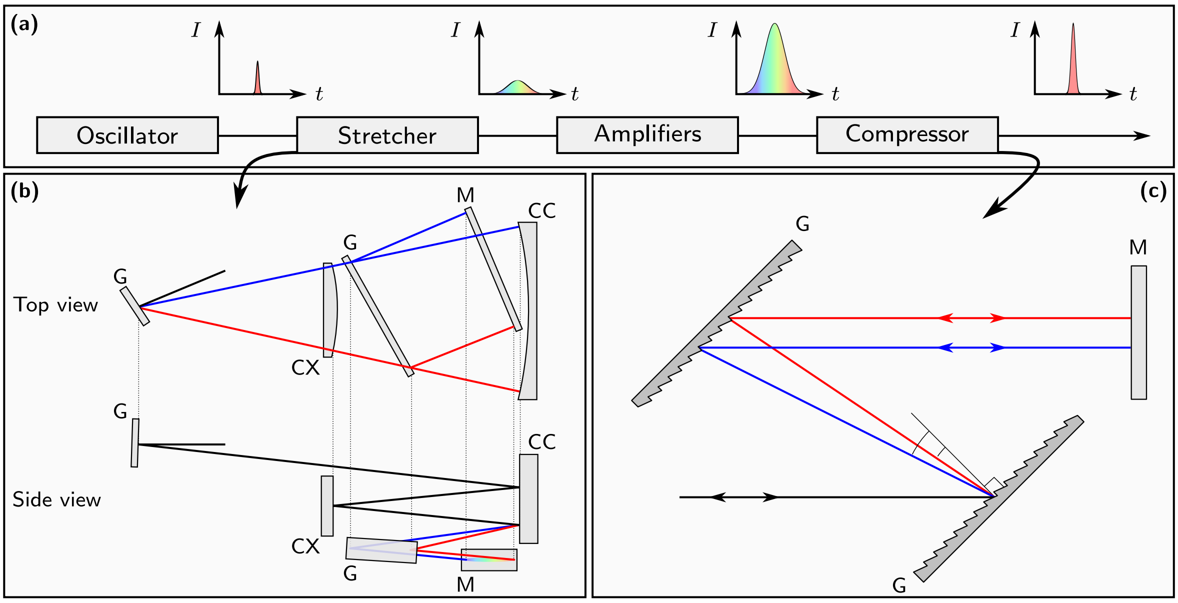

**Figure 1.1.: Main building blocks composing CPA-based laser systems. (a)** Femtosecond pulses are stretched in time before being amplified. They are re-compressed at the end of the chain. **(b)** Diagram of an Offner stretcher, viewed from the top and from the side (inspired from [47, fig.2]). **(c)** Diagram of a grating-based compressor. **G:** Grating, **M:** Plane mirror, **CX:** Convex mirror, **CC:** Concave mirror

In most current high-power lasers, stretching is accomplished using an Offner stretcher. This fundamental building block is based on an original imaging system invented by Offner in 1971 [48]. Ten years later, this system was analyzed extensively by Suzuki *et al.* [49], who notably pointed out that it is theoretically free from any aberration in the horizontal plane. Offner's set-up was then combined to diffraction gratings—as shown on panel (b) of figure 1.1—and applied to high-power lasers to stretch ultrashort pulses by four orders of magnitude [47, 50, 51]. The general idea behind this concept consists of adding a strong positive Group Delay Dispersion

(GDD, quadratic spectral phase) to the low power femtosecond beam. This has the effect of spreading the pulse energy over a longer period of time, effectively reducing its peak power. Offner stretchers add this positive GDD by making the optical path of high frequencies longer than the optical path of low frequencies.

Most of high-power femtosecond lasers currently available [18, 19] employ Ti:Sapphire amplifiers in order to increase the energy of stretched pulses. This solid-state amplifying medium has indeed great qualities that makes it a solution of choice. Notably, its large bandwidth (640–1100 nm) allows the amplification of very short pulses [52], and it has a large energy storage density compared to other materials. More recently, projects for multi-petawatt femtosecond systems [19, 53] have been proposed and use non-linear Optical Parametric Amplification (OPA) to replace or complement Ti:Sapphire amplifiers. This promising way of producing high-power femtosecond pulses is however not well-spread for the moment, and all lasers studied experimentally during my thesis were based on solid-state amplification in Ti:Sapphire crystals.

After their amplification by the successive amplifiers, high-power pulses are most of the time compressed using grating compressors [54]. This set-up is essentially in charge of canceling the positive GDD added by the stretcher at the beginning of the laser chain, by adding an identical amount of negative GDD. As illustrated by panel (c) of figure 1.1 on the facing page, grating compressors are much simpler than Offner stretchers. Optimal re-compression is ensured by precisely tuning the amount of GDD. This is done experimentally by adjusting the distance between gratings [55, p. 540].

### 1.1.2. Post-compression

In Ti:Sapphire based CPA chains, the output pulse duration is usually Fourier-transform limited to $\simeq 20\,\text{fs}$ owing mainly to gain narrowing in amplifiers. Some specific applications—such as attosecond-pulses generation—highly benefit from even lower pulse duration and higher repetition rates. Post-compression in non-linear media can be used to broaden the spectrum of a femtosecond laser beam and decrease its Fourier-limited duration, as illustrated by figure 1.2.

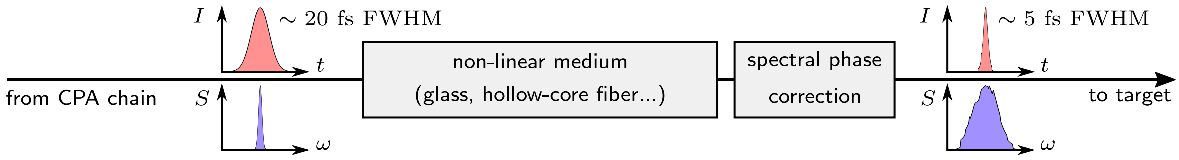

**Figure 1.2.: General concept of post-compression in non-linear media.** FWHM stands for *Full-Width at Half Maximum.*

A few implementations of this idea are in use nowadays, but one of the most efficient method since 1996 is probably post-compression in Hollow-Core Fibers (HCF) [56, 57]. This technique consists of focusing amplified mJ-level pulses into a hollow-core (porous) optical fiber filled with rare gas. During their propagation in the HCF, pulses experience Self-Phase Modulation (SPM) which broaden their spectrum. After compensation of residual spectral phase, output pulses are compressed to a few femtoseconds.

## 1.2. Description of the Generated Electric Field

Ultrashort pulses generated by lasers—and electromagnetic waves in general—are typically described in three dimensions as a complex-valued function $\hat{E}$. This function depends on time $t$, and on the two spatial dimensions $x$ and $y$ which are transverse to the direction of propagation:

$$\hat{E}(x,y,t) = \hat{A}(x,y,t)\, e^{\mathrm{i}\,\hat{\varphi}(x,y,t)} \ . \tag{1.1}$$

In this expression, $\hat{E}(x,y,t)$ is the electric field, $\hat{A}(x,y,t)$ its amplitude and $\hat{\varphi}(x,y,t)$ the phase expressed in radians. Generally, the intensity $I(x,y,t)$ (expressed in $\mathrm{W/cm^2}$) has more physical meaning than amplitude, so we will use this quantity far more often in the rest of this manuscript. In vacuum, $I(x,y,t)$ is written:

$$I(x,y,t) = \frac{c\epsilon_0}{2}\hat{A}(x,y,t)^2 \ , \tag{1.2}$$

with $c$ the velocity of light, and $\epsilon_0$ the vacuum permittivity[1].

Generally, the pulse electric field $\hat{E}(x,y,t)$ is described either in the temporal domain, or in the spatial domain. In the next few pages, we will adopt both perspectives independently to describe the field and explain how it is measured in most laser facilities.

### 1.2.1. Spatial Description

The pulse electric field can first be considered in a purely-spatial approach. In this case, we define the field as a complex-valued quantity written:

$$E(x,y) = \sqrt{F(x,y)}\, e^{\mathrm{i}\,\varphi(x,y)} \ , \tag{1.3}$$

where $F(x,y)$ is the fluence, expressed in $\mathrm{J/cm^2}$ and $\varphi(x,y)$ is the spatial phase in radians.

As its unit suggests, fluence is obtained by integrating intensity along the temporal dimension. It corresponds to the energy received by a surface, per unit area:

$$F(x,y) = \int \mathrm{d}t \; I(x,y,t) \ . \tag{1.4}$$

Usually, fluence profiles of high-power femtosecond lasers are *top-hat*, which means that fluence is nearly-uniform on a central disk, and rapidly goes to zero on the edges.

### 1.2.2. Temporal & Spectral Description

In a purely temporal approach, we consider that the field is fully homogeneous spatially. In this case, it is expressed as:

$$\hat{E}(t) = \sqrt{I(t)}\, e^{\mathrm{i}\,\omega_0\, t} \ . \tag{1.5}$$

---

[1] In the rest of this manuscript, intensity measurements are never absolute and most often expressed in arbitrary units. Therefore, we sometimes assume that intensity is simply the square of the temporal amplitude.

Panel (a) of figure 1.3 shows a typical femtosecond pulse that is Gaussian in time and 20 fs long at half-maximum power.

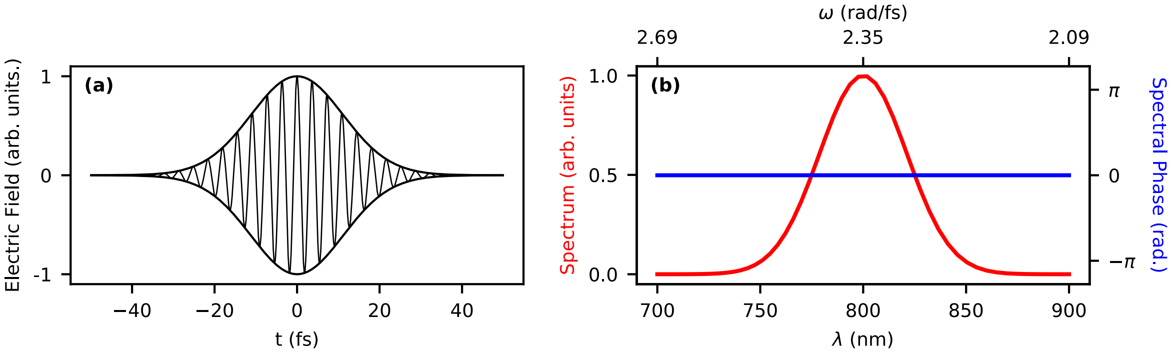

**Figure 1.3.: One-dimensional description of ultra-short pulses (simulation). (a)** Temporal evolution of the electric field $\hat{E}(t)$. Bold black line represents the electric field envelope, $\sqrt{I(t)}$. **(b)** Spectral view of the same pulse, wherein energy spectral density $S(\omega)$ is displayed in red, and spectral phase $\varphi(\omega)$ is displayed in blue.

Additionally to this temporal approach, oscillating signals are oftentimes described in the spectral domain. The mathematical operation linking these two domains is the Fourier transform:

$$E(\omega) = \mathcal{F}\left(\hat{E}(t)\right) = \int_{-\infty}^{+\infty} \mathrm{d}t\; \hat{E}(t)\, e^{-\mathrm{i}\,\omega\, t} = \sqrt{S(\omega)}\; e^{\mathrm{i}\,\varphi(\omega)}\ . \tag{1.6}$$

In this new equation, $S(\omega)$ is the energy spectral density—henceforth called *spectrum*—and $\varphi(\omega)$ is the spectral phase. Note that the reciprocal operation can be performed through inverse Fourier transform, which means that spectrum and spectral phase fully determine the temporal distribution of energy.

Because of the time-frequency uncertainty principle, the fact that ultrashort pulses have a finite duration implies that they cannot be described in the spectral domain by a single carrier component $\omega_0$. Instead, the spectrum $S(\omega)$ is a continuous frequency distribution centered around the carrier $\omega_0$, as shown in panel (b) of figure 1.3.

Spectral phase represents the synchronization of frequency components. A flat spectral phase such as the one displayed in figure 1.3 signifies that the field of all frequency components will eventually add up constructively at one specific time, triggering the apparition of an ultrashort pulse. On the contrary, most spectral phase degradation will weaken the peak power by spreading some energy before or after the temporal peak. In order to differentiate spectral phase effects, this quantity is generally expressed as Taylor series:

$$\varphi(\omega) = \varphi_0 + \varphi_0'\,(\omega-\omega_0) + \frac{1}{2!}\varphi_0''\,(\omega-\omega_0)^2 + \frac{1}{3!}\varphi_0'''\,(\omega-\omega_0)^3 + \mathcal{O}(\omega^4)\ , \tag{1.7}$$

where

$$\varphi_0' = \left.\frac{\partial\varphi(\omega)}{\partial\omega}\right|_{\omega=\omega_0}\ , \quad \varphi_0'' = \left.\frac{\partial^2\varphi(\omega)}{\partial\omega^2}\right|_{\omega=\omega_0}\ , \text{ and } \quad \varphi_0''' = \left.\frac{\partial^3\varphi(\omega)}{\partial\omega^3}\right|_{\omega=\omega_0} \tag{1.8}$$

are respectively the Group Delay, the Group Delay Dispersion (GDD) and the Third Order Dispersion (TOD). Spectral phase can be decomposed into an infinite number of terms.

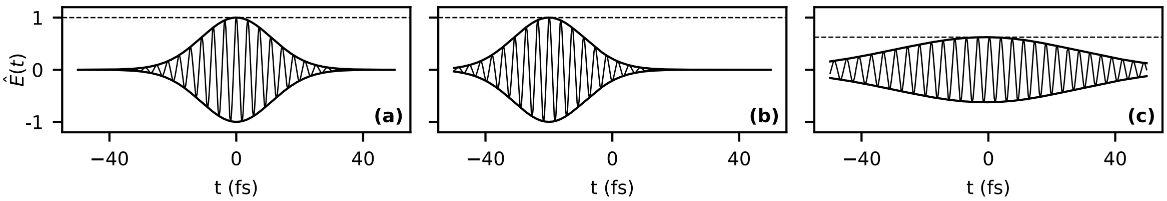

**Figure 1.4.: Effect of group delay (b) and group delay dispersion (c) on an ultrashort pulse.**

The temporal consequence of the two first orders—illustrated on figure 1.4—is of particular importance. $\varphi_0'$ is the first order derivative of the spectral phase and hence has the dimension of a delay. This particular term shifts every spectral component in time, but *keeps them synchronized with respect to each other*. Temporally, this is simply a delay which does not change the shape of the pulse.

$\varphi_0''$ for its part, is the quadratic term of spectral phase called Group Delay Dispersion. It can be interpreted as the first order derivative of $\varphi_0'$ and therefore as a *chromatic* delay, i.e., a delay which depends on frequency. As a consequence, pulses having Group Delay Dispersion are *chirped* temporally and their carrier frequency depends linearly on time. This reduces the peak power of the pulse by increasing its duration.

## 1.3. Spatial & Temporal Metrology of High-Power Laser Systems

In this section, we go over the main instruments that are used routinely by experimentalists to characterize ultrashort pulses. Generally speaking, quantities derived from energy such as intensity or fluence are easily measured because these observables can be sensed by various optoelectronic devices. However, obtaining the phase is always more complicated, because it is not a physical quantity—despite being essential to describe the pulse shape. Therefore, clever methods have to be found in order to obtain it indirectly in the spatial domain or in the temporal/spectral domain.

### 1.3.1. Purely-Spatial Metrology

Experimentally, fluence—defined in equation (1.4) on page 12—is measured very easily with image sensors which are based on the Charge Coupled Device (CCD) or Complementary Metal–Oxide–Semiconductor (CMOS) technologies. Silicon-based cameras typically have pixels of 5 to 10 µm in width, which gives very good resolution when large beams are measured, like before focusing. If the beam is too small (at focus for example), then it can be expanded with an imaging set-up in order to use all the chip of the camera and increase the resolution. Moreover, silicon-based cameras are usually able to capture all wavelengths contained in the measured laser pulses, because the bandwidth of high-power laser is most of the time limited to wavelengths between 700 and 900 nm.

There are many different documented ways to appreciate the spatial quality of a laser beam in fluence [58, 59] or in phase [60]. For instance, users can extract the mode diameter from fluence profile in near-field or in far-field and compare it to theoretical values. Secondary quantities can also be computed, such as the $M^2$ parameter which is a good indicator of spatial focusability [61].

As we explained before, spatial phase, is actually less accessible than fluence. Its measurement in ultrashort laser systems is carried out using three main techniques:

**Shack–Hartmann wavefront sensor (SHWFS)** is a self-referenced device where the input wavefront is sampled using an array of small lenses [27, 28]. As illustrated by figure 1.5, each lens focuses its sampled sub-aperture to a camera sensor, where fluence is measured. The resulting image consists of a matrix of focal spots, of which the individual centroid positions give an information about the local *slope* of the wavefront at each sub-aperture. Specific algorithms are dedicated to the reconstruction of the wavefront from Hartmanngrams.

**Quadri-wave lateral shearing interferometry (QWLSI)** is similar to the Shack-Hartmann technique because of the way it is used; QWLSI is also a small standalone device that simply needs to be placed in the path of the collimated beam to be characterized. However, its working principle is quite different [29, 30]. The mask used in this technique is not a micro-lenses array anymore, but a custom 2D transmission grating composed of regularly spaced pinholes. The fluence profile formed on the camera sensor is classically analyzed as an interference pattern between vertical and horizontal diffraction orders of the input beam through the mask. Analysis is similar to classical lateral shearing interferometry, wherein the phase is retrieved from the interferogram via Fourier processing. Advantage of QWLSI over Shack–Hartmann devices is its higher resolution and better dynamic range [30].

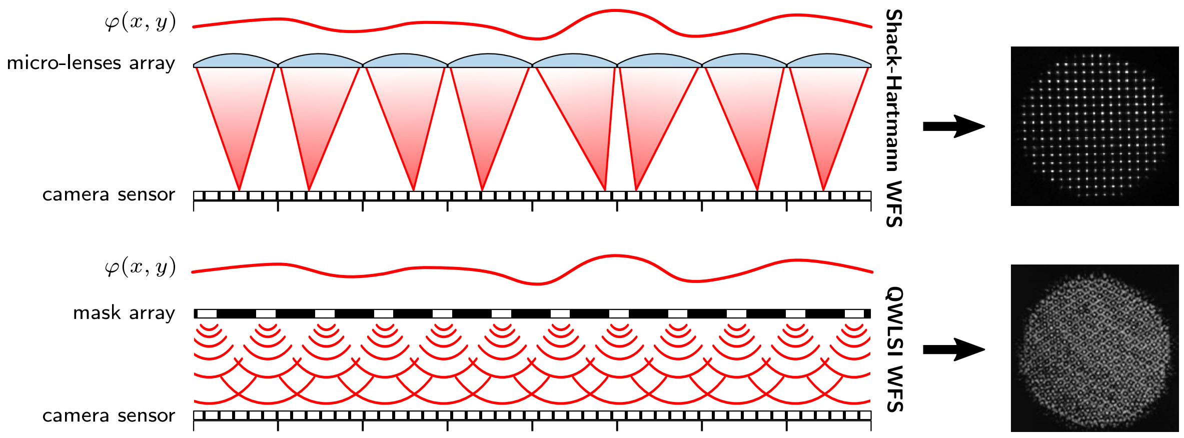

**Figure 1.5.: Two standalone devices used for laser wavefront measurement.** The output of the Shack-Hartmann sensor is composed of local focal spots, whereas the output of the QWLSI is an interference pattern resulting from the overlap of the mask array diffraction orders.

**Phase Retrieval** is a third approach to wavefront measurement, and is strongly based on numerical processing [62, p. 141]. This technique consists of measuring the fluence profile of the measured beam at multiple optical planes separated by propagation in free space. These measurements taken individually are only partial views of the actual field because the sole measured quantity is fluence. However, wavefront can be deduced numerically from the evolution of profile between each plane, because the relation between each plane is known. This inversion problem is typically solved using the Gerchberg–Saxton algorithm [63] or gradient-descent methods [64]. Although this method can theoretically be used on col-

> limated beams, it is actually applied around focal position, wherein the fluence profile changes faster with longitudinal position and retrieval algorithms converge more easily.

One of the most used figure of merit to assert the *quality* of a wavefront is the Strehl ratio [65]. This quantity is computed as the ratio between the maximum fluence obtained at focus ($\max F_k$), and the maximum fluence achievable at focus ($\max F_k^0$), if the wavefront was perfectly flat:

$$SR_{\text{WFS}} = \frac{\max F_k}{\max F_k^0} \ , \tag{1.9}$$

with:

$$\begin{array}{l} \bullet \quad F_k = \mathcal{F}\left(\sqrt{F(x,y)}\, e^{\mathrm{i}\,\varphi(x,y)}\right) \\ \bullet \quad F_k^0 = \mathcal{F}\left(\sqrt{F(x,y)}\, e^{\mathrm{i}\times 0}\right) \end{array} . \tag{1.10}$$

This definition of Strehl ratio is particularly suited to characterize high-power lasers, where the goal is to produce the highest intensity at focus. In the approximation that no spatio-spectral coupling affects the measured field, $SR_{\text{WFS}}$ can be used to estimate directly the intensity loss caused by wavefront imperfections. We will explain in more details at the end of chapter 2 that this is not so simple when the wavefront depends on frequency.

### 1.3.2. Purely-Temporal Metrology

When it comes to optimizing the peak intensity generated at focus of a high-power laser beam, temporal characterization is as important as spatial characterization, and certainly more challenging. Because time scales are so small, the fastest photodiodes are far from being able to measure the properties of any femtosecond pulse. Simultaneously with the general improvement of ultrafast science in the last decades, new methods had to be found in order to resolve temporally the pulses. Many different techniques have been designed progressively, and were used to define new ultrafast metrology standards [66, 67]. In their review of ultrashort characterization techniques [26], Walmsley and Dorrer state:

> The basic elements required for the complete [temporal] characterization of optical pulses are quite simple: at least one fast shutter or phase modulator, a spectrometer or an element to temporally stretch the pulse via dispersion, and one or two beam splitters.

Many different implementations were therefore invented to sample unknown pulses accurately and retrieve their temporal properties. As these techniques have already been reviewed and compared extensively [25, 26, 68], we will only go through the most ubiquitous devices to understand underlying concepts. Those will be useful in chapter 2 to understand more complicated spatio-temporal techniques.

### Intensity Autocorrelation

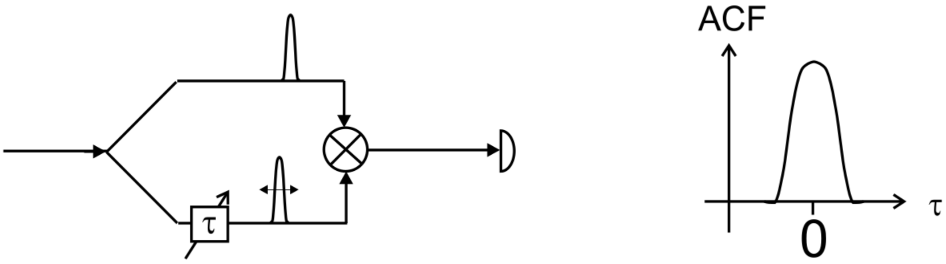

**Figure 1.6.: Autocorrelation technique principle. ACF:** Auto-Correlation Function. *Adapted[1] from G. Steinmeyer's review [68, fig.6]*

Intensity autocorrelation is probably the simplest solution to obtain a rough estimation of an ultrashort pulse duration. As shown in figure 1.6, the idea of this measurement device is to use a replica of the measured pulse as a sampling element for the measurement [69, p. 458] The replica is delayed with respect to the main pulse, and both pulses are then multiplied in a Second Harmonic Generation (SHG) crystal. The resulting $2\omega$ signal depends on delay between the two pulses, is maximum at zero-delay, and is symmetrical.

The fundamental issue of this technique resides in the fact that the reference is identical in duration and in shape to the unknown pulse. As a consequence, duration is estimated from the autocorrelation signal width, by assuming the analytic temporal shape of the pulse. Because the temporal shape of femtosecond pulses can be very far to Gaussian or $sech^2$ distributions, this method is considered very unreliable. However, intensity autocorrelation can be useful to do a first rough optimization of compression for instance, before using more complex tools to precisely retrieve the pulse shape.

### FROG

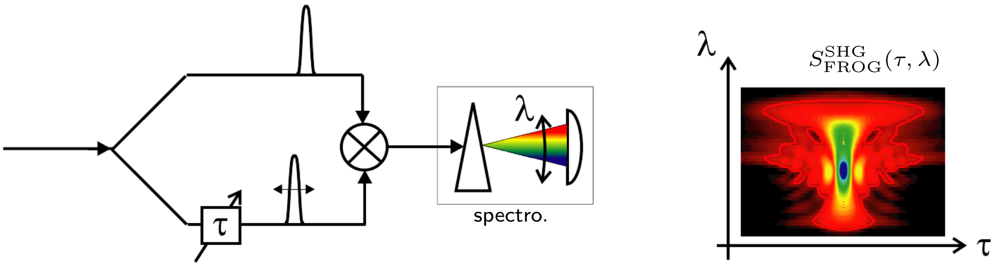

**Figure 1.7.: FROG technique principle.** *Adapted[1] from G. Steinmeyer's review [68]*

The SHG-FROG technique—among many other implementations of FROG [70]—can be seen as an improvement of the intensity autocorrelation technique in the sense that it adds spectral resolution to the detection device (see figure 1.7). The result of the FROG measurement is the peculiar 2D image $S^{\mathrm{SHG}}_{\mathrm{FROG}}$, which is simply the autocorrelation function resolved along another dimension which is wavelength:

---

[1] © IOP Publishing. Reproduced with permission. All rights reserved.

$$S^{\text{SHG}}_{\text{FROG}}(\tau,\lambda) = \left| \int \mathrm{d}t\ E(t)E(t-\tau)e^{-\mathrm{i}\omega t} \right|^2 \tag{1.11}$$

This SHG-FROG trace contains much more information than a simple autocorrelation function. The biggest difference in terms of result resides in the fact that the raw image produced by FROG can be inversed to retrieve the pulse shape. The algorithm responsible for this operation is very similar to the phase retrieval algorithm that we briefly described on p.15. Its precise working principles are described in details in a book dedicated to the technique [25, p. 157].

### SPIDER

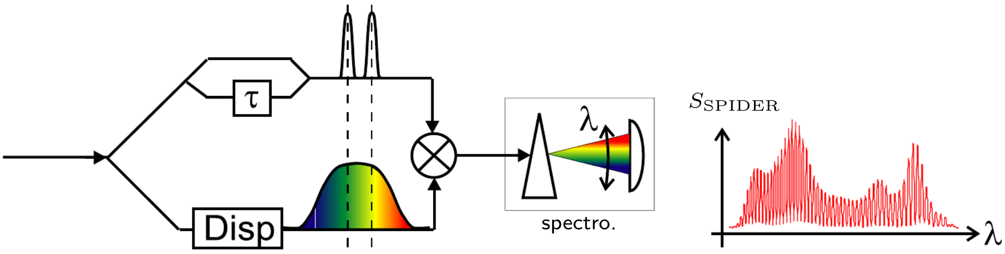

**Figure 1.8.: SPIDER technique principle.** *Adapted[1] from G. Steinmeyer's review [68]*

Finally, SPIDER [71] is a device which aims to retrieve the same information as FROG—spectrum and spectral phase—but using an interferometric approach. The set-up of SPIDER is summarized in figure 1.8. In this technique, two replicas of the beam are separated by a delay and summed non-linearly with a third replica which is chirped. This generates two frequency-doubled replicas of the pulse, of which the central frequencies are slightly shifted in relation to each other. This sheared overlap is then measured with a spectrometer, and the theoretical expression describing the result is the following:

$$S_{\text{SPIDER}}(\omega) = S(\omega) + S(\omega+\Omega) + 2\sqrt{S(\omega)\,S(\omega+\Omega)}\,\cos\left(\varphi(\omega) - \varphi(\omega-\Omega) - \omega\tau\right)\ , \tag{1.12}$$

with $\tau$ the delay, and $\Omega$ the spectral shear between the two up-converted signals. The last term of this equation oscillates in frequency with a period of $\frac{2\pi}{\tau}$ due to the delay between the two pulses. Processing this raw measurement is done by Fourier-transforming it in order to remove the time-series components around $t=0$ and $t=-\tau$. After an inverse Fourier transform and removal of the linear spectral phase, the spectral phase of the pulse is retrieved directly. This technique does not use any iterative algorithm such as for the FROG technique, which makes it very precise and robust.

⁂

In this first chapter, we laid the foundations for the rest of the manuscript, which will be dedicated specifically to defects called *spatio-temporal couplings*. This involved explaining the basic principles about ultra-short pulses and high power lasers. Finally, we went over the main techniques that are used for the purely-spatial or purely-temporal characterization of pulses in the absence of spatio-temporal couplings.

Chapter 2.

# Spatio-Temporal Couplings in High-Power Lasers

In chapter 2, we will introduce the main matter concerning this thesis: Spatio-temporal couplings. They are firstly introduced in sections 2.1 and 2.2. Instead of developing the concept of spatio-temporal couplings in a general and exhaustive way, we chose to focus specifically on some emblematic couplings. The source of each coupling is explained theoretically, which will be helpful to understand experimental results in the rest of this manuscript.

Secondly, we will discuss about spatio-temporal measurement in sections 2.3 and 2.4. In the first section, we explain how spatio-temporal couplings are diagnosed currently and what are the main principles of spatio-temporal metrology. In the last one, we investigate some ways to interpret three-dimensional complex-valued datasets obtained from spatio-temporal metrology.

## Contents

**2.1. Spatio-Temporal Description of the Electric Field** ........ 22
**2.2. Definition & Examples of Space-Time Couplings** ........ 23
  2.2.1 Spatially Linear Spatio-Temporal Couplings
  2.2.2 Spatially Quadratic Spatio-Temporal Couplings
  2.2.3 Spatio-Spectral Streak

**2.3. Spatio-Temporal & Spatio-Spectral Characterization** ........ 30
  2.3.1 Spatially Resolved Spectral Measurement
  2.3.2 Spectrally Resolved Spatial Measurement

**2.4. Interpretation of Spatio-Temporal Measurements** ........ 36
  2.4.1 Spectrally-Resolved Zernike Polynomials
  2.4.2 Spatio-Temporal Strehl Ratio

## 2.1. Spatio-Temporal Description of the Electric Field

In the previous chapter, we described the laser electric field $\hat{E}(x, y, t)$ as:

$$\hat{E}(x, y, t) \propto \sqrt{I(x, y, t)}\; e^{\mathrm{i}\,\hat{\varphi}(x,y,t)} \,, \tag{2.1}$$

with $I(x, y, t)$ its spatially-resolved intensity profile and $\hat{\varphi}(x, y, t)$ its *spatio-temporal* phase. We explained later in page 13 how a field described purely along the temporal domain could also be expressed along the spectral domain using the Fourier Transform. Similarly, Fourier transforming a 3D spatio-temporal field such as $\hat{E}(x, y, t)$ along its temporal dimension outputs the *spatio-spectral* field $E(x, y, \omega)$:

$$E(x, y, \omega) = \sqrt{\varepsilon(x, y, \omega)}\; e^{\mathrm{i}\,\varphi(x,y,\omega)} \,, \tag{2.2}$$

with $\varepsilon(x, y, \omega)$ the spatially-resolved spectrum—or *spectrally-resolved fluence*—and $\varphi(x, y, \omega)$ the spatially-resolved spectral phase.

Because of the large diameter of beams that are obtained at the output of high-power laser chains, the energy contained in each pulse is spread over a wide area. Pulses are therefore focused on the experimental target in order to concentrate their energy spatially and reach the maximum intensities. For this reason, we will differentiate collimated fields of large diameters—that we routinely call *near-field*—from fields which are observed around the focal plane of a focusing optic—called *far-field*. Admittedly, the terms *near-field* and *far-field* have a broader definition in optics, but are commonly used to designate those two specific planes in high-power laser facilities.

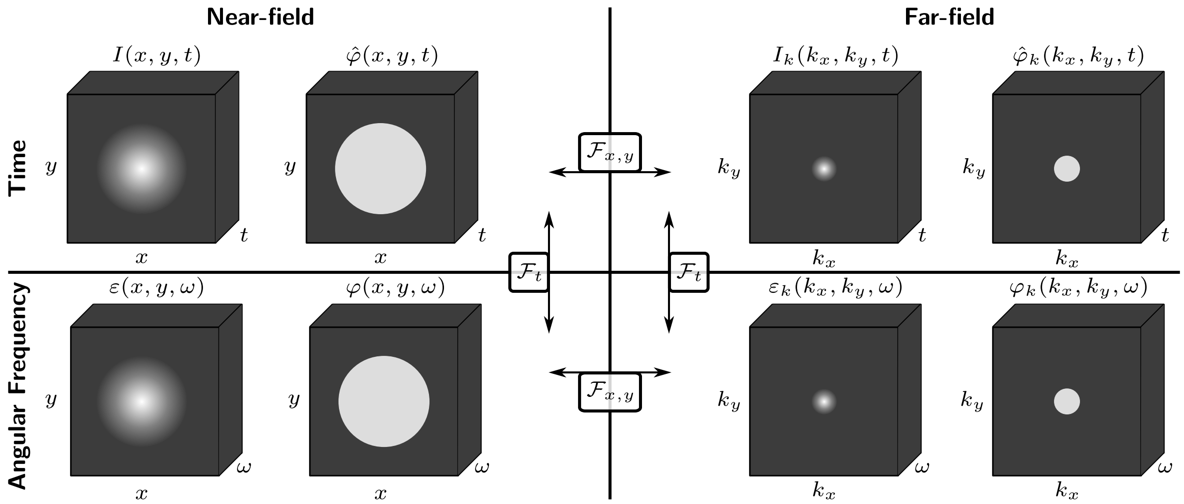
Near-field
Far-field
$I(x, y, t)$
$\hat{\varphi}(x, y, t)$
$I_k(k_x, k_y, t)$
$\hat{\varphi}_k(k_x, k_y, t)$
Time
$y$
$x$
$t$
$k_y$
$k_x$
$\mathcal{F}_{x,y}$
$\mathcal{F}_t$
$\mathcal{F}_t$
$\varepsilon(x, y, \omega)$
$\varphi(x, y, \omega)$
$\varepsilon_k(k_x, k_y, \omega)$
$\varphi_k(k_x, k_y, \omega)$
Angular Frequency
$\omega$
$\mathcal{F}_{x,y}$

**Figure 2.1.: Four domains of interest.**

This distinction between the two spatial domains adds a little complexity to our description because the electric field of an ultrashort pulse can now be described in four different domains, as illustrated by figure 2.1. Going from the near-field domain to the far-field is simply done by computing the two-dimensional Fourier transform along the transverse dimensions $x$ and $y$—owing to Fraunhofer diffraction [72, p. 101].

## 2.2. Definition & Examples of Space-Time Couplings

Before addressing the measurement of spatio-temporal couplings, let us describe what they are and shed some light upon their repercussion in the context of high-power laser systems. Conventional measurement devices presented in section 1.3 on page 14 perform measurement of ultrashort pulses separately in space and in time. These informations about fluence, spectrum or wavefront are used to estimate the spatial and temporal *focusability* of a given amount of energy—in joules—into a spatio-temporal volume—in fs·cm$^2$. In high-power laser applications, this volume must be as small as possible in order to achieve the highest peak intensities on target.

In most situations, the electric field $E(x, y, \omega)$ of the beam before focusing is assumed to be represented in the spectral domain by:

$$E(x, y, \omega) = \sqrt{F(x, y)\, S(\omega)}\, e^{\mathrm{i}\, \varphi(x,y)\, \varphi(\omega)} \, . \tag{2.3}$$

Here, $F(x, y)$ is the fluence which is measured with a camera and therefore integrated spectrally. $S(\omega)$ is a spectrum which is either measured at one spatial position or integrated by a lens over the whole aperture. $\varphi(x, y)$ is the wavefront measured with a wavefront sensor which integrates the actual spatio-temporal phase on the frequency axis. Finally, $\varphi(\omega)$ is the spectral phase which is also measured at one particular position or integrated in space.

The equivalent expression in the temporal domain is:

$$\hat{E}(x, y, t) = \sqrt{F(x, y)\, I(t)}\, e^{\mathrm{i}\, \varphi(x,y)\, \hat{\varphi}(t)} \, , \tag{2.4}$$

with $I(t)$ the temporal intensity profile at one position or integrated spatially, and $\hat{\varphi}(t)$ the temporal phase.

Both equations respectfully illustrate the spatio-spectral and spatio-temporal decoupling approximations, where the field is estimated as a simple product of purely-spatial and purely-temporal quantities. Alas, in a large number of practical situations, estimating the actual intensity at focus using this shortcut can lead to overly optimistic numbers. As a matter of facts, spatio-spectral and spatio-temporal couplings make equations (2.3) and (2.4) invalid. Indeed, spatial quantities (like fluence or spatial phase) depend in this case on the optical frequency or on time.

As we learned in the previous chapter, the spectral domain is linked to the temporal domain by a simple Fourier Transform. Therefore, a laser beam having *spatio-spectral* couplings also have *spatio-temporal* couplings—as demonstrated by G. Pariente in his thesis [42, p. 22]. Because of this equivalence, different types of spatio-spectral couplings are called by their temporal denomination and vice-versa, leading to a certain confusion about the definition of each coupling. Some very comprehensive studies [73, 74] were proposed to describe couplings in a formal way. While this approach is necessary to design chromatic optical systems carefully, we chose to only present in the next few pages some couplings which are recurrent in CPA-based laser systems.

### 2.2.1. Spatially Linear Spatio-Temporal Couplings

Spatially linear couplings are the most well-known, because they are used in massive amounts for stretching and compressing ultrashort pulses. In figure 1.1 on page 10, we explained that frequency components of ultrashort pulses are separated spatially in the stretcher and the compressor devices. Diffraction gratings generate *angular dispersion* which makes the propagation direction of the reflected beam depend on wavelength. After some propagation, the relative angle of different frequency components makes them fan out in the horizontal plane. In the case of stretchers and compressors, this effect is used to make the optical path length depend on wavelength, and to manage spectral phase of the output beam. Normally, the angular dispersion added by these devices is precisely canceled out at their output so that the different frequency components overlap in space, but also propagate in the same direction.

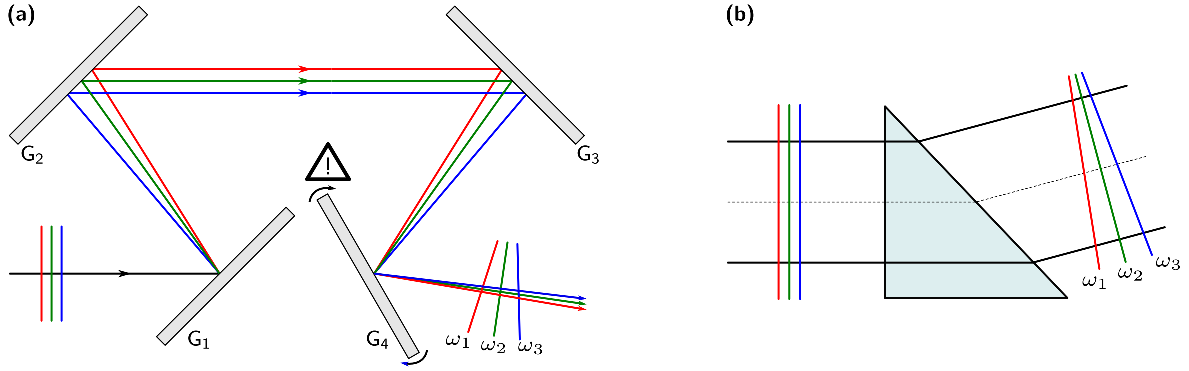
(a)
G$_2$
G$_3$
G$_1$
G$_4$
$\omega_1$ $\omega_2$ $\omega_3$
(b)
$\omega_1$ $\omega_2$ $\omega_3$

**Figure 2.2.: Two ways of adding Angular Dispersion (AD) to a broadband laser pulse. (a)** Angular dispersion added by a compressor wherein the last grating is misaligned. **(b)** Angular dispersion added by a prism. **G$_1$–G$_4$**: Compressor gratings. $\omega_1, \omega_2, \omega_3$: Example wavefronts at three different wavelengths.

In actual experimental conditions, small horizontal rotation of one of the compressor gratings can let residual angular dispersion remain in the output beam, as it is illustrated by panel (a) of figure 2.2. This imperfection adds angular dispersion which consists of a spatio-spectral phase written:

$$\varphi_{\mathrm{PFT}}(x, \omega) = \xi_{\mathrm{AD}}\, x\, (\omega - \omega_0) \tag{2.5}$$

with $\xi_{\mathrm{AD}}$ the angular dispersion coefficient, in fs/mm.

Additionally to the misaligned compressor, figure 2.2 also features—in panel (b)—one of the simplest ways to introduce angular dispersion in a broadband laser field. Refraction in the prism adds a tilt to the beam which depends linearly on the considered wavelength. The amount of angular dispersion can be calculated simply using Snell-Descartes law.

Until now, I defined angular dispersion as a wavefront tilt which depends on angular frequency through equation (2.5). In this equation, $\xi_{\mathrm{AD}}$ can also be seen as a spatially-dependent group delay, as its unit (fs/mm) suggests. As a matter of fact, angular dispersion is better known under the name of its temporal implication: *Pulse Front Tilt* (PFT). Examples of PFT are displayed in panels (a)–(c) of figure 2.3 on the facing page. This illustration shows that despite a perfectly plane wavefront, the intensity profile is tilted with respect to the wavefront in the $(x, t)$ domain. In practice, this means that the arrival time of the pulse depends on the horizontal position.

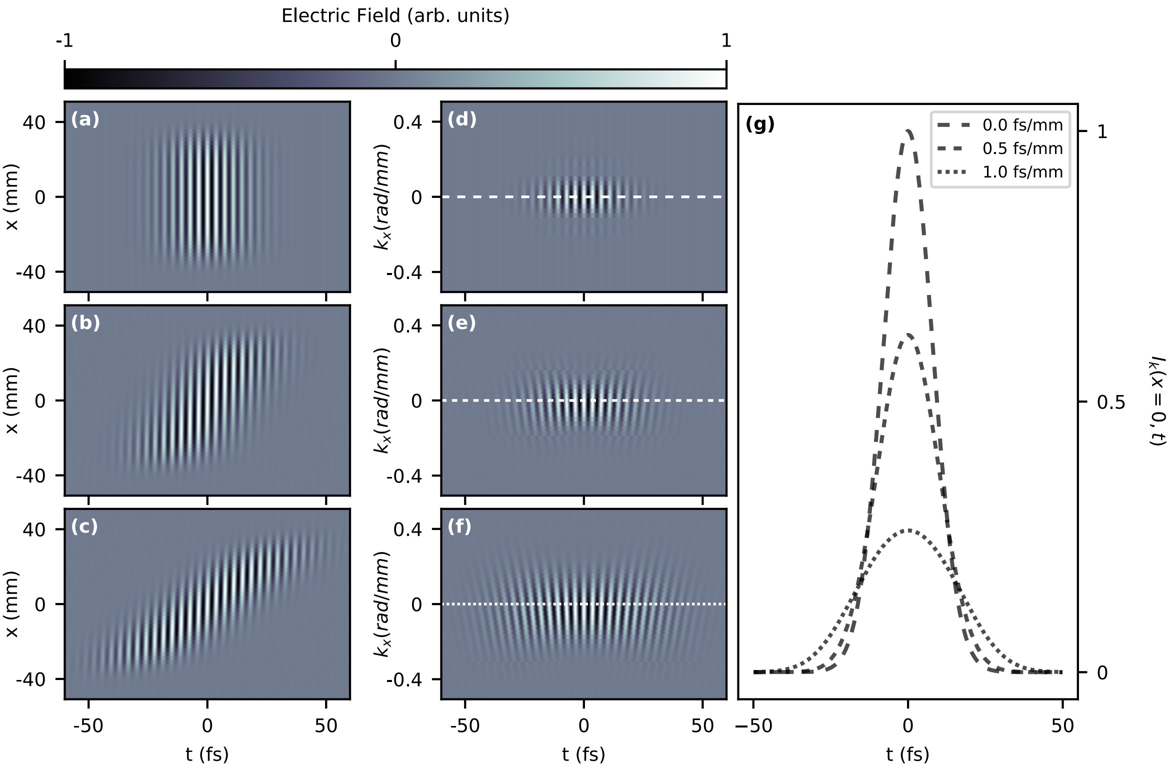

**Figure 2.3.: Pulse Front Tilt observed in near-field and its consequence in far-field. (a)–(c)** Real part of an ultrashort pulse field of which the pulse front is tilted with respect to its average wavefront $\overline{\varphi(x, y)}$ (near-field). Values of Pulse Front Tilt are respectively $0$, $0.5$ and $1.0\,\mathrm{fs/mm}$. **(d)–(f)** Real part of the same field at focus, obtained by Fourier-transforming panels (a)–(c) in the spatial dimension. **(g)** Intensities measured at center of the focal spot, along dashed white line in panels (d)–(f).

Figure 2.3 also displays the same pulses in the spatio-temporal domain, after propagation to the focal plane (panels (d)–(f)). This operation of going to the far-field using a Fourier Transform actually *converts* the initial PFT that was visible in the near-field, into a combination of other couplings. The main effect resides in a spreading of the pulse energy in space and in time. Panels (d)–(f) demonstrate that the pulse is focused in a volume that goes increasing with the amount of PFT introduced before focusing. Besides, the net effect on peak intensity is clearly visible on the intensity plots drawn in panel (g).

The second effect of near-field PFT on the field at focus is wavefront rotation. This feature is visible in panel (f) of figure 2.3 wherein the wavefront tilt evolves with time. In this case, the direction of propagation points downwards at the beginning of the pulse and upwards at the end. Incidentally, this particular consequence at focus of PFT can be controlled and leveraged in *ultrafast lighthouse effect* experiments, in the goal of producing individual attosecond pulses [31, 32].

As we said, propagation of an angularly dispersed beam spreads its frequency components in the dispersion direction. The result is a linear dependence of central frequency $\omega_0$ on the spatial position, also called *Spatial Chirp*. Figure 2.4 on the next page features a spatially chirped beam in near-field, obtained by propagating an angularly dispersed field. Focusing an angularly dispersed field also generates spatial chirp, but at focus this time. This is why misalignment

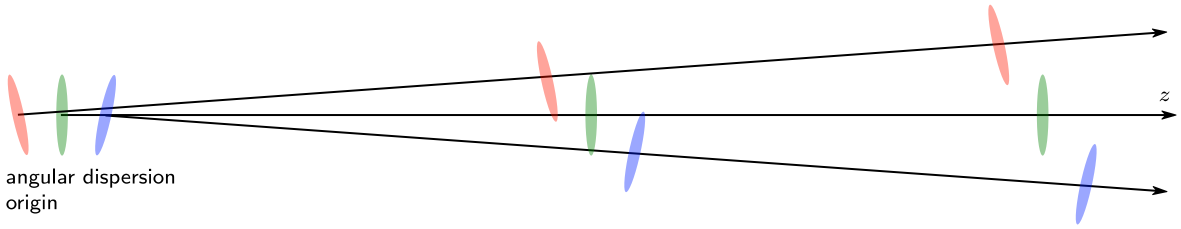

**Figure 2.4.: Spatial Chirp generated from angular dispersion.**

of compressors is generally done by looking at far-field fluence diagnostics. Ellipticity of the fluence profile at focus is a direct consequence of spatial chirp, which is itself a consequence of unwanted angular dispersion in near-field.

Despite the close relation between angular dispersion, pulse front tilt and spatial chirp, these three spatially linear effects affect three different domains and must absolutely be distinguished. One common misconception is the strict equivalence between angular dispersion and pulse front tilt. Although I mentioned that pulse front tilt is a *temporal implication* of angular dispersion, it must be clear that PFT can also be generated from other effects. For instance, if a spatially chirped beam goes through a glass plate and acquire some amount of dispersion, the field will be delayed by a duration depending linearly on the position [75]. The generated effect corresponds exactly to the definition of Pulse Front Tilt, yet it does not imply any chromatism in the propagation direction of the field.

### 2.2.2. Spatially Quadratic Spatio-Temporal Couplings

The second important spatio-temporal coupling is known as *Pulse Front Curvature* (PFC). In near-field this coupling is constructed similarly to Pulse Front Tilt, except that the pulse arrival time depends quadratically on radius—instead on depending linearly on the horizontal or vertical position. Figure 2.5 on the facing page shows the curved spatio-temporal profile of a beam for different values of PFC in near-field (panels (a)–(c)) and after propagation in far-field (panels (d)–(f)). Similarly to Pulse Front Tilt, the first outcome of PFC is the intensity loss caused by the global pulse duration being longer than the Fourier-limited local duration. However, since this coupling is symmetric radially, the wavefront at focus does not rotate like it was the case for PFT.

The most common way to generate PFC is to introduce *chromatic curvature* in the beam, instead of angular dispersion for PFT. Phase added by chromatic curvature is written:

$$\varphi_{\mathrm{PFC}}(r,\omega) = \xi_{\mathrm{PFC}}\, r^2\, (\omega - \omega_0) \tag{2.6}$$

with $\xi_{\mathrm{PFC}}$ the radial group delay created by Pulse Front Curvature, in fs/mm$^2$.

The simplest way to generate chromatic curvature consists of placing a singlet lens in the path of a broadband laser beam. As computed by Z. Bor [76, eq.9], the group delay $T_{\mathrm{PFC}}(r)$ added by chromatic curvature after a singlet lens is:

$$T_{\mathrm{PFC}}(r) = \frac{r^2}{2cf(n-1)} \left( -\lambda_0 \left.\frac{\mathrm{d}n}{\mathrm{d}\lambda}\right|_{\lambda=\lambda_0} \right) \tag{2.7}$$

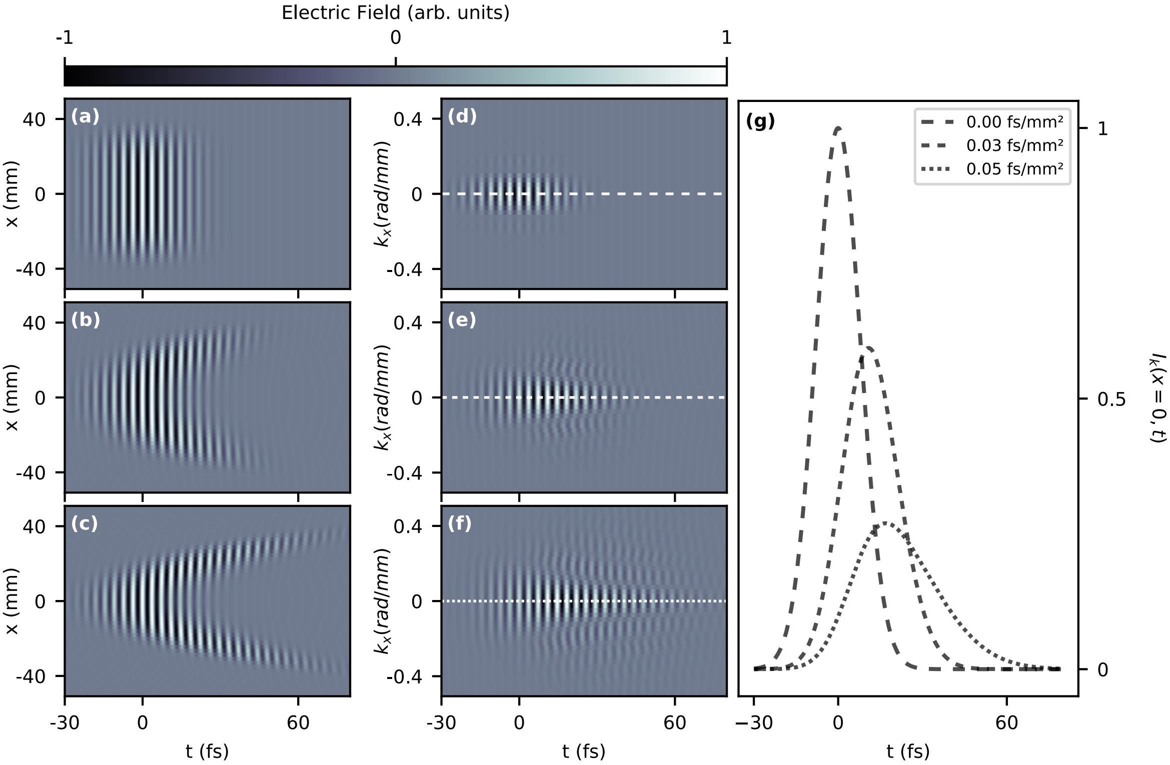

**Figure 2.5.: Pulse Front Curvature observed in near-field and its consequence in far-field. (a)–(c)** Real part of an ultrashort pulse field of which the pulse front is curved with respect to its average wavefront $\overline{\varphi(x,y)}$ (near-field). Values of Pulse Front Curvature are respectively $0$, $0.03$ and $0.05\,\mathrm{fs/mm^2}$. **(d)–(f)** Real part of the same field at focus, obtained by Fourier-transforming panels (a)–(c) in the spatial dimension. **(g)** Intensities measured at center of the focal spot, along dashed white line in panels (d)–(f).

with $r$ the distance from the center of the lens, $f$ its focal distance, $n$ the refractive index and $\lambda$ the central wavelength of the beam. For a Ti:Sapphire laser ($\lambda_0 = 800\,\mathrm{nm}$), and a BK7 lens of 2 inches in diameter and $1\,\mathrm{m}$ in focal length, the supplementary delay is $32\,\mathrm{fs}$ at the outer edge of the beam. The significance of this value depends on the local duration of the pulse and on the intended application for the laser beam. If the local duration is a few tens of femtoseconds—like for most current high-power lasers—then the delay we have just computed is significant and degrades strongly the intensity estimated in the spatio-temporal decoupling approximation.

The most intriguing effect of chromatic curvature is visible in the $(k_x, \omega)$ domain. Since the divergence of the beam in near-field varies with the angular frequency, the focusing position after a focusing element of fixed focal length is different for each spectral component of the beam. This effect is called *Longitudinal Chromatism* or *Chromatic focal shift*. As displayed by figure 2.6 on the next page, there is no distance $z$ for which all frequencies are fully focused. Additionally to the increase in global pulse duration, this is another way to explain the peak intensity loss in presence of chromatic curvature. This chromatism also leads to an extended frequency-integrated Rayleigh range as illustrated by the dashed black line on figure 2.6 on the following page. When combined with a global temporal chirp, chromatic curvature is used for producing *Chirped Pulses with Longitudinal Chromatism* (CPLC)—also called *Flying focus*—and to control the speed of the intensity peak at focus [33–37].

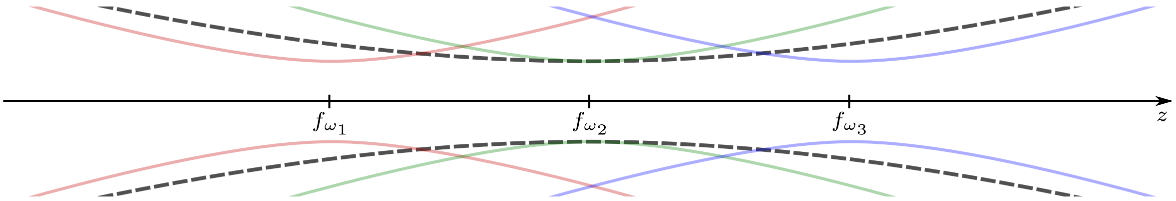

**Figure 2.6.: Illustration of Longitudinal Chromatism (or chromatic focal shift).** The three colored outlines represent the outer edges of three frequency components of a chromatic pulse at focus. The three wavelengths are not focused at the exact same position along the $z$ axis. Dashed black lines represent the outline the fluence profile—i.e., spectrally-integrated intensity—at each $z$ position.

To sum up, table 2.1 classifies the low-order couplings that we presented, and their correspondence in the four Fourier domains. In the next section, we will introduce spatio-temporal couplings which are more complex to define formally.

| Fourier Domain | Spatially Linear Couplings | Spatially Quadratic Couplings |
|---:|---|---|
| $(x, \omega)$ | **Angular Chirp** | **Chromatic Curvature** |
| $(x, t)$ | Pulse Front Tilt | Pulse Front Curvature |
| After some propagation *or* $(k_x, \omega)$ | Transverse Spatial Chirp | Longitudinal Spatial Chirp |
| $(k_x, t)$ | Wavefront rotation | *Flying Focus* * |

**Table 2.1.: Consequences of near-field angular chirp and near-field chromatic curvature in the other Fourier domains.** **When associated to a quadratic spectral phase*

### 2.2.3. Spatio-Spectral Streak

In section 1.1.1 on page 10, the CPA technique was introduced and the working principles of stretchers and compressors were explained. We showed in section 2.2.1 on page 24 that the optical elements constitutive of these devices introduce large amounts of spatio-spectral couplings—namely, angular dispersion and spatial chirp—which can lead to significant intensity losses if canceled improperly. In this last example, we will show that spatio-spectral couplings can arise from angular dispersion–based devices even after having perfectly canceled the angular dispersion.

Panel (a) of figure 2.7 on the facing page illustrates the first kind of error susceptible to affect the spatio-spectral profile of a pulse in a compressor. In this case, the laser profile is clipped by the edge of the mirror or grating because its size is not properly matched, or because of a misalignment in the preceding optics. Since the beam is spatially chirped in the plane we are considering, the different frequencies are not all clipped the same way.

Panel (b) shows a second type of spatio-spectral degradation, which also concerns mirrors or grating where the laser beam is spatially chirped. If the surface of such optics is degraded, modulations are added to the phase profile of the reflected beam. In the same way as for the

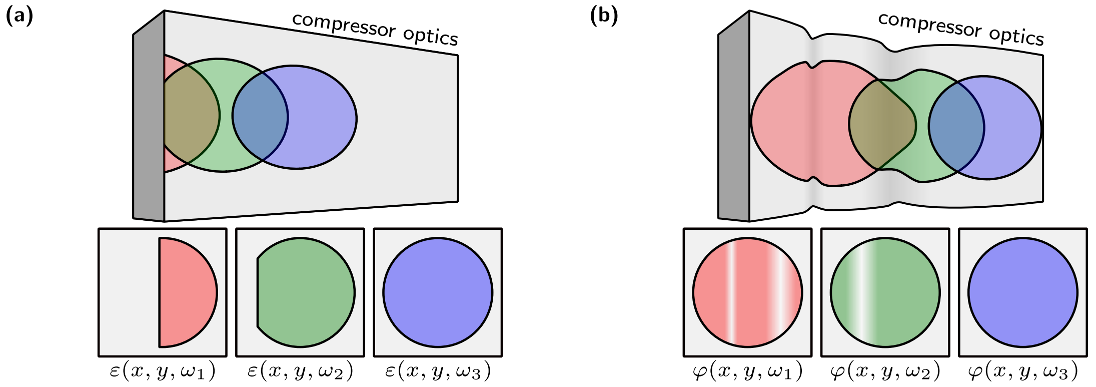

**Figure 2.7.: Spatio-spectral couplings created on compressor optics. (a)** Spectral clip caused by bad centering of the beam in presence of spatial chirp. **(b)** Spectrally-dependent wavefront defect caused by bad quality of a mirror, in presence of spatial chirp.

previous defect, the horizontal position of these modulations depends on the beam wavelength. This is also a spatio-spectral coupling because in this situation, the focusability of the beam depends on wavelength, and this cannot be easily corrected. It is worth noting that after some propagation, phase modulations generated by such degraded optic also affect the spectral fluence profile of the beam, and have an influence on the maximum achievable intensity at focus. Z. Li *et al.* notably concluded in their numerical study [77] that laser manufacturers need to have strong requirements on the surface quality of compressor grating, in addition to only adapting their size to the pulse energy.

Both kinds of spatio-spectral defect produce modulation patterns that travel in the direction of the compressor or stretcher dispersion plane. The *speed* at which the patterns travel depends on the spatial chirp value (in µm/nm) in the plane of the defective optical component. In spatio-spectral views of fluence or phase, traveling modulations are easily distinguished as oblique streak of more or less strong slope.

Let us understand the consequence of spatio-spectral streak on the actual intensity profile at focus, using a simple model. From now on, we consider that the transfer function of the defective optical component is described by a function $f(x)$ written:

$$f(x) = 1 + \epsilon(x) \ , \tag{2.8}$$

where $\epsilon(x)$ is the amplitude or phase error added by the component. In this demonstration, we consider that the error is purely sinusoidal of period $\lambda_\epsilon$ in the direction $x$ of the compressor spatial dispersion:

$$\epsilon(x) = \epsilon_0 \ \sin(2\pi \ \lambda_\epsilon x) \ . \tag{2.9}$$

At the output of the compressor of spatial dispersion $s$, the degraded field $E^D(x,\omega$ is of the form:

$$E^D(x,\omega) = E(x,\omega) \, f(x - s\omega) \ , \tag{2.10}$$

which, after spatial Fourier-transform, gives the expression of the far-field:

$$\begin{aligned} E_k^D(k_x,\omega) &= E_k(k_x,\omega) * \left[ f_k(k_x)\, e^{isk_x\omega} \right] \ , \\ &= E_k(k_x,\omega) + E_k(k_x,\omega) * \left[ \epsilon_k(k_x)\, e^{isk_x\omega} \right] \ , \end{aligned}$$

$$E_k^D(k_x,\omega) = \underbrace{E_k(k_x,\omega)}_{\text{main focal spot}} \underbrace{+\epsilon_0\, E_k(k_x,\omega)\, \delta\left(k_x \pm \frac{2\pi}{\lambda_\epsilon}\right)}_{\text{satellite foci}} \underbrace{e^{\mathrm{i}\, sk_x\omega}}_{\text{delay}} \ . \tag{2.11}$$

This result shows that the field obtained at focus is composed of the main focal spot, and of two secondary foci on both sides. It is interesting to note that the foci are delayed with respect to the main pulse, and that the amount of delay depends on the spatial dispersion $s$. This has a direct influence on the temporal contrast of the pulse since a fraction of the initial beam energy is spread before and after the main pulse. If the same spatial modulations were introduced in an optical plane without any spatial dispersion, the satellite foci would still be present in far-field but would not be delayed.

Our simple model is analogous to the study published by J. Bromage *et al.* in 2012 [78]. In this paper, the authors analyze the influence of surface roughness of stretcher mirrors on temporal contrast. The main difference with our case is that the authors modeled mirrors roughness whereas we focused on the effect of lower spatial frequency aberrations. Instead of creating delayed satellite foci in far-field, stretcher mirror roughness produce a diffusion pattern at focus, of which the time of arrival depends linearly on the distance to the main focal spot. This effect has been observed experimentally on petawatt laser facilities [79, 80], and is one of the most challenging limit for obtaining better contrasts.

## 2.3. Spatio-Temporal & Spatio-Spectral Characterization

The examples developed in the last few pages showed that spatio-temporal couplings can be caused by various optics and lead to very different effects after some propagation. Some couplings—chiefly those generated in spatially dispersive components like compressors—can be arbitrary and of high order both spatially and spectrally. Since the measurement techniques presented in chapter 1 only concern purely-temporal or purely-spatial characterization, supplementary devices had to be designed so that spatio-temporal couplings could be measured and fixed. Although some low-order couplings can be estimated using clues of their presence—e.g., elliptical focal spot caused by PFT—a much more precise knowledge of the laser field is needed in order to truly achieve the best possible intensities on target.

When looking for ways to characterize spatio-temporal couplings, one could think of simply measuring the temporal properties of the beam at multiple positions across its spatial profile. This can be done quite simply by spatially selecting which part of the beam is measured using an optical fiber or a simple aperture. The fiber or aperture can then be moved sideways to characterize another position of the beam. We demonstrate in figure 2.8 on the next page why this technique would work only partially. This approach is not able to measure wavefront or spatially-dependent group-delay, because purely-temporal measurement techniques are blind to the CEP phase and to the time of arrival of the pulse. This includes Pulse Front Tilt and Pulse

Front Curvature couplings which are quite predominant in high-power lasers. Higher-order couplings, such as spatial variations of the pulse width, could however be characterized.

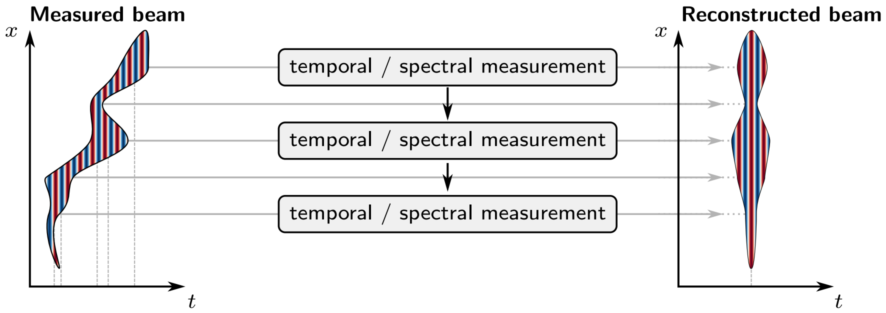
Measured beam
x
temporal / spectral measurement
temporal / spectral measurement
temporal / spectral measurement
t
Reconstructed beam
x
t

**Figure 2.8.: Regularly-spaced temporal measurements is not a full spatio-temporal measurement.** Scanning the spatial profile of a laser pulse with a purely-temporal characterization device does not provide spatially-dependent group-delay couplings, although higher order spatio-temporal defects would be correctly measured.

Full spatio-temporal characterization not only requires to extend the dimensionality of existing techniques, but also to find a proper way to reference spatio-temporal samples between each other. Since this challenge dates from the beginning of ultrafast science, a profusion of spatio-temporal techniques were developed to characterize spatio-temporal couplings. They all have their issues and benefits, and some are better-known than the others, but none is considered as an absolute reference technique—e.g., like Shack-Hartmann is for wavefront sensing, or FROG for temporal metrology.

A comprehensive review of existing spatio-temporal measurement devices has recently been published by C. Dorrer [40]. In the next pages, we will rather try to focus on some chosen examples, and to find some common characteristics for the different methods, before providing a summary table on page 35. For instance, two main groups of techniques can be defined: some techniques are based on spatially-resolved spectral measurements and some others are based on spectrally-resolved spatial measurements.

### 2.3.1. Spatially Resolved Spectral Measurement

As we said, the issue with scanning the spatial profile of the beam with a temporal characterization device is the absence of reference and the subsequent blindness to the most common types of couplings. The idea behind STARFISH and SEA-TADPOLE consists of solving this issue by performing a relative spectral phase measurement between two positions in the beam profile. Spatial sampling is usually done by using one fixed optical fiber (e.g., at center) to capture a reference pulse, and a scanning fiber to capture the unknown spectral phase.

The exact implementation used to retrieve the relative spectral phase between the test pulse and the reference then depends on the technique, but both techniques hinge on spectral interferometry [81]. In STARFISH [82, 83], a small delay is introduced between the two pulses, producing interference fringes in the spectral domain. The spectrum is recorded using a one-dimensional spectrometer. Numerical processing then consists in retrieving the spectral phase from the interferogram for each spatial position, using Fourier processing.

---

[1] © Optical Society of America. Reproduced with permission. All rights reserved.

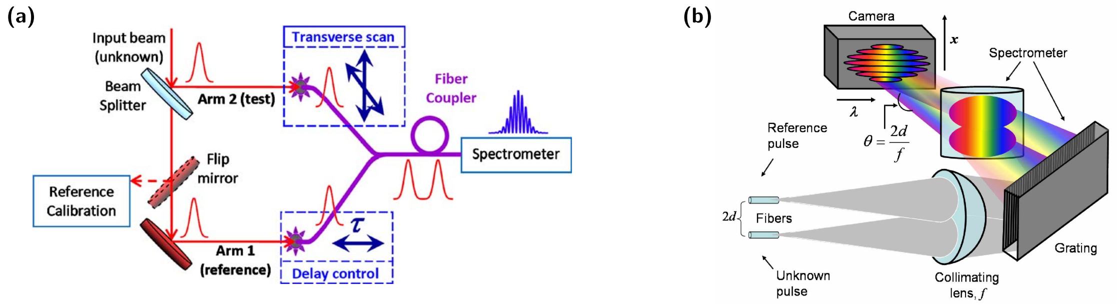
(a)
Input beam
(unknown)
Beam
Splitter
Arm 2 (test)
Transverse scan
Fiber
Coupler
Spectrometer
Flip
mirror
Reference
Calibration
Arm 1
(reference)
$\tau$
Delay control
(b)
Camera
$x$
Spectrometer
$\lambda$
Reference
pulse
$\theta = \frac{2d}{f}$
$2d$
Fibers
Unknown
pulse
Collimating
lens, $f$
Grating

**Figure 2.9.: Layouts of the STARFISH (a) and SEA-TADPOLE (b) techniques.** *STARFISH figure reprinted from article by B. Alonso* et al. *[82]. SEA-TADPOLE figure reprinted from article by P. Bowlan* et al. *[84].*

Although being based on the same principle, SEA-TADPOLE [84] uses a different optical implementation which provide better quality measurements. Outputs from the sampling fibers are overlapped and measured using an imaging spectrometer. Because of the small angle between the two pulses, spatial fringes are formed on the sensor of the imaging spectrometer. In this technique, the Fourier processing carried out to extract the encoded phase is done in the spatial dimension, which remove some constraints on the spectral resolution, and the need to introduce a delay between the two pulses. Thanks to this technical trick, SEA-TADPOLE provides better quality measurements in terms of dynamic range and spectral sampling than traditional spectral interferometry.

The spatial scanning techniques that we have just presented propose a quite intuitive solution to the issue explained in figure 2.8 on the preceding page. Yet, scanning a fiber over two spatial dimensions of the whole beam profile reveals to be very tedious in practice. Moreover, some technical difficulties linked to spatial phase wrapping can lead to some ambiguities in the result.

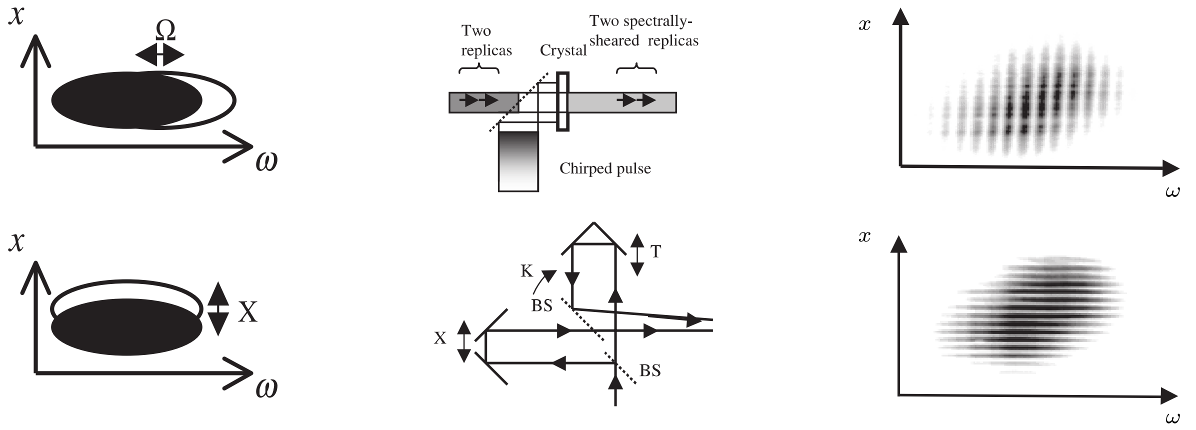
$x$
$\Omega$
$\omega$
Two
replicas
Crystal
Two spectrally-
sheared replicas
Chirped pulse
$x$
$\omega$
$x$
X
$\omega$
K
T
BS
X
BS
$x$
$\omega$

**Figure 2.10.: Spectral and spatial shearing interferometry in SPIDER-2D.** Top-panels illustrate the spectral shearing interferometry measurement. Bottom-panels show the spatial shearing interferometry measurement done in a second step. *Figure adapted from figures 1–3 by C. Dorrer* et al. *[85].*

SPIDER-2D [85] uses an imaging spectrometer to perform a measurement of the pulse shape resolved along one spatial dimension. This measurement is done following the same principle as SPIDER—explained in section 1.3.2 on page 16—and returns the spectral phase gradient $\frac{\mathrm{d}\varphi}{\mathrm{d}\omega}$

resolved spatially. Because of the issue illustrated by figure 2.8 on page 31, a second measurement is done to obtain the phase relation between each spatial sample. As illustrated by figure 2.10 on the preceding page, the spatial phase gradient $\frac{\mathrm{d}\varphi}{\mathrm{d}x}$ is measured through spatial shearing interferometry this time. Spatial and spectral phase gradients are then integrated to return an absolute measurement of the spatio-spectral phase along the entrance slit of the imaging spectrometer.

Other spatially-resolved temporal characterization techniques exist and will be mentioned in the summary table on page 35. It is worth noting that TERMITES—to which a substantial part of this manuscript is dedicated—is listed among the spatially-resolved spectral measurement techniques. This device will be described for its part in chapter 3 on page 43.

## 2.3.2. Spectrally Resolved Spatial Measurement

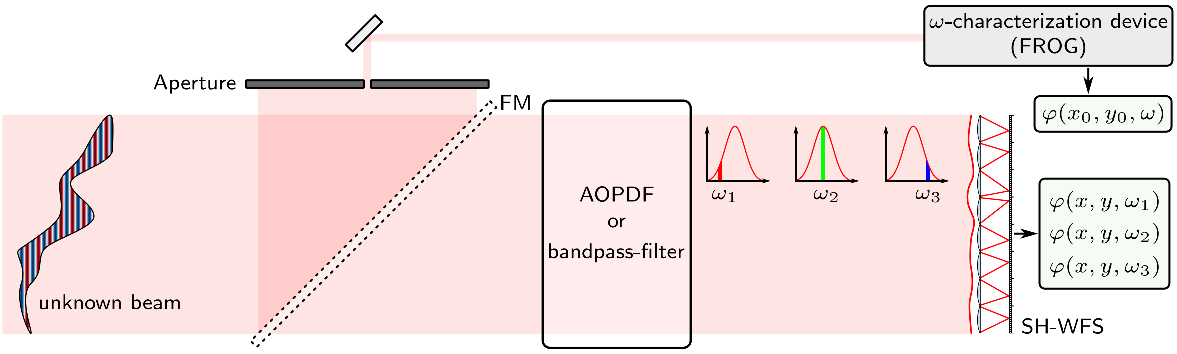
ω-characterization device
(FROG)
Aperture
FM
$\varphi(x_0, y_0, \omega)$
AOPDF
or
bandpass-filter
$\omega_1$
$\omega_2$
$\omega_3$
$\varphi(x, y, \omega_1)$
$\varphi(x, y, \omega_2)$
$\varphi(x, y, \omega_3)$
unknown beam
SH-WFS

**Figure 2.11.: Layout of the HAMSTER technique. FM:** Flipping mirror. **AOPDF:** Acousto-Optic Programmable Dispersive Filter. **SH-WFS:** Shack-Hartmann Wavefront Sensor

The second approach to spatio-spectral characterization consists of performing multiple fluence and wavefront measurements at different wavelengths. As its name suggests, HAMSTER—as in *Hartmann–Shack Assisted, Multidimensional, Shaper-based Technique for Electric-field Reconstruction* [86]—employs a Shack-Hartmann sensor to measure quasi-monochromatic wavefronts selected from the unknown pulse.

As depicted in figure 2.11, the different wavelength are selected sequentially by an Acousto-Optic Programmable Dispersive Filter (AOPDF), or using narrow-band filters. Each time, the wavefront is measured thanks to a Shack-Hartmann sensor, of which the working principles are explained in section 1.3.1 on page 14. These measurements provide spatial slices of $\varphi(x, y, \omega)$ which are not related to each other, as Shack-Hartmann sensors are blind to constant spatial phase (piston).

A last measurement is performed to fix this uncertainty. The goal is to provide the local spectral phase of the unknown beam at a fixed spatial position (for instance at the center of the beam profile). This measurement is then used to determine the constant phase value of wavefronts obtained with the Shack-Hartmann sensor.

Finally, INSIGHT [87] is another technique that can be qualified as an extension to the spectral domain of a purely spatial method. Indeed, the basic concept of this technique consists of measuring the fluence profile of the unknown beam at multiple points around far-field, and to extract the wavefront information from these raw measurements. This is done using phase-retrieval algorithms, which has been already described in section 1.3.1 on page 14, when we explained how phase retrieval can be used to retrieve the average wavefront of a laser beam.

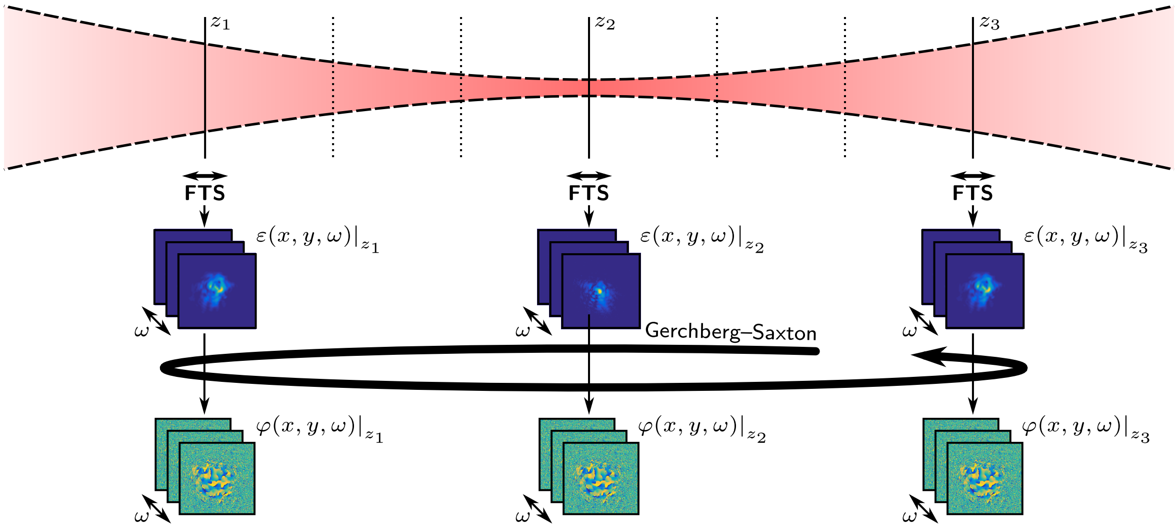
$z_1$
$z_2$
$z_3$
FTS
FTS
FTS
$\varepsilon(x,y,\omega)|_{z_1}$
$\varepsilon(x,y,\omega)|_{z_2}$
$\varepsilon(x,y,\omega)|_{z_3}$
Gerchberg–Saxton
$\omega$
$\varphi(x,y,\omega)|_{z_1}$
$\varphi(x,y,\omega)|_{z_2}$
$\varphi(x,y,\omega)|_{z_3}$

**Figure 2.12.: Working principle of the INSIGHT technique [87].** Imaging Fourier transform spectroscopy is carried out at multiple positions around focus, in order to obtain the spectral fluence at each of them. Then, phase retrieval (see section 1.3.1 on page 15) is applied to the fluence profile of each wavelength in order to retrieve the full spatio-spectral profile of the pulse at focus.

The key-idea behind INSIGHT is to apply this phase retrieval method to several spectral samples of the broadband beam, in order to reconstruct the full electric field of the pulse. For this, it is necessary for each fluence measurement taken around focus to be resolved spectrally. The method that was chosen to perform each spectral fluence measurement is the Imaging Fourier Transform Spectroscopy (IFTS). As FTS is also a fundamental principle of TERMITES, it will be explained in more details in chapter 3 on page 43.

| | Technique name | Spectral phase obtained by | Spatial phase obtained by | Spatial dimension | Needs Imaging spectrometer | Non-linear | Shots needed |
|---|---|---|---|---|---|---|---|
| **Spatially resolved temporal measurement** | SEA-F-SPIDER | Shearing Interferometry | not obtained | 1D | Yes | Yes (frequency-sum) | 1 |
| | **2D-SPIDER** | Shearing Interferometry | Shearing Interferometry | 1D | Yes | Yes (frequency-sum) | 2 |
| | SRSI-ETE | Spectral interferometry w/ homogeneous reference | Spatial resolution of spectral interferograms | 1D | Yes | Yes (XPW) | 1 |
| | **SEA-TADPOLE** | Spectral interferometry with a fixed reference | Raster scanning | 1D (can be 2D, but cumbersome) | Yes | No | Spatial sampling |
| | **STARFISH** | Spectral interferometry with a fixed reference | Raster scanning | 1D (can be 2D, but cumbersome) | Yes | No | Spatial sampling |
| | TERMITES | FTS | Imaging | 2D | No | No | approx. 1000 |
| **Spectrally resolved spatial measurement** | **HAMSTER** | Any purely-spectral characterization method | Shack-Hartmann | 2D | No | No | Spectral sampling + 1 |
| | Shackled-FROG | FROG | Shack-Hartmann | 1D | Yes | Yes | 2 |
| | Hyperspectral WFS | Any purely-spectral characterization method | Shack-Hartmann, QWLSI | 2D | No | No | Spectral sampling + 1 |
| | CROAK | Any purely-spectral characterization method | Phase retrieval | 1D | Yes | No | 3 |
| | **INSIGHT** | Any purely-spectral characterization method | Phase retrieval | 2D | No | No | approx. 3000 |
| | STRIPED-FISH | Spectral resolution of spatial interferograms | Interference with a *perfect* reference | 2D | No | No | 1 |

**Table 2.2.: Summary of the main spatio-temporal measurement techniques.** Devices described in the previous pages are typeset in bold.

## 2.4. Interpretation of Spatio-Temporal Measurements

Thanks to spatio-temporal measurement techniques, users are able to obtain the three-dimensional complex field of ultrashort pulses, resolved in any of the four domains described in section 2.1 on page 22. Unlike for purely-spectral or purely-spatial measurements, there is no ISO standard defining figures of merits for spatio-temporal measurements. After all, what is the point of measuring $E(x, y, t)$? What quantities should laser users compute in order to retrieve intelligible information from the full electric field of a pulse?

The first way to use the measured data actually does not require to interpret the results, but is worth mentioning here. In the context of ultrahigh intensity experiments, the measured electric field can be directly fed into *Particle-in-cell* (PIC) simulations, in order to simulate the behavior of particles in the target during its exposure to the high-intensity laser beam. Generally, the field of the input laser beam is modeled by its theoretical expression, but an increasing number of computational physicists are interested in using the output of actual measurement devices as initial conditions for simulations.

### 2.4.1. Spectrally-Resolved Zernike Polynomials

All other approaches to ease the interpretation of our measurements involve reducing the dimensionality of data by either projection or more advanced computations. In some cases, the only interesting information for the user is the quantity of a specific spatio-temporal coupling such as Pulse Front Tilt. The best way to retrieve this information consists of fitting the measured field to the spatio-temporal coupling of interest, in order to get its magnitude.

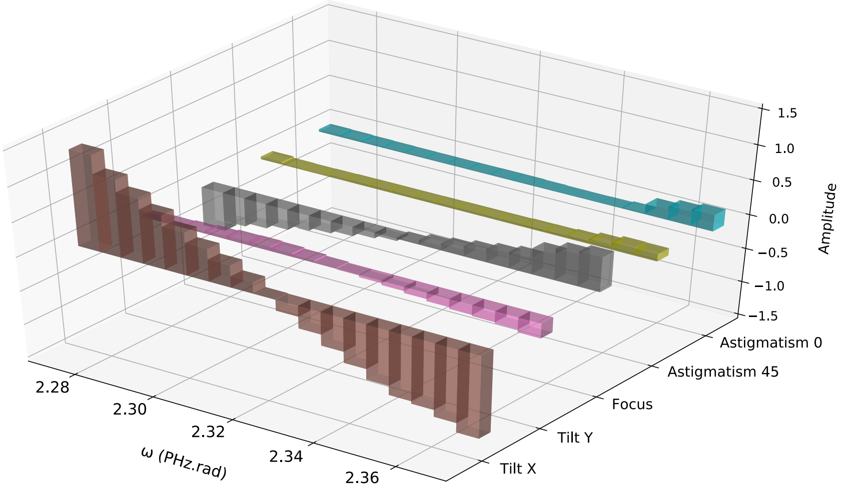

**Figure 2.13.: Spectrally resolved Zernike polynomials.** For each angular frequency, the wavefront is projected on the Zernike polynomials basis [88]. Data of this particular plot are from a TERMITES measurement, but the same diagnostic can be computed for virtually any complete spatio-spectral measurement device.

Spectrally-resolved Zernike polynomials are very informative in this type of situations, because they discriminate the different aberration basis of a 3D phase profile, and help noticing immediately each specific spatio-spectral coupling. Figure 2.13 shows the kind of Zernike plot that can be computed from a complete spatio-temporal measurement. In this specific case, it is very apparent that the measured beam has two major couplings: Angular Dispersion and Chromatic Curvature. Indeed, the plot displays a linear evolution of both the horizontal wavefront tilt and of the wavefront curvature.

### 2.4.2. Spatio-Temporal Strehl Ratio

Spectrally-resolved Zernike polynomials represent a very practical way to understand the precise nature of spatio-spectral couplings measured in an unknown beam. However, it is sometimes useful to assert the general quality of a spatio-temporal profile without going too deep into the interpretation of data. Experimentalists should be able to quickly compute a *score* that takes into account the general spatio-temporal profile and represent its quality. This concept exists for purely-spatial measurements and is called *Strehl ratio.* We presented it in equation (1.9) on page 16. Can we extend this idea to qualify our spatio-temporal ultrashort pulses?

As a matter of fact, measuring the full electric field of ultrashort pulses gives the powerful ability to compute the actual peak intensity on target, instead of simply getting a peak *fluence* as it was the case with purely-spatial diagnostics. Therefore, we can now compute the *spatio-temporal* Strehl ratio which is a ratio of intensities, and constitute a perfect candidate for the score we were looking for. As for the traditional achromatic Strehl ratio, the idea is to provide a ratio between the peak intensity on target $\max I_k$—computed from the measurement—and the peak intensity on target *if the beam were perfect*, $\max I_k^0$:

$$SR = \frac{\max I_k}{\max I_k^0} \,, \tag{2.12}$$

By definition, this ratio is always less than or equal to one. Each intensity distribution is computed from the spatial Fourier transform of collimated fields.

The challenge in this definition is to settle on what we consider as a perfect beam in near-field, and to define it with respect to the measurement. The easiest solution is to consider all phase errors, by comparing the measurement $E(x, y, \omega)$ to a perfect field $E_0(x, y, \omega)$ which has the same spectral fluence distribution, but a flat phase for all angular frequencies:

$$\begin{aligned} &\bullet\ E(x,y,\omega) = \varepsilon(x,y,\omega)\, e^{\mathrm{i}\,\varphi(x,y,\omega)} \\ &\bullet\ E^0(x,y,\omega) = \varepsilon(x,y,\omega)\, e^{\mathrm{i}\times 0} \end{aligned} \tag{2.13}$$

The Strehl ratio $SR_{\text{full}}$ computed from these two fields takes into account any deviation from zero of the phase. This includes purely spectral phase and purely spatial phase.

While this number can be interesting, the user might want to quantify only the impact of spatio-temporal couplings on intensity at focus. In this case, the purely-spectral and purely-spatial phase of $E(x, y, \omega)$ can simply be subtracted before computing the spatio-temporal Strehl Ratio $SR_{\text{STC}}$:

$$\begin{aligned} &\bullet\ E(x,y,\omega) = \varepsilon(x,y,\omega)\, e^{\mathrm{i}\,\varphi(x,y,\omega) - \overline{\varphi(x,y)} - \overline{\varphi(\omega)}} \\ &\bullet\ E^0(x,y,\omega) = \varepsilon(x,y,\omega)\, e^{\mathrm{i}\times 0} \end{aligned} \tag{2.14}$$

In this equation, $\overline{\varphi(x, y)}$ represent the purely-spatial phase that is computed from the spatio-spectral measurement. We decided to compute this quantity by simulating its measurement by an actual wavefront sensor. In experiments, the phase profile measured by a Shack-Hartmann or QWLSI device (see section 1.3.1) from a broadband laser beam can reasonably be considered as a frequency-average of the spatio-spectral phase. This quantity is computed as the average of the spatio-spectral phase $\varphi(x, y, \omega)$ over the frequency axis $\omega$, weighted by the spectral fluence $\varepsilon(x, y, \omega)$:

$$\overline{\varphi(x, y)} = \frac{\int \mathrm{d}\omega \; \varphi(x, y, \omega)\, \varepsilon(x, y, \omega)}{F(x, y)} \, , \tag{2.15}$$

with $F(x, y)$ the beam fluence which is used here to normalize the obtained 2D phase profile.

Both $SR_{\text{full}}$ and $SR_{\text{STC}}$ represent accurately the intensity loss caused by phase couplings such as angular dispersion or chromatic curvature. However, they will always be 1 in presence of pure spectral fluence couplings, such as spatial chirp. Defining a Strehl ratio that indicates accurately the intensity loss due to spectral fluence couplings is a lot more challenging than Strehl ratios based on the phase. This is because a perfect phase is flat, whereas a perfect spectral fluence profile depends on what is really achievable experimentally.

A reasonable solution would consist of deciding that the *perfect* spectral fluence profile is the frequency-integrated fluence multiplied by the spatially-integrated spectrum. After taking the precaution of normalizing the resulting spectral fluence by its energy, this could be one of the best solutions to compute a Strehl ratio based of spectral fluence.

| | $E(x, y, \omega)$ | $E^0(x, y, \omega)$ |
|---|---|---|
| $SR_{\text{WFS}}$ | $\sqrt{F(x, y)}\, e^{\mathrm{i}\,\overline{\varphi(x,y)}}$ | $\sqrt{F(x, y)}\, e^{\mathrm{i}\times 0}$ |
| $SR_{\text{full}}$ | $\varepsilon(x, y, \omega)\, e^{\mathrm{i}\,\varphi(x,y,\omega)}$ | $\varepsilon(x, y, \omega)\, e^{\mathrm{i}\times 0}$ |
| $SR_{\text{STC}}$ | $\varepsilon(x, y, \omega)\, e^{\mathrm{i}\,\varphi(x,y,\omega)-\overline{\varphi(x,y)}-\overline{\varphi(\omega)}}$ | $\varepsilon(x, y, \omega)\, e^{\mathrm{i}\times 0}$ |
| $SR_{\text{fluence}}$ | $\frac{\varepsilon(x,y,\omega)}{\iiint \mathrm{d}x\mathrm{d}y\mathrm{d}\omega \; \varepsilon(x,y,\omega)}\, e^{\mathrm{i}\,\varphi(x,y,\omega)}$ | $\frac{\sqrt{F(x,y)\, S(\omega)}}{\iiint \mathrm{d}x\mathrm{d}y\mathrm{d}\omega \; \sqrt{F(x,y)\, S(\omega)}}\, e^{\mathrm{i}\,\varphi(x,y,\omega)}$ |

**Table 2.3.: Summary of the fields derived from spatio-temporal measurement and used to compute different types of Strehl ratios**

Table 2.3 sums up the different Strehl ratios that can be computed from the same spatio-temporal measurement. The last line concerns the possible *fluence* Strehl ratio which was tested far less than the others, and should therefore be used carefully.

⁂

In this chapter, we have introduced spatio-temporal and spatio-spectral couplings by providing examples of widespread chromatic aberrations. Some of them—like Pulse Front Tilt and Pulse Front Curvature—are well known by experimentalists and generally avoided. Some others, like spatio-spectral streaks generated in CPA compressors, often go unnoticed and are hardly measurable by traditional measurement devices. We then explained the general principles linked to spatio-temporal measurement and provided a few examples of devices which are dedicated to this specific task. Finally, we explained how spatio-temporal couplings can be interpreted despite their sometimes complicated nature. We notably introduced spectrally-resolved Zernike polynomials and proposed a few ways to compute spatio-temporal Strehl ratios.

Since the beginning of chapter 1, we went through increasingly complex aspects of high-power laser systems and attempted to demonstrate that current laser pulses are far from being definable by their sole duration anymore. The different spatio-temporal characterization devices we showed are often complex and each of them has its limitations. For this reason, finding new innovative ways to fully characterize high-power systems is crucial. Finally, we believe that it is necessary to elaborate relevant figures of merit that could be used as universal standard to assert the spatio-temporal quality of high-power systems. Spatio-temporal Strehl ratio is a good candidate, but some work is left to do in order to check the robustness of its computation.

# Part II.

# TERMITES: Technique Principles & Optimization of the Design

Chapter 3.

# Fundamentals of the Technique

Before analyzing in details the specifications of the instrument as well as its technical limitations, let us first describe the basic principles of TERMITES in the present chapter. We start the study by explaining the general concept of the instrument and how the signal is acquired. All numerical steps required to process the raw signal are then explained in a second part. All figures presented in this chapter are numerical simulations.

## Contents

**3.1. Experimental Setup: Concepts & Legacy** . . . . . . . . . . 44
- 3.1.1 Imaging Fourier Transform Spectroscopy
- 3.1.2 From IFTS to TERMITES

**3.2. Numerical Retrieval of the Pulse Structure** . . . . . . . . . . 48
- 3.2.1 Going Back to the Spectral Domain
- 3.2.2 Curvature Removal & Data Resampling
- 3.2.3 Reference Compensation
- 3.2.4 Retropropagation
- 3.2.5 Spectral Phase Stitching

## 3.1. Experimental Setup: Concepts & Legacy

### 3.1.1. Imaging Fourier Transform Spectroscopy

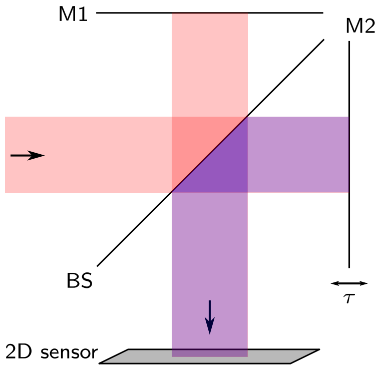

**Figure 3.1.: IFTS implementation, based on a simple Michelson interferometer.** M1 and M2 are plane mirrors, BS is a beam splitter. M2 is gradually translated in order to generate a varying delay $\tau$ between the main pulse and its replica.

Many techniques provide knowledge about spatio-temporal properties of ultrashort pulses and each of them rely on different underlying methods. TERMITES, for its part, largely relies on Fourier Transform Spectroscopy (FTS) and more specifically on spatially resolved FTS, here called *Imaging* Fourier Transform Spectroscopy (IFTS) [89–91]. This technique is described in figure 3.1 and essentially consists of a Michelson interferometer and a camera sensor. During an IFTS scan, the delay between the two arms is changed step-by-step while the camera records images at the output of the interferometer. Spectrally-resolved—or *hyperspectral*—images are obtained after numerical post-processing of this measurement.

Let us understand the basic principles of IFTS. At each delay $\tau$, the field of the input pulse $\hat{E}(\boldsymbol{r}, t)$ overlaps with a delayed replica of itself. In the case of IFTS, the two pulses are identical because the replica is generated using the plane mirror M2 in figure 3.1. Henceforward, we will differentiate the two pulses and note them $\hat{E}_1(\boldsymbol{r}, t)$ and $\hat{E}_2(\boldsymbol{r}, t)$ for the purpose of a more general demonstration.

The signal $\hat{W}(\tau)$ measured at each pixel of the sensor is the squared amplitude of the total field, integrated over the exposure time (a few milliseconds), which is considered infinite in comparison to the pulse length:

$$\hat{W}(\boldsymbol{r}, \tau) = \int_{-\infty}^{+\infty} \mathrm{d}t \left| \hat{E}_1(\boldsymbol{r}, t) + \hat{E}_2(\boldsymbol{r}, t - \tau) \right|^2 . \tag{3.1}$$

The dependence on the spatial variable $\boldsymbol{r}$ is implicit in the next equations, in order to lighten the notations. This is inconsequential because IFTS is only a 1D technique, applied the same way on all pixels of the sensor. Equation (3.1) is developed as follows:

$$\begin{aligned}
\hat{W}(\tau) &= \int_{-\infty}^{+\infty} \mathrm{d}t \left[ |\hat{E}_1(t)|^2 + |\hat{E}_2(t-\tau)|^2 + \hat{E}_1(t)\hat{E}_2^*(t-\tau) + \hat{E}_1^*(t)\hat{E}_2(t-\tau) \right] , \\
&= F_1 + F_2 + \int_{-\infty}^{+\infty} \mathrm{d}t \ \hat{E}_1(t) \, \hat{E}_2^*(t-\tau) + \left( \int_{-\infty}^{+\infty} \mathrm{d}t \ \hat{E}_1(t) \, \hat{E}_2^*(t-\tau) \right)^* , \\
&= F_1 + F_2 + (\hat{E}_1(t) \star \hat{E}_2(t))(\tau) + (\hat{E}_1(t) \star \hat{E}_2(t))^*(\tau) ,
\end{aligned}$$

$$\hat{W}(\tau) = \underbrace{F_1 + F_2}_{\text{incoherent term}} \underbrace{+ 2 \, \mathrm{Re} \left[ (\hat{E}_1(t) \star \hat{E}_2^*(t))(\tau) \right]}_{\text{coherent term}} , \tag{3.2}$$

where $F_1$ and $F_2$ are the respective fluences of $\hat{E}_1(t)$ and $\hat{E}_2(t)$, and the $\star$ symbol represents the cross-correlation product.

This result demonstrates that the signal measured by the camera along the whole scan is the sum of an incoherent term—always constant—and a coherent term evolving with the delay $\tau$. The latter is the only term that depends on the input beam temporal profile. This oscillating part contains the information used by Fourier Transform Interferometry to retrieve the input beam spectrum.

Raw signals obtained by IFTS at each spatial position are then processed numerically in order to obtain the input beam spectrum. The Cross-Correlation Theorem [92, p. 951] implies that the Fourier Transform of the recorded time signal is defined in the spectral domain, as the product of the input field and of the reference complex conjugate:

$$\begin{aligned} \mathcal{F}\left(\int_{-\infty}^{+\infty} \mathrm{d}t \; \hat{E}_1(\boldsymbol{r},t)\, \hat{E}_2^*(\boldsymbol{r},t-\tau)\right) &= \mathcal{F}\left(\hat{E}_1(\boldsymbol{r},t)\right)\, \mathcal{F}\left(\hat{E}_2(\boldsymbol{r},t)\right)^*, \\ &= E_1(\boldsymbol{r},\omega)\, E_2^*(\boldsymbol{r},\omega) = W(\boldsymbol{r},\omega)\,, \end{aligned} \tag{3.3}$$

with $E_1(\boldsymbol{r},\omega)$ and $E_2(\boldsymbol{r},\omega)$ the two fields resolved in the spatio-spectral domain, and $\omega$ the angular frequency. The resulting signal $W(\boldsymbol{r},\omega)$ is defined as the Cross Power Spectral Density (CPSD), and its spectrum and phase are related to those of the two pulses by the following expressions:

$$\begin{aligned} &\bullet \quad \left|W(\boldsymbol{r},\omega)\right|^2 = \varepsilon_1(\boldsymbol{r},\omega)\;\; \varepsilon_2(\boldsymbol{r},\omega) \\ &\bullet \quad \mathrm{Arg}\Big(W(\boldsymbol{r},\omega)\Big) = \varphi_1(\boldsymbol{r},\omega) - \varphi_2(\boldsymbol{r},\omega) \end{aligned} \;. \tag{3.4}$$

The spatially-resolved spectrum of the input field $E_1(\omega)$ is simple to retrieve from $W(\omega)$, because the input pulse is identical to its replica in this IFTS technique. Therefore:

$$\varepsilon_1(\boldsymbol{r},\omega) = \frac{\left|W(\omega)\right|^2}{2}\,. \tag{3.5}$$

However, the phases $\varphi_1(\omega)$ and $\varphi_2(\omega)$ of the two fields are also identical for all frequencies $\omega$. As a consequence, the spectral phase of the CPSD is always flat, for any input field (see equation (3.4)). Because it inherently looses the phase information, Imaging Fourier Transform Interferometry is not sufficient to retrieve the full spatio-temporal structure of the laser pulse.

### 3.1.2. From IFTS to TERMITES

TERMITES can be seen as an evolution of the IFTS scheme considering that it is intended to bypass the fundamental phase-blindness issue we just described. Since its origin, the core-idea behind this new device has been to use one of the two interferometer beams as a spatially homogeneous reference. The goal was to make the input pulse interfere with a well-known and consistent reference instead of a replica of itself. This new device is able to retrieve the spatio-spectral phase of the input beam, in addition to the spatially resolved spectrum. Therefore, TERMITES is able to produce data that can be used to fully reconstruct the spatio-temporal structure of the beam.

A first way of generating the homogeneous reference was notably introduced by Point Diffraction Interferometry (PDI) [93] and consists of using a centered pinhole in order to create a point-source diffracting reference. This method was used by Miranda *et al.* to build an alternative technique to TERMITES [94]. Their spatio-temporal characterization device and TERMITES were developed simultaneously and independently in Lund and in Saclay.

TERMITES, for its part, is a self-referenced technique where the homogeneous reference is created by replacing the M2 plane mirror of the IFTS device by a convex one. As shown by figure 3.2, the $E_2(\boldsymbol{r}, \omega)$ beam—which is written $E_R(\boldsymbol{r}, \omega)$ from now on— is expanded as it propagates towards the sensor, where it interferes with the input beam $E(\boldsymbol{r}, \omega)$. This new optical scheme is very similar to Radial Shearing Interferometers [95, 96], in which the wavefront of the beam to be characterized is compared with a magnified version of itself.

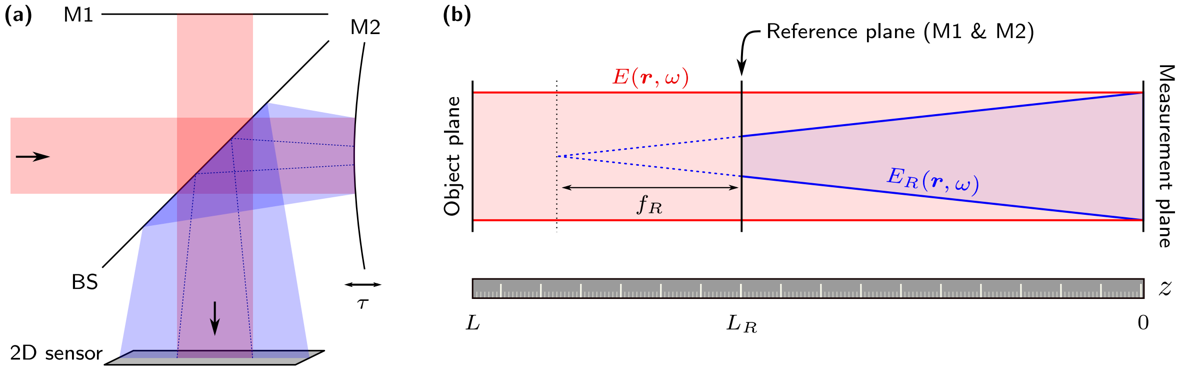
(a)
M1
M2
BS
2D sensor
$\tau$
(b)
Reference plane (M1 & M2)
$E(\boldsymbol{r}, \omega)$
Object plane
$f_R$
$E_R(\boldsymbol{r}, \omega)$
Measurement plane
$z$
$L$
$L_R$
0

**Figure 3.2.: Simplified drawings of the optical paths inside TERMITES. (a)** Schematic representing the Michelson interferometer of TERMITES, which uses a convex mirror (M2) in lieu of a plane one used in the IFTS technique (figure 3.1 on page 44). **(b)** One-dimensional projection of the same schematic, featuring the unknown input beam (in red) and the homogeneous reference (in blue). The reference is a diverging copy of the input beam, generated at the reference plane by the curved mirror of focal length $f_R$. Object plane is the optical plane that the user needs to characterize. Its position $L$ is arbitrary.

Only a central portion of the dilated reference actually interferes with the input beam. As illustrated in figure 3.2, this useful part is generated in the reference plane from a sample of the input beam. The ratio between the size of this sample and the size of the input beam is the *reference size ratio* and is noted $\beta$. This reference size ratio is a parameter of paramount importance for all studies related to TERMITES. As shown by figure 3.2, $\beta$ dependence on other design variables is simply dictated by the intercept theorem:

$$\beta = \frac{f_R}{f_R + L_R}\,, \tag{3.6}$$

with $f_R$ the curved mirror focal length and $L_R$ the propagation distance between the reference plane and the measurement plane. Ideally, $\beta$ should be very small in order to generate a reference as homogeneous as possible, and exempt from any significant spatio-temporal coupling in the measurement plane. Unfortunately, the value of $\beta$ is limited by experimental constraints which will be described in details in the next chapter (section 4.1.1 on page 67). As a result, $\beta$ typically ranges from 0.3 to 0.7 depending on the exact implementation of TERMITES.

Adapting the IFTS signal development made in equation (3.2) on page 44, we obtain the expression describing the CPSD signal recorded by TERMITES, where $F(\boldsymbol{r})$ and $F_R(\boldsymbol{r})$ are respectively the fluence of the input beam and of the reference:

$$\hat{W}(\boldsymbol{r},\tau) = \underbrace{F(\boldsymbol{r}) + F_R(\boldsymbol{r})}_{\text{incoherent sum}} + \underbrace{2\,\mathrm{Re}\left[\,(\hat{E}(\boldsymbol{r}) \star \hat{E}_R^*(\boldsymbol{r}))(\tau)\,\right]}_{\text{coherent sum}} . \tag{3.7}$$

At the measurement plane, the reference is expanded spatially and still diverging. Therefore, its spatio-spectral phase is dominated by a curvature term defined as:

$$\varphi^m_{\mathrm{curv}}(\boldsymbol{r},\omega) = \xi^m_{\mathrm{curv}}\,|\boldsymbol{r}|^2\,\omega\,, \tag{3.8}$$

with $\omega$ the angular frequency, and $\xi^m_{\mathrm{curv}}$ the Radial Group Delay caused by wavefront curvature, expressed in fs/mm$^2$. The major part of the phase difference between the input beam and the reference stems from this curvature.

The most visible consequence of this curvature resides in circular fringes formed on the camera sensor of TERMITES at measurement plane. They are displayed on figure 3.3, where we computed the fluence profile measured by the camera of a TERMITES device. The input beam used in this first simulation is purely monochromatic so that only spatial effects are displayed for the moment.

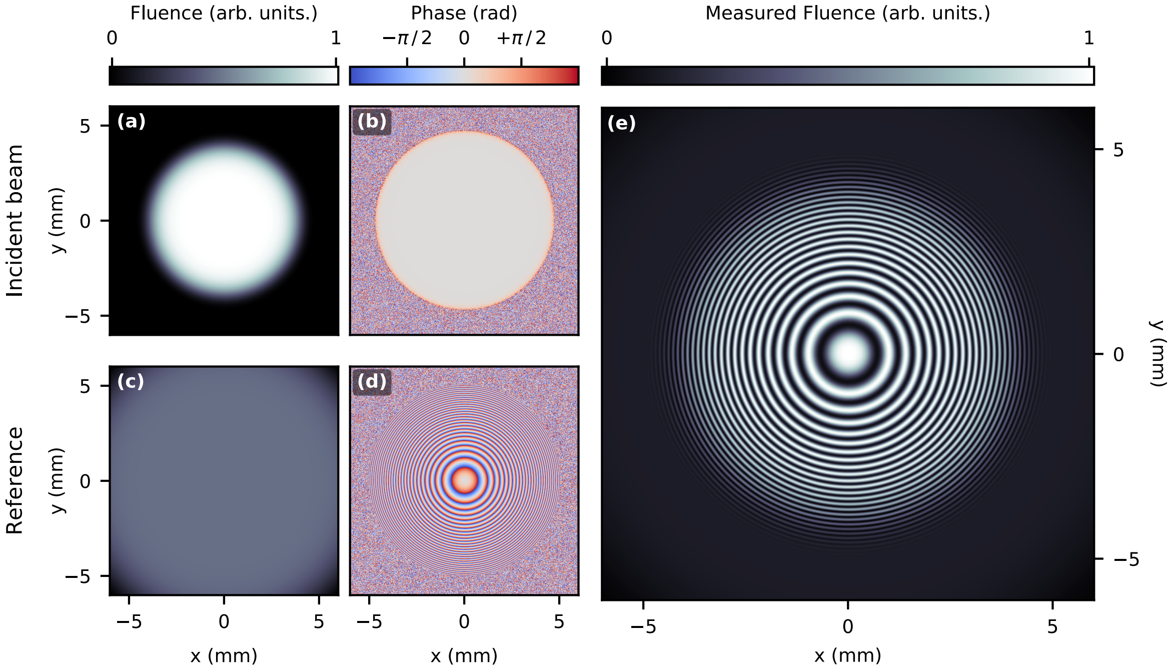

**Figure 3.3.: Interferogram generated by a simulated monochromatic input beam and its corresponding reference, observed at measurement plane. (a)–(d)** Fluence and phase profiles of the input beam and the reference. **(e)** Circular interferogram resulting from the overlap of the input beam and the reference.

Experimentally, TERMITES is in fact employed to characterize ultrashort (broadband) pulses, as opposed to the monochromatic input used in figure 3.3. Radial Group Delay $\xi^m_{\mathrm{curv}}$ of the curvature at measurement plane has a direct influence on the raw signal $\hat{W}(\boldsymbol{r},\tau)$ because the envelope of the cross-correlation $\hat{E}(\boldsymbol{r},t) \star \hat{E}_R^*(\boldsymbol{r},t-\tau)$ is maximum when the delay between the input beam and the reference is zero.

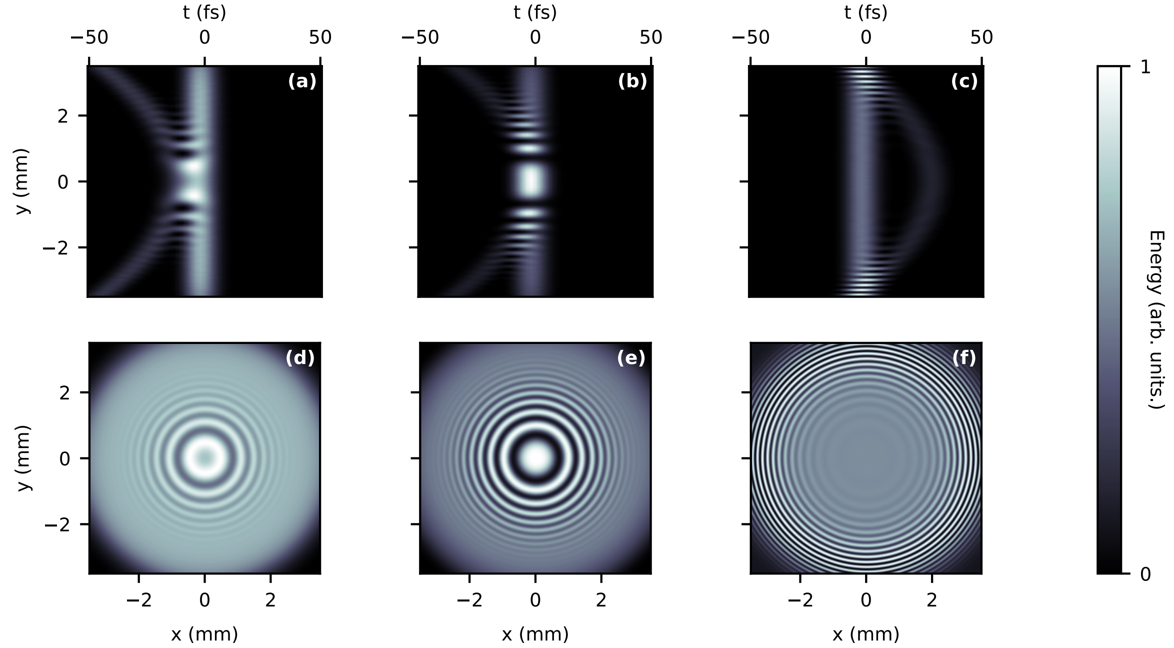

**Figure 3.4.: A simulated input beam and its reference, interfering on the measurement plane at three different intermediate delays $\tau$.** The top panels display the intensity of the resulting field, resolved in space and time: $I_W(\boldsymbol{r}, t) = \left|\hat{E}(y,t) + \hat{E}_R(y,t)\right|^2$. The bottom panels display the fluence $\widehat{W}(\boldsymbol{r}, \tau)$ as seen by the camera sensor and described by equation (3.7) on the previous page. Note how the spatial fringes radial position evolves with delay.

As shown in figure 3.4, the temporal overlap between the input beam and the reference depends quadratically on the radius, and so does the maximum fringe contrast. During a TERMITES scan, the contrast of the spatial fringes is first maximum at the center of the beam. As delay $\tau$ changes, the zone of maximum contrast travels radially to the outer edge of the image.

The final output data is a three-dimensional array of the interferograms, resolved in the two spatial dimensions of the camera sensor ($x$ and $y$), and also resolved in delay $\tau$ by the motorized translation stage. A schematic TERMITES raw dataset is shown by figure 3.5 on the next page. The right part of this figure shows a "spatio-temporal" slice of the measurement, which incidentally illustrates that the maximum contrast delay depends quadratically on the transverse position.

## 3.2. Numerical Retrieval of the Pulse Structure

Now that the technique and its implementation are described, let us focus on how to retrieve the desired information from raw TERMITES measurements. Some very basic properties of the input beam can be guessed directly from the raw interferograms. For example, its spectral bandwidth can be estimated from the input beam coherence time, which is deducible from temporal interferograms envelope. Some simple spatio-temporal couplings can also be approximated from 3D features of measurement datasets. Examples are developed in the thesis

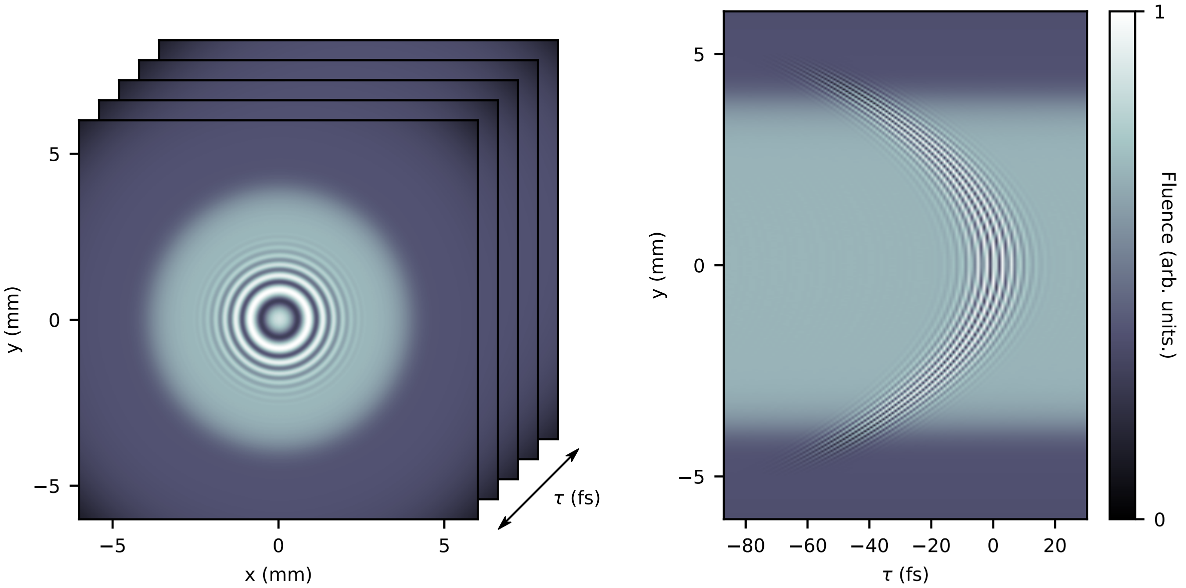

**Figure 3.5.: Representation of a typical TERMITES measurement output $\hat{W}(\boldsymbol{r},\tau)$.** On the left are represented examples of 2D spatial interferograms. The right panel shows a spatio-temporal view of the same cube of data, taken at $x = 0$ and resolved along the second spatial dimension $y$ and the interferometer delay difference $\tau$.

of V. Gallet [41, pp. 79–82], and are analogous to *Time-of-Flight* techniques [97, 98] previously applied to ultrashort pulses. It is also possible to go much further and to compute the full spatio-spectral complex field of the input beam $E(\boldsymbol{r},\omega)$ from the raw TERMITES signal $\hat{W}(\boldsymbol{r},\tau)$. The next few pages will detail the five main processing steps required to achieve this much more precise and quantitative comprehension of pulses structure.

### 3.2.1. Going Back to the Spectral Domain

We determined that the signal measured by TERMITES is the sum of an incoherent term—i.e., the fluence of the pulse and its reference—and of an interference term, which is defined in time and contains the pulse structure information (equation (3.7) on page 47). This coherent signal is the real part of the cross-correlation between the unknown beam and its reference, at a given transverse position $\boldsymbol{r}$.

As most spatio-temporal couplings are more easily processed in the spectral domain, the first step of TERMITES data processing is to convert the pulse information from its original "time-encoded" format to a spectral quantity, as in the IFTS technique. This is done similarly with our device, by relying on the cross-correlation theorem that was defined in equation (3.3) on page 45. It is now applied to the TERMITES raw signal $\hat{W}(\boldsymbol{r},\tau)$. The Cross Power Spectral Density (CPSD) $W(\boldsymbol{r},\omega)$ that results from the Fourier Transform of $\hat{W}(\boldsymbol{r},\tau)$ is a function of the input and reference fields:

$$W(\boldsymbol{r},\omega) = E(\boldsymbol{r},\omega)\, E_R^*(\boldsymbol{r},\omega)\,, \tag{3.9}$$

and its spectral fluence and phase are:

$$\begin{array}{ll} \bullet & \left|W(\boldsymbol{r},\omega)\right|^2 = \varepsilon(\boldsymbol{r},\omega)\ \ \varepsilon_R(\boldsymbol{r},\omega) \\ \bullet & \mathrm{Arg}\Big(W(\boldsymbol{r},\omega)\Big) = \varphi(\boldsymbol{r},\omega) - \varphi_R(\boldsymbol{r},\omega) \end{array} . \tag{3.10}$$

Considering that the resulting phase is the difference between the phase of the beam and the phase of its reference, any identical term in the beam and in the reference is canceled. Specifically, the spectral phase at the center of the beam should normally be flat because the beam and its reference are identical at this position (see middle-right panel of figure 3.6). Similarly, if the incident beam shows a constant spectral phase term across all of its profile—a large quadratic phase for example—then this will not have any impact on the measurement because the reference will possess the same average spectral phase. This has a strong repercussion on the measurement device: TERMITES is able to characterize the spatio-spectral phase of ultrashort pulses (unlike IFTS [89–91]), nevertheless this result is obtained up to an unknown global spectral phase of the beam. The positive side is that TERMITES can be used to measure the spatio-temporal couplings at any position along the Chirped Pulse Amplification chain, because it is not sensitive to the average dispersion of pulses.

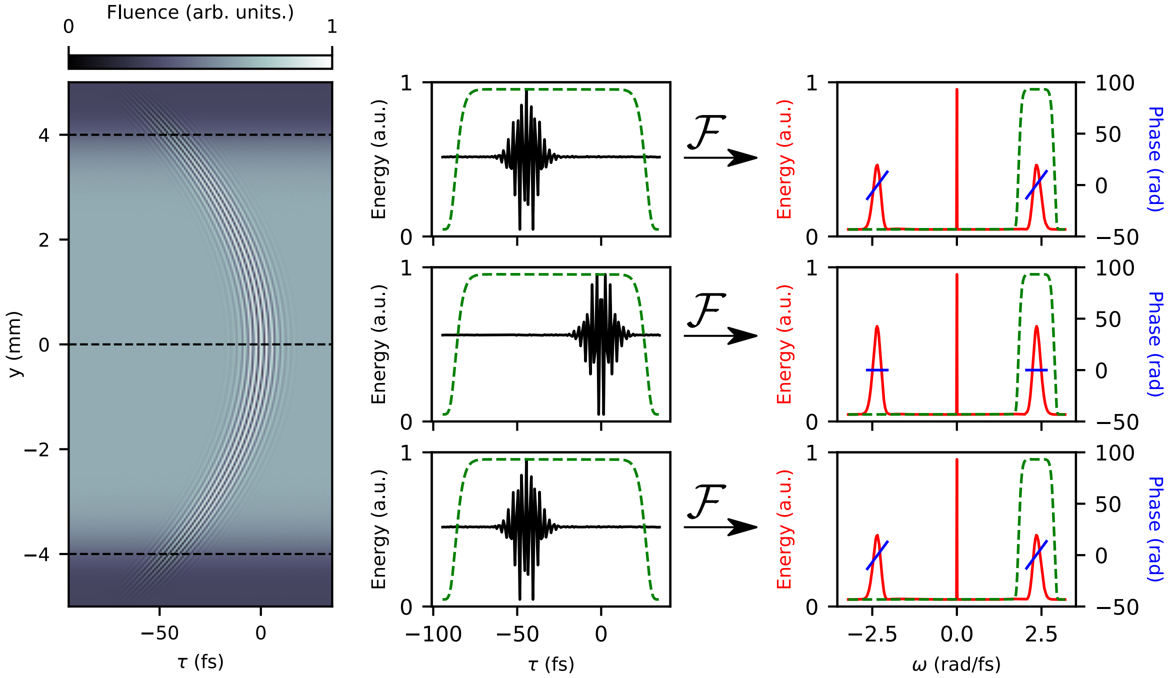

**Figure 3.6.: Visualization of the 1-D Fourier Transform step of TERMITES data processing.** The 1D temporal Fourier Transform is applied on all spatial pixels of the measurement data $\hat{W}(\boldsymbol{r},\tau)$. As proved by the cross-correlation theorem, Fourier transforming the temporal signal provides the cross power spectral density $W(\boldsymbol{r},\omega)$ (right panels of this figure & equation (3.10)). Dashed green curves represent the temporal and spectral filters (hyper-Gaussian windows) which are applied to the signals.

The operation linking $\hat{W}(\boldsymbol{r},\tau)$ to $W(\boldsymbol{r},\omega)$ is a 1D Fourier Transform, applied along the temporal dimension of $\hat{W}(\boldsymbol{r},\tau)$. Nowadays, the method of choice to perform Discrete Fourier Transform (DFT) operations on a uniformly sampled array is the Fast Fourier Transform algorithm (FFT) [99]. The result obtained from applying the FFT algorithm on our raw TERMITES data is illustrated by figure 3.6 on the preceding page. For the sake of clarity, this example is voluntarily displayed for only three transverse positions. Note that the 1-D Fourier Transform is run on all $N_x \times N_y$ pixels of the dataset in order to obtain the necessary spectral amplitude and phase for all positions the beam profile.

As illustrated by figure 3.6 on the facing page, the result of the Discrete Fourier Transform is an array of values spanning from $-\omega_{\max}$ to $\omega_{\max}$, with $\omega_{\max}$ the Nyquist angular frequency. The central peak gathers the continuous part of the signal recorded by the camera, and corresponds to the Fourier Transform of incoherent terms in equation (3.7) on page 47. The only valuable part of this spectral result is the band around $\omega_0$—central frequency of the input beam—which contains informations about the beam and the reference. This band is therefore filtered out and kept for further processing.

In practice, the most straightforward way to obtain the desired result would consist in loading the full raw data in memory and then computing the 1-D FFT of our 3-D volume, along its temporal dimension. This solution works, but is actually quite slow. Because of the high spatial resolution of TERMITES—see section 4.1.1 on page 67—waiting for the whole raw dataset to be loaded into memory before actually computing the FFT on one CPU core would be very inefficient. Instead, a sub-task was designed to be applied to $N_x$ spatial slices by a pool of available CPU cores, thus parallelizing efficiently the process. Each 2-D vertical slice of the dataset is resolved along the $y$ and $\tau$ dimensions, and are only one pixel thick in $x$. For each of them, the five following steps are applied:

**Load raw data from disk:** Depending on hardware specifications and actual data resolution, this can be the most time-consuming step.

**Optionally *zero-pad* the raw data:** By adding null values to the end of the temporal recording hence enlarging the range, *zero-padding* virtually increases the output spectral resolution. This method is harmless to the actual spectral content of the output signal, and can be necessary to make some large scale spatio-spectral features easier to distinguish by eye. This artificial interpolation of the signal should be used cautiously, by keeping in mind that the resolution of the *actual information* is limited by the physical range of the interferometer delay stage (see section 4.1.1 on page 65).

**Apply a temporal filtering window:** Because of the finite nature of our temporal recording—interpretable as a rectangular or Dirichlet window—non-physical frequencies show up as lobes in the spectrum. In order to avoid this undesired effect, an apodization window is applied on the temporal raw data. This ensures that the fluence signal smoothly goes to zero, hence effectively filtering out the artefact high-frequency components.

**Compute the actual 1-D FFT:** This is simply done thanks to the Python `numpy` library [100], in its version optimized for *Intel* CPUs.

**Apply a spectral filtering window:** We are only interested in the amplitude and phase values that are contained in the laser spectral bandpass. The FFT algorithm returns all frequency components, from negative to positive Nyquist frequency. A band-pass filter—properly adjusted around the incident laser spectrum—is applied to the FFT result in order to only keep the useful information and reduce the memory footprint.

Computing this Fourier Transform in parallel performs faster and only takes less than 5 minutes for a typical TERMITES dataset. This value globally scales linearly with spatial resolution (in number of pixels), and as $N\,log(N)$ with temporal sampling. It also consumes much less memory—only the space taken by one vertical slice, multiplied by the number of cores, instead of the complete raw dataset.

Since the beginning of this chapter, TERMITES has been described as a fundamentally 1D measurement, which is made independently over all pixels of the camera sensor. The Fourier Transform step that we just explained is a purely temporal/spectral process as well. Now that we made the jump from the temporal measurement of $\hat{W}(\boldsymbol{r}, \tau)$ to the cross power spectral density $W(\boldsymbol{r}, \omega)$, it will be more suitable to talk and to process *spatial* quantities, resolved along a frequency axis. From now on, we will therefore perform operations on *fluence profiles* or *wavefronts* to obtain the desired result.

### 3.2.2. Curvature Removal & Data Resampling

The output of the previous Fourier Transform step is the complex quantity $W(\boldsymbol{r}, \omega)$. The phase of this cross power density is the difference between the incident beam wavefront—mostly flat—and the reference wavefront—strongly curved. This strong curvature is the largest component of the retrieved cross power density $W(\boldsymbol{r}, \omega)$, as seen in panel (a) of figure 3.7 on the facing page. Additionally, the spatial resolution of $W(\boldsymbol{r}, \omega)$ is very high because of experimental constraints: depending on the setup dimensions, some spatial fringes can be very small and need to be resolved by the camera.

Neither the curvature nor the high spatial resolution is a fundamental issue for the measurement. Yet, both of them considerably overload the next computational steps, and are not necessary for interpreting the spatio-temporal profile of the measured beam. The curvature can be considered as a measurement artifact because it does not contain any information about the pulse spatio-temporal structure, and is only linked to the TERMITES optical layout. It can therefore be removed without degrading the results. Subtracting the theoretical reference curvature $\varphi^m_{\text{curv}}(\boldsymbol{r}, \omega)$ from the CPSD is the most straightforward way to go. $W_0(\boldsymbol{r}, \omega)$ is the result of this operation and is used for the subsequent processing steps.

$$W_0(\boldsymbol{r}, \omega) = W(\boldsymbol{r}, \omega)\ \exp\left(-\mathrm{i}\,\varphi^m_{\text{curv}}(\boldsymbol{r}, \omega)\right). \tag{3.11}$$

Even if the value of $\varphi^m_{\text{curv}}(\boldsymbol{r}, \omega)$ can be deduced from design characteristics of TERMITES (appendix A.1 on page 137), we prefer to obtain it from the two-dimensional polynomial fit of the curvature at $\omega_0$. This method does not depend on experimentally measuring the propagation distance in the device and is much more accurate. When executed correctly, subtraction of the fitted value of $\varphi^m_{\text{curv}}(\boldsymbol{r}, \omega)$ removes the exact amount of curvature from $W(\boldsymbol{r}, \omega)$. The fit operation itself is done by minimizing the least-square residual $\epsilon$ written as:

$$\epsilon = \left| \operatorname{Arg}(W(\boldsymbol{r}, \omega_0)) - \Big(C_x(\omega_0)\, x + C_{xx}(\omega_0)\, x^2 + C_y(\omega_0)\, y + C_{yy}(\omega_0)\, y^2\Big) \right|^2, \tag{3.12}$$

with $\operatorname{Arg}(W(\boldsymbol{r}, \omega_0))$ the wavefront at central frequency of the CPSD, and $C(\omega_0)$ the coefficients of the polynomial fit at central frequency.

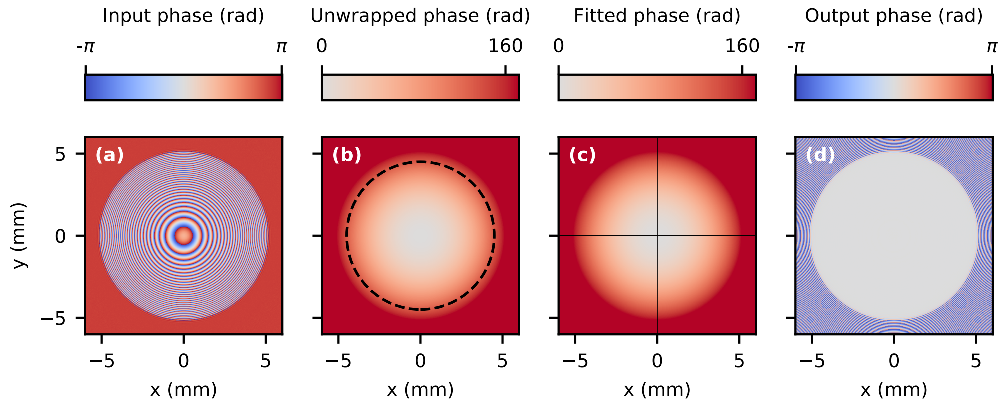

**Figure 3.7.: Evolution of the central frequency wavefront, along the curvature removal process.** **(a)** Arg($W(\boldsymbol{r},\omega_0)$). **(b)** Corresponding unwrapped phase. The dashed circle represents the fit zone, used for next image. **(c)** 2D polynomial fit (degree 2) of the unwrapped phase. The vertical and horizontal line show the roots $x_c$ and $y_c$ of the fit i.e., the center of curvature measured with sub-pixel precision. **(d)** Arg($W_0(\boldsymbol{r},\omega_0)$) (Wavefront obtained after subtraction of the fit).

In equation (3.12) on the facing page, the two interesting fitted values are $C_{xx}(\omega_0)$ and $C_{yy}(\omega_0)$ because those coefficients respectively refer to the horizontal and vertical curvatures at central frequency. The reference mirror is considered stigmatic so the curvature that should be removed is the average of $C_{xx}(\omega_0)$ and $C_{yy}(\omega_0)$. Moreover, the center of curvature $\boldsymbol{r_c}$ can be extracted from the first linear coefficients. As a result, the quadratic phase that is finally subtracted from $W(\boldsymbol{r},\omega)$ is:

$$\varphi_{\text{curv}}(\boldsymbol{r},\omega) = \frac{C_{xx}(\omega_0)+C_{yy}(\omega_0)}{2}\,\frac{\omega}{\omega_0}\,|\boldsymbol{r}-\boldsymbol{r_c}|^2\,. \tag{3.13}$$

In equation (3.13), the $\omega/\omega_0$ factor is necessary to scale the curvature wavefront obtained at central frequency to each frequency of the spectrum. The full curvature removal operation is illustrated by figure 3.7 for the wavefront of a simulated CPSD, at $\omega_0$.

After subtraction of the curvature from the dataset, camera sampling is oftentimes far larger than the wavefront modulations of $W_0(\boldsymbol{r},\omega)$. This high resolution is excessive at this point, but was necessary during interferograms acquisition because the pixels of the sensor have to be smaller than the smallest spatial fringes. A first way to reduce the data size would have consisted in keeping only a fraction of the sensor pixels from the start. Oftentimes, *decimation* is even directly available on industrial cameras, and allows for sending only the necessary pixel values to the processing computer. By reducing the data size from the start, this method eradicates our high resolution issue, and considerably accelerate the measurement as well as the Fourier Transform step previously described.

Even though the simplicity of this first approach is rather tempting, the resampling method described in G. Pariente's thesis [42, p. 103] provides better signal-to-noise ratio. Relying on well-known signal processing filtering techniques—see [101] or [102, pp. 403–411]—this process is comprised of two steps: *Convolution* and *Decimation.*

Convolving the measured complex quantity has the immediate effect of reducing the noise, by computing a weighted sum of all neighbouring pixels. This method replaces one output pixel by a *macro-pixel*, made of $N_{\mathrm{DS}}^2$ pixels ($N_{\mathrm{DS}}$ being the adjustable downsampling ratio). Given the large initial dataset resolution, it is common to use macro-pixels formed by thousands of physical pixels in order to measure the average fluence and phase at one $(x, y)$ position. This has a significant positive impact on the Signal-to-Noise ratio of the measurement, making this method more robust than simply selecting relevant pixels from the initial data.

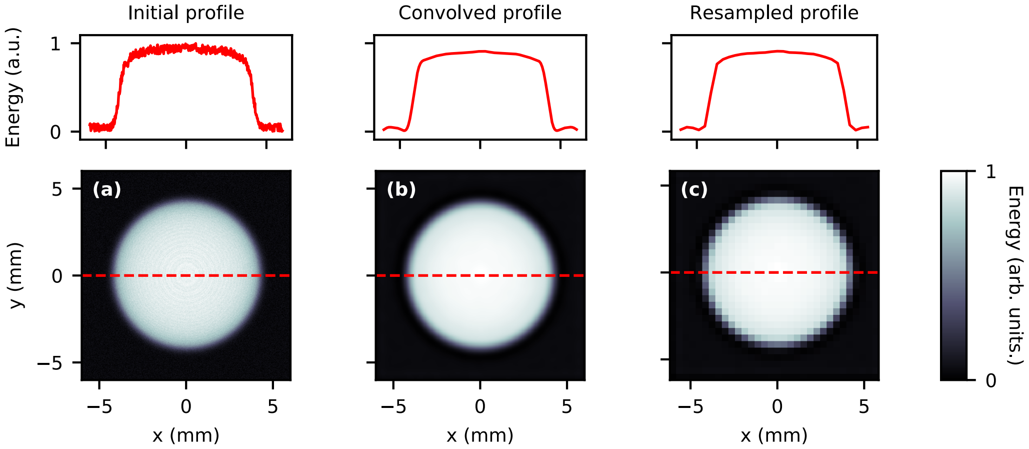

**Figure 3.8.: Resampling of the beam spectral fluence profile $\varepsilon(\boldsymbol{r}, \omega)$, at one frequency.** The noisy measured profile **(a)** is convolved with a Lanczos kernel in **(b)** and then decimated to a more appropriate resolution in **(c)**. Upper plots are horizontal slices of the profiles. The same steps are applied separately on the phase profile. In this realistic example, the input resolution is $1600 \times 1600$ and the output resolution is only $32 \times 32$. Each macro-pixel is composed of $N_{\mathrm{DS}}^2 = 2500$ physical pixels.

The convolution is performed with a Lanczos kernel of $N_{\mathrm{DS}} \times N_{\mathrm{DS}}$ pixels, which has a nearly perfect impulse response—explaining why it is commonly used for this type of image processing tasks. As explained in details in Gustave Pariente's thesis [42, p. 105], directly performing the convolution on complex data can imprint phase defects on the amplitude and *vice versa*. This would constitute a strong numerical artifact, as the spectral fluence and phase profiles are separate physical quantities which can be measured independently in experiment. That is why we rather perform the convolution separately on spectral fluence and phase before decimating spatially the data. Finally the downsampled fluence and phase profiles are recombined in the output complex array.

Figure 3.8 illustrates the convolution and decimation of a fluence profile. Doing the same thing on the phase is a bit more delicate, because of phase jumps. Those are visible on the phase profile because our interferometric device returns the phase of the beam, *modulo* $2\pi$. It means that if large aberrations ($\gtrsim \lambda_0$) are in the incident beam, then numerical jumps will appear on the wavefront. This ambiguity—well known in the field of optics e.g., in holography or tomography—is generally not an issue, but has to be eliminated at this point because computing the convolution of a wrapped phase does not have any physical meaning. Several phase unwrapping techniques exist and I chose to use the quality-guided path method developed by Herraez *et al.* [103] because of its high reliability and thanks to its implementation in the Python module `scikit-image` [104]. After having applied this unwrapping step, the resampling of the wavefront can be done following the same steps as for the fluence profile.

### 3.2.3. Reference Compensation

A common problem in metrology lies in the fact that most of diagnostic devices do not return absolute quantities. TERMITES is no exception. As a self-referenced technique, our device performs a comparative measurement using a reference generated from a central part of the unknown beam—which by nature is not defined. The reference can therefore also suffer from unknown aberrations and be impaired. In the case where the reference size ratio $\beta$—defined in equation (3.6) on page 46—is significantly small, then the spatial aberrations of the reference can be considered negligible over its diameter, and the assumption $E(\boldsymbol{r},\omega) = W_0(\boldsymbol{r},\omega)$ can be considered valid. However, design constraints—developed later in section 4.1 on page 64—require that most configurations of TERMITES have to use a large part of the incident beam to construct the reference. In those cases, the measured cross power density $W_0(\boldsymbol{r},\omega)$ obtained after the previous processing steps cannot be directly used to get to the incident beam $E(\boldsymbol{r},\omega)$.

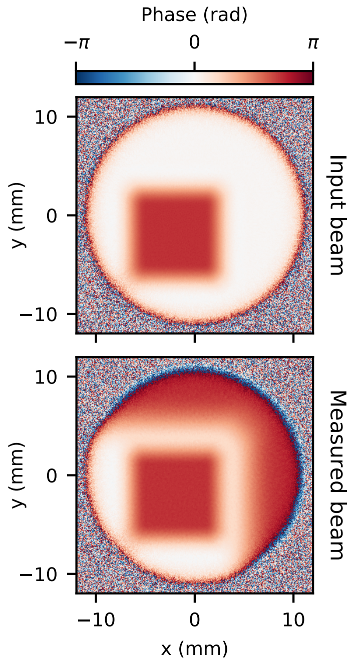

**Figure 3.9.: Influence of the reference on the measured beam.** The upper panel shows the phase profile of a simulated beam at the optical plane of measurement. The bottom panel shows the phase which is actually measured by TERMITES wherein the square shape is magnified by $1/\beta$ and subtracted from the desired wavefront. The white square visible in the bottom panel is directly caused by the subtraction of reference wavefront.

Figure 3.9 shows that the main effect caused by the imperfect reference comes from the magnified beam profile being imprinted on the cross power density $W_0(\boldsymbol{r},\omega)$. As it was developed in equation (3.10) on page 50, the measured spectral fluence is the product of the incident beam spectral fluence ($\varepsilon$) and of the reference beam spectral fluence ($\varepsilon_R$). Equivalently, the measured wavefront is the difference between the phase of the input beam profile, and the phase of the reference. Depending on the input beam features, and on the parameters of the instrument, this can have a more or less strong effect on the resulting measurement. In the situation that is simulated in figure 3.9, the square-shaped aberration visible in red on the incident beam is magnified by a factor $1/\beta$ and then subtracted from the actual wavefront in the TERMITES measurement. This is where the white square comes from in the bottom panel of figure 3.9, and this is why the retrieved field can represent imperfectly the true input beam field at this stage.

The different methods used to address this inverse problem mainly come from the Radial Shearing Interferometry (RSI) community. Indeed, after the first step of our data processing, the signal resulting from a TERMITES measurement can be seen as a spectrally resolved RSI measurement. In this well-established interferometry technique, the reference is usually compensated using iterative algorithms as explained e.g., in [105, 106] (applied only on phase) or [107] (applied on phase and spectral fluence profiles). It is possible to estimate how the beams propagate in the instrument because TERMITES is a relatively simple linear device. The reference can be defined in the optical plane of the curved mirror (reference plane) as being equal to the input beam at this position, with an added curvature:

$$E_R(\boldsymbol{r},\omega) = E(\boldsymbol{r},\omega)\ \exp\Big(\mathrm{i}\ \varphi^r_{\text{curv}}(\boldsymbol{r},\omega)\Big), \tag{3.14}$$

with $\varphi^r_{\text{curv}}(\boldsymbol{r},\omega)$ the phase curvature created by the convex mirror, in the reference plane (see appendix A.1 on page 137 for its exact expression). The diverging reference then propagates linearly to the measurement plane, without further alteration.

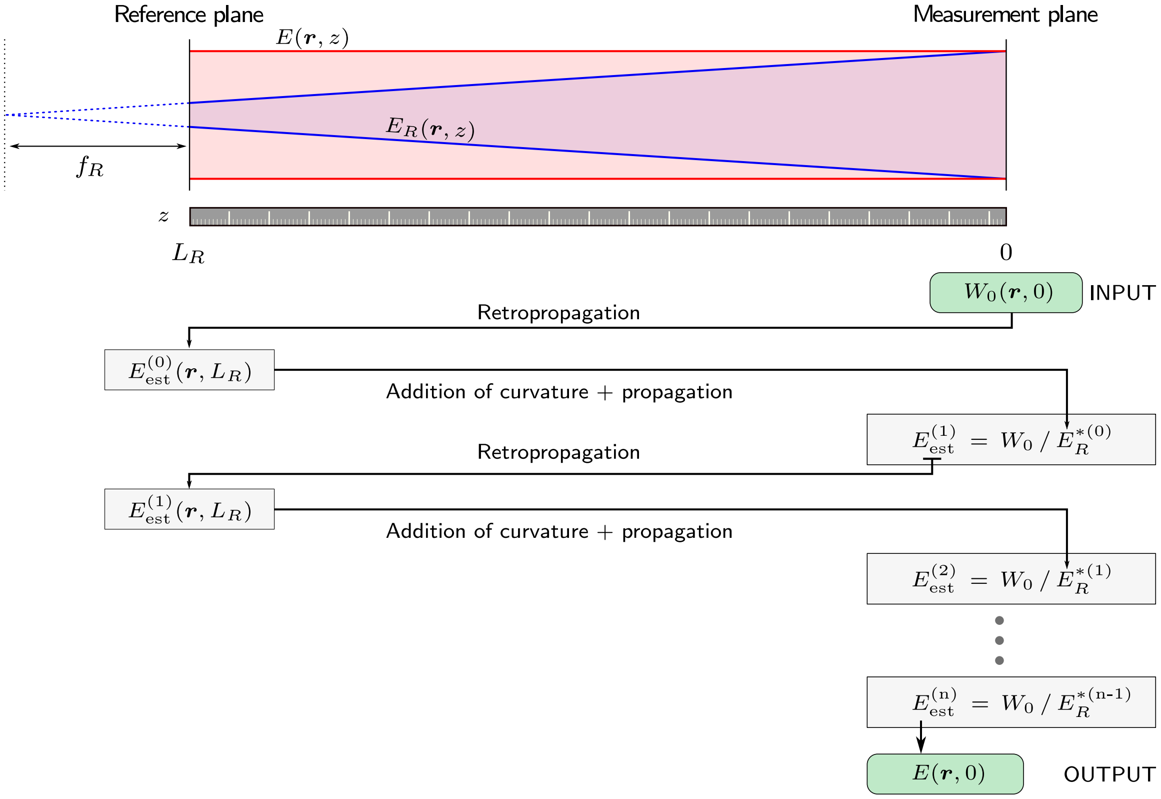
Reference plane
Measurement plane
$E(\boldsymbol{r},z)$
$E_R(\boldsymbol{r},z)$
$f_R$
$z$
$L_R$
0
$W_0(\boldsymbol{r},0)$
INPUT
Retropropagation
$E^{(0)}_{\text{est}}(\boldsymbol{r},L_R)$
Addition of curvature + propagation
$E^{(1)}_{\text{est}} = W_0\ /\ E_R^{*(0)}$
Retropropagation
$E^{(1)}_{\text{est}}(\boldsymbol{r},L_R)$
Addition of curvature + propagation
$E^{(2)}_{\text{est}} = W_0\ /\ E_R^{*(1)}$
$E^{(n)}_{\text{est}} = W_0\ /\ E_R^{*(n-1)}$
$E(\boldsymbol{r},0)$
OUTPUT

**Figure 3.10.: Schematic diagram of the current reference compensation algorithm.** $W_0(\boldsymbol{r},0)$ is the measured signal, which is used as a first guest of $E_{\text{est}}$ for the algorithm. $E^{(n)}_{\text{est}}$ is the estimated incident beam, computed at the measurement plane and then at the reference plane, at each step of the computation. $E(\boldsymbol{r},0)$ is finally the best estimated field, after the reference has been compensated by the iterative algorithm.

A first implementation of iterative algorithm was developed and adapted to TERMITES by G. Pariente during his thesis [43, p. 105]. His algorithm is based on the approximation that the reference observed in the measurement plane is an homogeneous dilation of the input beam. The algorithm works by computing the dilation of the measured phase profile and then subtracting it from successive estimation of the input beam. In this work, we improved further this idea in order to take into account the effects of the free-space propagation and to extend the algorithm so that it corrects not only the wavefront but the spectral fluence profile as well. Despite being more complicated, this version does not rely anymore on any approximation and is closer to reality of the instrument. Let us go into the details of the most recent solution.

As illustrated in figure 3.10, compensating for the reference mainly consists of computing the estimated input beam step-by-step, by going through an iterative algorithm. The general idea is to compute at each step $n$ the reference that would be generated by the beam estimated at the $n-1$ step. The cross power density $W_0(\boldsymbol{r})$ serves as the first guess $E_{\text{est}}^{(0)}$ and is divided at each step by this corrected reference, after having computed the latter in the measurement plane ($z=0$):

$$E_{\text{est}}^{(n)}(\boldsymbol{r}) = \frac{W_0(\boldsymbol{r})}{E_R^{*(n-1)}(\boldsymbol{r})} \; . \tag{3.15}$$

This algorithm is applied independently on each spectral sample, as it is purely spatial. After a few ($< 15$) iterations, the estimated beam eventually converges to the true input beam profile with a reasonable accuracy.

At each step of the process, the reference $E_R^{*(n-1)}(\boldsymbol{r})$ is computed as precisely as possible. While the previously mentioned implementations approximated the reference as a simple dilation of the estimated beam, we chose to *simulate* accurately the true propagation of the beam and to use plane-wave decomposition when going back and forth between the measurement plane and the reference plane. Spending this extra computation time has two profits. First, this method takes into account the free-space propagation occurring between the two optical planes. Even if this effect can be neglected in some cases, we found that not taking it into account has a noticeable negative effect on the retrieved beam profile in a standard TERMITES configuration. Secondly, using plane-wave propagation has a practical benefit. As the device is never perfectly aligned, it is important to take into account the center position of the reference beam in the reference plane. This information is measured experimentally for calibration, and simply translated into a virtual tilt which is added to the estimated beam before propagation during the iterative algorithm.

Assessing the absolute convergence of the algorithm is not trivial, since it cannot be summarized as a purely arithmetic progression. Nevertheless, it is possible to understand it intuitively by reasoning like if the computed reference was only a dilation of the beam, as in simpler versions of the algorithm. Let us adapt the convergence demonstration made by López Lago and Fuente [107, p. 373] to our situation. The successive estimated fields can be computed iteratively from equation (3.15), by developing each time the previous estimation:

$$\begin{aligned}
E_{\text{est}}^{(n)}(\boldsymbol{r}) &= \frac{W_0(\boldsymbol{r})}{E_{\text{est}}^{(\text{n-1})}(\beta\boldsymbol{r})^*} \; , \\
&= \frac{W_0(\boldsymbol{r})}{\left(\frac{W_0(\beta\boldsymbol{r})}{E_{\text{est}}^{(\text{n-2})}(\beta^2\boldsymbol{r})^*}\right)^*} \\
&= \frac{W_0(\boldsymbol{r})}{W_0{}^*(\beta\boldsymbol{r})}\, E_{\text{est}}^{(n-2)}(\beta^2\boldsymbol{r}) \; , \\
&= \frac{W_0(\boldsymbol{r})}{W_0{}^*(\beta\boldsymbol{r})} \left(\frac{W_0(\beta^2\boldsymbol{r})}{E_{\text{est}}^{*(n-3)}(\beta^3\boldsymbol{r})}\right) \; , \\
&= \dots
\end{aligned} \tag{3.16}$$

Let us recall the approximation we made about the reference which is considered to be a simple dilation of the input beam:

$$W(\boldsymbol{r}) = E(\boldsymbol{r})\, E(\beta\boldsymbol{r})^* \; .$$

Equation (3.16) therefore simplifies to:

$$E_{\text{est}}^{(n)}(\boldsymbol{r}) = \begin{cases} E(\boldsymbol{r})\ W_0(\beta^n \boldsymbol{r})\ /\ E(\beta^n \boldsymbol{r}) \text{ when } n \text{ is even.} \\ \\ E(\boldsymbol{r})\ E(\beta^n \boldsymbol{r})\ /\ W_0(\beta^n \boldsymbol{r}) \text{ when } n \text{ is odd.} \end{cases} \tag{3.17}$$

In both cases, terms that depend on $\beta^n \boldsymbol{r}$ end up being spatially homogeneous as their magnification tends to infinity, because $\lim_{n\to\infty} \beta^n = 0$ (for $\beta < 1$, which is verified in our case). This means that the iterative algorithm theoretically always converges to the $E(\boldsymbol{r})$ field, up to an irrelevant scalar multiplicative constant. The derivative of the root-mean-square difference between consecutive estimations is a good stopping criterion to determine that no further improvement can be brought by the iterative method.

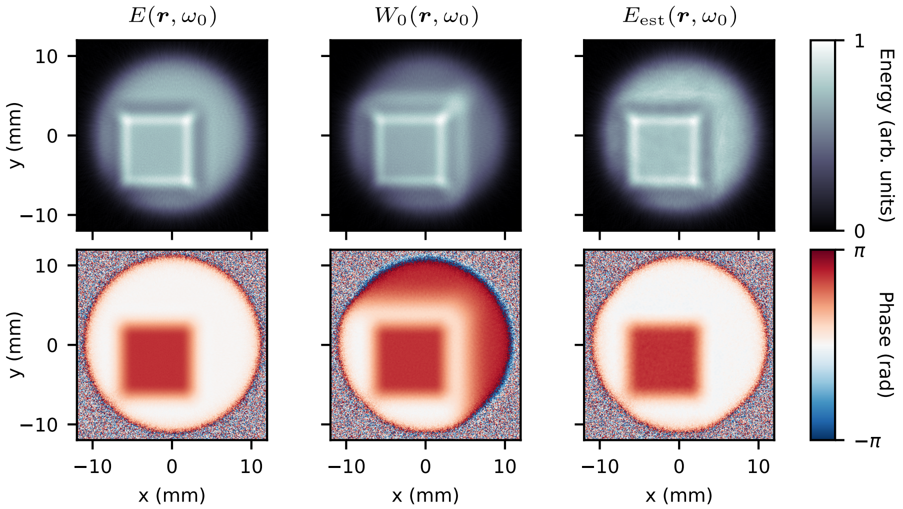

**Figure 3.11.: Reference effect in the measurement plane, and correction by the reference compensation algorithm.** The left column shows the fluence and phase profiles at one wavelength of a simulated beam $E(\boldsymbol{r}, \omega_0)$ that went through a square-shaped phase defect in the object plane, before being measured in the plane of the camera. The central column shows the field $W_0(\boldsymbol{r}, \omega_0)$ that is actually measured by TERMITES. Lastly, the right column shows the estimated field $E_{\text{est}}(\boldsymbol{r}, \omega_0)$, retrieved from $W_0(\boldsymbol{r}, \omega_0)$ by the reference compensation algorithm.

Figure 3.11 is an example of a successful compensation of the reference by the iterative algorithm. As figure 3.9 on page 55 was already illustrating, the influence of the reference can badly alter the field $W_0(\boldsymbol{r}, \omega_0)$ which is measured by TERMITES. After the algorithm has converged, the retrieved field $E_{\text{est}}(\boldsymbol{r}, \omega_0)$ is significantly closer to the expected input beam, both in appearance and in magnitude. Even if most of the bias linked to the reference is canceled, some additional filtering steps might be necessary so that the retrieved profile can be even closer to the expected result, in particular in situations where the measured beam is noisy. Nevertheless, considering that this simulated aberrated profile is already quite exotic compared to typical experimental aberrations, the present simulation shows that the reference compensation method is well suited for obtaining a correct TERMITES measurement in the general case.

### 3.2.4. Retropropagation

Now that the field $E(\boldsymbol{r}, \omega)$ is accessible and disentangled from the reference, we can analyze it and start to draw some conclusions about the laser beam properties. However, the experimentalist should understand that this field is measured in the camera plane, and that it does not necessarily represent the field in the plane of interest (i.e., in the *object plane*, illustrated in figure 3.2 on page 46). When spatial aberrations are limited, propagation effects occurring from the object plane to the measurement plane can be considered negligible. However, if features of relatively high frequency are affecting the complex field in the object plane, they will diffract and will not be easily recovered in the measurement plane.

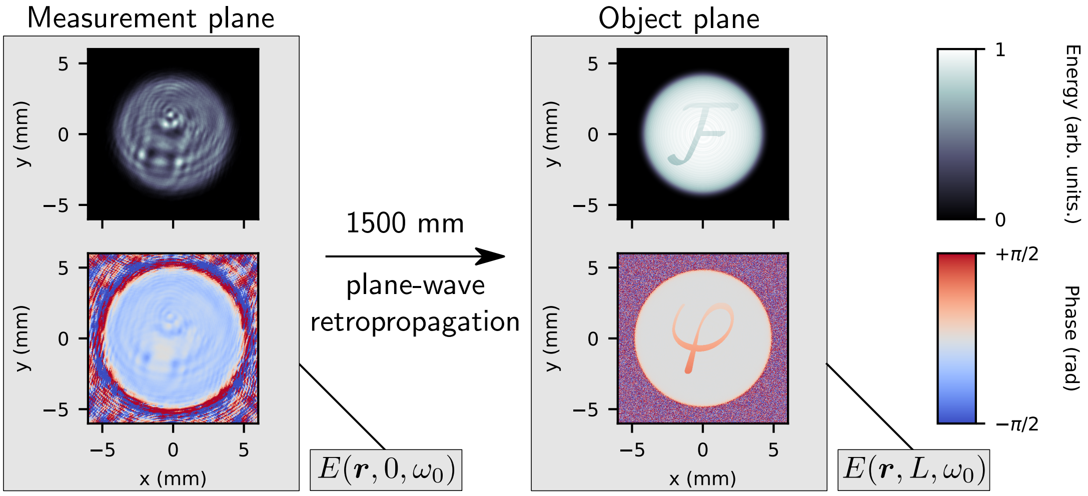

**Figure 3.12.: Retropropagation of the measured field to the object plane.** This example shows how the object field can be modified by diffraction in certain conditions. In this case, numerically imaging the object plane thanks to plane-wave retropropagation of $-1500\,\text{mm}$ from the measurement plane restores completely the initial patterns.

Fortunately, TERMITES unravels the full spatio-spectral profile of the beam in amplitude and in phase. It is therefore rather straightforward to numerically retropropagate this result to the plane of our choice—by plane-wave decomposition—so that the object plane can be numerically imaged. Figure 3.12 is an example of retropropagation from the measurement plane to the object plane. This case is rather exaggerated because we overprinted some letters on the profiles, in order to see their evolution across 1500 mm of propagation in free-space. The letters possess some high spatial frequencies, which tend to evolve faster over distance, changing the profiles significantly. Nevertheless, I observed experimentally during validation measurements that retropropagating the measured fields could be crucial for a correct interpretation, even in realistic test-cases (see chapter 6 on page 89 and part III on page 103).

This step cannot retrieve the original beam if too large aberrations affect it. In such cases, some portions of the laser energy can diverge too much and be filtered out by the instrument pupil. Information is then lost because this signal does not contribute to the interferogram measured by the camera. This is not a critical issue because those hypothetical strong aberrations would already be noticed and corrected for in the early stages of the laser alignment, thanks to more simple wavefront-sensing techniques, or even by simply looking at the near-field profile of the beam after some propagation.

### 3.2.5. Spectral Phase Stitching

The complex field $E(\boldsymbol{r}, L, \omega)$ that is retrieved after the three previous steps now describes accurately the spatio-spectral profile of the input beam seen at the object plane. The main remaining issue lies in the fact that TERMITES is blind to any *global* spectral phase, i.e., any spectral phase component present at all positions in the beam. By principle, the result retrieved by our instrument is known up to an unknown spectral phase, because TERMITES is a self-referenced technique. For example, TERMITES would be unable to tell if the input beam was uniformly chirped due to a bad compression, because the chirp would affect both the input beam and the reference, at all positions of their profile.

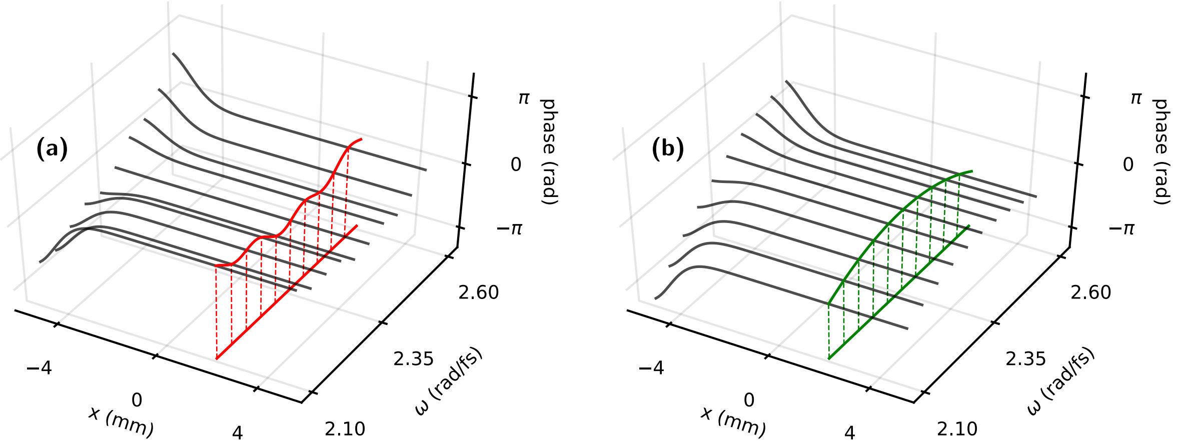

**Figure 3.13.: Forcing global spectral phase using an independent measurement.** Several spatially resolved phase profiles are extracted from a 3D dataset and plotted on panel **(a)**, for different frequencies. The red curve highlight the arbitrary spectral phase at one position along $x$, which arose from previous steps of the post-processing. In order to get a rigorous representation of the input beam, the spectral phase is forced to match a local measurement made at this position with an independent diagnostic tool (green curve in panel **(b)**).

Fortunately, this difficulty is easily surmounted experimentally. We explained that the output of a TERMITES measurement can be considered as a spatial measurement which is resolved in spectrum. The current problem is explained by the fact that at the end of the data processing, the spectral wavefront samples are unrelated between themselves, because they were processed independently through retropropagation and iterative algorithm. The independent wavefronts can be *stitched* back together thanks to an independent measurement of the spectral phase $\varphi(x_0, y_0, \omega)$, at one position across the beam profile.

Spectral phase stitching is usually carried out using FROG [70] or SRSI [108] devices, which easily provide the required local spectral phase. As illustrated in figure 3.13, a spatially invariant spectral phase is then added to the TERMITES result $E(x, y, \omega)$, so that the spectral phase of the TERMITES measurement matches perfectly the local spectral phase measured at position $(x_0, y_0)$. This operation do not change the spatio-temporal properties of the beam because it affects the phase at all positions in the same manner. $E_s(x, y, \omega)$ is the field resulting from this adjustment:

$$E_s(x, y, \omega) = E(x, y, \omega) \exp\left[\, \mathrm{i}\, (\varphi(x_0, y_0, \omega) - \mathrm{Arg}(E(x_0, y_0, \omega))\, \right] . \tag{3.18}$$

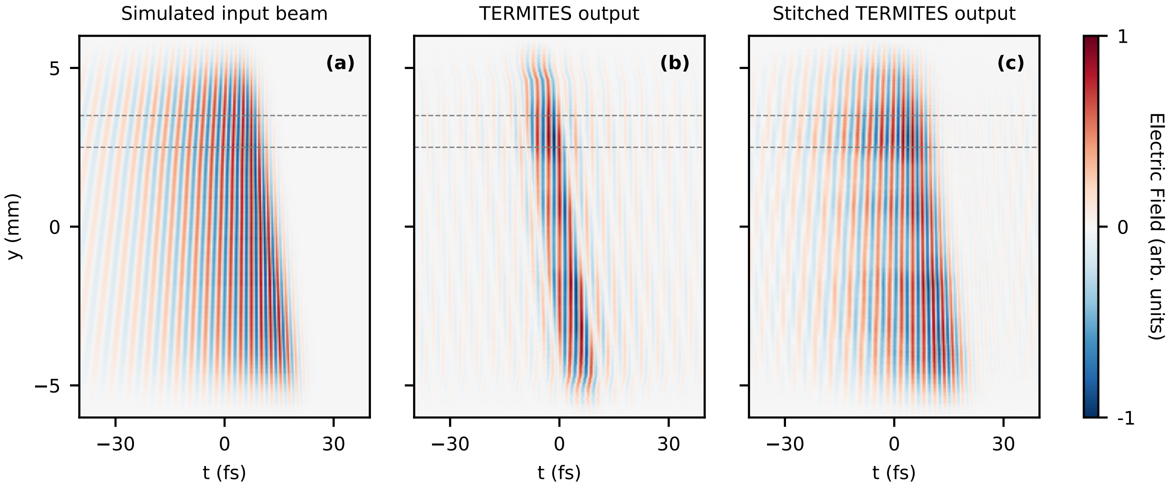

**Figure 3.14.: Spectral Phase Stitching of the result.** Panel **(a)** represents the spatio-temporal slice of a simulated input beam which is affected by a Pulse Front Tilt coupling, and also by a non-flat global spectral phase. Panel **(b)** shows the field which is retrieved by a simulation of the TERMITES instrument, using the previous field as its input. Finally, panel **(c)** shows the TERMITES result, corrected by an independent spectral measurement, made between the dashed horizontal lines.

Figure 3.14 illustrates the effect of this correction on a simulated TERMITES measurement. The input beam we used to generate this particular figure exhibits a combination of purely-temporal and spatio-temporal effects. Panel (a) shows that the input profile is temporally dispersed and also tilted spatio-temporally (by Pulse Front Tilt). Panel (b) shows that Pulse Front Tilt is retrieved without any problem by TERMITES. However, the general temporal spread—due to Group Delay Dispersion (GDD) and Third Order Dispersion (TOD)—is not obtained. After spectral phase correction, the resulting field (in panel (c)) is closer to the real input beam and can be safely used to estimate the intensity at focus or assert other secondary results.

However important this step can be to truly characterize the input field, it is generally not mandatory if the user only needs to measure spatio-spectral couplings (i.e., chromatism). Oftentimes, the phase can simply be forced to zero for all frequencies at one spatial position. While simulating a perfect compression at this position, this fast method effectively stitches the spectrally resolved wavefront for further examination of space-time couplings, without the need to perform an independent measurement each time.

⁂

In this first chapter concerning TERMITES, I focused on the in-depth description of its working principles. This was done by understanding the raw signal measured by our modified interferometer (section 3.1 on page 44), and by going through the whole numerical processing used to extract the desired input field (section 3.2 on page 48).

The simplicity of design of TERMITES is undoubtedly one of its biggest strength compared to other characterization techniques. Using linear optics and simple optical components reduces the number of error sources to the minimum, while enabling full spatio-spectral characterization of the laser at any point along its amplification chain. This would not be possible without careful post-processing of measurements. However fastidious it may seem after these few pages of detailed explanation, each step of the process relies on simple concepts, and is based on well-established signal processing techniques.

## Chapter 4.

# Specifications & Performance

Making careful choices about the instrument design was essential to optimize the quality of measurements. Going from proof-of-concept to the final device requires studying the theoretical limits of TERMITES and optimizing its design variables accordingly.

Theoretical constraints of the instrument are related to signal acquisition limits and to hardware limitations. They will be fully described in the first part of this chapter. We explain in a second part the optimization choices that we made to build the prototypes of TERMITES.

## Contents

**4.1. Design Parameters and their Constraints** . . . . . . . . . . 64
  4.1.1 Hard Constraints
  4.1.2 Soft Constraints
**4.2. Settling for an Optimal Set of Parameters** . . . . . . . . . . 71
  4.2.1 Optimization Procedure
  4.2.2 Two Input Requirements, Leading to Two TERMITES Designs

## 4.1. Design Parameters and their Constraints

As for any other optical instrument, the design of TERMITES depends on a set of independent variables which are themselves constrained by various physical limits. In the case of our instrument, its design parameters are linked to three elements: the optical layout, the camera sensor, and the piezoelectric delay stage. In addition to these parameters, the input laser beam also has properties that have to be considered. Those are not directly linked to TERMITES itself, but should nevertheless be defined by their limits in the instrument specifications and taken into account for the optimization. All independent variables, which are described in table 4.1, were studied so that TERMITES can deliver the best performances for specifications as broad as possible.

| **Laser Beam Specifications** | | | **Design Parameters** | | |
|---|---|---|---|---|---|
| $\lambda_{\min}$ | (nm) | Minimum wavelength | **Optics Layout** | | |
| $\lambda_0$ | (nm) | Central wavelength | $f_R$ | (mm) | Reference mirror focal length |
| $r_{\max}$ | (mm) | Input beam radius | $L_R$ | (mm) | Reference propagation distance |
| | | | **Camera** | | |
| | | | $\Delta x$ | (mm) | Sensor width |
| | | | $\delta x$ | (µm) | Pixel size |
| | | | **Translation Stage** | | |
| | | | $\Delta z$ | (µm) | Scan range |
| | | | $\delta z$ | (µm) | Scan step size |

**Table 4.1.:** The nine main independent variables for the design of TERMITES.

Even though the number of variables is somewhat limited, optimizing such a system without any method is burdensome. This is due to multiple *secondary* variables which are directly linked to these design parameters, such as device footprint, components cost or acquisition time. There is no perfect configuration fully satisfying each specification. Instead, a few optima exist, depending on which parameters is of particular importance for the end-user. In order to understand the choices we made for the final solutions, let us examine the constraints of this problem.

I chose to divide them into two categories: *hard constraints*—which absolutely have to be met, because they are linked to some fundamental physical limits—and *soft constraints*—which are parameters we would rather keep in certain ranges, even though no hard threshold exists on their values.

### 4.1.1. Hard Constraints

#### Hard Constraint #1: Temporal Sampling Resolution

TERMITES is a modified Fourier Transform interferometer. Some of its fundamental limitations are therefore linked the temporal sampling of its coherent signal. The most obvious limitation is the delay step size needed to resolve the full spectrum of the laser beam. The following relation is implied by the Nyquist–Shannon sampling theorem:

$$\Delta\omega = \frac{2\pi}{\delta\tau} \ ,$$

with $\delta\tau$ the delay step size and $\Delta\omega$ the output frequency range, from $-\omega_{\max}$ to $\omega_{\max}$. Expressing this relation as a function of the minimum wavelength $\lambda_{\min}$ instead of $\omega_{\max}$ ($\omega_{\max} = \frac{2\pi\mathrm{c}}{\lambda_{\min}}$) leads to:

$$\delta\tau_{\max} = \frac{\lambda_{\min}}{2\,\mathrm{c}}$$

and after converting this maximum delay step size $\delta\tau_{\max}$ to the spatial translation of the reference mirror $\delta z$ (with $\delta z = \frac{\mathrm{c}\delta\tau}{2}$), it comes:

$$\delta z_{\max} = \frac{\lambda_{\min}}{4} \ . \tag{4.1}$$

This equation has a significant implication on the technological choice of the translation stage: it means that in order to resolve correctly the minimum wavelength of the input laser spectrum, the translation steps shall not exceed a fourth of the wavelength in question. Using larger steps would produce *aliasing* artefacts and could seriously distort the retrieved signal. The maximum delay step $\delta\tau_{\max}$ is represented on figure 4.1 on the next page.

Solving this constraint is straightforward: based on the desired input beam specifications, and in particular on its minimum wavelength, the motorized stage model needs to be chosen so that the necessary step size can be achieved.

### Hard Constraint #2: Delay Range

After having defined the maximal delay step size $\delta\tau_{\max}$, let us determine the necessary delay range $\Delta\tau$ of a TERMITES measurement. This parameter has notably a direct impact on the durations of measurement and processing, as well as on hardware decisions. The delay range should therefore be limited to what is necessary for obtaining a good quality measurement, without taking too large margins and risking to reduce the global efficiency of the device.

As defined by equation (3.7) on page 47 the signal recorded by TERMITES is the sum of an incoherent signal and of a coherent one that will be noted $\hat{W}_c(\boldsymbol{r},\tau)$. This coherent term contains all the information about the pulse and is defined as:

$$\hat{W}_c(\boldsymbol{r},\tau) = 2\,\mathrm{Re}\left[\hat{E}(\boldsymbol{r},t) \star \hat{E}_R^*(\boldsymbol{r},t-\tau)\right] \ . \tag{4.2}$$

As illustrated by figure 4.1 on the next page, this coherent signal corresponds to the temporal oscillations in the raw TERMITES data. The problem of deciding the temporal range of a TERMITES measurement comes down to determining for which interval of delays $\Delta\tau$ the coherent signal $\hat{W}_c(\boldsymbol{r},\tau)$ has a non-zero value. Two specific delay ranges are indicated on this figure, and are noted $\Delta\tau_{\mathrm{curv}}$ and $\Delta\tau_c$. They add up to give the minimum delay range $\Delta\tau_{\min}$:

$$\Delta\tau_{\min} = \Delta\tau_{\mathrm{curv}} + \Delta\tau_c \ . \tag{4.3}$$

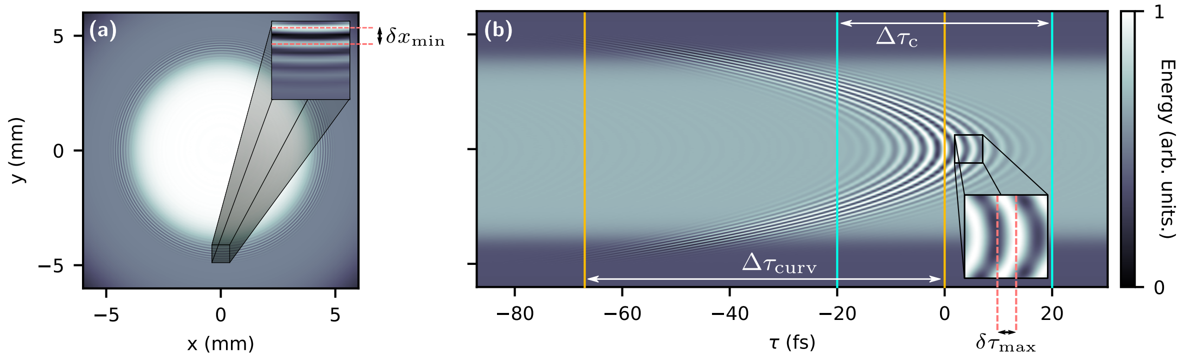

**Figure 4.1.: Views of a typical TERMITES dataset $\hat{W}(\boldsymbol{r},\tau)$, exposing the strong dimensioning constraints of the device.** A spatial slice is shown on panel **(a)**, taken at $\tau = \Delta\tau_{\text{curv}}$ and showing high spatial frequency fringes. On panel **(b)**, a spatio-spectral view of the same dataset is displayed, illustrating the temporal constraints.

$\Delta\tau_{\text{curv}}$ is the delay range that is linked to the reference curvature. As derived in more details in appendix A.1.3 on page 138, a laser pulse of which the wavefront is curved exhibits a group delay $T_{\text{curv}}(\boldsymbol{r})$, which is zero at center and increases monotonically with radial position $\boldsymbol{r}$:

$$T_{\text{curv}}(r) = \frac{R}{c}\left[1 - \frac{1}{\sqrt{1+(\frac{r}{R})^2}}\right] . \tag{4.4}$$

with $r$ the radial position and $R$ the radius of curvature of the wavefront. In the measurement plane of TERMITES, $R$ is the sum of the curved mirror focal length $f_R$ and of the propagation distance $L_R$ (see figure 3.2 on page 46). Therefore, the radial group delay of the reference at measurement plane of TERMITES is:

$$T^m_{\text{curv}}(r) = \frac{f_R + L_R}{c}\left[1 - \frac{1}{\sqrt{1+\left(\frac{r}{f_R+L_R}\right)^2}}\right] . \tag{4.5}$$

This has the direct effect of also delaying the cross-correlation in $\hat{W}_c$ and therefore the zero delay of interferograms. In order to fully measure all temporal interferograms at all positions without clipping any useful information, this delay must be taken into account. $\Delta\tau_{\text{curv}}$ is simply the maximum delay caused by the curvature at the edge of the input beam:

$$\Delta\tau_{\text{curv}} = T^m_{\text{curv}}(\boldsymbol{r}_{\text{max}}) . \tag{4.6}$$

$\Delta\tau_c$, for its part, is the delay range associated with coherence of the input laser. For a fixed position (e.g., at image center) the coherent signal has indeed a certain delay span $\tau_c$, which is linked to the spectral contents of the input beam and of the reference. In order to estimate roughly this delay, let us consider that the beam and the reference pulses are both Gaussian in time. The FWHM duration of the cross-correlation signal is the same as the duration of a convolution. In our Gaussian profile approximation, the FWHM duration of the convolution (see [25, p. 616] and [109, p. 168]) is:

$$\Delta\tau_c{}^2 = \tau_c(\hat{E})^{\,2} + \tau_c(\hat{E}_R)^{\,2} \,, \tag{4.7}$$

with $\tau_c(\hat{E})$ the coherence time of the input beam and $\tau_c(\hat{E}_R)$ the coherence time of the reference. If we consider that because the spectral contents of $\hat{E}$ and $\hat{E}_R$ are very similar, their coherence time is similar too, then:

$$\Delta\tau_c \approx \sqrt{2}\,\tau_c(\hat{E}) \approx \frac{\sqrt{2}\,\lambda_0{}^2}{c\,\Delta\lambda} \,, \tag{4.8}$$

with $\lambda_0$ the central wavelength of the input beam and $\Delta\lambda$ its spectral bandwidth.

The duration $\Delta\tau_c$ we found by considering a temporally *Gaussian* input beam is an absolute minimum. Any pulse having a non-Gaussian spectrum also have a longer coherence time compared to this best-case scenario. TERMITES is designed to characterize space-time couplings, on laser beams that have big chances to be imperfect at some positions across the beam. This means that some spectral information can be measured even quite far from the zero delay position. Some comfortable delay margin should be taken to include as much signal as possible in the measurement.

At which point should a tumultuous spectrum be a concern for the user? Our temporal measurement is the product of the actual physical signal $\hat{W}_P(\boldsymbol{r},\tau)$, with an apodization window $A(\tau)$ that is applied during data processing (see figure 3.6 on page 50). In the spectral domain, the measurement is therefore the physical Fourier transform of the physical signal, convolved by the Fourier Transform of the apodization window:

$$\begin{aligned} \hat{W}(\boldsymbol{r},\tau) &= \hat{W}_P(\boldsymbol{r},\tau)\,A(\tau) \,, \\ \hat{W}(\boldsymbol{r},\omega) &= \hat{W}_P(\boldsymbol{r},\omega) * A(\omega) \,. \end{aligned} \tag{4.9}$$

Choosing a too small delay window for the measurement unavoidably wipes out some information. However this is *only* translated in the spectral domain into a convolution by the Fourier Transform of the apodization window, which in most cases simply smooths the spectrum without adding complex artifacts and degrading further the signal. Rapidly oscillating spectral modulations are indeed lost, but the general shape of the pulse—as well as low order couplings—can still be measured. This means that the answer to our question depends on the required spectral resolution of the end result. The user shall suit the temporal range of the measurement to the level of spectral resolution he needs, following the simple law:

$$\delta\omega = \frac{2\pi}{\Delta\tau} \,, \tag{4.10}$$

with $\delta\omega$ the spectral resolution and $\Delta\tau$ the chosen delay range. If the ambition of a given measurement is to characterize a first-order coupling such as Pulse Front Tilt, then $\Delta\tau$ can be fixed to a very small value, as long as it is kept higher than $\Delta\tau_{\mathrm{curv}}$.

### Hard Constraint #3: Spatial Resolution

This temporal sampling relation is not the only strong requirement of TERMITES. Because the wavefront of the reference is curved, some circular fringes are also visible in the spatial domain of the measured signal, and their spacing evolves with radius. It was shown by figure 3.4 on page 48 that the smallest spatial fringes occur when the reference overlaps with the outer part of the incident beam.

Why could this be an issue? In principle, it is not necessary to resolve the small spatial fringes, because TERMITES performs the measurement of a *temporal* signal which is then converted to the spectral domain with a 1-D Fourier Transform. The subsequent processing steps do not depend on the spatial fringes being resolved either. The issue rather comes from the fact that the camera pixels are not punctual. At each delay step $\tau$, each one of them returns a signal value $\hat{W}(x, y, \tau)$ expressed in number of electrons, which actually corresponds to the integral of the physical signal $\hat{W}_P(x, y, \tau)$ over their spatial extent $(\delta x, \delta y)$, weighted by the quantum efficiency of silicon $\eta$:

$$\hat{W}(x, y, \tau) = \int_x^{x+\delta x} \int_y^{y+\delta y} \eta \, \hat{W}_P(x, y, \tau)\,. \tag{4.11}$$

If the spatial variations of $\hat{W}(x, y, \tau)$ over the pixel area happens to be non-negligible, then the temporal oscillations of the signal are less contrasted. Pushing the idea even further, if the spatial fringes were significantly smaller than the pixel size, then the measured energy at a given position would be average and *constant* over the whole temporal scan. The spectral information would be totally lost.

In order to avoid this artefact, choosing the TERMITES parameters so that the outer spatial fringes are significantly larger than the sensor pixels is absolutely essential. A quick geometrical analysis (detailed in appendix A.2 on page 138) shows that the spatial fringes get smaller as radial position $\boldsymbol{r}$ increases:

$$\delta f_{\text{min}} = \frac{\lambda_{\text{min}}\,(L_R + f_R)}{r_{\text{max}}}\,, \tag{4.12}$$

with $\lambda_{\text{min}}$ the minimum wavelength of the laser, $f_R$ the focal length of the reference, $L_R$ its propagation distance, and $r_{\text{max}}$ the radius of the input beam. As demonstrated in the PhD thesis of G. Pariente [42, p. 80], it is wise to sample the minimal fringe spacing with at least ten pixels so that the impact on temporal measurement contrast is negligible. As a consequence, the maximal spatial pixel size for TERMITES can be written:

$$\delta x_{\text{max}} = \frac{\lambda_{\text{min}}(f_R + L_R)}{10\; r_{\text{max}}}\,. \tag{4.13}$$

This equation is the main constraint linking together the input beam specifications, the optical layout variables and the internal hardware features.

### 4.1.2. Soft Constraints

#### Soft constraint #1: Magnification of the reference

A central parameter in our technique is the reference size ratio, $\beta$. This parameter designates the size of the input beam portion used as a reference after being magnified by the convex mirror. Even though $\beta$ is not one of the primary physical variables of the set-up, and is not directly linked to a strong limitation of the device, it has a significant importance in the design of TERMITES. The reference size ratio $\beta$ was defined in figure 3.2 on page 46 and is written:

$$\beta = \frac{f_R}{f_R + L_R}\,. \tag{4.14}$$

Modifying the reference magnification has two major consequences on the measurement. The most obvious is the interferogram maximum contrast (also known as *interferometric visibility*). In a Michelson interferometer, the maximum contrast of the fringes depends on the relative fluence $F_1(\boldsymbol{r})$ and $F_2(\boldsymbol{r})$ of both interferometer arms at a single wavelength, and is defined as:

$$C_{\max} = \frac{2\sqrt{F_1(\boldsymbol{r})\,F_2(\boldsymbol{r})}}{F_1(\boldsymbol{r}) + F_2(\boldsymbol{r})}\,. \tag{4.15}$$

This equation is true in the approximation that both arms have the same dispersion, which is verified because the experimental set-up includes a dispersion compensation plate in one arm. Furthermore, if the beam splitter and both plane mirrors are balanced, the throughput of both arms is equally 25 % of the input beam power. It means that at zero-delay, the contrast should in theory be perfect ($C_{\max} = 1$) and that the interferogram intensities distribution should fill the whole dynamic range of the sensor.

The magnification of the reference has an influence on maximum contrast, because total energy of the reference is conserved while its spatial profile is expanded by a factor $\beta$. This means that, at measurement plane, the fluence of the reference is inversely proportional to $\beta^2$, and the maximum contrast of the device ends up being

$$C_{\max} = \frac{2\,\beta}{1 + \beta}\,. \tag{4.16}$$

In practice, this contrast loss is only an issue that happened during the development of TERMITES prototypes, when the tested magnification was too high. As soon as the design of the device—and particularly its $\beta$ parameter—is frozen, the relative throughput of interferometer arms can be balanced in a permanent way pretty easily. This is done by adjusting the reflectivity of one of the two mirrors.

Now, let us detail a more complex issue linked to the reference magnification. When $\beta$ is large, the influence of the reference on final measurement is compensated for using an iterative algorithm which was referred to in section 3.2.3 on page 55. In order for the algorithm to converge as closely as possible to the input field, it is advisable to keep $\beta$ as low as possible. Equation (4.13) on the preceding page can be combined to equation (4.14) in order to express the relation linking multiple key parameters of TERMITES, and in particular $\beta$:

$$\delta x_{\max} = \frac{L_R\,\lambda_{\min}}{10\,r_{\max}\,(1-\beta)}\,. \tag{4.17}$$

This equation clearly summarizes a trade-off of particular importance for our device. For a fixed input beam diameter, decreasing $\beta$ requires to either increase the propagation length $L_R$ or to decrease the camera pixel size $\delta x_{\max}$ (by using a higher resolution camera). These solutions are not ideal because they contribute to increase the instrument footprint or its direct cost, or both.

### Soft constraint #2: Input Pupil, Sensor Size, Device Footprint

One of the first questions coming to the mind when thinking about the specifications of TERMITES is the input beam size. Generally, the entrance pupil of a diagnostic device is the kind of parameters which should be kept as small as possible for the practical reasons of cost and device footprint. Concerning our *spatio*-temporal diagnostic, it is not only practical but essential to characterize the input beam over a section as large as possible, and preferably over its whole spatial profile.

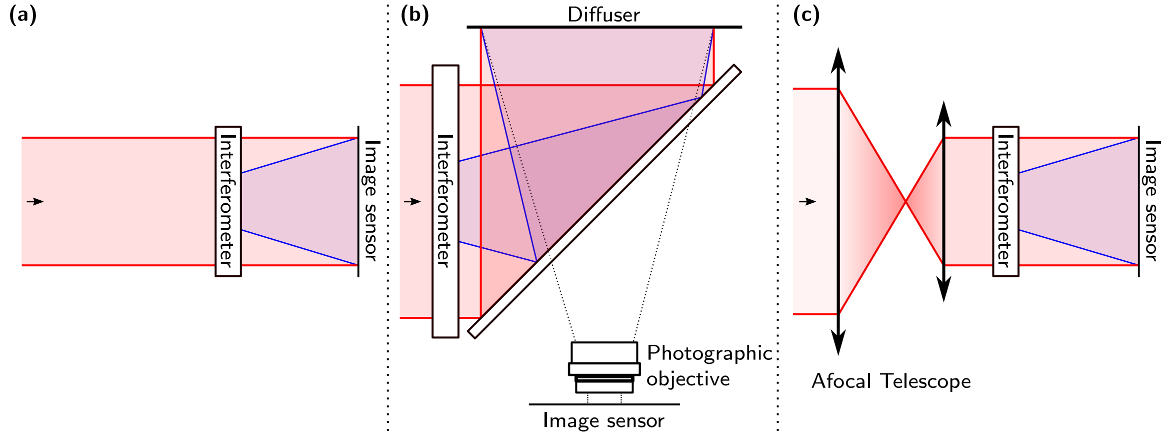

**Figure 4.2.: Three different imaging configurations dealing with various beam diameters. (a)** Standard configuration of TERMITES for beams smaller than sensor area. **(b)** Scaled up device, with interferograms forming on a diffusing screen, while a camera and its objective image the screen. **(c)** Standard configuration of TERMITES with accompanying refractive or reflective telescope. The telescope is used to reduce the input beam and to comply with TERMITES input pupil specification.

An important element to consider is the maximum achievable size of image sensors, and their cost. The vertical size of standard industrial cameras ranges from a few millimeters to 2.4 cm (photographic *Full frame* format). This means that any pupil size up to 24 mm can be chosen without making any strong modification to the layout of TERMITES, as shown in panel (a) of figure 4.2. This is the preferred situation because optics are kept within reasonable dimensions, and no additional component is required. Interferograms are directly projected on the sensor and recorded along the scan.

However, it is not sufficient to simply hold maximum input beam diameter below the size of the sensor chip. Most of the time, users employ TERMITES in order to characterize challenging systems which are susceptible to exhibit spatio-temporal couplings. Those systems are oftentimes high power lasers with large apertures. How can such large diameter beams be measured in full using our device?

The first way of doing so is illustrated on panel (b) of figure 4.2 and consists of scaling up all optics to adapt to the higher pupil size. As the beam could not possibly be contained on the chip of a camera, interferograms are diffused by a screen which is then imaged by a photographic objective on an image sensor. The resulting set-up involves large optics and usually have a big footprint due to the propagation of a large beam in the instrument, which is hard to fold efficiently.

The second way of measuring a large beam is probably the most obvious: reduce its diameter using a telescope, so that interferograms can fit on the camera sensor of a tolerably sized TERMITES. This method is illustrated on panel (c) of figure 4.2 on the facing page and was first rejected because of the initial ambition of TERMITES. As previously explained in chapter 2 on page 21, our device was originally designed to characterize ultrashort lasers in space and time, using the simplest set-up as possible, so that the measurement would be the closest to reality. Reducing the beam using a refractive telescope is highly susceptible to introduce undetermined aberrations that would add some uncertainty to the measurement.

## 4.2. Settling for an Optimal Set of Parameters

### 4.2.1. Optimization Procedure

The design parameters of TERMITES are now defined. Instead of providing one example of design, I suggest here a simple procedure that can be used to design TERMITES in accordance with the input beam properties and the physical constraints that were just described.

**Step 1: Establish input beam specifications and imaging configuration**
*Estimation of* $\{r_{max}, \lambda_0, \lambda_{min}, \Delta x, \delta x\}$.

In order to establish the properties of TERMITES, defining the input beam specifications is essential. Its central wavelength, bandwidth and diameter are the three principal parameters, and were already listed in table 4.1 on page 64.

The beam properties are easy to find if the TERMITES device is built for a specific usage, i.e., characterizing a particular system at a known position along its amplification chain. If the goal is rather to obtain a versatile instrument, which can be adapted to multiple systems, then a more elaborate study must be made to determine for which category of systems the instrument have to be designed.

Knowing the beam diameter, the imaging configuration of TERMITES can be chosen among the three possibilities shown in figure 4.2 on the preceding page. Then, the required sensor size can also be established, and a first choice of camera model can be made. If needed the model will be modified at the end of the first computations, and the typical pixel size value $\delta x = 9\,\mu\text{m}$ can be used for now.

**Step 2: Optimize spatial dimensions**
*Estimation of* $\{\beta, f_R, L_R\}$.

Using the parameters established during the previous step, we can now compute the allowed spatial design parameters of TERMITES, thanks to equations (4.14) and (4.17) on page 69.

Figure 4.3 on the following page shows that all combinations of parameters $\beta, f_R$ and $L_R$ are not achievable. They are mainly limited by resolution power of the camera, and by the minimum inter-fringes spacing of the interferograms. This constraint was explained on page 67 and is expressed by equation (4.17). All configurations placed along this resolution limit (black curve in the figure) are optimal because they make full use of the camera resolution.

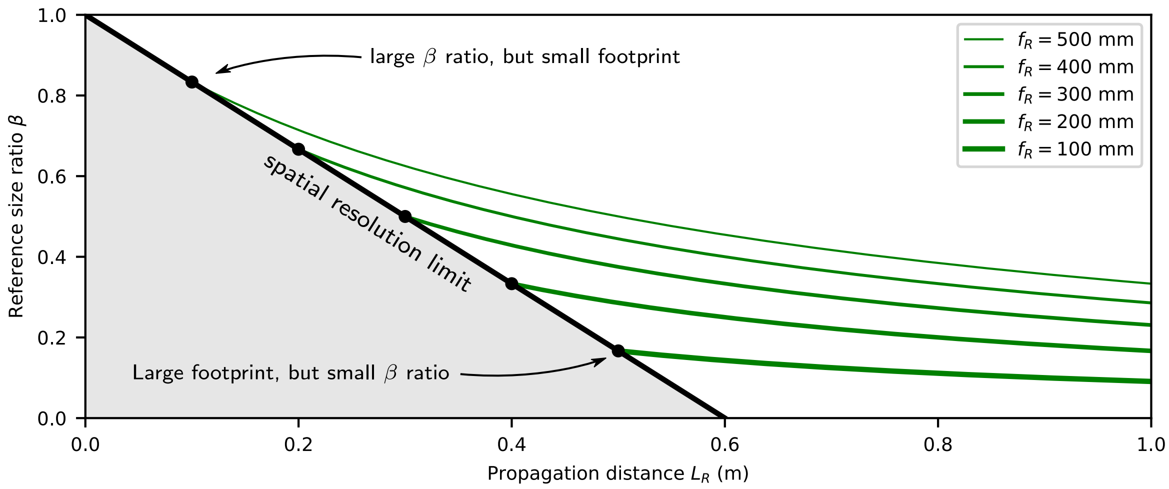

**Figure 4.3.: Example parameters space of TERMITES, for fixed input beam specifications** ($r_{\mathsf{max}} = 5\,\text{mm}, \lambda_{\mathsf{min}} = 750\,\text{nm}$) **and fixed camera pixel size** ($\delta x = 9\,\mu\text{m}$)**.** The black linear curve correspond to equation (4.17) on page 69, and delimits a forbidden zone (in gray) where no measurement is possible due to spatial sampling requirements. Optimal configurations are found along this black curve. Depending on the curved mirror focal length $f_R$, $\beta$ can be chosen as needed. The green curves represent all solutions $(\beta, L_R)$, achievable by simply increasing propagation length in a given TERMITES device, without modifying the curved mirror (see equation (4.14) on page 69).

At this stage, the only parameter to choose is the focal length $f_R$ which determines the position of the instrument configuration along this limit. The trade-off between $\beta$ and $L_R$ is governed by this choice. Using a small focal length reduces the propagation length and allows a small device footprint. On the contrary, choosing a large focal length reduces the reference size ratio $\beta$ (which is desirable, see page 68) but imposes a large instrument footprint.

It is always possible to increase $L_R$ after TERMITES configuration has been chosen, by moving the camera away from the interferometer. In this case, the solution is not at the resolution limit anymore, and moves along its corresponding green curve (equation (4.14) on page 69, with $f_R$ fixed). This change can be useful to set $\beta$ to another value, without changing any optics to the setup. Doing so was particularly useful in experiment, to easily try different magnification values.

### Step 3: Check consequences on temporal scan properties and on the device

*Estimation of $\{\Delta z, \delta z\}$, as well as total cost and achievable footprint.*

During the two previous steps, the design of TERMITES was adapted to input beam properties and to the most critical constraints. After having drafted this preliminary configuration, it is necessary to check a few more elements. Namely, the temporal sampling and range should be computed from the beam specification and from the dimensioning values. These constraints are crucial but have been left for the end of the optimization because they are generally less restrictive.

If the choice of $\beta$ and $L_R$ does impose too large constraints on the required delay range of the motorized stage (equation (4.5) on page 66), then the curved mirror focal length $f_R$ can be adjusted down by going back to step 2. After a few iterations of this protocol, the best configuration can be determined and implemented afterwards in the actual prototype of TERMITES.

### 4.2.2. Two Input Requirements, Leading to Two TERMITES Designs

Depending on the requirements imposed by the input laser beam and by cost or footprint wanted by the user, TERMITES set-ups can be totally different.

The starting point of this work was the proof-of-concept developed by G. Pariente during his thesis [42]. His prototype was designed to measure as directly as possible a large input beam such as UHI-100 at the output of its compressor (80 mm in diameter). As a consequence, this first version used configuration (b) of figure 4.2 on page 70, wherein spatial interferograms are projected on a screen and imaged by a camera objective. Following steps 2 and 3 of the optimization we just described, and playing with the trade-off between reference size ratio $\beta$ and propagation length $L_R$, the specifications of this first prototype were established to the values shown in table 4.2.

| **Laser Beam Specifications** | | **Design Parameters** | |
|---|---|---|---|
| $r_{\max} =$ | 40 mm | **Optics Layout**<br>($\beta = 0.54$) | |
| $\lambda_0 =$ | 800 nm | $f_R =$ | 5.2 m |
| $\lambda_{\min} =$ | 770 nm | $L_R =$ | 4.5 m |
| | | **Camera**<br>(KAI-29050) | |
| | | $\Delta x =$ | 24 mm |
| | | $\delta x =$ | 20 µm* |
| | | **Translation Stage**<br>(PI P-622) | |
| | | $\Delta z =$ | 130 µm |
| | | $\delta z =$ | 150 nm |

**Table 4.2.: Set of parameters chosen for TERMITES proof-of-concept.** **In this particular configuration, the spatial sampling value does not match the actual pixel size of the camera (5.5 µm in this case). Interferograms are indeed projected on a screen which is then imaged by the camera objective, which explains why $\delta x$ is larger.*

Although this version did fit the bill for the successful measurement of UHI-100 [43], some of its characteristics made it impossible to distribute as a product. The large beam size inside the device was the source of all issues : its footprint was very large (1500 × 750 mm) and TERMITES was not portable at all. Additionally, it used large costly optics and the mirror placed on the nanometric translation stage was too heavy, making the interferometer unstable.

In the end, the instrument had to be modified so that we could test it on other laser systems providing available space for diagnostics. The choice was made of building a device with a much smaller input pupil to relax the constraints on the design. The particular diameter of 20 mm is very convenient, because it fits on full frame camera sensors and on standard 1 inch optics at normal incidence, thus reducing a lot the total direct cost of the instrument.

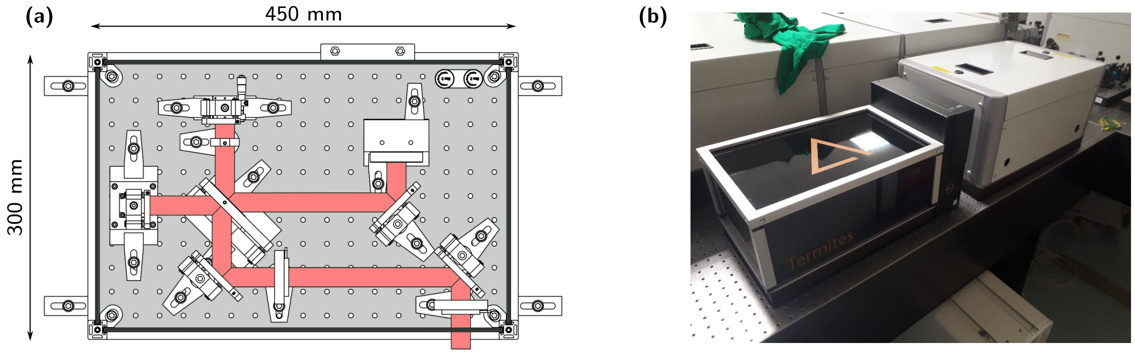

**Figure 4.4.: New prototype of TERMITES.** Panel **(a)** is a view of a Computer-Assisted Design of the device, as implemented by Amplitude Laser Group mechanical engineers. Panel **(b)** is a picture of the assembled device, installed in a laser chain and ready for a measurement. This version has an input diameter of 20 mm and was used for most of the measurements presented in this work.

This new configuration has the practical advantage of being very versatile. Small laser beams can be characterized as long as their diameter is smaller than the input pupil of TERMITES (configuration (a) in figure 4.2 on page 70). Larger systems can be measured as well, using the exact same instrument in configuration (c), by adding a carefully designed reducing telescope. Even if this solution seems inconvenient, large laser systems often feature areas dedicated to diagnostics at the end of the chain, wherein the full energy beam is attenuated and reduced in size in order to be characterized. Another option is to re-collimate the beam just after the experimental focal plane thanks to a parabola or an achromatic lens. Although it requires to use some space near the experimental vacuum chamber, this case is probably the most desirable because only one optical element and a few centimeters separate TERMITES from the target plane where we need to characterize the laser beam. An experiment has been done to test this option and results will be explained in chapter 9 on page 132.

| **Laser Beam Specifications** | | **Design Parameters** | |
|---|---|---|---|
| $r_{\max} =$ | 10 mm | **Optics Layout** | |
| | | ($\beta = 0.57$) | |
| $\lambda_0 =$ | 800 nm | $f_R =$ | 600 mm |
| $\lambda_{\min} =$ | 750 nm | $L_R =$ | 450 mm |
| | | **Camera** | |
| | | (KAI-11002) | |
| | | $\Delta x =$ | 24 mm |
| | | $\delta x =$ | 9 µm |
| | | **Translation Stage** | |
| | | (PI P-622) | |
| | | $\Delta z =$ | 130 µm |
| | | $\delta z =$ | 150 nm |

**Table 4.3.: Set of parameters chosen for new industrial version of TERMITES.**

This new version of the instrument is visible in figure 4.4 and its specifications are shown in table 4.3 on the facing page. Reducing the constraint on pupil size was mainly used to reduce $L_R$ and fit the instrument on a 450 × 300 mm breadboard. Minimum admissible wavelength $\lambda_{\min}$ was also decreased from 770 nm to 750 nm so that shorter pulses can be measured without issues.

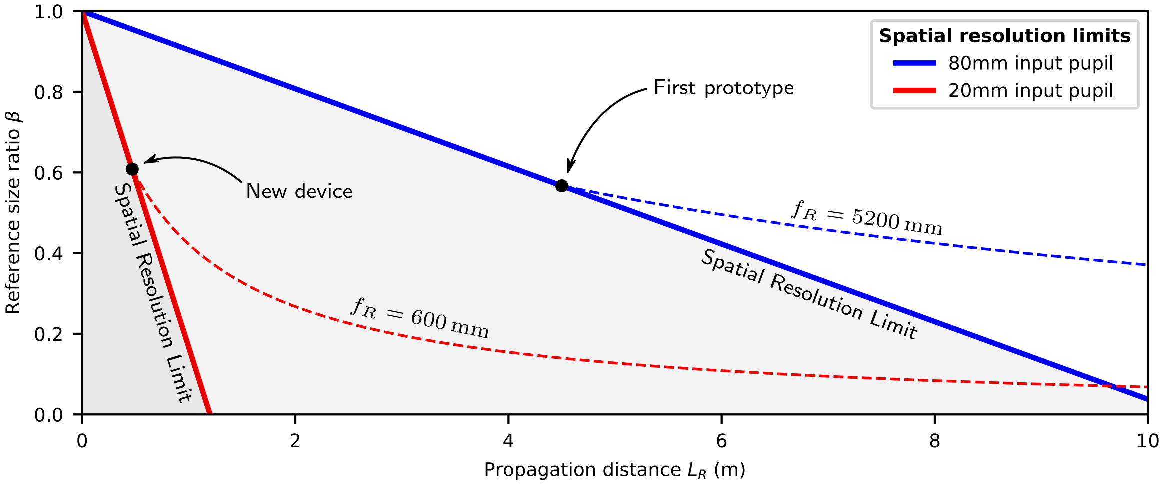

**Figure 4.5.: Two possibilities for the design of TERMITES.** As in figure 4.3 on page 72, this figure shows spatial resolution limits, but this time for both 20 and 80 mm prototypes. The two dots illustrate the focal length choice that has been made in each case. Reducing pupil size from 80 mm to 20 mm has the direct effect of changing the slope of the spatial resolution limit, thus allowing lower propagation lengths if $\beta$ is kept the same.

In the end, the two prototype configurations are illustrated on figure 4.5. This figure can be used to estimate a new version corresponding to other needs. For example, obtaining a new version with a very low $\beta$ ratio could be done by sliding down the plain red curve. This would translate into a reduction of the focal length $f_R$ and then a growth of the propagation distance $L_R$ so that interferograms can be correctly resolved.

⁂

In this chapter, we explored further the design details of the instrument, and developed the tools to taylor its characteristics to the studied laser system. Constraints linked to signal acquisition limits and hardware constraints were developed in section 4.1 on page 64. We drew conclusions about the design of TERMITES in section 4.2 on page 71.

Provided that an inspection of the few aforementioned constraints is done properly, TERMITES can be adapted to pretty much any currently available high-power laser. The product developed in the context of this work was designed with flexibility in mind. This has been particularly useful for experimental measurements, because the set-up was able to characterize a broad range of small systems, while remaining portable. In more specific cases, when other constraints like footprint or measurement speed are declared critical, the set-up can be optimized at will.

Chapter 5.

# Numerical Study of Potential Error Sources

Following chapters 3 and 4 which described the technique in itself and its expected performance, let us now focus on the consequences of potential complications. Indeed a number of experimental or numerical errors can accumulate along the long path from the measurement to the end of the processing. To study the occurrence of these independent sources of errors, I have developed during my thesis a simulation program that will be used heavily in this chapter.

First, the principles of the simulation library will be described. Then, we will study independently the measurement errors caused by input beam properties and by instrument properties.

## Contents

**5.1. Numerical study of TERMITES measurements** . . . . . . . . 78
  5.1.1 Simulating TERMITES measurements
  5.1.2 Interpreting the Generated Results
**5.2. Errors Linked to Instrument Properties** . . . . . . . . 80
  5.2.1 Delay Fluctuations
  5.2.2 Reference Pointing Errors
**5.3. Errors Linked to Beam Properties** . . . . . . . . 84
  5.3.1 Energy Fluctuations
  5.3.2 Pointing Fluctuations

## 5.1. Numerical study of TERMITES measurements

### 5.1.1. Simulating TERMITES measurements

Numerically reproducing the behaviour of TERMITES is essential to the improvement of its design. The principal purpose is to determine the main independent sources of errors, and to quantify their respective effects on final results.

Figure 5.1 shows the key aspects of the program. Initialization mainly consists of reading the simulation variables and generating the input beam $E(x, y, \omega)$ according to its main characteristics (diameter, spatial shape, spectral bandwidth...). Potential aberrations are then added to this ideal beam if requested. Then, computing TERMITES interferograms essentially follows the physical description of the instrument that was developed in section 3.1 on page 44.

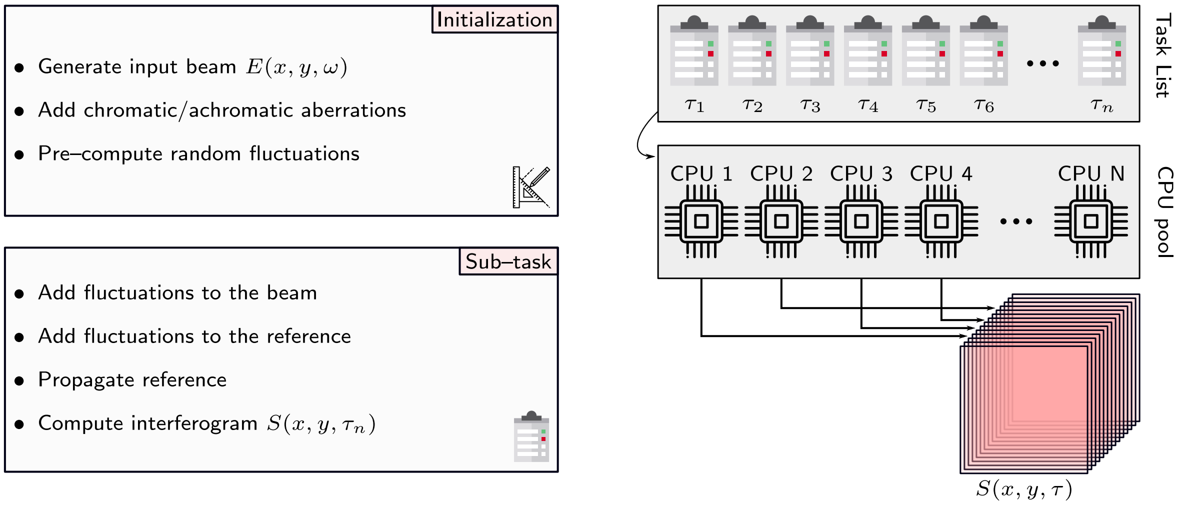
Initialization
Generate input beam $E(x, y, \omega)$
Add chromatic/achromatic aberrations
Pre–compute random fluctuations
Sub–task
Add fluctuations to the beam
Add fluctuations to the reference
Propagate reference
Compute interferogram $S(x, y, \tau_n)$
Task List
$\tau_1$ $\tau_2$ $\tau_3$ $\tau_4$ $\tau_5$ $\tau_6$ ... $\tau_n$
CPU pool
CPU 1 CPU 2 CPU 3 CPU 4 ... CPU N
$S(x, y, \tau)$

**Figure 5.1.: Simplified diagram of a TERMITES measurement simulation**

The simulation library is intended to manage as many input variables as possible while avoiding to make any strong assumption about the system. Input beams can have arbitrary aberrations and all design parameters of the interferometer can be tuned. Several sources of input fluctuations or instrument instabilities are implemented and their respective strength are tunable as well.

Because the program is intended to model the fluctuations of our system—e.g., pulse-to-pulse beam fluctuations or interferometer instabilities—the beam and the reference have to be corrected and propagated to the measurement plane *at each delay $\tau$ of the scan.* In order to keep the computation time manageable, the full process is optimized to run on multi-core architectures. I chose to split the total workload in $N_\tau$ sub-tasks which are processed by a pool of $N$ CPU cores. Each sub-task computes the interferogram produced by TERMITES at a single interferometer delay. As the number of sub-tasks is well above the number of CPU cores, a queue is created and fed to a process pool, as illustrated by figure 5.1. Each time a CPU finishes computing a sub-task, it is assigned to a new one until the queue is eventually empty.

The parallelization of this calculations is based on the `multiprocessing` standard Python library. In the case where parametric simulations are needed—e.g., to study the influence of one parameter on the TERMITES results—it is necessary to also perform multiple simulations.

On the laboratory cluster (2× Intel Xeon Gold 6152 CPU and 380 GB RAM), the most efficient configuration consists of running 16 TERMITES simulations in parallel, each one disposing of four CPU core. In this configuration, the 16 simulations take one hour to run with standard TERMITES design parameters. This means that for the parametric studies developed in this chapter, each simulation took a little less than four minutes to run.

### 5.1.2. Interpreting the Generated Results

Generated data follow the exact same file format that is used by the TERMITES acquisition interface to save experimental data. This ensures that numerically generated TERMITES measurements can be managed by the same post-processing library as real measurements. The spatio-spectral spectra and phase resulting from the processing of numerical measurements are therefore directly comparable with experimental results.

Now that measurement results can be simulated, let us think about interpretation. We need to assert the influence of a few simulation parameters on the results *quality*. How should we quantify the difference between data obtained from a perfect TERMITES simulation, and data obtained with numerically-introduced perturbations? Most imperfections of the input beam properties or in the measurement set-up have undesirable effects both on the retrieved spectral fluence $\varepsilon(\boldsymbol{r},\omega)$ and on the phase $\varphi(\boldsymbol{r},\omega)$. Variation of continuous quantities such as spectrum can be quantified using the Root-Mean-Square (RMS) difference. In our case, it is applied as follows:

$$\Delta\varepsilon_{\mathrm{RMS}} = \sqrt{\overline{\left(\varepsilon(\boldsymbol{r},\omega)-\varepsilon_i(\boldsymbol{r},\omega)\right)^2}}\ , \tag{5.1}$$

with $\varepsilon_i(\boldsymbol{r},\omega)$ being the spectral fluence of TERMITES results obtained in perfect conditions. As described in appendix A.3.1 on page 139, the average operation visible in this equation is done spatially and spectrally to return a scalar value. The resulting RMS difference $\Delta\varepsilon_{\mathrm{RMS}}$ has the dimension of a spectral fluence ($\mathrm{J/m^2/(rad/fs)}$), and is zero if $\varepsilon(\boldsymbol{r},\omega)$ and $\varepsilon_i(\boldsymbol{r},\omega)$ are identical.

In order to express this RMS deviation in a more intuitive manner, $\Delta\varepsilon_{\mathrm{RMS}}$ can also be normalized by the average spectral fluence of the field retrieved in perfect conditions. The result is the normalized spectral fluence deviation $\Delta\varepsilon_{\mathrm{NRMS}}$ given in percentage:

$$\Delta\varepsilon_{\mathrm{NRMS}} = \frac{\Delta\varepsilon_{\mathrm{RMS}}}{\overline{\varepsilon_i(\boldsymbol{r},\omega)}}\ . \tag{5.2}$$

$\Delta\varepsilon_{\mathrm{NRMS}}$ is null if both spectral fluence distributions are exactly the same and increases as errors rise. A value of 50 % indicates that the most of the spectral fluence errors are between −50 % and 50 % of the average spectral fluence of the beam. While it does not give any information on the *shape* of fluence errors nor on the spatial frequency of the aberrations, it is a good figure of merit to determine how well the input beam is retrieved by TERMITES. There is no absolute way to determine the limit at which fluence errors make the measurement worthless because it highly depends on their distribution in space and frequency. Nevertheless, we noticed empirically that spectral fluence deviation of 20 % or below generally does not degrade too badly the computation of far-field energy distribution or spatio-temporal Strehl Ratio (detailed in section 2.4.2 on page 37). We will therefore use this value as a threshold to determine if the simulated perturbations are acceptable or not.

Assessing the robustness of phase measurement is also done using RMS deviation. As phase is a cyclic quantity, it must be unwrapped before any RMS value can be computed. Therefore, the RMS phase deviation $\Delta\varphi_{\text{RMS}}$ is written:

$$\Delta\varphi_{\text{RMS}} = \sqrt{\,\overline{\left(\varphi^u(\boldsymbol{r},\omega) - \varphi^u_i(\boldsymbol{r},\omega)\right)^2}\,} \ , \tag{5.3}$$

with $\varphi^u(\boldsymbol{r},\omega)$ the unwrapped phase of the TERMITES output field obtained with perturbations and $\varphi^u_i(\boldsymbol{r},\omega)$ the same quantity obtained in perfect conditions. Because phase is dominated by noise when intensity signal is too low, values which are outside of the beam aperture or outside of the spectrum bandpass are ignored. For each simulation, this $\Delta\varphi_{\text{RMS}}$ value gives the deviation—expressed in radians—of the retrieved 3D phase profile compared to the simulated input beam. In the case of phase, giving a normalized figure of merit would have no meaning because a phase considered perfect is zero for all positions and frequencies.

## 5.2. Errors Linked to Instrument Properties

### 5.2.1. Delay Fluctuations

The first kind of error that could occur in an interferometer is a pulse-to-pulse delay fluctuation. Fluctuation of the optical path difference $z$ between the two arms of a Michelson interferometer can be caused by either variations of the air refractive index in the device (turbulences), or by the unwanted movement of mirrors. We unfortunately encountered both sources of instabilities during the experiments with the prototypes of TERMITES. Turbulences are generally caused by improper airflow management in the laboratory, but this problem was easily overcome by designing a custom case for our device, and closing it during every measurement. On the contrary, unwanted movements of mirrors are harder to totally cancel. They are usually caused by vibration of the optical table or by imprecise translation of the piezo-electric stage. At each step of the scan, the interferometer optical path difference $z$ is modeled as:

$$z = z_T + z_\epsilon \ , \tag{5.4}$$

with $z_T$ the ideal targeted path difference and $z_\epsilon$ a random error following the Gaussian probability function $f_{z_\epsilon}(z)$:

$$f_{z_\epsilon}(z) = \frac{1}{\sigma_z\sqrt{2\,\pi}}\, e^{-\frac{1}{2}\left(\frac{z}{\sigma_z}\right)^2} \ . \tag{5.5}$$

The issue with pulse-to-pulse fluctuations in a Fourier Transform Spectrometer is linked to the processing of raw data. Cross-power spectra are retrieved after the measured cross-correlation signal has been Fourier Transformed. The details about this steps were explained in section 3.2.1 on page 49. By nature, Fourier transform operation expects uniformly sampled input arrays. In the event of an irregular sampling of delays during a FTS—or TERMITES—scan, raw signal is distorted which leads to the output spectrum being recovered incorrectly.

### 1D study

Let us determine the maximum acceptable fluctuations of the optical path difference that can be sustained by TERMITES without notably distorting the retrieved spectra. This study can be done in one dimension as a first approach. Figure 5.2 shows the result of FTS measurement simulations that were done with the parameters of a typical TERMITES scan, which is degraded by varying levels of fluctuation in optical path difference $\sigma_z$. The main noticeable effect is the spectral leakage of signal information to other neighbouring frequencies, leading to a loss of gain in the spectrum window of interest, and to a higher noise floor. Total energy of retrieved spectra (red curves in panel (a)) are normalized so that the signal strength can be compared between different levels of fluctuations.

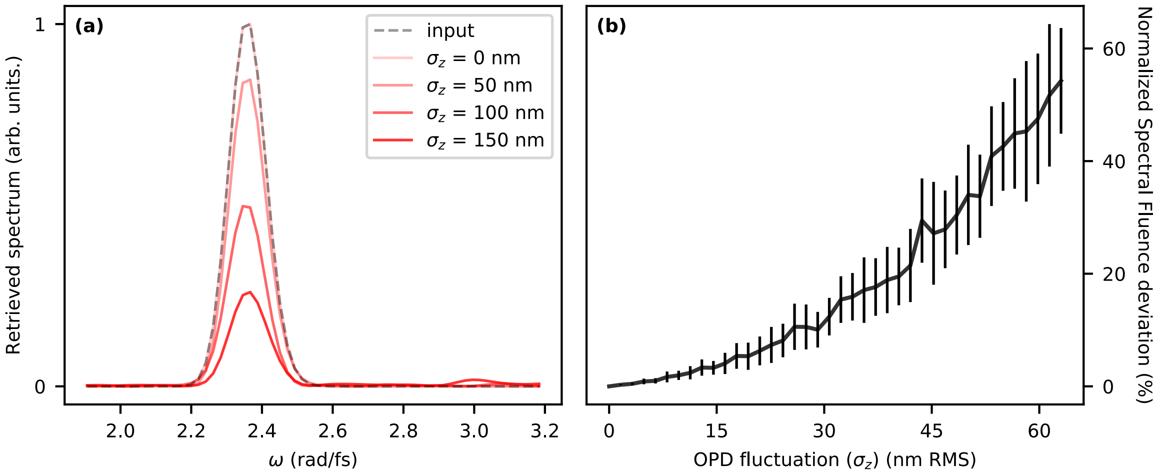

**Figure 5.2.: Effect of interferometer delay fluctuations on FTS output spectrum.** Panel **(a)** shows four simulated retrieved spectra, for different values of RMS fluctuations of the interferometer optical path difference. Panel **(b)** displays normalized energy deviation ($\Delta\varepsilon_{\mathrm{NRMS}}$ defined by equation (5.2) on page 79) of simulated measurements for an increasing amount of delay fluctuations in the interferometer. Energy errors have been computed over twenty measurements for each value of RMS delay fluctuation. The optical path fluctuations follow the random Gaussian distribution written in equation (5.5) on the preceding page, and their RMS value is expressed in nm.

As seen on panel (b) of figure 5.2, total energy error is strictly increasing with the level of delay fluctuation. According to this 1-D simulation and considering standard TERMITES design parameters, it is necessary to keep optical path difference fluctuations below 30 nm RMS in order to be sure that retrieved spectrum error is under 20 %.

### 3D study

Thanks to the simulation program that was developed during this work, it is also possible to study the effect of delay fluctuations on the three dimensional results given by TERMITES. Following the same principle as in the 1D study, we simulate TERMITES measurements with varying levels of delay errors in the interferometer. The energy and phase errors are expected to rise as the delay errors increase because TERMITES is strongly based on FTS. Using the 3D simulation enables deeper inspection of possible spatial and/or spatio-spectral features generated by the fluctuations.

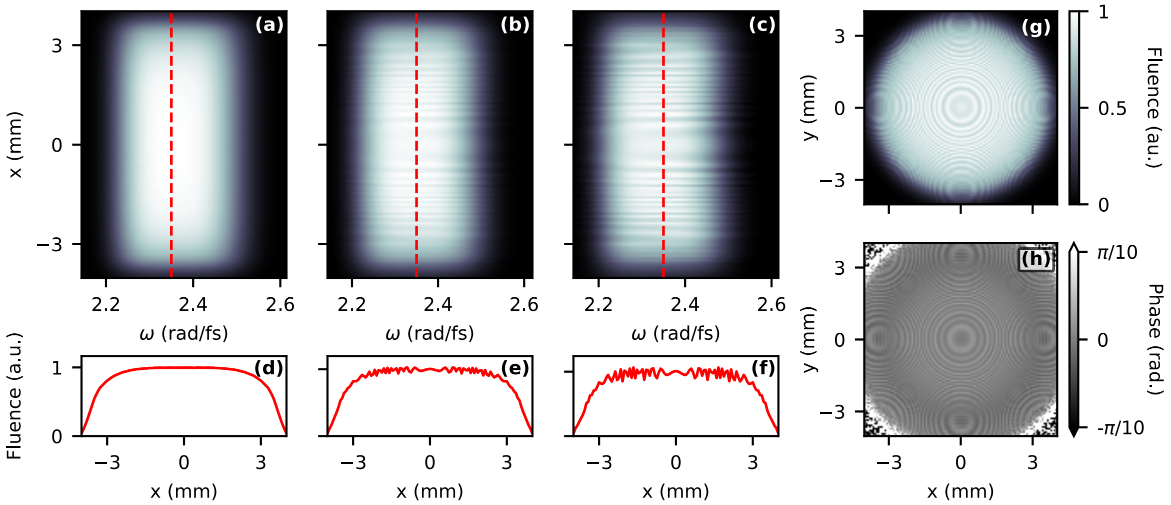

**Figure 5.3.: Effect of interferometer delay fluctuations on the laser profile retrieved by TERMITES. (a)–(c)** Vertically resolved spectra obtained respectively with delay fluctuations of 0, 10, and 20 nm RMS. **(d)–(f)** Line-outs of the fluence profile at central angular frequency $\omega_0$. **(g)–(h)** Fluence and phase profiles at central angular frequency $\omega_0$, corresponding to the worst case simulation (20 nm RMS).

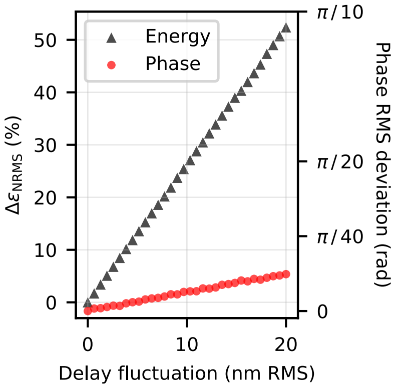

**Figure 5.4.: Fluence measurement error for different values of delay fluctuation.**

In order to study the dependence of this spatial artifact on the amount of delay fluctuation, 32 experiments were simulated using values of RMS fluctuations ranging from 0 to 20 nm. For each of them, we ran simulated experiments followed by standard TERMITES data processing. Views of the results are displayed in figure 5.3. According to this 3D study, a ring-shaped artifact appears on the spatial fluence profile, and does not depend significantly on the wavelength. Although its peak-to-valley magnitude is very small, this artifact is also visible on the retrieved phase profile (see panel (e) of figure 5.3). The concentric rings are very similar to the interferogram fringes both in shape and in size.

As shown in figure 5.4, the artifact strength clearly depends linearly on the amount of delay fluctuations. Note that it probably depends on other parameters of the device as well, but we decided to set them to typical design values such as those we used for the new prototype of TERMITES.

Analyzing this artefact in 3D helps drawing conclusions about the influence of delay fluctuations. Even if strong signal scrambling appears for variations of 30 nm or more in the purely spectral analysis, finer spatial defects actually start to appear much sooner. The consequences of a given artifact depends on the signal that the user is actually looking for. Even with very strong fluctuations in delay, a first-order coupling such as spatial chirp remains easily measurable. However, it makes more advanced calculations—such as spatio-temporal Strehl Ratio—less reliable because propagation of the retrieved beam can be strongly affected. As we explained earlier, we hence consider that the normalized spectral fluence deviation should not exceed the value of 20 %. In this case, this means that the amount of RMS optical path fluctuations should be kept below 10 nm RMS for the measurement to remain exploitable. Albeit rather arbitrary, this boundary ensures that fluctuations of delay in the device have no chance to cause any strong fluence modulation on the final result.

### 5.2.2. Reference Pointing Errors

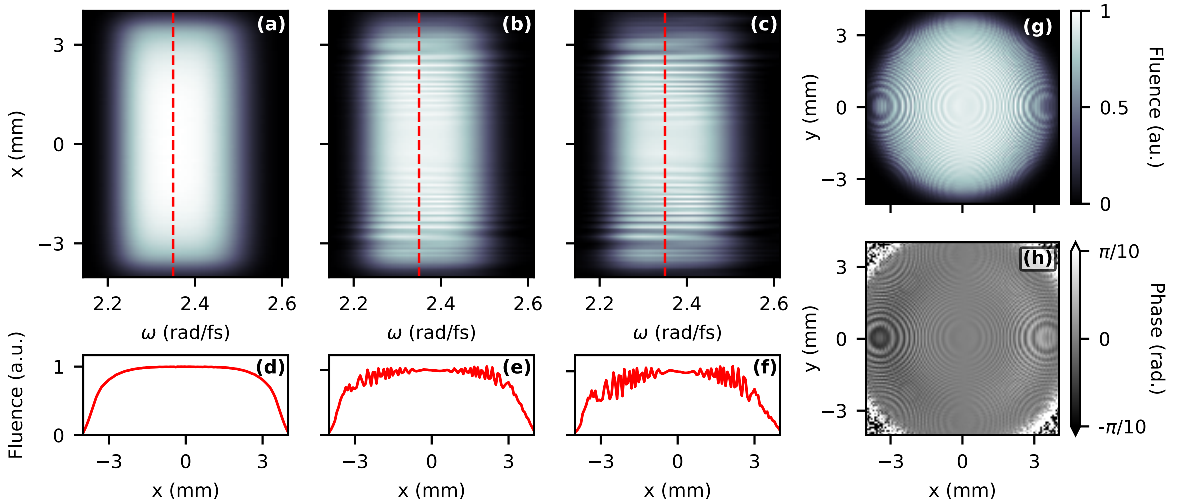

**Figure 5.5.: Effect of yaw fluctuations of the reference on the laser profile retrieved by TERMITES.** **(a)–(c)** Vertically resolved spectra obtained respectively with tilt fluctuations of 0, 10, and 20 µrad RMS. **(d)–(f)** Line-outs of the fluence profile at central angular frequency $\omega_0$. **(g)–(h)** Fluence and phase profiles at central angular frequency $\omega_0$, corresponding to the worst case simulation (20 µrad RMS).

During a TERMITES scan, one of the plane mirror in the interferometer is translated over a range of typically tens of microns. In order to allow this degree of freedom in the setup, a custom mount is designed to place the mirror on the surface of a piezo-electric translation stage. Due to technological aspects of this motor, the moving mirror is exposed to small tilt variations over travel range of the temporal scan. A simulation is done to determine the maximum acceptable level of reference tilt variation over a TERMITES scan.

Figure 5.5 illustrates the results of this study, where horizontal tilt of the reference is slightly different at each sample of the measurement. Horizontal tilt is a random variable following a normal distribution. TERMITES measurements were computed numerically for increasing levels of tilt fluctuation, by adjusting standard deviation of the normal distribution.

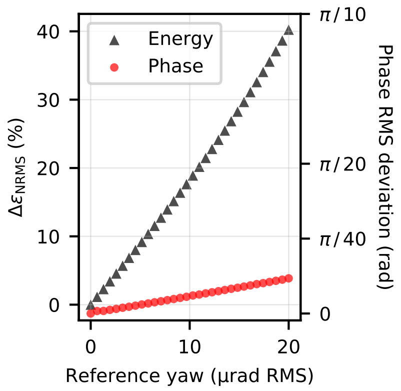

**Figure 5.6.: Fluence measurement error for different values of reference pointing fluctuation.**

Similarly to delay fluctuations, horizontal tilt fluctuations principally generate achromatic artifacts. Panels (b) and (c) show that spatial fluence modulations are the same for all frequencies. According to panel panel (d) which shows the retrieved spatial beam profile, generated artifacts also have a circular shape. Yet, contrast of circular modulations depends on the horizontal distance to the center of the beam: the artifact is more visible at the left and right edges of the beam than at its center. To appreciate this particularity, panel (d) of figure 5.5 on the previous page can be directly compared to panel (d) of figure 5.3 on page 82. This difference can be explained intuitively: tilt adds a random delay of which standard deviation depends linearly on the horizontal position. As described generally in section 5.2.1 on page 80, intensity errors increase with level of delay fluctuations. In the particular case of tilt fluctuations, it therefore means that the amount of intensity error depends on the horizontal position.

Figure 5.6 on the preceding page is a quantitative plot of the error magnitude in energy and in phase, for increasing amounts of fluctuations. The effect on phase is noticeable but very limited, even for large fluctuations. Also, we learn from this figure that the amount of tilt fluctuations should be kept under 10 µrad in order to preserve measurement quality—and stay below our 20 % normalized spectral fluence limit.

## 5.3. Errors Linked to Beam Properties

### 5.3.1. Energy Fluctuations

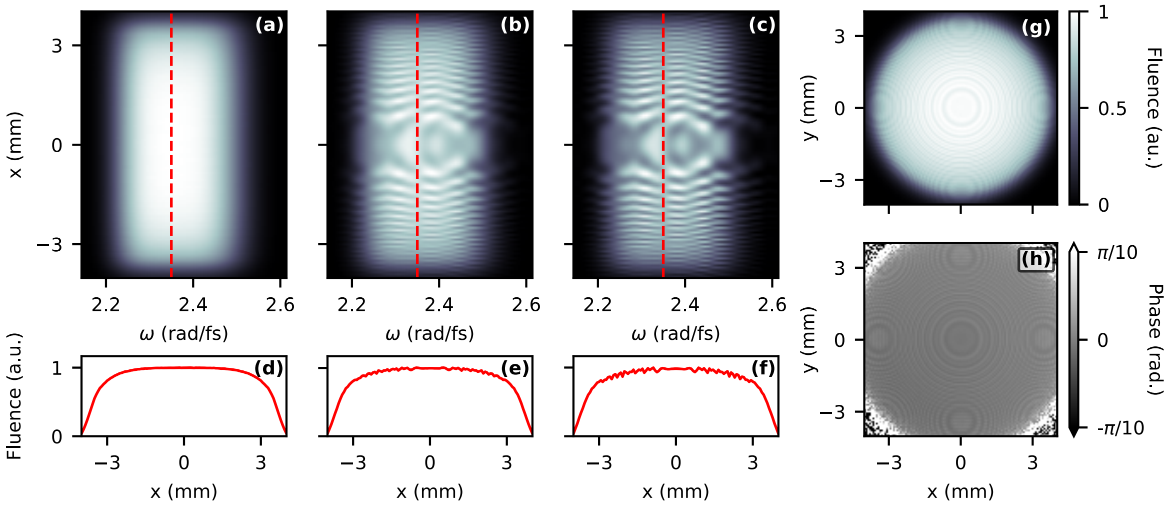

**Figure 5.7.: Effect of input energy fluctuations on the laser profile retrieved by TERMITES.** **(a)–(c)** Vertically resolved spectra obtained respectively with energy fluctuations of 0, 5, and 10 % RMS. **(d)–(f)** Line-outs of the fluence profile at central angular frequency $\omega_0$. **(g)–(h)** Fluence and phase profiles at central angular frequency $\omega_0$, corresponding to the worst case simulation (10 % RMS).

Similarly to TERMITES alignment, pulse-to-pulse variations of the input beam during the measurement can be strongly detrimental and should be avoided. Here, we estimate numerically the effect of pulse energy variations of the input beam, which are always encountered on laser systems. The same simulation program was used, but this time the changed parameter is the input pulse energy

Figure 5.7 on the preceding page represents spatio-temporal effects of input beam energy fluctuations. Similarly to measurement artifacts that were previously studied, energy fluctuations generate concentric circular modulations both in fluence and in phase profiles (see panels (d)–(e)). In the previous cases, these concentric modulations did not depend on the wavelength, which made them easy to numerically compensate. In contrast, features generated by energy fluctuations highly depend on wavelength as it can be observed on panels (b) and (c), which makes them more detrimental.

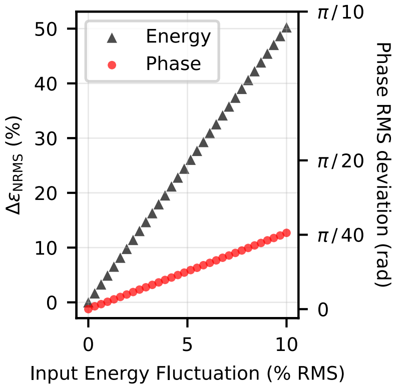

**Figure 5.8.: Measurement errors for different values of input energy fluctuation.**

Figure 5.8 shows the influence of input beam energy fluctuations on energy and phase RMS errors. As for other types of error sources, energy and phase errors increase steadily with the amount of fluctuation. In this specific case, we learn that in order to keep the amount of energy fluctuations below our tolerance limit (20 % RMS), it is desirable to avoid exceeding 5 % input energy fluctuation.

Energy fluctuations highly depend on the technologies that are used in the laser chain. Diode-pumped lasers generally deliver pulses more stable in energy than flash-pumped systems, and lasers amplified by multiple small lasers are also more stable than systems pumped by one big laser. As most high-power laser systems have pretty low energy fluctuations (percent-level) compared to the tolerance of TERMITES, this parameter is not critical for our spatio-temporal measurements. However, it is important to keep in mind that TERMITES measurements will be severely impinged for energy fluctuations of more than 5 % RMS, as displayed by figure 5.8.

### 5.3.2. Pointing Fluctuations

The last source of errors we propose to describe here are pointing fluctuations of the input beam. Pointing fluctuations are random variations of the beam propagation direction principally caused by vibration sources along the amplification chain, causing small cumulative alignment errors. Depending on the considered optical plane, they can be described as random tilt of the wavefront (near the source of perturbation) or as random beam centering variation (at focus). Most often, pointing fluctuations affecting TERMITES are a combination of these two manifestations at the same time. For simplicity, we consider in this simulation that pointing fluctuations only consists of random wavefront tilt.

As for previous studies, we modeled the effect of such pointing fluctuations on the quality of TERMITES measurements. In the study concerning pointing fluctuations caused by the TERMITES translation stage (section 5.2.2 on page 83), we only simulated *horizontal* variations of the beam direction because there were mechanically more susceptible to occur. In this case, the input beam is randomly tilted in both vertical and horizontal directions.

Figure 5.9 on the next page shows how input pointing fluctuations degrade spatio-temporal profiles retrieved by TERMITES. Artifacts are again circular in shape both for fluence and phase profiles.

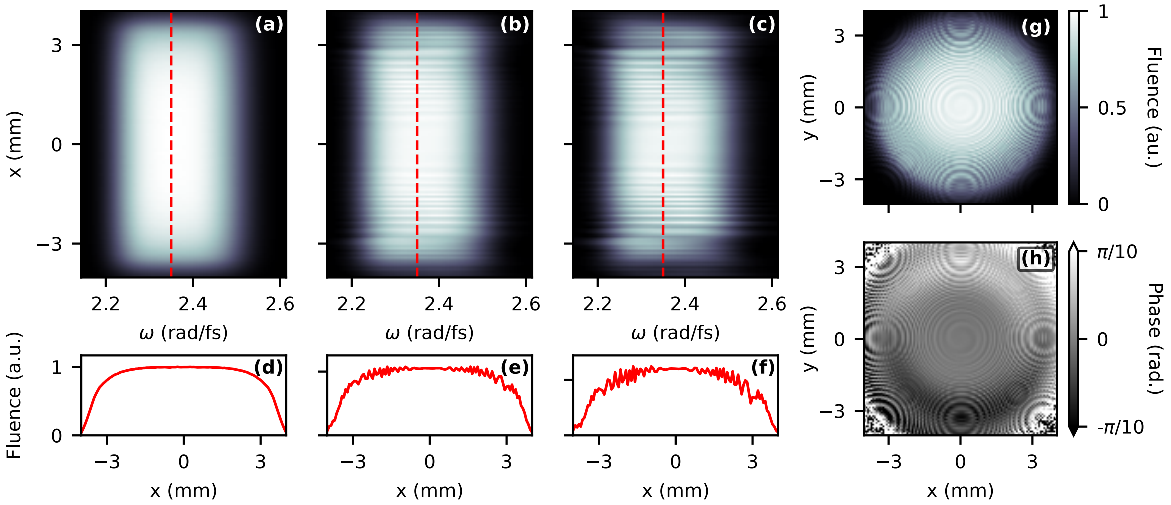

**Figure 5.9.: Effect of input pointing fluctuations on the laser profile retrieved by TERMITES.** **(a)–(c)** Vertically resolved spectra obtained respectively with pointing fluctuations of 0, 15, and 30 µrad RMS. **(d)–(f)** Line-outs of the fluence profile at central angular frequency $\omega_0$. **(g)–(h)** Fluence and phase profiles at central angular frequency $\omega_0$, corresponding to the worst case simulation (30 µrad RMS).

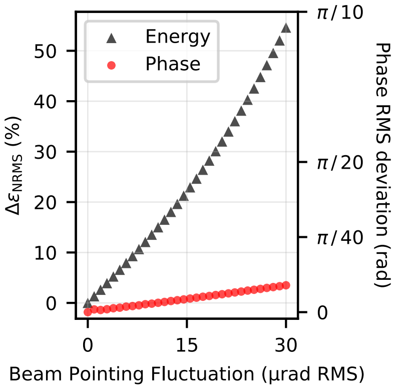

**Figure 5.10.: Measurement errors for different values of input pointing fluctuation.**

As already discussed in section 5.2.2 on page 83, tilt fluctuations generate delay errors that depend on the transverse position in the beam profile. Because reference yaw generated only horizontal tilt fluctuations, the amount of delay errors depended only on the horizontal position. In the present case, tilt is both vertical and horizontal and delay errors directly depend on radius. Figure 5.9 demonstrates that the importance of artifacts depends on the distance to the center of the beam.

Comparably to studies developed previously in this chapter, the effect of pointing fluctuations on retrieved fluence and phase profiles is quantified by figure 5.10. Once again, fluence and phase errors increase with the amount of perturbation. We learn from this plot that the maximum acceptable level of pointing fluctuations is 15 µrad. As a comparison, this limit is fifteen times higher than the pointing fluctuations observed in actual experimental conditions on the BELLA petawatt laser [110] and on other high-power femtosecond lasers. Pointing fluctuations should not constitute a strong limitation to spatio-temporal measurement with TERMITES.

⁂

In this chapter, we focused on the numerical tools that I developed during my thesis, with the goal of fully simulating a full TERMITES measurement, in arbitrary conditions. The algorithm principles were first defined in section 5.1 on page 78. We also explained in this section the method that was used to quantify fluence and phase errors in the retrieved spatio-temporal fields. We then interpreted the independent influence of common perturbations that can arise from the instrument itself (section 5.2 on page 80) or from the input beam (section 5.3 on page 84).

| Noise Source | Maximum acceptable level |
|---|---|
| Optical path difference fluctuation | 10 nm |
| Reference pointing errors | 10 µrad |
| Input beam energy fluctuations | 5 % |
| Input beam pointing fluctuation | 15 µrad |

**Table 5.1.: Summary of maximum acceptable level of fluctuation for each identified source.**

These results were particularly instructive when compared to actual experimental measurements, because they helped understanding the source of noisy features on data acquired in actual experimental conditions. Ultimately, the resulting measurement error is the sum of all possible artefacts coming from TERMITES and from its environment. It is worth noting that a lot of different sources of error could be studied with our numerical tool, but we limited the scope of this chapter to the ones that we think are the more susceptible to occur. Good quality measurements can be ensured by keeping the sources of noise as low as possible and below the limits that we defined numerically and summed up in table 5.1. This is done by choosing carefully TERMITES hardware and by performing experiments in steady conditions.

Chapter 6.

# Experimental Validation of TERMITES

In order to close this part dedicated to the design of TERMITES, let us focus on some actual experimental measurements. More specifically, we need to determine if the device meets the expected performance in real-life conditions, taking into account the main experimental perturbations susceptible to occur in a laboratory.

First, a simple test is performed to identify possible delay fluctuations in the interferometer, and check if they comply with the limits we defined in the previous chapter. Then, some secondary quantities measured by TERMITES are compared to the data produced by other well-established techniques, in order to assert the general reliability of our results. Finally, we study the measurement of well calibrated spatio-temporal couplings with TERMITES, to check that the device is able to retrieve them correctly.

## Contents

**6.1. Measurement of Interferometer Delay Stability** . . . . . 90
**6.2. Comparison with Simpler Measurement Devices** . . . . . 91
  6.2.1 Spectrally Averaged Profiles
  6.2.2 Spatially-Resolved Spectrum
**6.3. Characterization of Calibrated Defects** . . . . . 94
  6.3.1 Calibrated Pulse Front Curvature
  6.3.2 Calibrated Streak from a Square-shaped Phase Defect

## 6.1. Measurement of Interferometer Delay Stability

We studied in section 5.2 on page 80 how vibrations and delay fluctuations in the interferometer can affect the retrieved data and the output quantities. In parallel of this numerical study, we took profit of one of the characterization measurements done in this thesis to check that typical fluctuations occurring along a standard TERMITES scan are reasonable. This was done by using our device to measure optically the optical path variation at each mirror position step.

In order to perform the measurement, the convex mirror was replaced by a plane mirror so that the replica delay could be the same across the full beam profile. Additionally, an interferometric bandpass filter was used to select wavelengths of $(800 \pm 5)\,\mathrm{nm}$. This increased the coherence time, allowing us to characterize the fluctuations during a longer scan. One of the mirror is slightly tilted vertically and horizontally so that 45° spatial fringes are generated on the camera. This ensures that the pulse-to-pulse energy fluctuations from the source laser could be canceled out by spatial Fourier filtering, and that the only measured fluctuations in phase come from the variation of delay steps between the two arms.

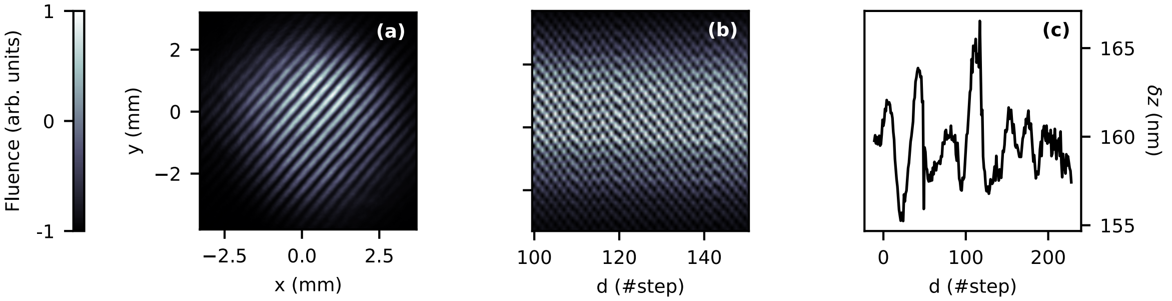

**Figure 6.1.: Experimental delay fluctuation measurement using TERMITES. (a)** Spatial interferogram obtained at zero-delay. Spatial fringes are necessary to discriminate the coherent signal from potential energy fluctuations of the laser source. **(b)** Fluence slice, taken on the white dashed line in panel (b), and resolved along the scan. **(c)** Mirror shift per step, computed from the instantaneous phase of panel (b) after some Fourier processing.

The optical path step is measured from the instantaneous phase contained in panel (b). Extraction of this instantaneous phase involved Fourier transforming the data displayed in panel (b) along its horizontal axis, filtering the signal in the frequency domain and then going back in the time domain using the inverse Fourier transform.

From the measurement shown in figure 6.1, we measure a mean step size of $\delta z = 159\,\mathrm{nm}$, to be compared to the targeted step of 160 nm. Along the scan, the step size fluctuated by 4 nm RMS. This instability corresponds to $\lambda_0/160$ and is well below the levels of fluctuation at which artifacts start to appear, according to numerical simulations (section 5.2 on page 80).

Ideally, this validation test should be conducted with a continuous wave laser so that the whole translation range could be tested. This measurement should also ideally be tried in various places and conditions. Nevertheless, the results are already giving a first idea of the kind of fluctuations affecting the new TERMITES prototype over a limited range of its translation stage. According to the numerical study developed in section 5.2 on page 80, the measured level of variations would generate around 1.4 % normalized modulations on the intensity spatial profile. Eliminating any obvious vibration sources nearby (vacuum pumps, hard disk drives...) and calibrating correctly the piezoelectric stage are mandatory steps to achieve this stability.

## 6.2. Comparison with Simpler Measurement Devices

### 6.2.1. Spectrally Averaged Profiles

In the process of measuring the spatio-temporal characteristics of different laser systems, a measurement campaign was performed on the petawatt laser BELLA [110], located in the Lawrence Berkeley National Laboratory, USA. The goal of this campaign—and of the related publication [111]—was to assess its spatio-temporal qualities, and, as a secondary objective, to validate TERMITES in field conditions. As it is illustrated by figure 6.2, a large bay is dedicated to laser diagnostics, and many different measurement devices were already installed on the system. TERMITES was implemented in this bay and it was therefore particularly easy to directly compare its results to the quantities measured on a daily basis by other instruments.

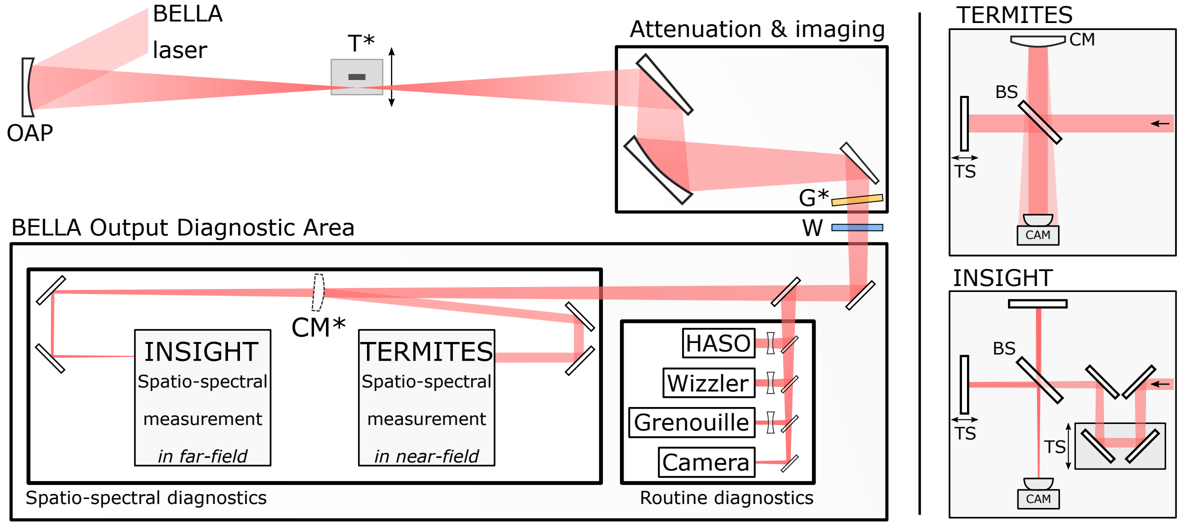
BELLA
laser
T*
OAP
Attenuation & imaging
G*
W
BELLA Output Diagnostic Area
CM*
INSIGHT
Spatio-spectral
measurement
in far-field
TERMITES
Spatio-spectral
measurement
in near-field
HASO
Wizzler
Grenouille
Camera
Spatio-spectral diagnostics
Routine diagnostics
TERMITES
CM
BS
TS
CAM
INSIGHT
BS
TS
TS
CAM

**Figure 6.2.: Experimental layout of the BELLA laser measurement** Sketch of the experimental set-up. The left panel shows the path of the BELLA laser beam from the compressor output to the experimental chamber, attenuation and imaging chamber, and finally to the diagnostic area. Here the INSIGHT and TERMITES devices have been installed, together with traditional space-only or time-only diagnostics used for such lasers. The right panels display sketches of the INSIGHT and TERMITES devices, which for practical reasons had to be used successively on two different weeks. The * symbol indicates retractable elements. **OAP:** off-axis parabola, **T:** target, **G:** gold foil, **W:** vacuum window, **CM:** convex mirror, **BS:** beam splitter, **TS:** translation stage.

The main interesting quantities to compare TERMITES results with are the fluence and phase profiles. Retrieving accurately those 2-D maps of the beam by a simple integration of the TERMITES 3-D data is a strong confirmation that no big artifact distorted the measurement and that the spatio-temporal structure also has good chances of being accurate. At BELLA, the fluence and wavefront images are retrieved by a Shack–Hartmann wavefront sensor (WFS)—introduced in section 1.3.1 on page 14—which was separated from TERMITES by only a few plane mirrors. The measurement campaign was also the occasion to use INSIGHT, which is a device that returns the same information as TERMITES, and that we described in section 2.3.2 on page 33. Even if this technique is still under development, it has been extensively tested and was also used as a comparison with TERMITES.

Figure 6.3 on the following page shows a comparison between the fluence and wavefront profiles

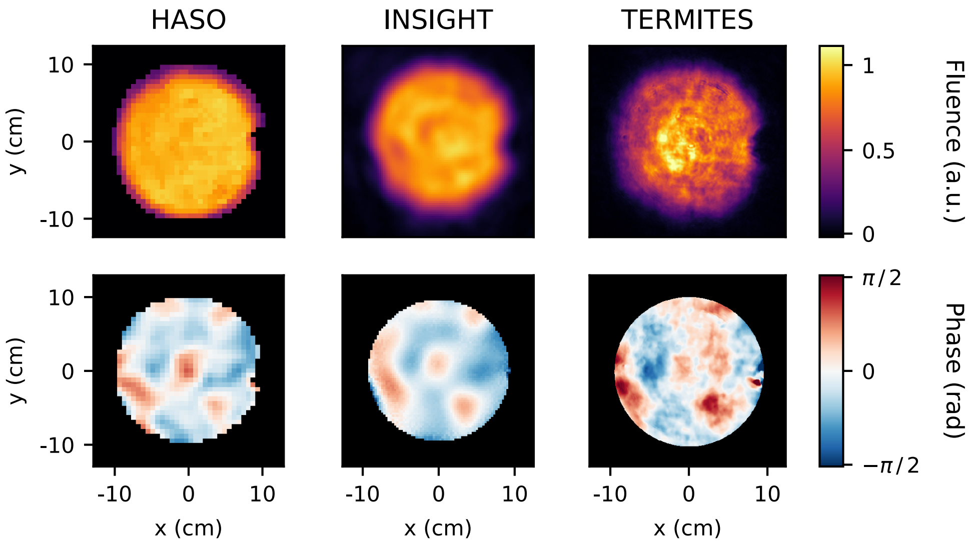

**Figure 6.3.: Spectrally averaged fluence and phase profile, as measured by TERMITES and other measurement techniques.** Results derived from TERMITES (third columns, obtained after frequency-averaging of the spectrally-resolved measurement outputs) are compared to the ones provided by a standard Shack–Hartmann wavefront sensor (HASO by Imagine Optics, left column), and by INSIGHT (middle column). The top row shows the frequency-averaged spatial intensity profile of the collimated BELLA beam, and the bottom row its frequency-averaged spatial phase profile. Note the small clip on the right edge of the beam: this is due to a small hole in the first wedge of the attenuation line, normally used to collect the accelerated electron beam in laser-wakefield experiments. This hole is usually placed at the center of the laser beam, but was moved to its edge for this measurement campaign. The resulting clip is well retrieved by TERMITES, after retropropagation of the field to the correct plane.

retrieved by TERMITES and by the two other techniques. Obtaining the spectrally averaged fluence and phase maps from TERMITES and INSIGHT spatio-spectral datasets required to use the computations described previously in section 2.4 on page 36. Additionally we removed tilt and defocus aberration modes from TERMITES and INSIGHT data in order to correctly compare the wavefronts, as this was also the case for the provided WFS wavefront. This validation test shows that the average spatial profiles retrieved by TERMITES are significantly close to those measured by the two other techniques. Fluence features such as the experimental round clip on the right edge of the beam as well as the generally top-hat energy distribution are well retrieved by TERMITES. Similarly, the phase patterns measured by our instrument match well with the reference techniques wavefronts, both in shape and in magnitude.

### 6.2.2. Spatially-Resolved Spectrum

As explained in section 3.1 on page 44, the only difference between TERMITES set-up and Imaging Fourier Transform Spectrometry (IFTS) resides in one of the interferometer plane mirrors being replaced by a convex mirror. This enables the retrieval of the spatio-spectral phase in addition to the spectral fluence of the input beam. Before checking that the recovered phase is correct, let us ensure first that TERMITES is at least capable of performing the same task as IFTS—retrieving spectral fluence couplings.

In order to do that, we used the first stages (oscillator–booster–stretcher) of a petawatt laser under construction at Amplitude. The beam at this position is around 10 mm wide and is easily measurable. We generated a strong intensity coupling by arbitrarily translating by 10 mm the convex mirror of the Offner stretcher—see figure 1.1 on page 10—along its optical axis. This introduced some *spatial chirp*—among other weaker aberrations—at the diagnostics position, roughly 2 meters after the stretcher. We checked with a fiber spectrometer that the spectrum of the pulse, and in particular its central wavelength, depended significantly on the horizontal position at which the measurement was done.

The beam was then measured with both TERMITES and the IFTS method, in order to compare their respective outputs. Switching between the two techniques is easy because it only consists of replacing the curved mirror of TERMITES by a plane mirror. This change between the two techniques being very small, alignment between the two datasets is nearly-perfect and spatially-resolved spectra can be directly compared.

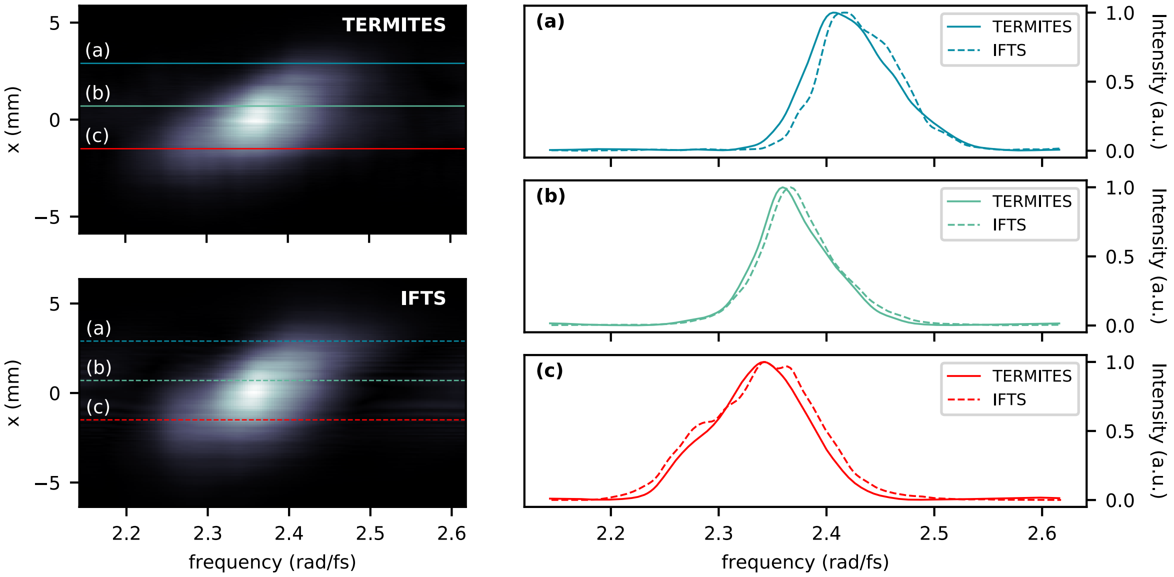

**Figure 6.4.: Measurement of a spatially-chirped pulse with TERMITES and with an Imaging Fourier Transform Spectrometer (IFTS).** The two left images are spatio-spectral intensity distributions measured by TERMITES & IFTS, across a centered horizontal line. The three plots on the right side display the spectra extracted from these 2D distributions, at three different horizontal positions (a), (b), & (c).

The output of both measurements is shown in figure 6.4. Both techniques are able to measure the horizontal spatial chirp with fine details and without any noticeable artifact. The spectrum line plots show that even if some small spectral intensity differences are visible between the two techniques, those are not affecting the interpretation for such low order space-time couplings. The small differences could also be caused by the two experimental datasets being not exactly superimposed.

Naturally, this validation test is one among many possible verifications, and does not demonstrate the validity of the technique in its entirety. Nevertheless, it constitute an experimental example of a strong low-order intensity coupling measurement made without issue with TERMITES.

## 6.3. Characterization of Calibrated Defects

### 6.3.1. Calibrated Pulse Front Curvature

A critical step of the experimental validation of TERMITES consists of actually checking that the spatio-temporal couplings measured by the device are quantitatively accurate. Generating a beam which is spatio-temporally distorted and comparing the information retrieved by TERMITES to independent measurements is one of the most direct method to check this.

Pulse Front Curvature (PFC) can be generated from a singlet lens very easily and in a quantifiable way. A more advanced optical system—displayed in figure 6.5—has been designed in the laboratory by O. Gobert, and introduces PFC in the beam, without adding any achromatic curvature (see the detailed design in Supplementary Materials of [33]). Contrarily to a simple lens, this optical element can simply be added in the collimated beam without changing its achromatic properties. It consists of two singlet lenses of which materials and curvatures are optimized to produce the desired effect. This optic is principally used as one of the components required to generate Chirped Pulses with Longitudinal Chromatism (CPLC) and to control the speed of the intensity peak at focus [33–37]. Incidentally, this well-calibrated component was also the perfect candidate to help quantify the ability of TERMITES to measure PFC.

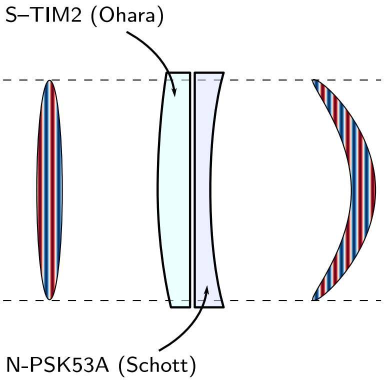

**Figure 6.5.: Effect of the PFC lens doublet on an ultrashort pulse.** The two lenses of the doublet are plano-convex and plano-concave, and made from different glass types. The optical design is optimized so that the system is afocal at central frequency *but* chromatic, adding a theoretical PFC of $0.059\,\mathrm{fs/mm^2}$. A detailed description of this system is available in [33]

A numerical study of the doublet effect is provided in the Supplementary Materials of [33]. The study was done using the design parameters of the doublet and anticipated a delay of $T_{\mathrm{PFC}} = 95\,\mathrm{fs}$ at a radial position $r = 40\,\mathrm{mm}$ which corresponds to a design Pulse Front Curvature $\xi_{\mathrm{PFC}}$ of $0.059\,\mathrm{fs/mm^2}$. This theoretical value is already a good point of comparison for our TERMITES measurement, but we chose to perform an independent measurement of the PFC to provide a direct complementary evaluation of the PFC quantity.

This independent measurement consists of overlapping a first reference pulse with a replica of itself which went through the PFC doublet. Adding a small temporal delay between the two pulses generates spectral fringes, which are then resolved spatially and measured with an imaging spectrometer. Our experimental set-up—visible in figure 6.6 on the facing page—also includes TERMITES, which is placed next to the imaging spectrometer to measure the same chromatically curved pulse. This way, spatio-temporal results coming from TERMITES can be directly compared against the results measured by the imaging spectrometer to validate or not that TERMITES is able to measure the artificial Pulse Front Curvature. The expected value of PFC as measured by both techniques is twice the theoretical value of the doublet, because of the necessary double-pass of this experimental layout. Both TERMITES and spectral interferometry method should return experimental estimations of $\xi_{\mathrm{PFC}}$ close to $2 \times \xi_{\mathrm{PFC}} = 0.119\,\mathrm{fs/mm^2}$

Post-processing the images produced by the imaging spectrometer mainly consists of Fourier Transforming the signal along its frequency axis, and then demodulating the information con-

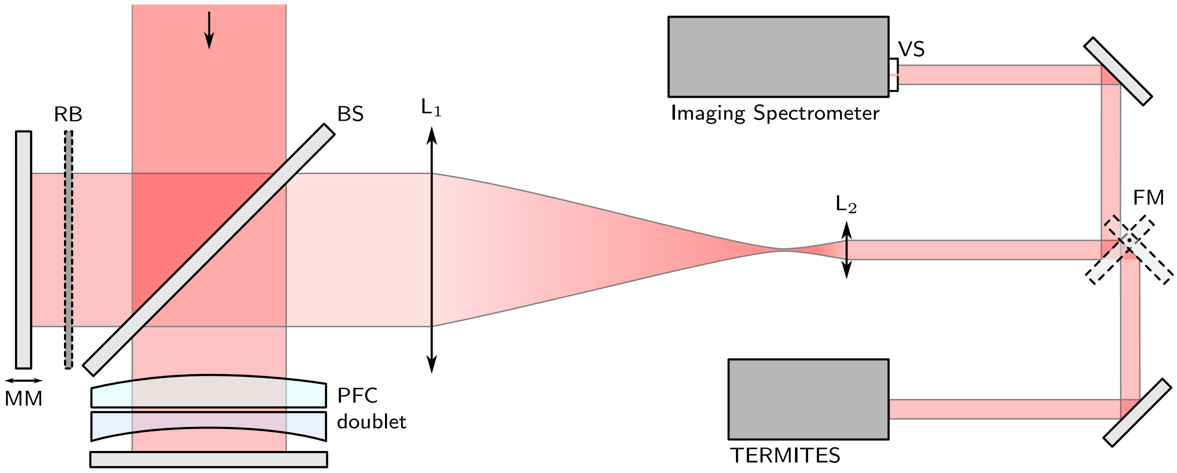

**Figure 6.6.: Experimental set-up used for validating the quantitative measurement of PFC by TERMITES.** MM: Moving Mirror, BS: Beam Splitter, $L_1$–$L_2$: Afocal telescope, FM: Flipping Mirror, VS: Vertical Slit, RB: Removable Blocker. This experiment is designed so that the imaging spectrometer and TERMITES are measuring the same beam, and are only separated by plane mirrors. During the spectral interferometry measurement, a delayed replica is generated from the input beam, in order for the PFC beam to be measured relatively to a perfect reference. During the TERMITES measurement, this interferometer arm is blocked because our method is self-referenced. The demagnifying telescope is made of achromatic doublets and considered to have a negligible effect on the measurement.

tained in the fringes by removing the constant and negative components in the time domain (see figure 6.7 on the next page). This step is facilitated by voluntarily generating small fringes, so that the information can be filtered out of the laser spectral fluctuations. Going back to the spectral domain then gives the spectral amplitude and phase of the measured beam resolved along the vertical entrance slit of the spectrometer. This spatio-spectral phase represents the difference between the phase of the pulse that went through the PFC doublet, and the phase of the reference pulse. Therefore, this quantity precisely represents the chromatic phase added by the PFC doublet.

How to quantify the amount of PFC added by the doublet then? First, line-outs of the measured spatial phase are plotted, for each frequency. Left panels of figure 6.8 on page 97 show that the line-outs mostly exhibit a quadratic dependence with the position. This curvature is fitted at each frequency by a second order polynomial, and results are plotted on the right panel. The second part of the process consists of extracting the PFC quantity from the retrieved curvatures. As explained in details in section 2.2.2 on page 26, the phase curvature $\varphi_{\mathrm{PFC}}(\boldsymbol{r},\omega)$ depends linearly on $\omega$.

$$\varphi_{\mathrm{PFC}}(\boldsymbol{r},\omega) = \xi_{\mathrm{PFC}}\,|\boldsymbol{r}|^2\,\frac{\omega-\omega_0}{\omega_0}\,, \tag{6.1}$$

with $\xi_{\mathrm{PFC}}$ the Radial Group Delay generated by PFC (in fs/mm$^2$), and $\varphi_{\mathrm{PFC}}(\boldsymbol{r},\omega)$ the corresponding phase profile. The linearity of the curvature with frequency is verified in this experiment by both techniques, as seen on figure 6.8 on page 97. Obtaining the PFC estimation is done by simply computing a linear fit of the retrieved curvatures.

Figure 6.8 on page 97 shows that both techniques are able to measure the chromatic curvature accurately. The PFC value retrieved by TERMITES ($\xi_{\mathrm{PFC}} = 0.125\,\mathrm{fs/mm^2}$) is 4 % lower than

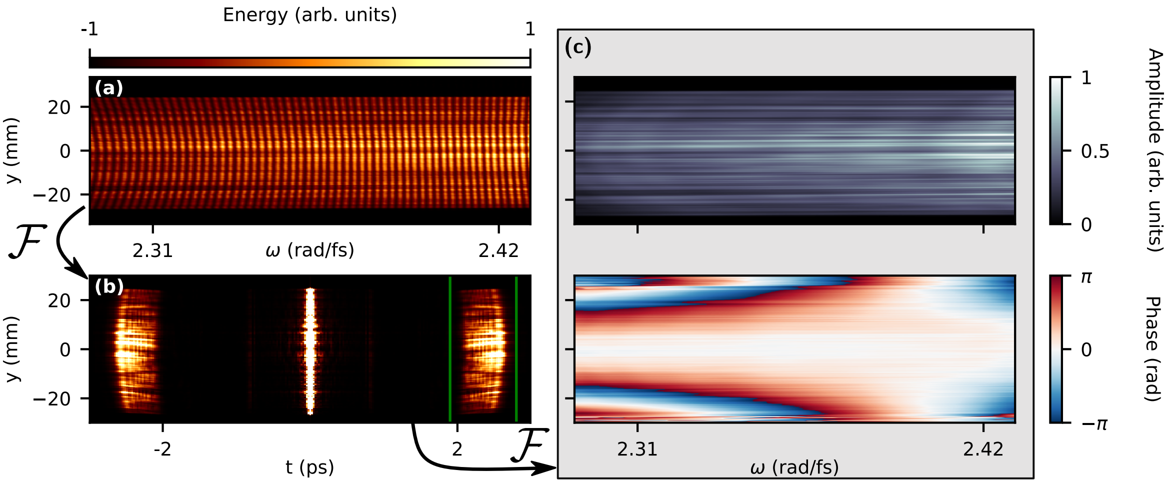

**Figure 6.7.: Spectral Interferometry data processing.** (a) Single-shot raw interferogram acquired by the imaging spectrometer. (b) Discrete Fourier Transform of the raw interferogram, showing the negative and positive frequencies, as well as the DC component. Only the positive frequencies (between green lines) are kept. (c) Spatio-spectral amplitude and phase images, obtained after performing an inverse Fourier Transform of the previously filtered image. It is worth noting here that the chromatic curvature is clearly visible on the phase profile.

the independent measurement ($\xi_{\mathrm{PFC}} = 0.130\,\mathrm{fs/mm^2}$) and 5 % higher than the expected PFC value ($0.119\,\mathrm{fs/mm^2}$).

Furthermore, the spectral interferometry measurement shows that the $\omega$-intercept of the measured PFC is 0.04 rad/fs higher than the input laser central frequency $\omega_0 = 2.355\,\mathrm{rad/fs}$. This offset is likely caused by a wrong distance between the two lens of the doublet at the time of the measurement. It was fixed easily by manually correcting the distance between the lenses. This error cannot be measured by TERMITES because our device is blind to curvature.

In this test, the high quality results obtained from spectral interferometry could make us question the gain of using TERMITES in the general case. This technique is indeed far simpler than our instrument while being single-shot, which is a great advantage. However, several drawbacks definitely exclude spectral interferometry from TERMITES competitors. The biggest is its inability to characterize the input beam over its full aperture. Because only a slice of the field is measured, it is not possible to propagate the characterized beam to other optical planes in a reliable manner. This limitation prevent any computation of the intensity at focus, which is one of the most needed results. Furthermore, even though measuring simple space-time couplings like PFC is done very accurately, more complex couplings are oftentimes invisible to spectral interferometry. It also makes use of an imaging spectrometer which has a large footprint and is usually high-priced.

### 6.3.2. Calibrated Streak from a Square-shaped Phase Defect

TERMITES is able to retrieve the input field in 3D and with high resolution. This makes it particularly suited to characterize high order couplings, as opposed to more accessible features such as Pulse Front Tilt or Pulse Front Curvature. Typically, high frequency structures can be generated in temporal shaping units like stretchers or compressors. In such elements, the

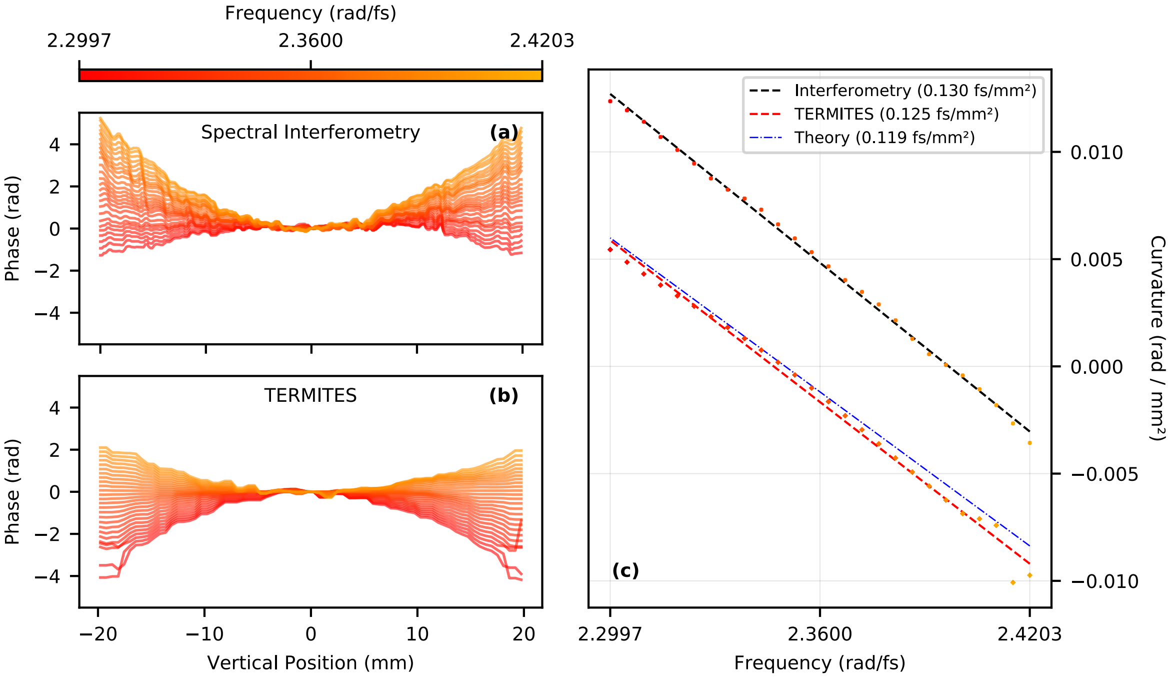

**Figure 6.8.: Measurement of the generated PFC using spectral interferometry.** Left panel shows lineouts of the measured spatial phase at different optical frequencies, measured after the PFC doublet. The main phase order is a curvature of which the radius changes with respect to the frequency. The second order polynomial fits of the spatial phase are plotted for each frequency on the right panel. The slope of the linear evolution of the curvature is directly the PFC value, given in $\mathrm{fs/mm^2}$. The expected curvature slope is also illustrated on this right panel for comparison. It simply corresponds to twice the theoretical PFC value, because of the inherent double-pass of the set-up.

frequency components of pulses propagate along different paths and small mirror defects can induce spatio-temporal couplings [77]. Those couplings can have complicated shapes with high spatial frequency, while generally being very small in magnitude.

In order to demonstrate the ability of our instrument to resolve such subtle defects, we designed a validation set-up where a small phase defect is induced in the beam. This was done by using a flat BK7 glass plate on which a custom coating is applied. As shown in panel (a) of figure 6.9 on the following page, the two-layers anti-reflection coating is applied everywhere except for a square of $10 \times 10\,\mathrm{mm}$. An appropriate mask was used during vacuum deposition in order to produce the desired effect. The custom optic is then used as shown in (b) of figure 6.9 on the next page. By placing it in the compressor between dispersion gratings G2 and G3, the square-shaped phase defect is applied on the beam. The horizontal position of this phase aberration depends on the considered optical wavelength: this is a spatio-temporal coupling of which the shape and magnitude can be reliably predicted. We have introduced this type of couplings in section 2.2.3 on page 28.

Panel (c) of figure 6.9 on the next page displays the result of a characterization measurement of the phase plate. It was conducted to validate that the square-shaped uncoated area had been correctly applied by the manufacturer, and to precisely measure the phase shift. This image was obtained by using the UHI–100 laser oscillator as a large aperture 800 nm collimated source, and by placing the custom optic in one of the arms of a purpose-built Michelson interferometer.

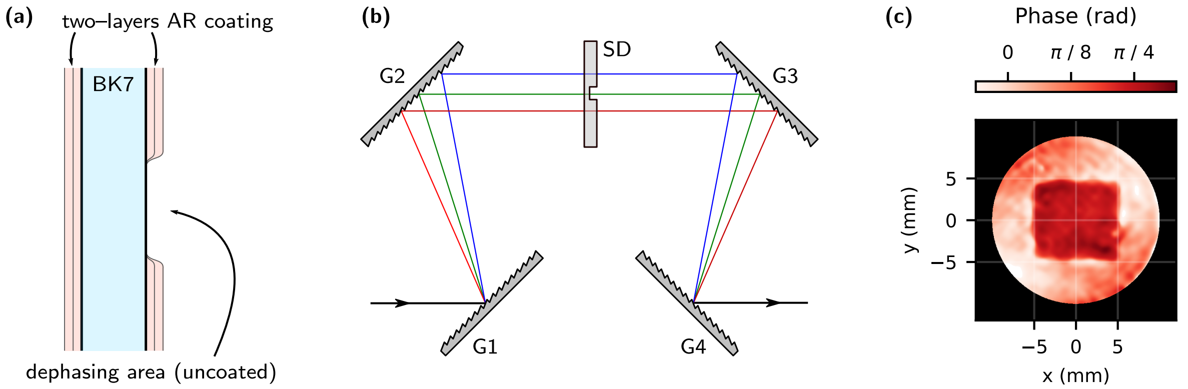

**Figure 6.9.: Design, characterization and positioning of the square defect phase plate in the UHI–100 compressor.** **(a)** Slice view of the custom phase plate. Panel **(b)** shows how this optic was placed in the UHI–100 compressor, with **G1–G4** designating the gratings and **SD** the square defect optic. The optic is placed at a position where all frequency components are normal to the beam path, but where they are spatially dispersed. **(c)** Interferometric wavefront measurement of the calibrated square defect optic, which confirms the shape of the defect and its phase value. From the measurement, the local phase jump provided by this phase plate is around $\pi / 4$, and the defect is a $40\,\mathrm{mm}$ wide square.

After processing the resulting interferograms, this wavefront is obtained and confirms that the desired specifications are met. The phase defect is roughly a square of $10 \times 10\,\mathrm{mm}$ in which the phase is offset by $\sim \pi/4\,\mathrm{rad}$ at $800\,\mathrm{nm}$.

The intentional space-time coupling is measured by simply placing TERMITES at the output of the UHI–100 compressor. After obtaining the confirmation that no major coupling is visible in the beam in normal condition by characterizing it with TERMITES, the phase plate is added in the compressor as planned.

TERMITES measurement of the resulting field is displayed in figure 6.10 on the facing page. Panels (b) to (e) clearly show that the added phase plate affects frequencies that are between 2.32 and $2.5\,\mathrm{rad/fs}$, and that the expected square shape of size $10 \times 10\,\mathrm{mm}$ is visible on their wavefronts. In addition to this defect, a magnified copy of the square is also visible. This supplementary feature is an artefact created by TERMITES, and caused by the reference. A more detailed explanation of this artefact was provided in section 3.2.3 on page 55. Unfortunately, the square duplicate could not be removed by the reference compensation algorithm. The high frequency components of the defect were indeed very difficult to propagate multiple times in a row. In this particular case, the interpretation of the phase profile has to been done without removing the artefact.

Despite this drawback, panel (a) of figure 6.10 on the facing page clearly shows that the square defect travels horizontally on the wavefront, leaving a linear streak on the spatio-spectral slice of the phase. The *traveling speed* of the phase defect across the beam profile directly depends on the spatial chirp and therefore on the compressor geometry. If frequency components are highly spread horizontally at the phase plate position, then the phase defect will only be visible on a small subset of the laser spectrum. In this case, the square shape will cross the beam very fast and the slope of the streak in panel (a) will be very steep. On the contrary, the geometry of UHI–100 compressor allows for the phase defect to embed in $\sim 50\,\%$ of the beam spectrum, making the created spatio-spectral coupling very easy to notice with TERMITES. The value

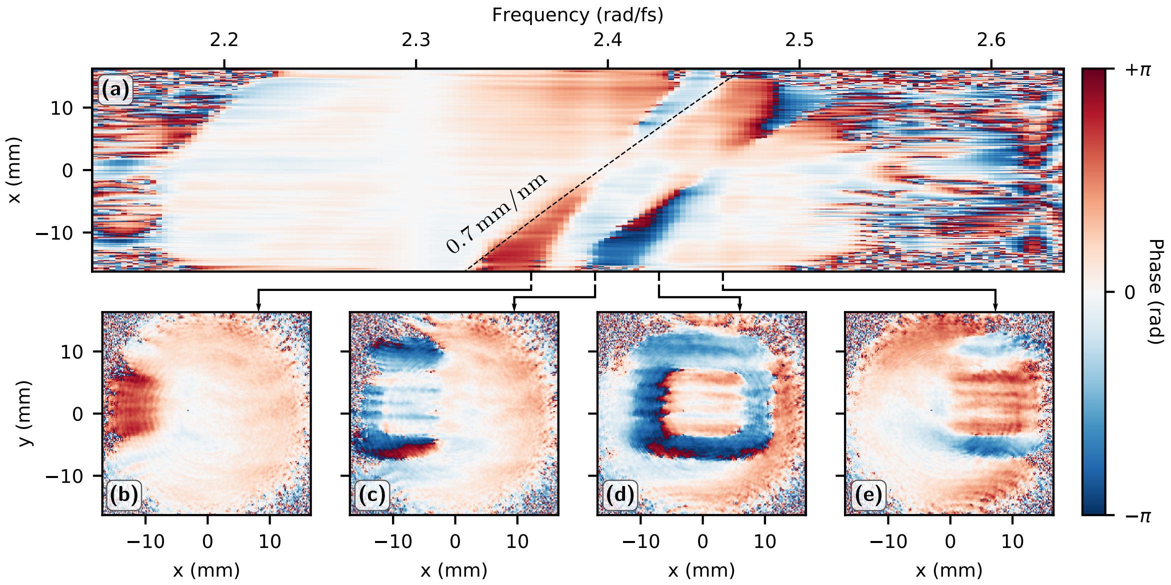

**Figure 6.10.: Phase streak caused by the phase defect plate, as measured by TERMITES. (a)** Horizontal slice $\varphi(x, y_0, \omega)$ of the spatio-spectral 3D phase obtained with TERMITES. The oblique dashed line corresponds to the expected streak slope of $0.7\,\mathrm{mm/nm}$ that is specific to UHI–100 compressor. **(b)–(e)** Monochromatic wavefronts of the input beam, observed at different frequencies affected by the square defect. As illustrated by these four panels, the shape and magnitude of the defect are similar to the validation measurement in figure 6.9 on the preceding page. The reference artefact is the larger square.

of the streak slope is conveniently expressed as a spatial dispersion, in mm/nm.

Interestingly, the slope of the streak created by the reference artefact is the product of the original streak slope, by the reference magnification. It is therefore $1/\beta$ steeper than the original streak, as explained in figure 6.11 on the next page. In the case of our experiment, the artefact travels horizontally 66 % faster than the square defect, and the slope of the corresponding streak is 1.17 mm/nm. If $\beta$ was significantly small, the artefact would travel very fast. This would alleviate its influence on the final result because it a smaller portion of the beam spectrum would be impacted.

This validation test pinpoints the specific difficulty caused by the reference artefact in our technique. The reference compensation algorithm is usually sufficient to correct the artefact when the wavefront aberrations are of sufficiently low order (e.g., simple curvatures, see section 6.3.1 on page 94). However, it is much more complicated when high frequency modulations affect the beam profile, like in the present case. In such situations, it is often easier to avoid applying the reference compensation algorithm and interpret the profile by identifying the relevant features and ignore the artefacts. This has an important consequence on future implementations of TERMITES: low $\beta$ values should absolutely be privileged in the general case, so that arbitrarily distorted beams can be characterized without even needing to apply the reference compensation algorithm. As it was explained in chapter 4 on page 63, this choice is perfectly achievable provided that the instrument pupil size is reasonably chosen.

This technical outcome put aside, the hereby presented results demonstrate that TERMITES is able to retrieve complex spatio-temporal couplings with great precision. To emphasize the performance of the instrument, let us stress that in this experiment, the coupling is a localized $\lambda/8$

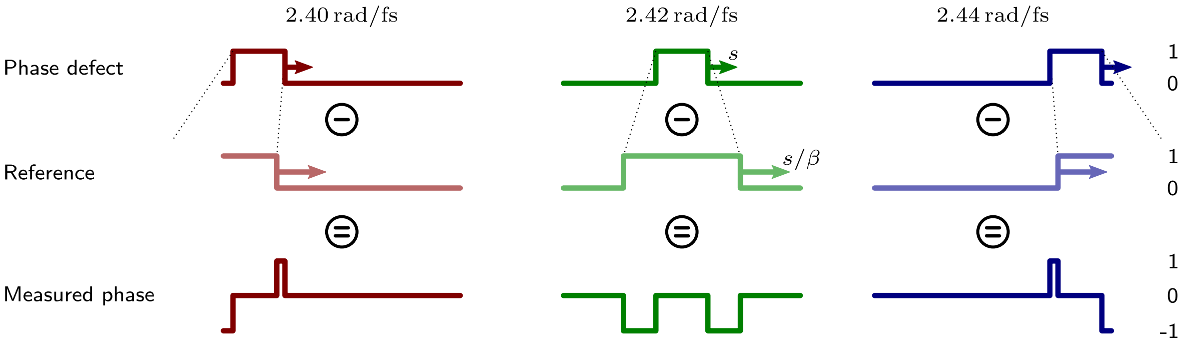

**Figure 6.11.: Interpretation of the square phase defect artefacts caused by the reference.** This sketch displays the square phase shift generated in this experiment by the phase plate placed in the compressor. Since the reference is a dilation of the object plane in first approximation, the phase shift is magnified and replicated on the reference. In the reference beam, the lateral dispersion $s$ (symbolized by an arrow) is multiplied by the magnification $1/\beta$. The measured phase is the difference between the two phase, which explains patterns observed in figure 6.10 on the preceding page.

phase offset of which the position evolves with wavelength at 0.7 mm/nm. The experiment validates that TERMITES is able to resolve correctly features that match these values.

⁂

This last chapter of part II described the various experimental tests with regard to the complete validation of our instrument TERMITES. First, a stability test was performed to check that no major delay fluctuation was affecting the interferometer in normal operating conditions (section 6.1, p.90). 3-D resolved TERMITES results were then integrated or projected along their spatio-spectral scales in order to compare the basic results with those produced by IFTS, Shack–Hartmann and INSIGHT techniques (section 6.2, p.91). Then, purpose-designed optics were employed to check quantitatively that TERMITES is able to retrieve fine spatio-temporal structures of ultra-short pulses (section 6.3, p.94).

More generally, part II was intended to provide an in-depth comprehension of TERMITES, by going through the details of the technique, and by establishing its abilities. As any metrology system, TERMITES also has inherent limits which are principally linked to input beam fluctuations and to the weakness of its reference compensation.

# Part III.

# Characterization of Laser Systems

Chapter 7.

# Experimental Protocol for Successful TERMITES Measurements

Before presenting in details the results produced with TERMITES during this work, we will discuss about the way our instrument should be used in actual experiment. Since we regularly tested the device along its design, we progressively understood the importance of some details that are decisive to obtain good quality results.

Elaborating a protocol for TERMITES is decisive and requires to think particularly about three elements. What is the best position to perform the measurement? Is it possible to reduce the beam diameter diameter without degrading too badly the measurement? How should the attenuation be handled?

## Contents

**7.1. Positioning TERMITES in the Laser Chain** . . . . . . . . . . 104
**7.2. Input Beam Size Reduction** . . . . . . . . . . 104
**7.3. Input Energy Requirements & Appropriate Attenuation** . . . . . . . . . . 106
    7.3.1 Maximal Input Pulse Energy
    7.3.2 Attenuation Methods

## 7.1. Positioning TERMITES in the Laser Chain

The first element to determine before considering any measurement with TERMITES is the actual location of the measurement device in the laser chain. As we saw in section 1.1 on page 10, ultra-intense laser systems are made of several elements susceptible to introduce spatio-temporal couplings.

Generally, experimentalists need to assert the properties of laser pulses at the end of the chain, in order to learn about physics taking place on target. Most of the time, TERMITES is therefore placed next to traditional diagnostic systems at the compressor output or just after the target chamber. This is what we did for nearly all the measurements carried out during this work—the characterization of BELLA's Petawatt beam for instance, which was presented in figure 6.2 on page 91.

Yet, it can also be interesting to study the specific spatio-temporal couplings introduced by a component of the laser chain, such as amplifiers, the stretcher or the compressor. Numerical retropropagation, presented in section 3.2.4 on page 59, can be used to precisely adjust the optical plane imaged by TERMITES, by a few meters if necessary. For instance, it can be used to quantify the precise amount of angular dispersion added by a compressor by propagating back the measured beam to the last grating, and canceling out any spatial chirp that would be created in free space. Nevertheless, we found that it was often more precise to place TERMITES as close as possible to the element of interest, and to only use retroprogation algorithms for fine adjustment of the imaged plane.

Thankfully, moving TERMITES at different places in the laboratory is quite straightforward, owing to two main elements. First, the technique is by nature insensitive to the global (or spatially homogeneous) spectral phase, making measurements possible at virtually any position along the laser chain. As seen in section 2.3 on page 30, some other spatio-temporal devices rely on non-linear optics and therefore need the measured beam to be compressed. Secondly, the footprint of TERMITES was strongly reduced during this work, making the device portable and quick to align.

In any case, experimentalists should keep in mind that TERMITES must always be kept away from vibration sources such as vacuum pumps or spinning hard-drives. The influence of vibrations on the measurement was shown numerically in chapter 5 on page 77. Also, air turbulences can be highly detrimental to the measurement quality and should be prevented before starting the measurement.

## 7.2. Input Beam Size Reduction

As it was explained on page 70, it can be necessary to resize the input beam so that it fits the entrance pupil of TERMITES. Beam reduction was particularly used during this work, in conjunction with the 20 mm input diameter version of TERMITES (see figure 4.4 on page 74). For this prototype, we made the informed choice of reducing the input diameter of TERMITES in order to improve other factors such as measurement stability and footprint of the device. This was done most of the time by using a Keplerian refractive telescope, consisting of two converging lenses.

In general, inserting any refractive element in front of an ultrashort pulse measurement device is considered bad practice because of the dispersion it introduces. In the present case, dispersion is not an issue because homogeneous spectral phase is not measured by TERMITES. However, using a Keplerian telescope—as it is done routinely to capture near-field fluence profiles—can severely alter the spatio-temporal properties of measured beams. This is due to the fact that central part of the pulse travels through longer distance of material in both lenses and gets significantly delayed with respect to the outer rays. This effect is known as Radial Group Delay (RGD) which is mostly quadratic in the case of a lens [76, 98, 112, 113]. Quadratic RGD is commonly called Pulse Front Curvature (PFC, described in section 2.2.2 on page 26).

The reason we decided that Keplerian telescopes were still a viable solution is twofold. Firstly, chromatic aberrations added by the telescope can easily be subtracted from the result. They are indeed well predicted theoretically and consists for the most part of PFC [76]. The group delay $T_{\mathrm{PFC}}$ added at radius $r$ by a Keplerian telescope is:

$$T_{\mathrm{PFC}}(r) = \frac{{r_{\mathrm{max}}}^2}{2\,c\,f_2\,(n-1)}\left(-\lambda\frac{\mathrm{d}n}{\mathrm{d}\lambda}\right)\left(1+\frac{1}{M}\right)\,, \tag{7.1}$$

with $f_2$ the focal length of the last lens, $n$ the refractive index of lenses material, and $M$ the magnification of the telescope.

Secondly, PFC can be strongly limited if achromatic doublets are used instead of simple plano-convex lenses. In order to verify this assertion, we used a commercial ray-tracing software (OSLO™) and modeled a 1/3 reducing telescope incorporating either singlet lenses or achromatic lenses. We used the characteristics of the lenses that were used during measurement of the LASERIX laser beam. Using this software was necessary because equations describing PFC generated from a doublet-based telescope would be much more complicated than equation (7.1). Figure 7.1 on the following page sums up the result of this short study. We plotted the chromatic focal shift measured by the software at the output of both telescopes. Chromatic focal shift was explained with figure 2.6 on page 28 and is a direct consequence of Pulse Front Curvature after beam focusing. The ray distribution for three different wavelengths at multiple positions around focus is also displayed on figure 7.1.

As expected, panel (a) demonstrates that the singlet-based telescope introduces large amounts of chromatic focal shift. The effective focusing distance after an artificial lens depends on wavelength and shifts by more than six times the monochromatic Rayleigh range (at 800 nm) for the telescope that we simulated. On the contrary, panel (b) shows that no strong chromatism affect the beam if the singlet lenses of the telescope are replaced with achromatic ones. In this case, the maximum focal shift is 0.02 mm which represents only 1.3 % of the monochromatic Rayleigh range.

This quick simulation shows that doublet-based Keplerian telescopes can be an acceptable way to reduce the input beam if they are designed and validated carefully. It essentially validates PFC measurements done with TERMITES, up to a systematic measurement uncertainty which corresponds to the PFC inserted by the telescope. Nonetheless, we decided that in the general case, having a small controlled PFC error is more desirable than using a large version of TERMITES which is less versatile and more prone to stability issues.

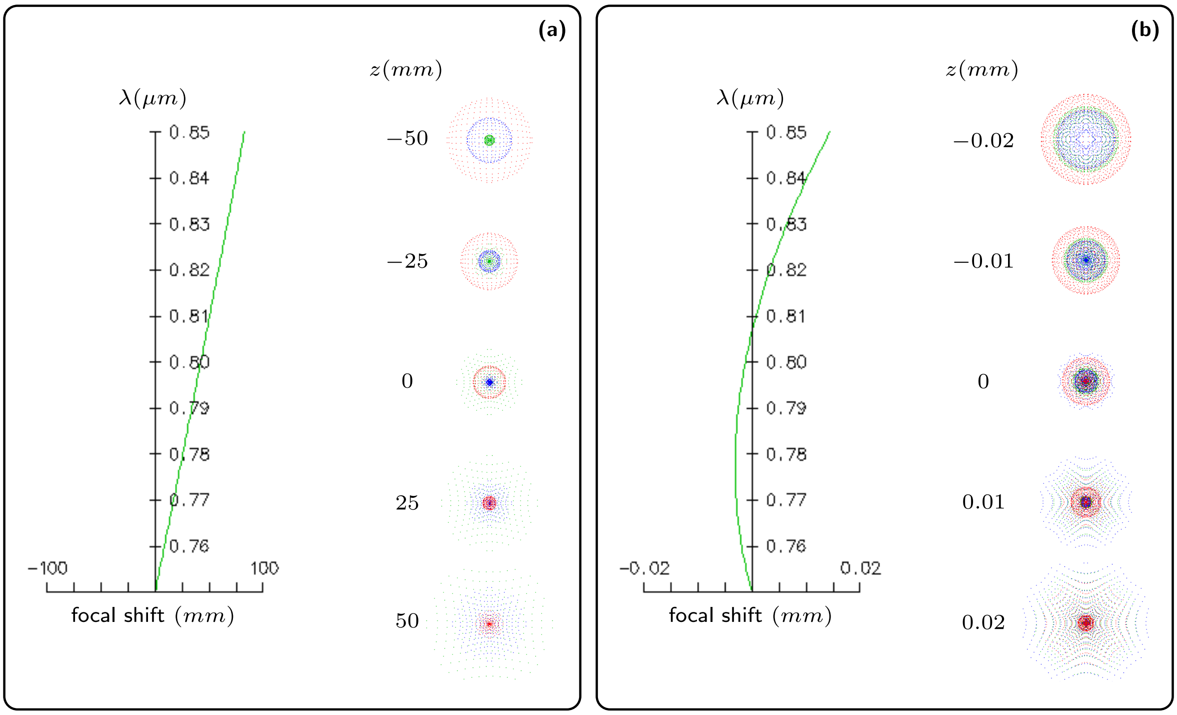

**Figure 7.1.: Focal shift generated by a $1/3$ reduction telescope.** **(a)** Case where both lenses are simple fused silica singlets. **(a)** Case where both lenses are achromatic doublets. For both cases, we plotted the spectral focal shift computed after a $1000\,\mathrm{mm}$ "perfect" lens that is simulated in software, as well as the spectral ray distribution around average focal distance for $750\,\mathrm{nm}$ (red), $800\,\mathrm{nm}$ (blue) and $850\,\mathrm{nm}$ (green). Even if chromatism is observed in both cases, note that the spatial scales are much larger in panel (a). This figure was obtained using OSLO™.

## 7.3. Input Energy Requirements & Appropriate Attenuation

As any measurement system, TERMITES has a maximum input beam energy which should not be exceeded. We will first compute this value theoretically, and then list the solutions available to the experimentalist to maintain input energy below the limit and avoid damaging the instrument.

### 7.3.1. Maximal Input Pulse Energy

During a TERMITES measurement, maximum fluence levels are achieved when delay between the input beam and the reference is zero. At this moment, the maximum fluence is located on circular constructive fringes (see figure 3.5 on page 49). If contrast is optimized adequately, the maximum fluence can be considered to be:

$$F_{\mathrm{max}} = 2R(1-R)(F^{I}_{\mathrm{max}} + F^{R}_{\mathrm{max}}) \;, \tag{7.2}$$

with $F^{I}_{\mathrm{max}}$ the input beam maximum fluence, $F^{R}_{\mathrm{max}}$ the reference beam maximum fluence and $R$ the reflectivity of the beam splitter. Apart from non-standard cases, $F^{I}_{\mathrm{max}}$ and $F^{R}_{\mathrm{max}}$ can be considered equal because both beams should be ideally balanced in a final version of TERMITES (see section 4.1.2 on page 68). Besides, the maximum throughput of the interferometer is achieved for $R = 0.5$. Therefore, equation (7.2) on the facing page simplifies to:

$$F_{\text{max}} = F^I_{\text{max}} \, . \tag{7.3}$$

The quantity of electrons $N_e$ stored in a camera pixel after being exposed to the interference pattern is the product of the number of photons captured by this pixel and the quantum efficiency of silicon $\eta_{\text{Si}}$. For this quick estimation, we consider that the input beam is monochromatic at 800 nm.

$$N_e = \eta_{\text{Si}} \, \frac{F^I \, {\delta_x}^2}{\hbar\omega} \, , \tag{7.4}$$

with $F^I$ the input beam fluence on the considered pixel, $\delta_x$ the camera pixel size, and $\hbar$ the reduced Planck constant.

Let us compute the pulse energy for which the optical fluence saturates camera pixels. At saturation fluence, $N_e$ reaches the maximum number of electrons that can be contained in each pixel of the camera. This quantity of electrons is called *saturation capacity* or *well depth* and will be noted $N_s$.

$$N_s = \eta_{\text{Si}} \, \frac{F^I_{\text{max}} \, {\delta_x}^2}{\hbar\omega} \, ,$$

The maximum fluence $F^I_{\text{max}}$ is the maximum pulse energy ${\varepsilon^T}_{\text{max}}$ divided by the area of the beam profile (assumed top-hat).

$$N_s = \eta_{\text{Si}} \, \frac{\left(\frac{{\varepsilon^T}_{\text{max}}}{\pi \, {r_{\text{max}}}^2}\right) {\delta_x}^2}{\hbar\omega} \, ,$$

$${\varepsilon^T}_{\text{max}} = \frac{N_s \, \pi \, {r_{\text{max}}}^2 \, \hbar\omega}{\eta_{\text{Si}} \, {\delta_x}^2} \, . \tag{7.5}$$

with $r_{\text{max}}$ the input beam radius. In our configuration, we have:

- $N_s = 20000\,\text{e}^-$
- $\eta_{\text{Si}}(800\,\text{nm}) \sim 0.1$
- $\delta_x = 5.5\,\mu\text{m}$
- $r_{\text{max}} = 10\,\text{mm}$

. (7.6)

The maximal input energy for the current prototype of TERMITES is therefore:

$${\varepsilon^T}_{\text{max}} \sim 0.5\,\mu\text{J} \tag{7.7}$$

### 7.3.2. Attenuation Methods

Depending on the laser system and where it is characterized, input beam energy varies considerably. It can be just at the right level if the measurement is done after one of the first amplifiers, but it can also reach tens of Joules if TERMITES is placed at the output of a Petawatt laser system. What is the best way to attenuate the measured beam to the µJ level required by TERMITES?

Usually, motorized attenuators are directly available in the laser chain and are designed to tune the energy and attenuate the beam by about one order of magnitude if necessary. Using such attenuation device is not a problem with TERMITES, provided that it does not introduce any post-pulse and that it does not change strongly the beam polarization. It is worth noting here that post/pre-pulses can be strongly detrimental to the measurement since they result in spectral interference.

However, attenuators that are already installed in the facility are usually not sufficient to decrease energy below our limit of 0.5 µJ. Two options are left:

**Using neutral densities** This is the common way of reducing pulse energy for diagnostics. For instance, neutral densities are usually of sufficient quality to be placed before cameras without affecting the fluence profile measurement. However, they do have some unpredictable influence on the wavefront, and can potentially degrade the spectrally-averaged phase profile. The other issue caused by neutral densities is their not-so-neutral spectral absorption. Because the beams we characterize with TERMITES are usually very large spectrally (up to 150 nm), neutral densities can severely alter the spectrum of the measured beam. This drawback occurred when we used a lot of neutral densities in front of our device.

**Using uncoated glass plates** This method is less harmful for the spectral content of the beam to be characterized. As only $\sim 4\,\%$ of the energy is reflected off uncoated BK7 glass at near-normal incidence, using a few plates is a good and low-cost solution to decrease the input energy by several orders of magnitude. Reflections from rear surface should be avoided, which is done easily using a plate where the back surface is wedged or sanded.

Note that spectral filtering caused by neutral densities can be taken into account and compensated numerically after TERMITES post-processing, provided that the total spectral absorption $F(\omega)$ from densities is known:

$$\varepsilon^{\mathrm{corr}}(\boldsymbol{r},\omega) = \varepsilon^{\mathrm{meas}}(\boldsymbol{r},\omega) \times \frac{1}{\sqrt{F(\omega)}} \tag{7.8}$$

However, this correction does not solve all issues in cases were spectral distortion is too high. In those situations, the signal at one end of the spectrum can go below the noise level of our device, destroying any information of amplitude and phase contained in this part of the spectrum. Consequently, we made sure to use neutral densities only when necessary in our experiments with TERMITES.

⁂

During the numerous measurements performed during this PhD, I discovered that a lot of aspects of the TERMITES technique are crucial for the success of a measurement. Most of them were discussed in the previous part, and essentially concern the design of our instrument.

A small amount is also closely linked to the measurement in itself, and to the handling of TERMITES with respect to other existing elements in the laser chain.

Among multiple small experimental details, I found that the position of measurement was critical, in particular for finding the source of a spatio-temporal defect. For this reason, the instrument had to be small and portable, and finding a way to reduce the beam without degrading its properties was necessary. We saw in section 7.2 that this is possible in certain conditions using a simple doublet-based refractive telescope. Such system was not used all the time, either because the beam was small enough to fit the entrance pupil of TERMITES, or because a reducing system was already implemented. Finally, we computed the maximum allowed pulse energy for our device and discussed about the best way to achieve the required attenuation.

# Survey of Spatio-Temporal Couplings Measured in Ultra-Intense Lasers

As introduced theoretically in chapter 2, space-time couplings can be generated by multiple elements in typical laser systems. Laser components which rely on spatial dispersion—namely stretchers or compressors—are usually the most significant sources of spatio-temporal or spatio-spectral aberrations. However, some other components, such as telescopes and amplifiers, are also susceptible of creating complex distortions and to affect the quality of ultra-intense pulses.

During my thesis, we conducted multiple measurements of very diverse laser systems. Each of them resulted in direct diagnoses of the laser chains global performance, and provided information about pulses focusability in space and time. However, a finer analysis of the laser three-dimensional field is oftentimes necessary to understand the precise nature of potential defects, and to trace back their sources.

In this last chapter, I will therefore describe the spatio-temporal and spatio-spectral couplings generated by the successive elements of a classic ultra-intense laser chain, by using experimental examples from my thesis work.

## Contents

**8.1. Effects of Pulse Stretching** . . . . . . . . . . 112
  8.1.1 Spatial Chirp Created from a Misaligned Offner Stretcher
**8.2. Effects of Pulse Amplification** . . . . . . . . . . 113
  8.2.1 Spatio-spectral Filtering by Amplification
  8.2.2 Gain Depletion in Chirped Pulse Amplifiers
**8.3. Effects of Beam Imaging** . . . . . . . . . . 116
  8.3.1 Telescope-induced Pulse Front Curvature
**8.4. Effects of Pulse Compression** . . . . . . . . . . 119
  8.4.1 Pulse Front Tilt
  8.4.2 Distortions Caused by Surface Defects of Compressor Optics
  8.4.3 Spatio-spectral Profile Masking
**8.5. Effects of Hollow-Core Fiber Compression** . . . . . . . . . . 124
  8.5.1 Spatially Resolved Spectral Broadening
  8.5.2 Effect of Spatial Chirp on Fiber Coupling

## 8.1. Effects of Pulse Stretching

### 8.1.1. Spatial Chirp Created from a Misaligned Offner Stretcher

Offner stretcher is the first element of which the spatio-spectral effects will be studied in this chapter. As explained in section 1.1.1 on page 10, stretchers are crucial components of Chirped Pulse Amplification (CPA) systems. They are used to spread femtosecond pulses in time up to the picosecond scale, by adding strong amounts of spectral dispersion. This process significantly reduces laser peak power and avoids damage in subsequent amplification steps.

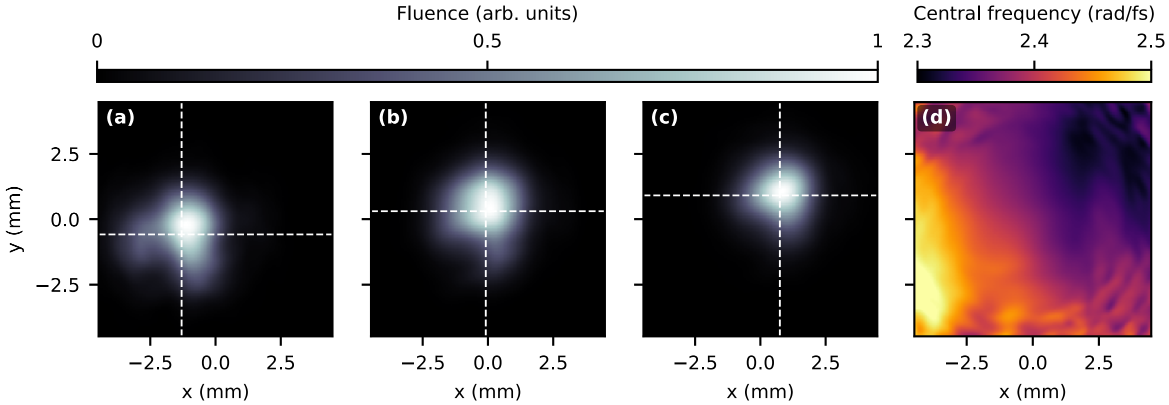

**Figure 8.1.: Spatial Chirp measured at the output of a misaligned stretcher with TERMITES.** **(a)–(c)** Fluence profiles of the beam at respectively $2.5$, $2.375$ and $2.25\,\mathrm{rad/fs}$. Centroids are computed for each profile and represented as white crosses. **(d)** Central frequency of the beam, for each transverse position of its profile. The central frequency is found by computing the barycenter of the spectrum, at each spatial pixel.

During this work, I had the opportunity to characterize a laser chain of medium size under construction in Amplitude Laser laboratories, which is intended to produce $1\,\mathrm{kHz}$, $20\,\mathrm{mJ}$, $20\,\mathrm{fs}$ pulses for users. Figure 8.1 displays the results from the measurement that was done immediately after the Offner stretcher of this laser system. Panels (a)–(c) show that despite its constant shape, the mode of the beam is centered differently for each wavelength of the spectrum. As explained by Gu *et al.* [114], spatial chirp can be interpreted as *spatial dispersion* or as *frequency gradient*. Those quantities are not trivial reciprocates. Spatial views displayed in panels (a)–(c) can be used to visualize intuitively spatial dispersion, which equals to $31\,\mathrm{\mu m/nm}$ in this measurement. This value of spatial dispersion is relatively important, given the large spectral bandwidth ($100\,\mathrm{nm}$) and the relatively small diameter of the beam ($\simeq 3\,\mathrm{mm}$).

Panel (d) of figure 8.1 features for its part the spatially-resolved central frequency of the measured beam, which is another way to look at the same spatio-spectral coupling. This panel shows unambiguously that the measured spatial chirp is monotonous and oblique. Frequency gradient can be directly visualized in this panel, and equals to $2.1 \times 10^{-2}\,(\mathrm{rad/fs})/\mathrm{mm}$.

The most probable explanation for this oblique spatial chirp is twofold. The horizontal component of the spatial chirp is very likely coming from a slight error in the distance between the two curved mirrors in the Offner stretcher, which is known to generate horizontal spatial chirp. For example, we used this method of moving longitudinally the convex mirror of an Offner stretcher as part of TERMITES validation in section 6.2.2 on page 92. The coupling we intended to add at this moment was precisely horizontal spatial chirp. The vertical component of the spatial chirp, for its part, is an uncorrectable aberration linked to geometrical constraints in the Offner stretcher. This interpretation should be validated by numerical ray-tracing, to understand more clearly the apparition of spatial chirp and maybe optimize slightly the performance of stretchers.

This result could seem concerning because of the importance of the measured spatial chirp. However, we will show in the next section why the issue is mitigated and does not impact the final performance of ultra-intense lasers in practice.

## 8.2. Effects of Pulse Amplification

### 8.2.1. Spatio-spectral Filtering by Amplification

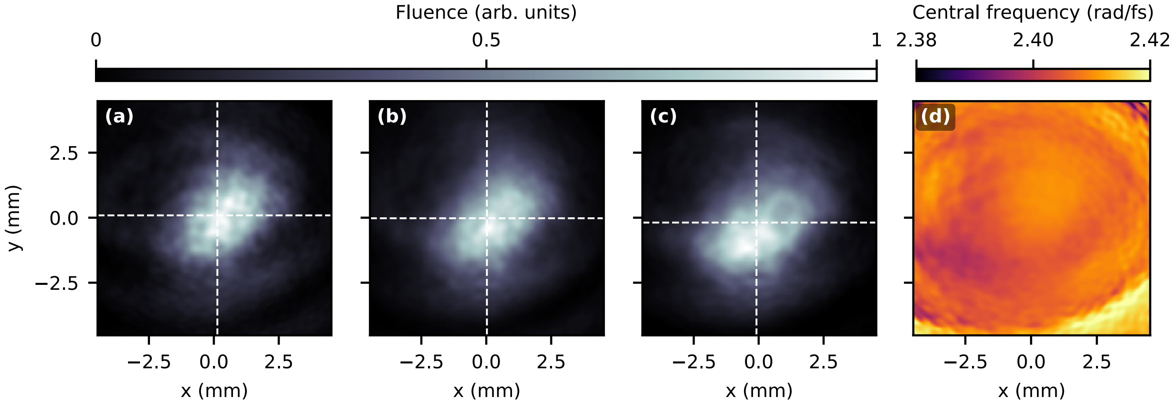

**Figure 8.2.: Spatial Chirp measured at the output of a multipass amplifier that is seeded by a misaligned stretcher. (a)–(c)** Fluence profiles of the beam at respectively $2.47$, $2.41$ and $2.35\,\mathrm{rad/fs}$. Centroids are computed for each profile and represented as white crosses. Because of spectral gain narrowing and red-shift occurring in the amplifier, the frequencies are not the same as in figure 8.1 on the facing page. **(d)** Central frequency of the beam, for each transverse position of its profile. The central frequency is found by computing the barycenter of the spectrum, at each spatial pixel.

The characterization done in section 8.1.1 on the preceding page was followed by other measurements further down the amplification chain. Notably, we placed TERMITES at the output of the multipass amplifier which is located directly after the Offner stretcher. The principal goal of this measurement was to observe a potential unfavorable spatio-spectral effect added by the amplifier. On the contrary, the result was found to be very positive.

Figure 8.2 features the same diagnostics as those we used previously to observe spatial chirp generated by the Offner stretcher. Comparing this figure to figure 8.1 on the preceding page shows immediately that the manifestations of spatial chirp have totally disappeared from the field. Both spatial dispersion and frequency gradient are down to unnoticeable levels in this new measurement. This behaviour is not formally explained at this time, but can be understood intuitively. As the spatially chirped seed pulse is amplified through its numerous passes in the gain amplifier, its spatio-spectral defects are iteratively smoothed out. Because multipass amplifiers are usually used near saturation, the spectrum of the output beam at each transverse position tend to become more uniform as it gets amplified.

An enlightening verification of this hypothesis, would be to perform the same TERMITES measurement we just presented, but for different number of passes in the multipass amplifier. If our hypothesis of gradual mitigation of the spatial chirp is correct, it should be possible to observe a slow reduction of spatial dispersion as the number of passes is increased. Numerical simulations of multipass amplification could also be helpful to understand more precisely our TERMITES measurement.

### 8.2.2. Gain Depletion in Chirped Pulse Amplifiers

The spatio-temporal characterization of BELLA laser beam proved that no strong coupling was affecting the electric field and that the peak intensity at focus was close to the expected value. Nevertheless, this measurement showed that the beam is not fully free of some small defects. The first defect that will be studied during this survey is a spectral fluence coupling which is created during the amplification process. It was measured by both TERMITES and INSIGHT during the characterization of BELLA [111].

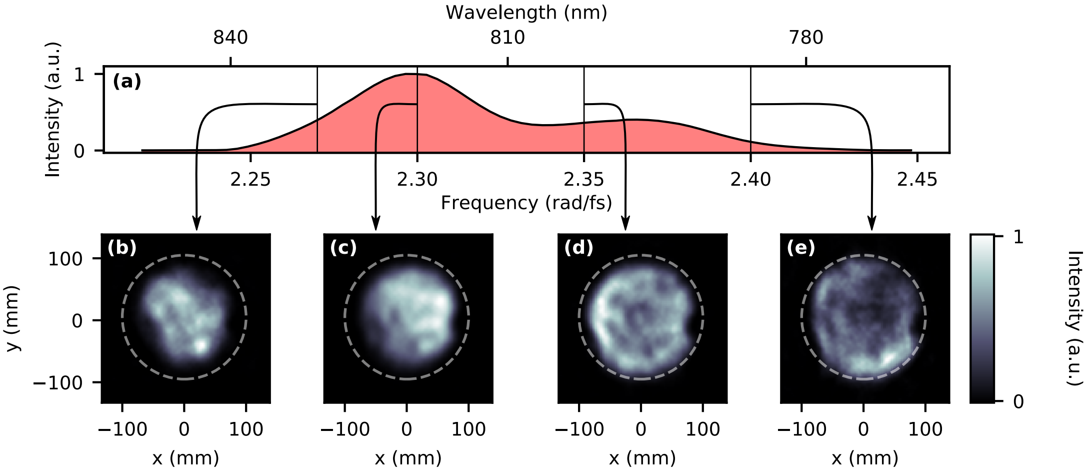

**Figure 8.3.: Spectral fluence of the full power BELLA beam as measured with INSIGHT. (a)** Spectral intensity, integrated spatially over the beam aperture. **(b)–(e)** Fluence profiles of the same quantity, taken at respectively 830, 820, 800 and 785 nm. Dashed white circle on panels (b)–(e) has a constant diameter, and provide a scale reference. To clearly highlight the spectral evolution of the beam spatial profile in these plots, the total energy in the beam at each frequency has been normalized following equation (8.1) on the next page.

Figure 8.3 illustrates the spectral fluence of the BELLA laser beam operating at full power, as measured by the INSIGHT device (described in section 2.3.2 on page 33). This picture shows that the beam profile is not spectrally constant, but evolves smoothly with laser frequency. In particular, we remark that the fluence profile can be qualified as top-hat around 830 nm (red side of the spectrum), and evolves to a ring shape around 780 nm (blue side of the spectrum). Furthermore, the diameter is also smaller for larger wavelengths before increasing for lower wavelengths. To observe more easily these effects, the views presented in figure 8.3 were normalized so that the energy is constant for each spectral sample:

$$\int \mathrm{d}x\mathrm{d}y\, \|\boldsymbol{E}(x, y, \omega)\|^2 = 1\,, \text{ for all } \omega. \tag{8.1}$$

We chose to use INSIGHT measurements in the current section to emphasize that this instrument is also very well capable of measuring the field of ultrashort pulses, and to diagnose complex spatio-temporal or spatio-spectral couplings. Even though TERMITES also measured the spatio-spectral intensity coupling featured in figure 8.3 on the preceding page, the images it provided for this particular case were a little less precise.

As this effect could not be explained by well-known sources of spatio-spectral couplings—like compressor or lenses—we looked for the culprit upstream in the laser chain. The amplification process taking place in the successive Ti:Sapphire amplifiers of the BELLA laser was studied in details by K. Nakamura at LBNL laboratory. Frantz-Nodvik equations [115] model the energy transfer from the population inversion of the medium (pumped by frequency-doubled Nd:YLF and Nd:YAG) to the amplified beam. They are used to compute numerically the profile of the output beam and of the gain medium at each passage through the amplifier.

Figure 8.4 shows slices of BELLA spectral fluence side-by-side. Panel (a) was generated from the amplification simulation while panel (b) is a slice of the quantity obtained experimentally with INSIGHT (figure 8.3 on the preceding page). This figure shows that the simulation is qualitatively very close to the experimental measurement. Both slices feature top-hat modes for low frequencies and ring shape for high frequencies, while beam diameter evolves linearly from 170 to 200 mm.

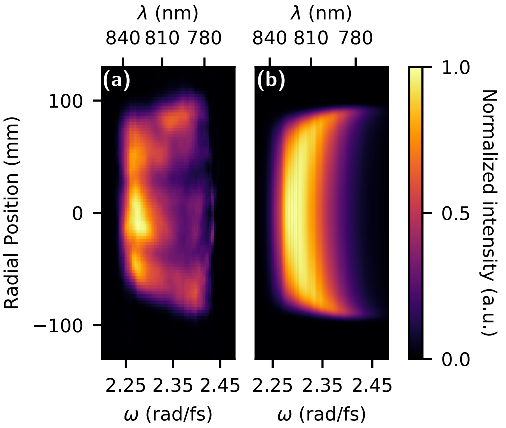

**Figure 8.4.: Spatio-spectral intensity of the full power BELLA beam. (a)** $(x, \omega)$ slice of the spatio-spectral intensity as measured by INSIGHT, taken across the horizontal plane and vertically centered. **(b)** Same quantity, now deduced from simulations of the CPA process based on the Frantz–Nodvik equations [115]. Both panel has been normalized following equation (8.1).

This spatio-spectral fluence coupling is very likely a direct side-effect of the Chirped Pulse Amplification technique. Figure 8.5 on the following page is a drawing which explains intuitively why the fluence profile of a chirped pulse can depend on the wavelength after its amplification. Fluence profile after amplification is a function of the seed profile and of the population inversion (or stored energy) profile in the gain medium. Considering that both quantities have radial Gaussian distributions at the beginning of the laser chain is a reasonable approximation that was used for the numerical simulations. When a chirped pulse is amplified, its leading edge (red part of the spectrum) depletes a fraction of the energy stored in the amplification medium (panel (a) in figure 8.5 on the next page). In the situation where the amplifier is in a saturated regime, more energy is depleted at the center of the beam because of the higher amplification gain. This affects the spatial distribution of population inversion *seen* by lower wavelengths in panels

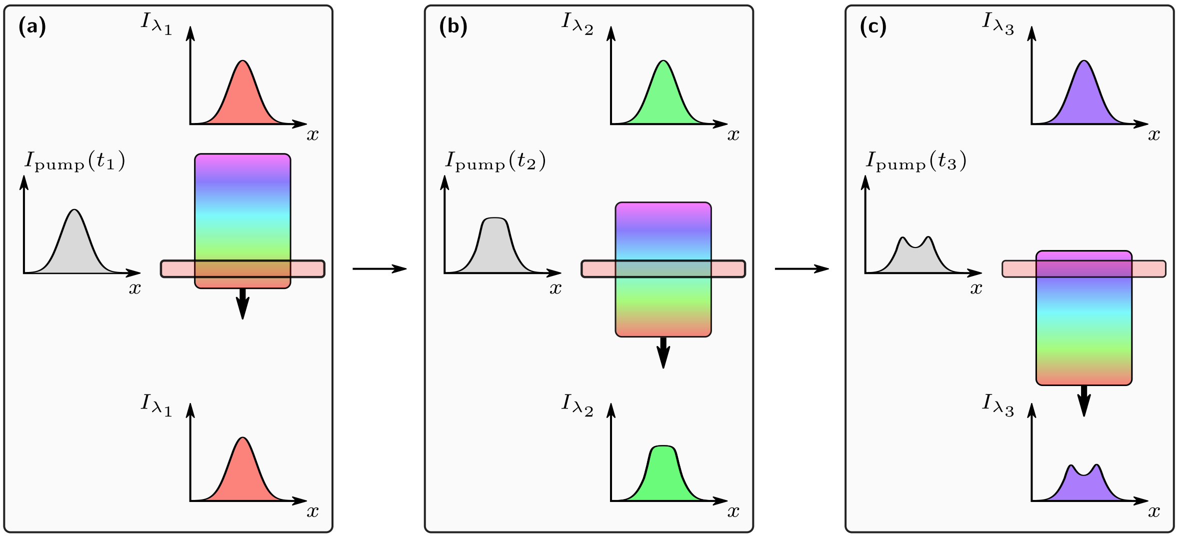

**Figure 8.5.: Sketch of a chirped pulse going through the gain medium of a laser amplifier.** This drawing shows a chirped pulse in the process of being amplified by a pumped Ti:Sapphire crystal. **(a)** Because the input beam is positively chirped, red components of the laser spectrum are amplified ahead. **(b)–(c)** As lower wavelength go through the amplifying medium, the population inversion profile is more depleted at the center than on the edges. Output fluence profiles at those lower wavelength is not Gaussian anymore.

(b)–(c) and hence modifies the fluence profile for those components. This spatio-spectral fluence coupling is strongly linked to the CPA scheme because it could not happen if all frequencies were amplified at the same time. It can be considered as a spatio-spectral extension to the traditional CPA-specific red-shift effect [116, 117]. Red-shift in CPA lasers is indeed well-understood, but has always been described solely in the spectral domain to the best of our knowledge.

## 8.3. Effects of Beam Imaging

### 8.3.1. Telescope-induced Pulse Front Curvature

As described formally in section 2.2.2 on page 26, Pulse Front Curvature (PFC) is a spatio-temporal intensity coupling which adds a delay between the phase front and the pulse front of the beam. This delay depends quadratically on the distance from the center of the beam, curving the pulse front spatio-temporally. As we already observed experimentally in section 6.3.1 on page 94, PFC is the temporal consequence of chromatic curvature, wherein the wavefront curvature depends linearly on angular frequency.

The infrared laser beam of LASERIX was characterized in a set-up which is illustrated in figure 8.6 on the facing page. We already mentioned this particular laser beam in section 2.2.1 on page 24 to show an example of Pulse Front Tilt and in section 8.4.3 on page 122 to illustrate some spatio-spectral intensity couplings. It will be used one last time to demonstrate how telescopes can generate significant amounts of Pulse Front Curvature in specific conditions. Figure 8.6 on the next page displays the telescope $L_1$–$L_2$ which is placed after the last Ti:Sapphire amplifier to reduce fluence on compressor optics in order to avoid optical damage. Telescope

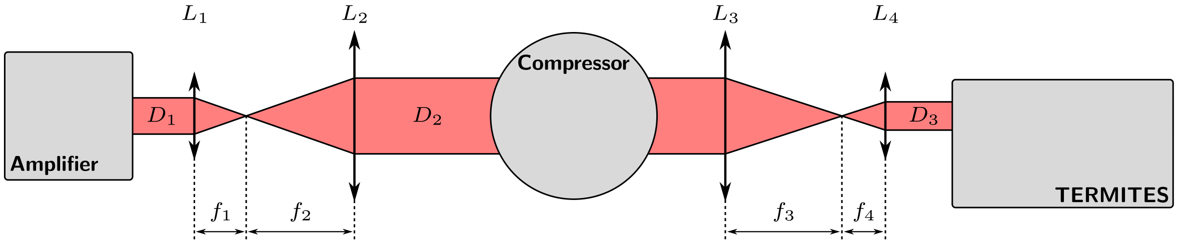

**Figure 8.6.: LASERIX measurement layout.** $L_1$ and $L_2$ are converging singlets forming a magnifying telescope that is used to avoid optical damages in the compressor. $L_3$ and $L_4$ are achromatic converging doublets used to reduce the beam size and characterize the input beam profile in whole with TERMITES. Values are detailed in table 8.1. The TERMITES device we used in this measurement is the new prototype that was described in more details in section 4.2.2 on page 73.

$L_3$–$L_4$ is composed of achromatic lenses and is used to reduce the diameter of the beam before its characterization with TERMITES. We verified that this telescope adds a negligible amount of PFC in the characterized beam by numerical ray-tracing in section 7.2 on page 104.

| | |
|---|---|
| $D_1$ | 22.4 mm |
| $D_2$ | 50.0 mm |
| $D_3$ | 16.7 mm |

| | |
|---|---|
| $f_1$ | 340 mm |
| $f_2$ | 760 mm |
| $f_3$ | 750 mm |
| $f_4$ | 250 mm |

| | |
|---|---|
| $L_1$ | Convergent singlet, fused silica |
| $L_2$ | Convergent singlet, fused silica |
| $L_3$ | Convergent achromatic doublet |
| $L_4$ | Convergent achromatic doublet |

**Table 8.1.: LASERIX measurement parameters**

Panel (a) of figure 8.7 on the next page features vertical slices of the phase of the LASERIX beam, as measured by TERMITES. Visually, the phase plots seem curved for peripheral spectral components (2.27 and 2.35 rad/fs), and the curvature evolves smoothly while its sign changes at the central frequency. Of course, curvature is not the only phase component because some other aberrations are visible in the spatial phase, albeit smaller in magnitude. In order to characterize quantitatively the potential chromatic curvature, each phase slice is fitted with a second order polynomials, and the resulting second order coefficients are plotted on panel (b) as a function of optical frequency. This second plot definitely shows that the chromatic curvature observed on panel (a) generates Pulse Front Curvature in the time domain, because the second order component evolves linearly with frequency. Moreover, this linear dependence was fitted and the resulting slope of 0.067 $\mathrm{fs/mm^2}$ represents immediately the Pulse Front Curvature quantity. For the considered beam diameter of 50 mm, it corresponds to a maximum delay of 41 fs on the edge of the laser beam.

Let us determine the source of this significant spatio-temporal coupling. PFC is generally added to a laser beam by suboptimal Keplerian telescopes [76, 98, 112, 113]. Owing to our previous analysis of the telescope $L_3$–$L_4$ that was inserted before TERMITES to reduce the beam—section 7.2 on page 104—the next suspected element is the telescope $L_1$–$L_2$ which is placed just before LASERIX compressor. As noted in table 8.1, this telescope is made of plain fused-silica singlets. The PFC that is inserted by such a simple system can be computed using a model obtained by Z. Bor [76] (equation (43)) and does not require to do any complex ray-tracing.

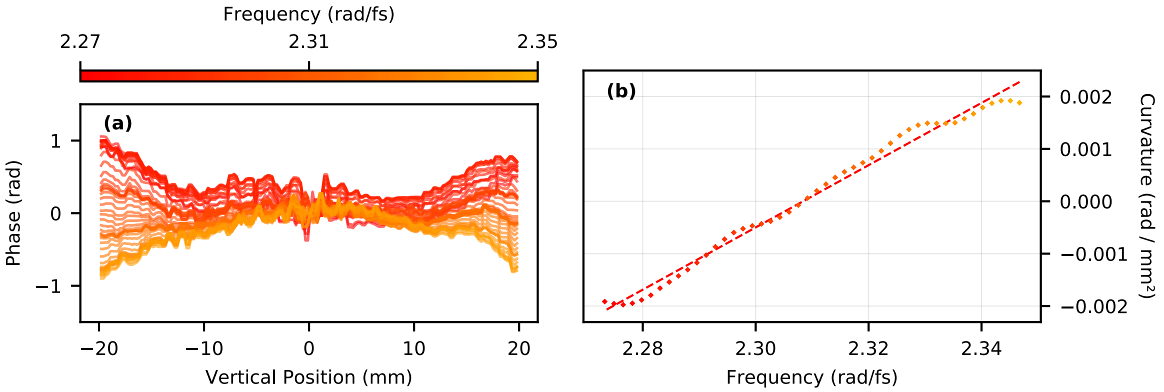

**Figure 8.7.: Quantitative measurement of telescope-induced Chromatic curvature on LASERIX. (a)** Line-outs of the measured spatial phase at different optical frequencies, resolved along the vertical dimension and taken at the center of the beam. **(b)** Second order coefficients of polynomial fit done on the line-outs in panel (a). The linear fit of these curvatures is shown as a red dashed line and its computed slope is $0.067\,\mathrm{fs/mm^2}$.

At transverse position $\boldsymbol{r}$, Pulse Front Curvature adds the delay $\Delta\tau(r)$ to the pulse:

$$\Delta\tau(\boldsymbol{r}) = \frac{\|\boldsymbol{r}\|^2}{2\,c\,f_2\,(n-1)}\left(-\lambda_0\frac{\mathrm{d}n}{\mathrm{d}\lambda}\right)\left(1+\frac{1}{M}\right), \tag{8.2}$$

with $c$ the speed of light, $f_2$ the focal length of lens $L_2$, $n$ and $\frac{\mathrm{d}n}{\mathrm{d}\lambda}$ the refractive parameters of fused-silica [118], $\lambda_0$ the central wavelength of the laser beam, and $M$ the telescope magnification.

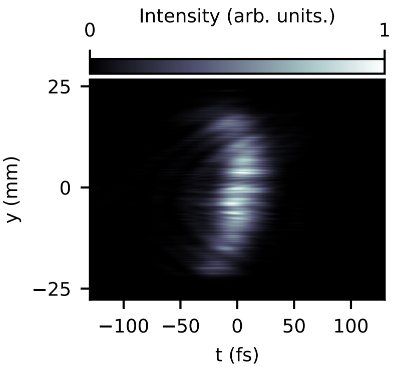

**Figure 8.8.: Spatio-temporal slice of *Salle Jaune* laser beam intensity.**

Equation (8.2) gives a maximum delay of 58 fs at the edge of the laser beam, when computed with the parameters of the system. This number is very close to the measured value of 41 fs measured with TERMITES. The similarity between this model computation and the measurement by TERMITES makes our hypothesis very convincing.

As we said earlier, the impact of spatio-temporal couplings on the LASERIX infrared beam is probably very limited due to the particular applications for this laser. Because the laser is routinely stretched in time and used in the picosecond regime, the delay of 50 fs that we measured on the edges of the beam is insignificant. Nevertheless, this measurement is a strong proof that TERMITES is capable to reliably quantify Pulse Front Curvature and that we are able to detect it without any prior knowledge that such coupling is present in the beam.

At the beginning of this thesis, Pulse Front Curvature was also measured on the 60 TW femtosecond laser beam of *Salle Jaune*, at *Laboratoire d'Optique Appliquée* (LOA). Even though the measurement set-up was not optimal at this time, figure 8.8 shows that the measured pulse front was noticeably curved. The delay value is approximately 40 fs at the edge of the beam ($y = 25\,\mathrm{mm}$), which equals approximately to a PFC of $0.064\,\mathrm{fs/mm^2}$. As this measurement was done with the first prototype of TERMITES—80 mm aperture, see section 4.2.2 on page 73—

extracted data is noisy and less reliable than the LASERIX measurement. Nevertheless, the source of this PFC was successfully identified following our measurement. Similarly to the case of LASERIX, it was found that the magnifying telescope before the compressor was responsible for excessive PFC. This aberration was fixed later by using a custom compensating afocal doublet, based on the set-up presented in figure 6.5 on page 94.

## 8.4. Effects of Pulse Compression

### 8.4.1. Pulse Front Tilt

Pulse Front Tilt (PFT) is probably the most familiar spatio-temporal coupling that can be induced in optical systems which rely on spatial dispersion, i.e., stretcher or compressor. As it was explained in section 2.2.1 on page 24, Pulse Front Tilt usually results from angular chirp not being fully compensated at the output of these laser chain elements. As a result, wavefront tilt—which defines the direction of propagation of the pulse—varies linearly with frequency.

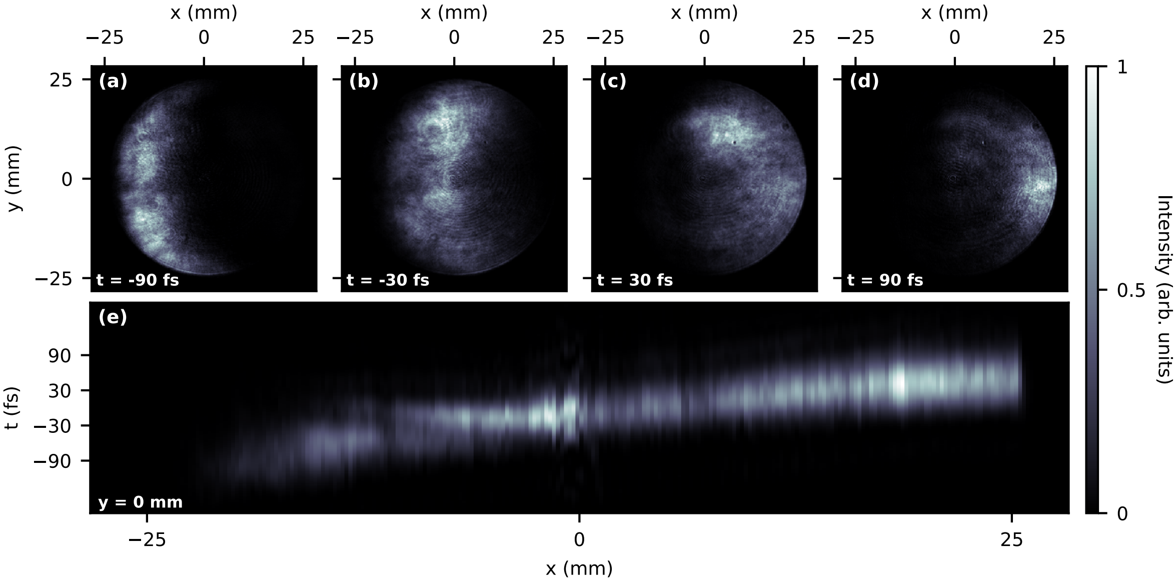

**Figure 8.9.: Measurement of Pulse Front Tilt on LASERIX pump laser beam. (a)–(d)** Fluence profile of the measured beam, at different times throughout the pulse duration. **(e)** Slice of the same pulse, viewed from the side and resolved along vertical position and time. In order to better see the delay added by PFT, we imposed a flat spectral phase to simulate a perfect compression of the pulse in time.

Because of the general awareness about angular dispersion effects on the laser peak intensity at focus, this first-order spatio-temporal coupling was generally insignificant on the systems we characterized. Full 3D reconstruction of the electric field is usually not necessary to measure residual angular dispersion. The spatial chirp generated in far-field spreads the spectrally-integrated beam profile (measured by a simple camera) in the PFT direction (vertically, horizontally, or a combination of both). Minimizing the focal spot ellipticity by rotating the gratings is generally considered sufficient to remove most of the remaining angular dispersion at the compressor's output. Some users also use a few narrow bandpass filters to look at the lateral drift of the focal spot depending on the considered wavelength.

Yet, we managed to measure with TERMITES an important amount of residual Pulse Front Tilt at the compressor output of LASERIX. The purpose of this infrared beam is creating a plasma channel on the surface of a metallic target, which is then used as an amplification medium for X-UV laser generation. This particular application does not require the driving laser to operate fully compressed, nor to have absolutely zero horizontal Pulse Front Tilt. That is justified because the laser is focused on the target at a grazing incidence, which makes the focal spot already very elliptic.

Figure 8.9 on the previous page illustrates the spatio-temporal intensity profile of the LASERIX laser. At explained at the beginning of this thesis (section 2.2.1 on page 24), Pulse Front Tilt adds a delay which depend linearly on the position (in the present case, $x$). This measurement features a very high value of PFT equivalent to 180 fs over the 50 mm width of the beam, or 3.6 fs/mm. Panels (a)–(d) show distinctly how the intensity is located on the left of the beam at the beginning of the pulse, and on the right of the beam at the end.

## 8.4.2. Distortions Caused by Surface Defects of Compressor Optics

### Spatio-Temporal Phase Couplings Observed on UHI–100

As this has been explained in section 2.2.3 on page 28, more complex phase couplings arise when mirrors or gratings in stretcher or compressor are not perfectly flat. The first measurement of space-time couplings that was done with TERMITES [43] featured a perfect example of such high spatial frequency phase defect depending on the laser wavelength. Figure 8.10 displays the crescent shape that was observed in phase on UHI–100 laser beam profile.

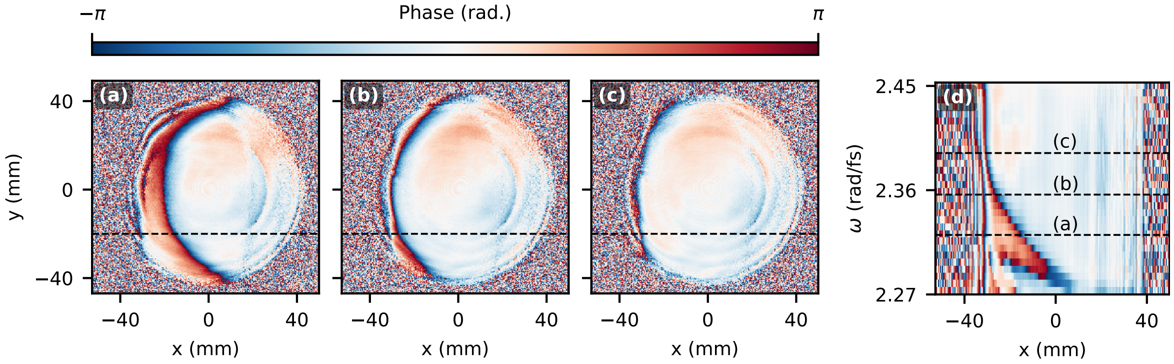

**Figure 8.10.: UHI–100 spatio-spectral phase defect. (a)–(c)** Wavefronts at 812, 800 and 788 nm. **(d)** Spatio-spectral intensity profile taken along a centered horizontal slice, represented by dashed horizontal lines on panels (a)–(c). White dashed vertical lines are frequencies corresponding to (a)–(c) panels. This measurement was carried out by G. Pariente's during his thesis [42]. Corresponding raw data were processed for this figure using the most recent algorithm developed during my thesis.

Wavefront distortion visible in figure 8.10 was studied extensively in G. Pariente's thesis [42]. It consists of a crescent-shaped phase defect affecting the wavefront at some specific wavelengths, on the red side of UHI–100 spectrum. As shown by panels (a)–(c), the defect moves inwards as wavelength increases. This lateral shift produces a phase streak visible in the spatio-spectral view of panel (d).

During the beginning of my thesis, I looked further for the root cause of this defect. This investigation lead us to characterize the flatness of periscope mirrors in the compressor, which were the principal elements suspected to cause the distortion. Flatness measurement was realized using a large aperture wavefront sensing device, composed of a commercial quadriwave lateral shearing interferometer [30] (Phasics SID4™) and of an all-reflective magnifying telescope that was provided by Amplitude Laser. This set-up operates at 800 nm which was a necessary condition to perform the measurement, due to the bandpass of mirrors reflection coatings.

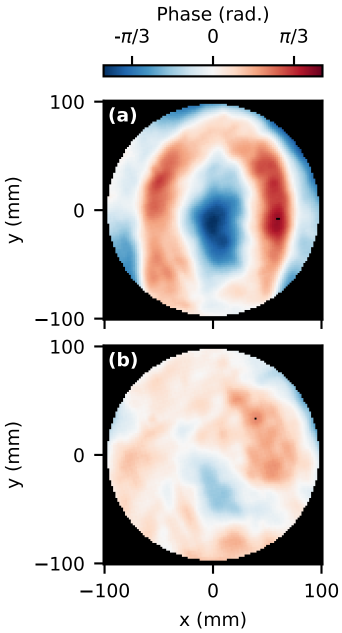

**Figure 8.11.: Flatness measurement of UHI–100 periscope mirrors.** **(a)** Initial total wavefront ($0.84\pi$ rad peak-to-valley). **(b)** Total wavefront after upper mirror replacement ($0.41\pi$ rad peak-to-valley).

Figure 8.11 displays the results from this flatness measurement. Panel (a) shows that the wavefront aberrations added by the compressor periscope are far from being negligible. The characterization device returns a peak-to-valley value of $0.84\pi$ rad at 800 nm (or 335 µm). This measurement corresponds to the summation of the aberrations introduced by the upper periscope mirror and of the lower periscope mirror. Although the peak-to-valley value of the measured wavefront is not as high as the $2\pi$ crescent-shaped phase error measured with TERMITES, the aberration is shaped similarly. In order to make sure that this imperfect flatness of the periscope mirrors was indeed the source of our spatio-spectral coupling, we decided to replace the two 20 × 20 cm mirrors by mirrors of higher quality.

Panel (b) of figure 8.11 shows the second wavefront measurement that was done just after having changed the mirrors of the periscope. This new picture clearly shows that the wavefront is much less aberrated than it was before changing the mirrors. Indeed, the new value of peak-to-valley phase error is $0.41\pi$ rad at 800 nm (or 170 µm). The periscope was installed back at its position in the compressor after this modification. A TERMITES measurement done after the compressor showed that the crescent-shaped defect was not affecting the beam profile anymore, as it was the case with the initial mirrors (figure 8.10 on the facing page).

### Spatio-Temporal Phase Couplings Observed on BELLA

A similar streak effect was measured on the spatio-spectral phase of the BELLA petawatt laser beam during its characterization with TERMITES [111]. Contrarily to the crescent-shaped defect affecting the beam profile of UHI–100, the modulations which are visible on BELLA profile have a high spatial frequency and are allotted uniformly on the beam profile, as shown in panel (a) of figure 8.12 on the next page. They are however much smaller in magnitude—$\approx \pi/4$ rad peak-to-valley—than the defect observed on UHI–100—$\approx 2\pi$ rad peak-to-valley.

As the considered wavelength increases, the spatial phase modulations move towards the left side of the beam profile. This linear translation creates—as it was also the case for UHI–100—linear phase streaks which this time affect all frequencies and all positions of the beam profile.

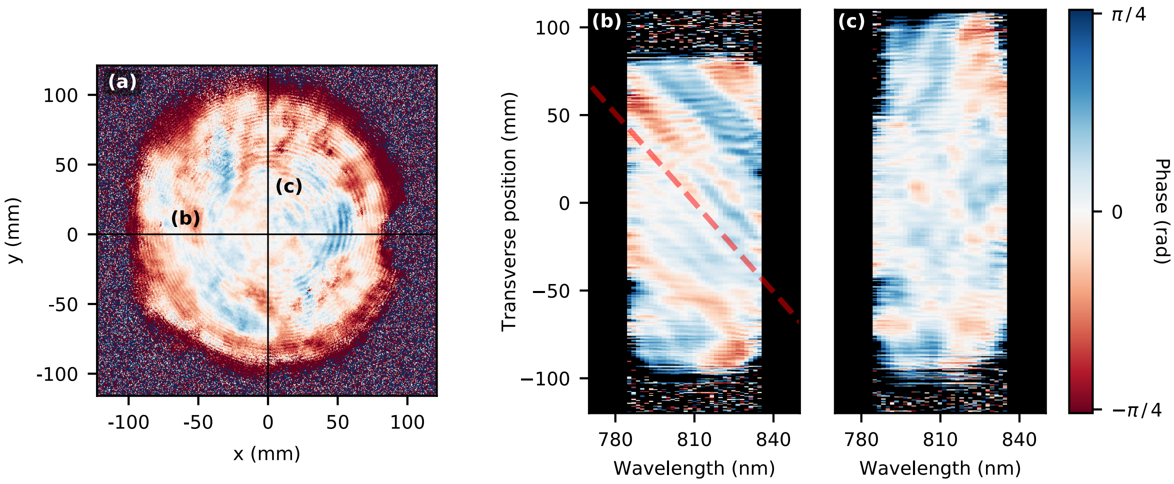

**Figure 8.12.: Spatio-spectral phase of the collimated BELLA beam, measured with TERMITES.** **(a)** BELLA wavefront observed at central wavelength $\lambda_0$. **(b)** Spatio-spectral view of the phase in the $(x, \omega)$ space taken along the horizontal black line in panel (a). Oblique red line represent the expected slope of the streak that would be induced by spatial defects of optical elements located within the compressor, given BELLA compressor characteristics. The origin of this line is arbitrary. **(c)** Spatio-spectral view of the phase in the $(y, \omega)$ space taken along the vertical black line in panel (a). The spectrally integrated wavefront was removed from all panels in order to see exclusively components of the phase that depend on wavelength.

The translation of the phase pattern is exclusively occurring in the dispersion plane of the compressor. Therefore, the linear streak pattern is only visible in the horizontal $(x, \omega)$ space (panel (b)) and not in the $(y, \omega)$ space (panel (c)).

In section 2.2.3 on page 28, we discussed about the effects at focus of such spatio-spectral couplings. Analytically, they create satellite focal spots that are shifted laterally with respect to the main spot. These satellites are also shifted in time and create an intensity pedestal, which could cause detrimental effects in the laser-matter interaction. The exact effect for BELLA should be characterized in more details to define if the pedestal created in this particular case is an issue for experiments. Since BELLA is mostly used for electron wakefield acceleration in capillary plasma discharge, this effect could be benign at focus if satellite spots are sufficiently separated from the main spot and do not couple in the fiber.

### 8.4.3. Spatio-spectral Profile Masking

Additionally to spatio-temporal couplings in phase, stretchers and compressors can also add amplitude couplings to the laser beam. In section 2.2.3 on page 28, we showed that any element masking the beam in presence of spatial chirp can create amplitude couplings by clipping differently each component of the laser spectrum. Throughout the characterization of different laser systems done during this work, we noticed that this kind of coupling was recurrent.

Figure 8.13 on the facing page illustrates spatio-spectral profile masking as observed with TERMITES on the LASERIX beam. A vertical shade starts to appear on right hand side of the beam at 815 nm and slides in the fluence profile for lower wavelengths, until 800 nm where it

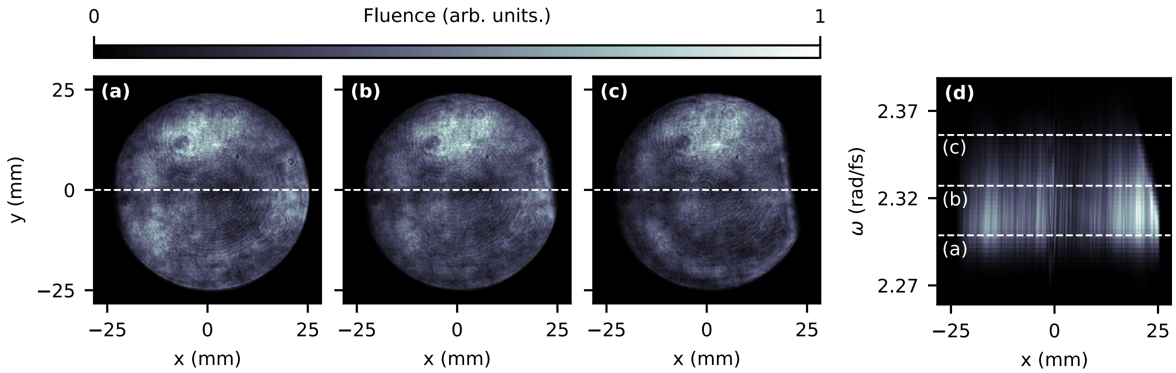

**Figure 8.13.: Spatio-spectral profile masking caused by misalignment of LASERIX compressor. (a)–(c)** Fluence profiles at 820, 810 and 800 nm. **(d)** Spatio-spectral intensity profile taken along a centered horizontal slice, represented by dashed horizontal lines on panels (a)–(c). White dashed vertical lines are frequencies corresponding to (a)–(c) panels.

masks 5 mm of the beam. This dependence of the edge position with laser wavelength produces a linear streak in panel (d) of figure 8.13.

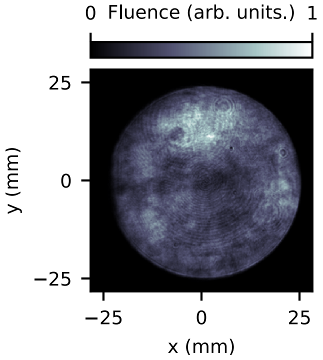

**Figure 8.14.: Spectrally integrated profile of LASERIX beam.**

The issue is hard to distinguish without any spatio-temporal diagnostic tool. As shown by figure 8.14, the fluence profile integrated over the laser spectrum seems normal and would not trigger suspicion. Near-field profile diagnostics are ubiquitous on laser systems and are generally simply made of silicon-based cameras. This much more precise measurement allowed the LASERIX team to locate the misalignment in the compressor and fix the issue by re-centering the beam on compressor optics.

UHI–100 laser also has a spatio-spectral profile masking which is small but measurable with TERMITES (see [43]). In the case of this system, wider mirrors would be necessary to fit the whole expanded beam in the compressor periscope.

Figure 8.15 on the next page is based on a measurement that was done just after compressor re-alignment on LASERIX. This figure can be compared to figure 8.13 to check that the spatio-spectral masking that was identified is correctly removed. Looking at panels (a)–(c), no vertical edge can be observed on the right side of the beam profile. No linear streak is visible at the top of panel (d) either, as it was the case previously.

However, this alignment correction added a new spatio-spectral coupling that is fainter than the previous one. For this reason, figure 8.15 on the next page does not display fluence profiles anymore but amplitude profiles, for which the visibility of the distortion is better. The new coupling can be seen as a diffuse shape on the left side of panel (a) and as a linear streak at the bottom-left side of panel (d). Because the only modification between this measurement and the previous one was the compressor re-alignment, we knew that this issue was coming from one of the compressor components.

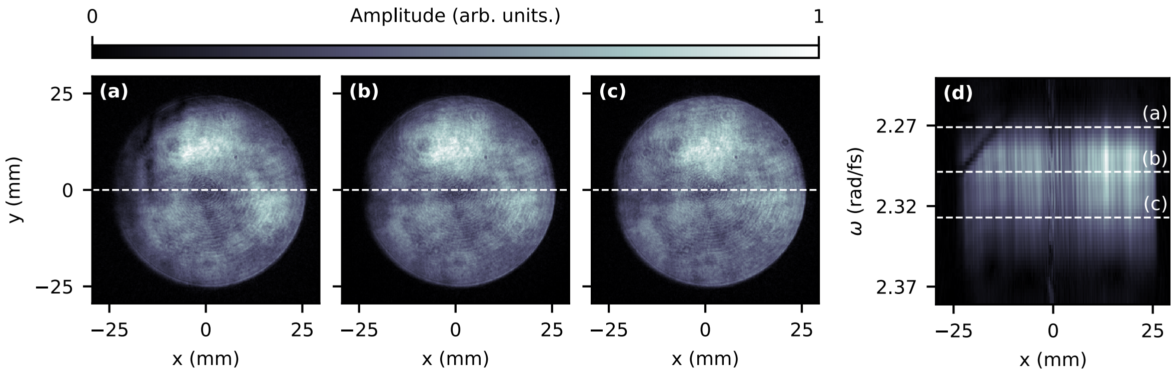

**Figure 8.15.: Amplitude profile degradation caused by coating defects on dielectric mirrors of LASERIX compressor. (a)–(c)** Fluence profiles at 830, 820 and 810 nm. **(d)** Spatio-spectral intensity profile taken along a centered horizontal slice, represented by dashed horizontal lines on panels (a)–(c). White dashed vertical lines are frequencies corresponding to (a)–(c) panels.

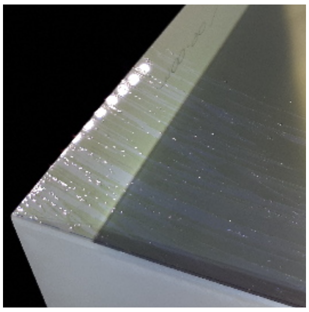

**Figure 8.16.: Coating peeling off from periscope mirror substrate.**

After visual inspection, the defect was found to originate from a degraded mirror. As shown in figure 8.16, its dielectric reflective coating was peeling off from the substrate, as it can sometimes happen for such mirrors exposed to high vacuum. This defect probably went unnoticed first because it was only affecting one side of the periscope mirror, while the beam was offset on the other side of the mirror. Our small alignment correction made the defective part of the mirror enter in the beam path. After having replaced this bad mirror with a fresh spare, a third TERMITES measurement was done, revealing no major spatio-spectral amplitude coupling.

Similarly to the previous results featured in this chapter, this fine defect could not have been detected with a low resolution spatio-temporal device, let alone with an achromatic one. Among the different devices listed in table 2.2 on page 35, TERMITES was the best suited instrument for this task, to the best of our knowledge.

## 8.5. Effects of Hollow-Core Fiber Compression

As we explained in section 1.1.2 on page 11, Hollow-Core Fiber (HCF) compressors are increasingly used at the end of ultra-high intensity laser chain to further compress ultrashort pulses in time. This is done by taking advantage of Self Phase Modulation (SPM) which reduces the Fourier-transform limited duration of the pulse by broadening its spectrum. The method essentially dwells in focusing pulses in a meter-scale hollow fiber, filled with noble gas at a controlled pressure. Compression in HCF results in millijoule-level few-cycle pulses, produced by medium scale facilities such as the *Salle Noire* laser located in *Laboratoire d'Optique Appliquée* [119].

Some spatio-temporal characterization studies of HCF compressed beams [120–122] were already conducted and used SEA-SPIDER and STARFISH devices. They did not show any strong aberration generated by this non-linear technique in optimal operating conditions. Yet, we decided to use TERMITES to characterize the set-up installed in *Salle Noire*, in order to study the generated beam with finer details (see figure 8.17). We also wanted to study the effect of small fiber-coupling misalignments which, to the best of our knowledge, had not been characterized before. Finally, the 300 nm wide spectrum provided a very good opportunity to test the bandwidth limits of TERMITES and validate its specifications.

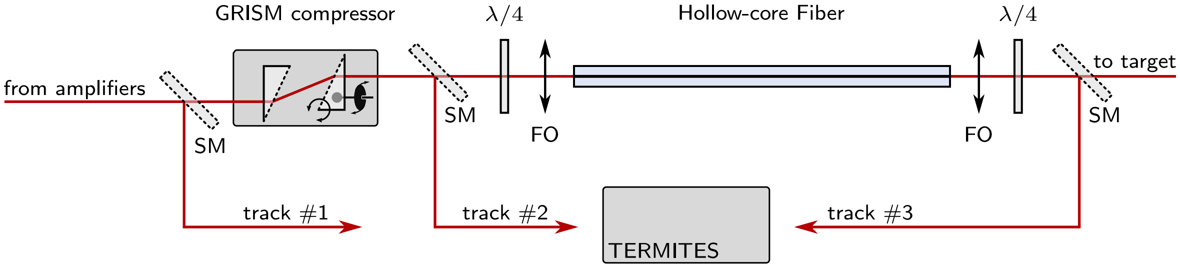

**Figure 8.17.: Layout of the HCF compressed beam characterization at *Salle Noire*.** Three different paths were installed and used to characterize the beam at relevant positions in the set-up. Quarter-wave plates are designed to control the polarization in the HCF and improve the SPM process. Energy levels at the entrance of TERMITES were adjusted using uncoated wedges and optical densities which are not represented on this drawing. **SM**: Temporary sampling mirrors. **FO**: Focusing optics.

### 8.5.1. Spatially Resolved Spectral Broadening

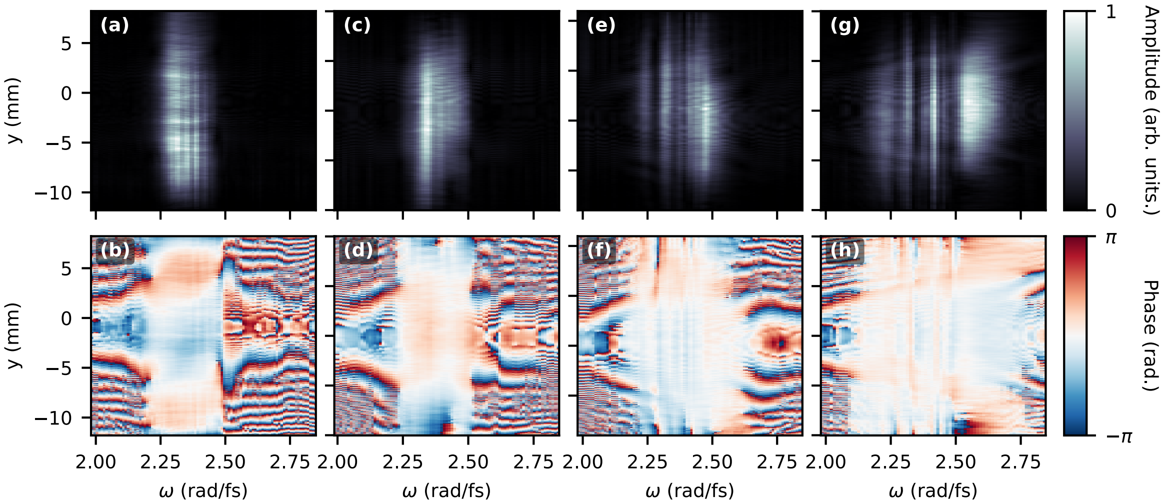

**Figure 8.18.: Effect of pressure increase in the HCF. (a)–(b)** Amplitude and phase of the beam before entering HCF. **(c)–(d)** Amplitude and phase of the beam after HCF, without gas. **(e)–(f)** Amplitude and phase of the beam with 400 mbar of helium. **(g)–(h)** Amplitude and phase of the beam with 800 mbar of helium.

Figure 8.18 shows slices of the spatio-spectral amplitude and phase retrieved from sampling track #2, and from sampling track #3 with different levels of gas pressure in the HCF. Amplitude profiles in panels (c), (e) and (g) show that the spectral broadening is correctly measured with TERMITES, and that the spectrum width is significantly increasing with helium pressure in the fiber. Phase is correctly obtained for frequencies where the signal is sufficiently high, and becomes dominated by noise for frequencies of low intensity. Furthermore, no strong spatio-spectral coupling is visible on the profiles, as all spectral modulations affect identically all positions in space. Interestingly, some spatially homogeneous spectral modulations are perceptible on panel (a), which represent the amplitude profile measured after the grism compressor. This feature is symptomatic of a pre-pulse or post-pulse that would be generated by a bad optical element. This ghost pulse seems to be filtered out by the fiber, as shown by panel (c) were no modulation is visible anymore.

The first obstacle for measuring this kind of wide spectrum beam is the bandpass of optics used in TERMITES. The prototype that was used for this measurement is described in table 4.3 on page 74. Optics and design were not modified specifically for this experiment. Consequently, the amplitude profiles shown in figure 8.18 on the preceding page are most certainly the product of the actual physical spectrum, and the spatially homogeneous response of the TERMITES device. Even though this issue should be taken into account for the interpretation of the results, it affects similarly the spectrum for all positions. Therefore, spatio-spectral properties of the beam can still be interpreted, as long as phase noise is not predominant.

Another difficulty to characterize such modulated spectrum with TERMITES is the curvature removal operation—of which the details were explained in section 3.2.2 on page 52. Fitting the curvature should be done at a frequency where the signal is the highest, to ensure that phase noise is low and that the correct curvature is removed from the field. The simplest way to do that is to process the data with default parameters ($\lambda_0 = 800\,\mathrm{nm}$ for instance) in order to obtain the power density function of the field, and then use this information to process the raw signal a second time with a new adjusted curvature fit frequency.

### 8.5.2. Effect of Spatial Chirp on Fiber Coupling

Lastly, let us study the effect of misalignment of the grism-based compressor—represented on figure 8.17 on the preceding page—on the HCF post-compression process. This setup is based on a pair of so-called grisms (contraction of grating–prism) [123], which are prisms where one face presents regularly spaced grooves, forming a transmission grating. The grism-based compressor is used in *Salle Noire* to precisely control dispersion of the beam before it enters the HCF fiber. This is crucial because SPM is a non-linear process which highly depends on pulse intensity.

Alignment of the compressor is very sensitive. Any deviation from optimal alignment settings adds complex aberrations to the beam and have the principal effect of changing the focal spot shape and size at the entrance of the HCF. In severe cases, the coupling efficiency can be significantly decreased and the fiber entrance can be damaged. To prevent this, the far-field fluence profile is actively monitored. Before sending the beam to the HCF, users check that the Strehl ratio is higher than a fixed safety threshold and adjust alignment if required.

During our measurements with TERMITES, we looked particularly at potential spatio-spectral defects that could appear when the alignment of the grism compressor is in compliance with safety standards, but still sightly sub-optimal. To do this, we played with two rotation axes of the last grism, represented by arrows on figure 8.17 on the previous page. Both rotations add a combination of different defects to the beam. However, rotation around the propagation axis is known to particularly add vertical Pulse Front Tilt (PFT), while change of the incidence angle principally adds horizontal PFT. At focus, rotation of the second grism around those two axis adds vertical or horizontal spatial chirp.

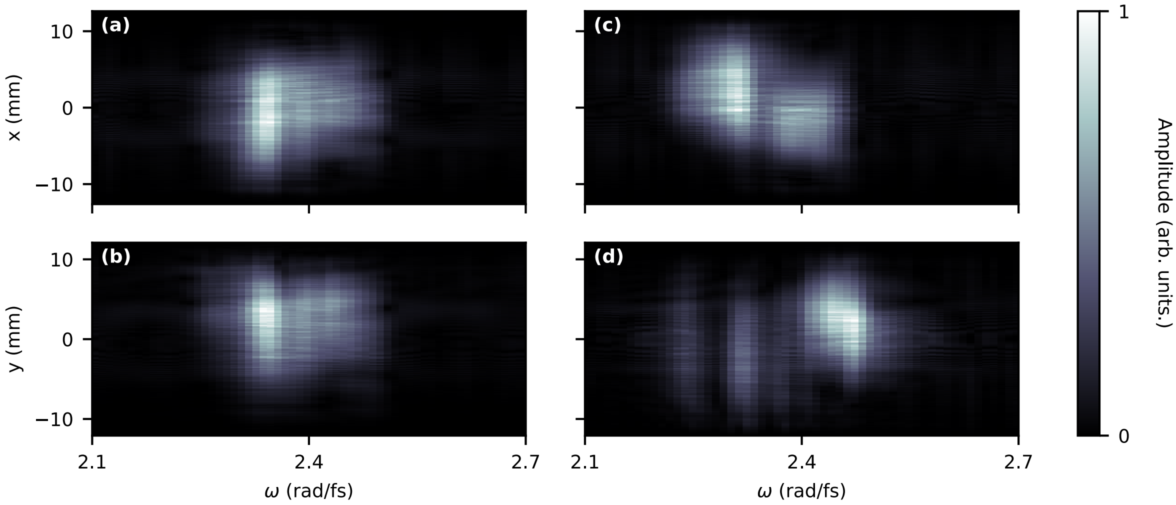

**Figure 8.19.: Effect of Grism misalignment on the HCF output field. (a)–(b)** Horizontal and vertical slices taken from the spatio-spectral amplitude profile at the output of the fiber, when the grism compressor is optimally aligned. **(c)** Horizontal slice of the same quantity, when the grism compressor is slightly misaligned in the horizontal direction. **(d)** Vertical slice of the same quantity, when the last prism of the grism compressor is slightly rotated around the incidence axis. All measurements are done without any gas in the fiber, except for panel (c) where some unwanted residual pressure slightly broadened and modulated the spectrum.

Figure 8.19 shows relevant slices taken from datasets that we acquired for this study. The four panels represent amplitude profiles resolved spectrally and along the horizontal or vertical position. Panels (a)–(b) show that the spectrum of the HCF output is uniform along the vertical and horizontal dimensions when alignment of the GRISM compressor is optimal.

Panels (c)–(d), for their part, show that the amplitude distribution in space depends strongly on frequency when the GRISM compressor is slightly misaligned. More particularly, horizontal spatial chirp at the entrance of the fiber is translated into horizontal spatial chirp at the output of the fiber (panel (c)), and the same is true for vertical spatial chirp (panel (d)). This effect occurs with very small misalignment values, that were of the order of magnitude of the micrometer drive hysteresis and hardly measurable. PFT values measured by TERMITES just after the GRISM compressor (track #2, in figure 8.17 on page 125) were close to zero and below the sensitivity level of our instrument.

Albeit current diagnostics installed at *Salle Noire* allow for a careful HCF coupling and avoid permanent damages, they are not very sensitive to small amounts of spatio-spectral defects such as angular dispersion. We showed with TERMITES that such angular dispersion is capable of creating significant spectral fluence couplings at the output of the fiber, which are susceptible in turn to generate spatio-spectral couplings on target. This study therefore demonstrates that a spatio-spectral understanding of the whole HCF compression is necessary, in addition to the traditional far field monitoring.

⁂

This last chapter is a comprehensive survey of the most common spatio-temporal and spatio-spectral couplings encountered throughout the experimental activities of my thesis. Spatio-temporal measurements, when executed at different positions of the laser chain, allowed to find the precise source of couplings. The amount of measurements carried out for each optical component is not sufficient to conclude about the occurrence frequency of each defect, and to generalize these findings. Nevertheless, this survey shows that all of the systems we characterized during this work were affected by couplings, which, most often, could not be anticipated using standard metrology. TERMITES proved to be a very precise and practical tool for this task, because it provided the full electric-field of the measured beam, allowing us to compute lots of different diagnostic quantities in each situation.

Couplings were sorted depending on the component responsible for each of them. We started the chapter by showing that Offner stretchers are capable of introducing significant amounts of spatial chirp in femtosecond beams (section 8.1, p.112), but that subsequent amplifiers tend to mitigate this effect (section 8.2, p.113). Then, we showed the spatio-spectral effect that can be induced by saturated amplifiers. We also showed that improper design of magnification telescope can induce a noticeable quantity of chromatic curvature and create Pulse Front Curvature in the temporal domain (section 8.3, p.116). More complex couplings were presented and involved compressors (section 8.4, p.119). They were caused by either misalignment, or bad surface quality of optics. Finally, we observed what spatio-spectral couplings could be measured at the output of HCF compressors, and found that very small amounts of spatial chirp at the input of the fiber had an influence on its spatio-spectral output profile (section 8.5, p.124).

# Conclusion & Perspectives

---

Spatio-temporal couplings are ubiquitous in high-power femtosecond laser systems. As we showed in part I (p. 9), they have a strong influence on ultra-intense experiments by significantly reducing the effective intensity on target. In order to assert the quality of a laser system, it is necessary to dispose of a simple device capable of providing users with the complete, spatio-temporally resolved, electric field of ultrashort pulses. Yet, none of the existing spatio-temporal techniques have been widely adopted in the community of ultrashort broadband lasers so far. Moreover, most of them are difficultly adaptable to large diameter laser systems. The essential prerequisites for a measurement technique to become a standard—apart from visible publications—are its precision, robustness, and scalability to many different systems. Just before the beginning of my work, a proof-of-concept of TERMITES had been developed by V. Gallet and G. Pariente during their respective thesis [41, 42], and was used for the first characterization of a multi-terawatt laser system [43]. At this point, the technique was very promising because of the simplicity of its implementation and the high resolution of its results. In order to make of TERMITES a new reference tool for spatio-spectral laser characterization, Amplitude Laser Group joined CEA LIDYL to co-supervise and fund my thesis. I chiefly benefited from this opportunity to study and improve the technique. These tasks constitute the industrial part of my work and were documented in part II. The other essential objective was more academic and consisted of characterizing the spatio-temporal couplings added by the different building blocks of CPA laser systems. This work was developed in part III.

In part II (p. 43), we focused on the improvement of the device, so that it could comply with new constraints that we judged necessary. Notably, we needed TERMITES to be easily scalable to other systems, while providing the best performances. Also, since the instrument was designed with the prospect of making a commercial instrument, it also had to be portable and cost-effective. With these goals in mind, we studied the various physical limits of TERMITES in chapter 4 and came up with a new prototype. The two next chapters (5 & 6) were dedicated to the validation of the technique. In chapter 5 (p. 77), we developed a numerical framework that we used to fully simulate TERMITES measurements. This was used to study numerically the influence of various internal and environmental perturbations on the measurement, and to define the limits within which the retrieved spatio-temporal results stay reliable. It has enabled us to check that in normal experimental conditions, the perturbations sustained by TERMITES remain within limits, and that noise is kept to a minimum. In chapter 6 (p. 89), we tested experimentally the device by voluntarily adding calibrated amounts of spatio-spectral couplings and verifying that TERMITES was able to measure them with satisfying precision.

Part III (p. 103) was mainly dedicated to characterization measurements of TW to PW-class CPA laser systems. This part notably featured the spatio-spectral characterization of the petawatt laser BELLA, which is currently the most powerful femtosecond laser in operation. Although most of these measurements were carried out with TERMITES, this part featured one measurement done with the spatio-spectral measurement device INSIGHT, also developed in CEA LIDYL (see section 2.3.2 on page 33). These characterization measurements were the occasion to observe that CPA laser systems are far from being perfect when carefully looked at. Chiefly, we noticed that spatio-temporal couplings could appear early in the CPA chain, e.g., in the stretcher were we observed noticeable amounts of spatial chirp. Amplifiers are also susceptible to introduce some spatio-spectral couplings, which can be seen as the spatio-spectral counterpart of the traditional CPA redshift, a purely-spectral process. Finally, optical defects in compressors can introduce very complex spatio-spectral streaks that need to be measured with a good spatio-spectral resolution, thanks to a device such as TERMITES.

In the next pages, I will briefly elaborate on two particular subjects, which I consider decisive for the future of the technique. Namely, I will conclude about the relevance of different analysis tools seen in this work, and show the preliminary results of a very compact implementation of TERMITES.

## Choosing Relevant Spatio-Temporal Diagnostics

Learning how to visualize efficiently complex-valued 3D datasets was one the hardest challenges of this thesis. The difficulty of this task comes from the fact that the most direct representations—like volumetric 3D rendering or 3D iso-surfaces—are generally the less descriptive ones. Conversely, more specific projections generally illustrate one particular aspect of the results, while occulting a lot of potentially interesting information.

All along this manuscript, we therefore analyzed spatio-temporal or spatio-spectral couplings using illustrations that we judged relevant in each situation. Most of the time, it meant that different types of plots had to be combined in order to prove or refute the presence of specific couplings. Among the different ways of visualizing the data, we mostly used:

**Spectrally-resolved spatial profiles** (e.g., on pages 99, 112, or 114).

**Spatio-spectral fluence or phase profiles** (e.g., on pages 93, 99, or 122).

**Spatio-temporal intensity profiles** (e.g., on pages 118, 119 or 133).

**Spatial map of parameters, like central wavelength or duration** (e.g., on pages 112 or 113).

**Spectrally-resolved polynomial fits of the phase or Zernike decomposition** (e.g., on pages 36, 97 or 118).

Additionally to these five types of plot, the Strehl ratio provide a single-value description of the aberrations present in the measured beam. As explained in section 2.4.2 on page 37, there are multiple ways of compute it, and each of them depends on the definition of a perfect spatio-temporal profile with respect to the measured profile. In table 1, we display Strehl ratios computed from the different measurements featured in chapter 8. Some useful informations can be extracted from such data. For example, the low value of $SR_{\mathrm{STC}}$ for LOA Salle Jaune and LASERIX are good indicators that spatio-spectral couplings in phase have some strong influence on the maximum intensity achievable on these chains. Also, one can conclude from this table that there is no significant phase coupling at the output of the Amplitude frontend.

| **Laser Systems** | $SR_{\mathrm{STC}}$ | $SR_{\mathrm{WFS}}$ | $SR_{\mathrm{full}}$ |
|---|---|---|---|
| UHI-100 with defective periscope mirrors (2015) | 0.81 | 1.00 | 0.82 |
| UHI-100 with new periscope mirrors (2017) | 0.88 | 0.96 | 0.86 |
| Amplitude frontend (before multipass) | 0.90 | 0.94 | 0.85 |
| Amplitude frontend (after multipass) | 0.91 | 0.98 | 0.89 |
| BELLA at full power (1.1 PW) | 0.92 | 0.95 | 0.88 |
| LOA *Salle Noire* (after HCF, no broadening) | 0.75 | 0.62 | 0.49 |
| LOA *Salle Noire* (after HCF, with maximum broadening) | 0.86 | 0.93 | 0.82 |
| LOA *Salle Jaune* | 0.66 | 0.94 | 0.65 |
| LASERIX | 0.56 | 0.95 | 0.56 |

**Table 1.: List of Strehl ratios measured from CPA laser systems during this thesis.** *The definitions regarding the three presented Strehl ratios are available in section 2.4.2.*

The power of such ratio—if computed reliably—is incontestable. After all, it represents for laser engineers and users one of the main goals of full beam characterization : obtaining a measurement of the true intensity at focus. The reason why we did not solely relied on these numbers to understand spatio-temporal couplings and their sources in chapter 8 is twofold:

- Strehl ratios often hide subtleties about the pulse structure, that can only be comprehended using more complex illustrations. Therefore, we never considered that they brought any more useful information than proper plots of the beam spatio-temporal or spatio-spectral profile.

- The computation of these Strehl ratios is described theoretically in section 2.4.2 on page 37, and results seems rather credible in table 1—values are always between zero and one, and are lower in situations where we know that couplings are present. However, the numerical implementation has never been tested extensively, and we cannot assert the precision of this computation, or its sensitivity to measurement noise.

In spite of the necessary precaution that we took here, spatio-temporal Strehl ratio should represent an indispensable tool for laser optimization. In the new era of machine learning, such quantities constitute an excellent metric to determine how well some parameters of the laser are set. Optimization algorithms could directly drive active spatio-temporal shaping devices, if such devices were to emerge in the years to come.

## Characterization of laser chains after target plane

Finally, I will present here one last idea about the implementation of TERMITES in ultra-intense laser facilities. One of the benefits of using our instrument to qualify laser systems is its versatility. By principle, a measurement can be done at any position along the CPA chain, even at positions where pulses are stretched in time. This is particularly useful for troubleshooting and for finding the source of space-time couplings. Yet, the most interesting information to the experimentalist is generally the space-time shape of pulses at the interaction plane, i.e., at the very end of the laser chain.

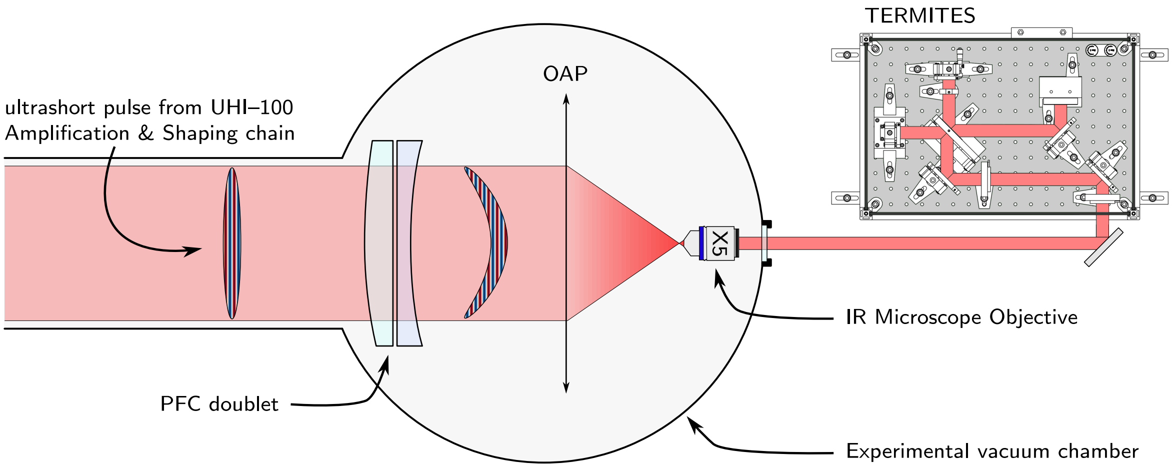
TERMITES
OAP
ultrashort pulse from UHI–100
Amplification & Shaping chain
X5
IR Microscope Objective
PFC doublet
Experimental vacuum chamber

**Figure 1.: Experimental set-up used to characterize UHI–100 laser beam after the target chamber.** Custom designed doublet is added just before the Off-Axis Parabola (OAP) in order to add a known amount of Pulse Front Curvature. For this experiment, the OAP focal length was 200 mm. A X5 microscope objective was aligned after target focal point in order to re-collimate the beam before TERMITES.

Oftentimes, the diameter of the beam before the focusing element makes it unsuited for a direct characterization with TERMITES. We drew a conclusion in section 4.2.2 on page 73 about the way to solve this issue: instead of adapting the input diameter of every TERMITES devices to each laser system, it is preferable to reduce the beam so that it fits in a standard TERMITES input pupil. As demonstrated in section 7.2 on page 104, building an afocal telescope is an acceptable way to do so if chosen optics are achromatic over the full spectrum. A more compact method that I would like to propose here consists of reducing the beam by re-collimating it just after the focal plane of the experimental focusing element. In addition to being more practical, this solution adds only one optical element between the characterized plane and TERMITES, making unwanted aberrations easier to estimate. It is also exceptionally compact because the input beam diameter for TERMITES is only a few millimeters in this situation.

In order to determine if this simple method is suitable to get precise results, we arranged a measurement of UHI-100 laser beam just after its target plane as illustrated by figure 1 on the preceding page. The beam was re-collimated to a diameter of 13 mm thanks to a X5 Near-IR microscope objective. The Pulse Front Curvature (PFC) afocal doublet—described in section 6.3.1 on page 94—was added immediately before the focusing parabola. This additional element adds a controlled amount of PFC which should be resolved by TERMITES in this new configuration.

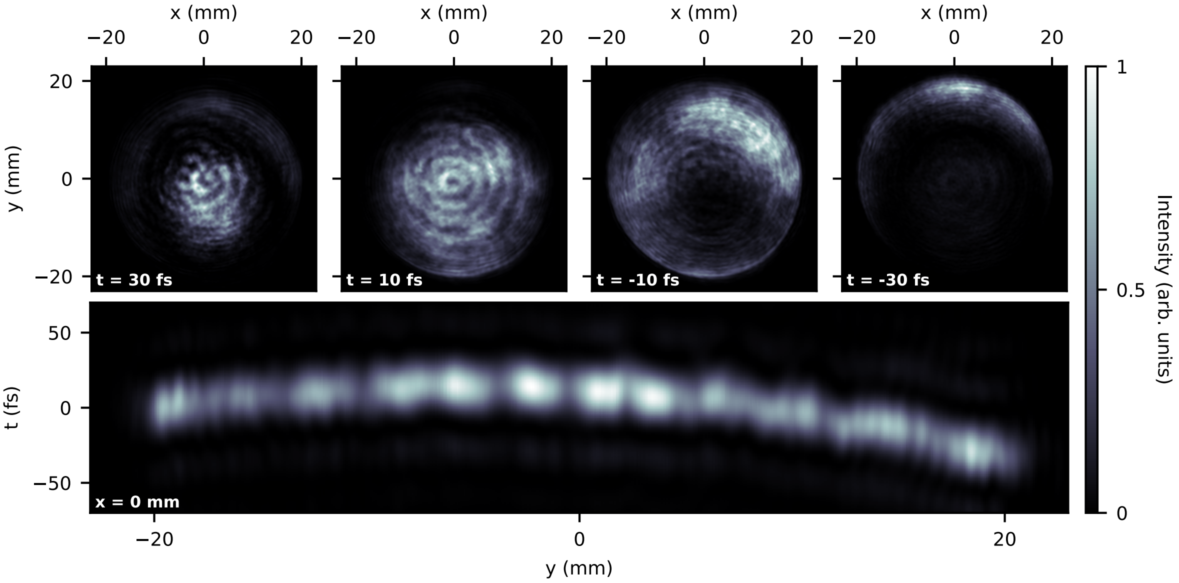

**Figure 2.: Curved pulse front measured by TERMITES in experimental chamber.** Upper panels show the fluence profile of the measured beam, at different times throughout the pulse duration. Bottom panel shows a slice of the same pulse, viewed from the side and resolved along vertical position and time.

A view of the result is displayed in figure 2. In this temporal view, the curvature is directly visible because it adds a delay to the pulse that depends quadratically on radius. The upper panels clearly show that the pulse energy is first observed exclusively at the center of the beam, before drifting to the edges in an annular shape during the end of the pulse. The curvature measured by this set-up adds a 50 fs maximum delay at the edge of the beam. This value corresponds to a measured PFC of $0.125\,\mathrm{fs/mm^2}$, very similar to the curvature measured by TERMITES and an independent technique in section 6.3.1 on page 94.

This last use case example demonstrates that our technique can be strongly adapted to the situation. In this particular implementation, TERMITES footprint can be drastically reduced to become comparable to other well-established diagnostic tools.

# Appendices

# Supplementary Demonstrations

## A.1. Curvature of the Reference in TERMITES

### A.1.1. Optical Path Difference

Let us compute the radial Optical Path Difference $\mathrm{OPD}_{\mathrm{curv}}(r)$ caused by a wavefront curvature. The expression of $\mathrm{OPD}_{\mathrm{curv}}(r)$ was useful for estimating the curvature term added by the convex mirror of TERMITES (section 3.2.2 on page 52) and to compute the required delay range of our instrument (section 4.1.1 on page 65).

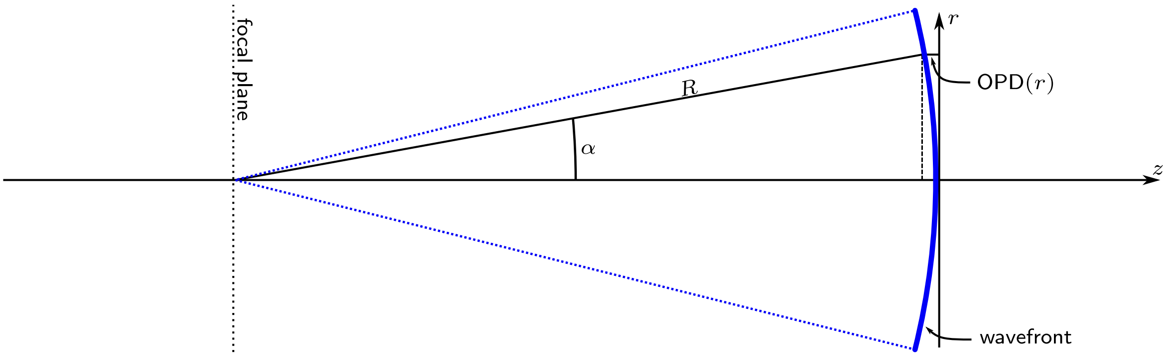

**Figure A.1.: Computing optical path difference caused by wavefront curvature.** $r$: radial position. OPD($r$): Optical Path Difference generated by the curvature at radial position $r$. $R$: Radius of curvature at the considered plane. $z$: longitudinal position.

As illustrated by figure A.1, the Optical Path Difference caused by the curvature is:

$$\begin{aligned}
\mathrm{OPD}_{\mathrm{curv}}(r) &= R\left[1-\cos(\alpha)\right] ,\\
&= R\left[1-\cos\left(\arctan\left(\frac{r}{R}\right)\right)\right] ,\\
\mathrm{OPD}_{\mathrm{curv}}(r) &= R\left[1-\frac{1}{\sqrt{1+\left(\frac{r}{R}\right)^2}}\right] , \qquad \text{(A.1)}
\end{aligned}$$

with $r$ the radial position, and $R$ the radius of curvature of the beam. Note that this function can be expanded in Taylor series at $r = 0$, and that its first term depends quadratically on $r$:

$$\mathrm{OPD}_{\mathrm{curv}}(r) = \frac{r^2}{2R} - \frac{3r^4}{8R^3} + \frac{5r^6}{16R^5} + \mathcal{O}(r^7) . \qquad \text{(A.2)}$$

This explains why a curved wavefront is often approximated as a purely quadratic phase when $r$ is small compared to the radius of curvature $R$.

### A.1.2. Curved Wavefront

Given the expression of equation (A.1) on the preceding page, the phase introduced by a curvature is written as:

$$\begin{aligned}\varphi_{\text{curv}}(r,\lambda) &= \frac{2\pi}{\lambda}\,\text{OPD}_{\text{curv}}(r)\ ,\\ \varphi_{\text{curv}}(r,\lambda) &= \frac{2\pi R}{\lambda}\left[1-\frac{1}{\sqrt{1+\left(\frac{r}{R}\right)^2}}\right]\ .\end{aligned}\tag{A.3}$$

### A.1.3. Radial Group Delay (RGD) Generated by a Curved Wavefront

Temporally, the radial optical path difference created by the curvature of the wavefront generates a delay which is simply:

$$\begin{aligned}T_{\text{curv}}(r) &= \frac{\text{OPD}_{\text{curv}}(r)}{c}\ ,\\ T_{\text{curv}}(r) &= \frac{R}{c}\left[1-\frac{1}{\sqrt{1+\left(\frac{r}{R}\right)^2}}\right]\ .\end{aligned}\tag{A.4}$$

## A.2. Spatial Fringes Spacing in TERMITES

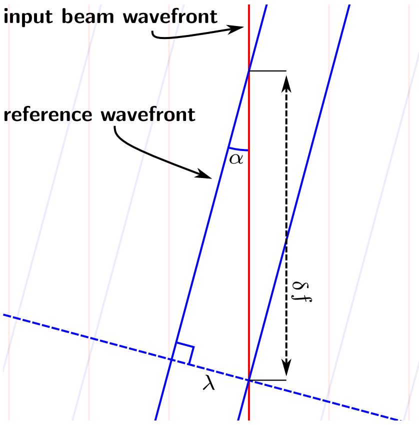

**Figure A.2.: TERMITES fringes spacing.**

Let us express the spatial fringe spacing in TERMITES raw interferograms, as this has already been done in previous works [42, 43]. From figure A.1 on the previous page, we write:

$$\sin\alpha = \frac{r}{R}\,. \tag{A.5}$$

Also, figure A.2 illustrates that, in the measurement plane,

$$\sin\alpha = \frac{\lambda}{\delta f}\,, \tag{A.6}$$

$\delta f$ being the inter-fringes spacing and $\alpha$ the angle between the input beam wavefront and the reference wavefront. Consequently, $\delta f$ verifies the following relation at all positions $\boldsymbol{r}$:

$$\delta f(r) = \frac{\lambda R}{r}\,. \tag{A.7}$$

At measurement plane, the radius of curvature $R$ is $L_R + f_R$. Therefore:

$$\delta f(r) = \frac{\lambda\,(L_R+f_R)}{r}\,. \tag{A.8}$$

## A.3. Averaging spatio-spectral quantities

### A.3.1. Mean Spectral Fluence

The average spectral fluence is computed from the spectral fluence as :

$$\varepsilon_{\text{avg}} = \frac{\iiint \mathrm{d}x\,\mathrm{d}y\,\mathrm{d}\omega\ \varepsilon(x,y,\omega)}{\Delta_x \Delta_y \Delta_\omega} = \frac{\varepsilon^T}{\Delta_x \Delta_y \Delta_\omega}\ , \tag{A.9}$$

with $\Delta_x$, $\Delta_y$, $\Delta_\omega$ the spatio-spectral extension of the considered domain and $\varepsilon^T$ the total pulse energy. Mean spectral fluence represents the average spectral fluence of a field (in $\mathrm{J/mm^2/(rad{\cdot}fs^{-1})}$). This quantity can be used for normalization, as in section 5.1.2 on page 79 for instance.

# Summary in French

Depuis plus de quarante ans, le développement rapide des systèmes laser ultrabrefs a permis de produire des impulsions de plus en plus courtes, qui atteignent seulement quelques femtosecondes aujourd'hui. Les lasers femtosecondes sont notamment utilisés dans le but de concentrer un maximum d'énergie lumineuse dans une impulsion la plus brève possible. L'éclairement crête qui est produit au foyer d'un système laser ultra-intense permet notamment de générer des trains d'impulsions attosecondes, ou même des faisceaux de particules relativistes. Les éclairements requis par de telles applications ont été obtenus grâce à plusieurs bonds technologiques, et notamment celui de l'amplification par dérive de fréquence (CPA en anglais). Cette méthode consiste à étirer temporellement des impulsions courtes émises par un oscillateur à basse énergie, qui sont ensuite amplifiées avant d'être comprimées temporellement en fin de chaîne.

Les éléments optiques utilisés dans la technique CPA, tels que l'étireur ou le compresseur, emploient des composants fortement chromatiques. Malgré une compensation parfaite de ce chromatisme en fin de chaine laser, des défauts spatio-spectraux peuvent subsister en cas de mauvais alignement, ou de défaut optique se produisant au niveau de l'étireur ou du compresseur. Les couplages spatio-spectraux occasionnent des couplages spatio-temporels de l'impulsion au niveau de la cible, ce qui implique systématiquement une diminution de l'éclairement crête. La mesure des couplages spatio-spectraux ou spatio-temporels est donc fondamentale. Plusieurs techniques différentes ont été développées dans l'objectif de fournir une information quantitative sur la forme spatio-temporelle des impulsions ultra-intenses. Néanmoins, aucune d'entre elles n'est véritablement considérée comme un standard de métrologie, et les couplages spatio-temporels restent bien souvent indéterminés. Cela est principalement dû au fait que ces techniques ne sont bien souvent pas adaptées aux caractéristiques bien spécifiques des faisceaux lasers ultra-intenses.

Ce travail de thèse est dédié à la conception et à l'optimisation de l'instrument TERMITES, qui est en développement au laboratoire LIDYL depuis 2014. TERMITES est un instrument de caractérisation spatio-spectrale d'impulsions laser femtosecondes basé sur la spectroscopie par transformée de Fourier. La partie II de ce manuscrit est tout d'abord consacrée à la description du principe de fonctionnement de TERMITES. La suite de cette partie s'attache à décrire les paramètres de conception de l'instrument, et à définir plusieurs compromis de dimensionnement. Des tests sont ensuite effectués pour montrer les performances de l'instruments, ainsi que ses limites fonctionnelles. Dans le chapitre 5, les tests sont purement numériques et démontrent l'impact de fluctuations rapides sur la mesure. Le chapitre 6 présente quant à lui des tests de validation expérimentale montrant la sensibilité et la fiabilité de l'appareil.

La troisième partie du manuscrit décrit les résultats de mesures spatio-spectrales qui ont été réalisées sur plusieurs installations laser ultra-intenses. Lors de ces différentes mesures, de multiples défauts ont été observés de manière très fine par TERMITES. Après avoir cherché l'origine des couplages mesurés, il apparaît que ceux-ci proviennent de sources variées et de composants optiques différents. Le chapitre 8 présente donc une revue des couplages qui ont été mesurés par TERMITES, ainsi qu'une hypothèse sur la source de chacun d'eux.

Ce travail de thèse détaille le fonctionnement d'un instrument de caractérisation spatio-spectrale qui est optiquement simple, car impliquant peu de composants optiques, et ne reposant pas sur l'optique non-linéaire. Le traitement de données nécessaires pour obtenir l'information recherchée est étudié en détail, et les tests de validation montrent que les mesures TERMITES sont non seulement valides mais aussi très précises. L'optimisation du dispositif a permis de rendre TERMITES portable et utilisable sur d'autres installations. Cela permet notamment de caractériser un plus grand nombre de chaines lasers différentes et d'obtenir une information plus précise sur l'incidence des couplages spatio-temporels en condition expérimentale.

# List of Publications

## Articles

- A. Jeandet, A. Borot, K. Nakamura, S. W. Jolly, A. J. Gonsalves, C. Toth, H.-S. Mao, W. P. Leemans and F. Quéré. 'Spatio-Temporal Structure of a Petawatt Femtosecond Laser Beam'. In: *J. Phys. Photonics* (2019). DOI: `10.1088/2515-7647/ab250d`
- S. Jolly, O. Gobert, A. Jeandet and F. Quéré. 'Controlling the Velocity of a Femtosecond Laser Pulse Using Refractive Lenses'. In: *Opt. Express* (2020). DOI: `10.1364/OE.384512`

## Oral Contributions

- SPIE Optics + Optoelectronics, Prague. 25th April, 2017
  *New advanced characterization tools for PW-class lasers*
- XI Workshop on Adaptive Optics for Industry and Medicine, Murcia. 5th March, 2018
  *Spectrally-resolved Wavefront Sensing of Broadband Laser Beams*
- ICUIL, Lindau. 10th September, 2018
  *Full 3D Spatio-Spectral Characterization of the BELLA Petawatt Laser*

IOP Publishing J. Phys.: Photonics 1 (2019) 035001 https://doi.org/10.1088/2515-7647/ab250d

JPhys Photonics

OPEN ACCESS

RECEIVED
27 February 2019

REVISED
19 April 2019

ACCEPTED FOR PUBLICATION
28 May 2019

PUBLISHED
13 June 2019

Original content from this work may be used under the terms of the Creative Commons Attribution 3.0 licence.

Any further distribution of this work must maintain attribution to the author(s) and the title of the work, journal citation and DOI.

PAPER

# Spatio-temporal structure of a petawatt femtosecond laser beam

Antoine Jeandet[1,2], Antonin Borot[1], Kei Nakamura[3], Spencer W Jolly[1], Anthony J Gonsalves[3], Csaba Tóth[3], Hann-Shin Mao[3], Wim P Leemans[3,4] and Fabien Quéré[1]

[1] LIDYL, CEA, CNRS, Université Paris-Saclay, CEA Saclay, F-91191 Gif-sur-Yvette, France
[2] Amplitude Laser Group, Business Unit Science, 2/4 rue du Bois Chaland, F-91090 Lisses, France
[3] Lawrence Berkeley National Laboratory, Berkeley, CA 94720, United States of America
[4] Currently with Deutsches Elektronen-Synchrotron DESY, Hamburg, Germany.

**E-mail:** knakamura@lbl.gov and fabien.quere@cea.fr

**Keywords:** ultrafast lasers, ultrafast metrology, high power lasers, ultrashort pulses

Supplementary material for this article is available online

## Abstract

The development of optical metrology suited to ultrafast lasers has played a key role in the progress of these light sources in the last few decades. Measurement techniques providing the complete *E*-field of ultrashort laser beams in both time and space are now being developed. Yet, they had so far not been applied to the most powerful ultrashort lasers, which reach the PetaWatt range by pushing the chirped pulse amplification (CPA) scheme to its present technical limits. This situation left doubts on their actual performance, and in particular on the peak intensity they can reach at focus. In this article we present the first complete spatio-temporal characterization of a PetaWatt femtosecond laser operating at full intensity, the BELLA laser, using two recently-developed independent measurement techniques. Our results demonstrate that, with adequate optimization, the CPA technique is still suitable at these extreme scales, i.e. it is not inherently limited by spatio-temporal couplings. We also show how these measurements provide unprecedented insight into the physics and operation regime of such laser systems.

## Introduction

The technology of ultrafast laser sources nowadays makes it possible to generate laser pulses of femtosecond duration with peak powers of up to several PetaWatts (PW) [1–3]. The development of such laser sources, now available or under construction in several laboratories worldwide, is motivated by two main prospects. The first is demonstrating compact particle accelerators for scientific or societal applications, with particle energies up to several GeV [4–8]. The second is exploring the physics of ultra-relativistic laser-matter interactions, and more particularly accessing regimes where highly nonlinear quantum electro-dynamical effects come into play, in order to perform new tests of this fundamental theory [9].

Due to their ultrashort durations, such lasers necessarily have broad spectra, typically covering several tens of nanometers in wavelength. As in any optical system using broadband light, chromaticity—i.e. the spectral dependence of the spatial properties of a beam, or of the spatial response of an optical system—can become a major impediment to optimize their performance. PetaWatt ultrashort lasers are particularly exposed to this issue; the key enabling technology for these systems, chirped pulse amplification (CPA), which is pushed to its present technical limits in these systems, relies on highly chromatic optical elements such as gratings or prisms, used to tailor the pulses temporal properties for the amplification process [10]. The large chromatic effects individually introduced by each of these optical elements should ideally perfectly compensate each other at the system output. But any imperfection or misalignment of these optics results in residual chromaticity, as so does the use of simple chromatic elements such as singlet lenses [11].

In standard optical assemblies, such as photographic lenses, chromaticity degrades the system performance by affecting its spatial response. The consequences are actually much more severe for ultrashort lasers, where all frequencies not only need to be focused on the same focal spot, but also with the appropriate relative phases, i.e.

© 2019 The Author(s). Published by IOP Publishing Ltd

those leading to the minimal pulse duration. In this case, undesired chromatic effects not only degrade the concentration of energy in space by inducing imperfect overlap of the different frequencies at focus, they can also increase the pulse duration by reducing the spectral width and degrading the spectral phase locally. The combination of these spatial and temporal effects, known in ultrafast optics as spatio-temporal or spatio-spectral couplings, can lead to very significant reductions in peak intensity even for relatively modest chromatic aberrations—especially as the beam size increases and the pulse duration decreases.

The first step in addressing this issue is the development of adequate metrology tools, which can measure the complete $E$-field of the laser beam in space-time, $E(x, y, t)$ or space-frequency, $\tilde{E}(x,\ y,\ \omega)$. Several suitable techniques have been developed in the last 15 years [12–17], and are now becoming more and more broadly used, especially on ultrashort lasers of moderate power. Only recently, two different and complementary techniques, TERMITES [18] and INSIGHT [19], have been successfully demonstrated for the characterization of laser systems of up to 100 TW peak power. Yet, none of the existing PW-class lasers have ever been characterized in space-time, thus leaving serious doubts on the actual performance of these cutting-edge sources.

In this article, we address this key issue by presenting the first complete spatio-temporal characterization of a 1.1 PW–40 fs system, using both TERMITES and INSIGHT, carried out on the BELLA PW laser at LBNL, operated *at full power and intensity on target*, thus revealing for the first time the type of spatio-temporal couplings that can affect such cutting-edge laser systems. This advanced characterization provides unprecedented insight into the physics and operation regime of such laser systems, and demonstrates that the CPA technique is still suitable at such extreme pulse powers. We first detail the implementation of these two techniques and summarize the validation tests that have been performed, and then present the main chromatic effects observed on the beam. We quantify the impact of chromaticity on the laser performance, and explain how the measurements provide insight into the laser system operating conditions and the physics of the beam amplification.

## Experimental set-up and measurement procedure

The BELLA laser, acquired from Thales and operated by LBNL for the last 5 years, is based on a double-CPA architecture: broadband pulses originating from an oscillator are amplified in a succession of six Ti:Sapphire amplifiers, and a cross-polarized wave contrast enhancement system is installed in between these two CPA systems. The exact system design is detailed in [1].

After temporal compression in the grating compressor, the beam of 20 cm diameter propagates under vacuum and is focused into the main experimental chamber by an off-axis parabola with a focal length $f = 13.5$ m, producing a focal spot with $w_0 \approx 53\ \mu$m (half width at $1/e^2$ of the field intensity). This chamber is generally used for laser-wakefield particle acceleration experiments, with a capillary discharge plasma as a target (T in figure 1). Here this target was removed from the beam path, letting the laser diverge away from the focus, until it gets large enough to avoid damaging subsequent optics.

An all-reflective chromatic-aberration-free telescope is then used to image the best focus, located in the target chamber, to an output diagnostic area, with a magnification factor of 1. This telescope has been extensively used for the diagnostics of all preceding experiments on BELLA (see [1]) and was proven to introduce negligibly small aberrations. The set of relay optics in this telescope includes three uncoated wedges (two in vacuum, one in air) to attenuate laser pulse energy by a factor of $2.7\ \times\ 10^4$. When BELLA is operated above 5 J pulse energy, a thin (5 $\mu$m) self-standing gold-coated pellicle with 6 inch inner diameter (G in figure 1) is inserted into the beam for a further attenuation by a factor 40. This unique attenuation system is what allows the beam to be safely operated at full power inside the vacuum chamber, and therefore also at full intensity at focus, while avoiding optical damage or nonlinear effects in the subsequent diagnostic line (in particular in the exit vacuum window W in figure 1).

The diagnostic area located after this attenuation system incorporates the spatial-only and temporal-only measurement devices typically used for such lasers, as indicated in figure 1. In the present work, we have implemented two additional measurement devices, based on the TERMITES and INSIGHT techniques, in order to determine the spatio-temporal field of the BELLA laser beam.

TERMITES is typically implemented on collimated beams. We therefore recollimated the converging BELLA image beam to a diameter of about 1.8 cm, by inserting a convex spherical mirror prior to the focus image plane (CM in figure 1). TERMITES then uses a Michelson interferometer with a flat mirror in one arm, and a convex spherical mirror in the other. In this second arm, the central part of the beam is converted into a diverging beam, which eventually fully overlaps with the beam to be characterized and is used as a reference, as in point diffraction interferometry. The spatio-spectral comparison of these two beams is achieved by measuring, on each pixel of the detector, the signal resulting from their superposition as a function of delay. Their cross-spectral density function is then obtained by a Fourier transformation of this first order cross-correlation

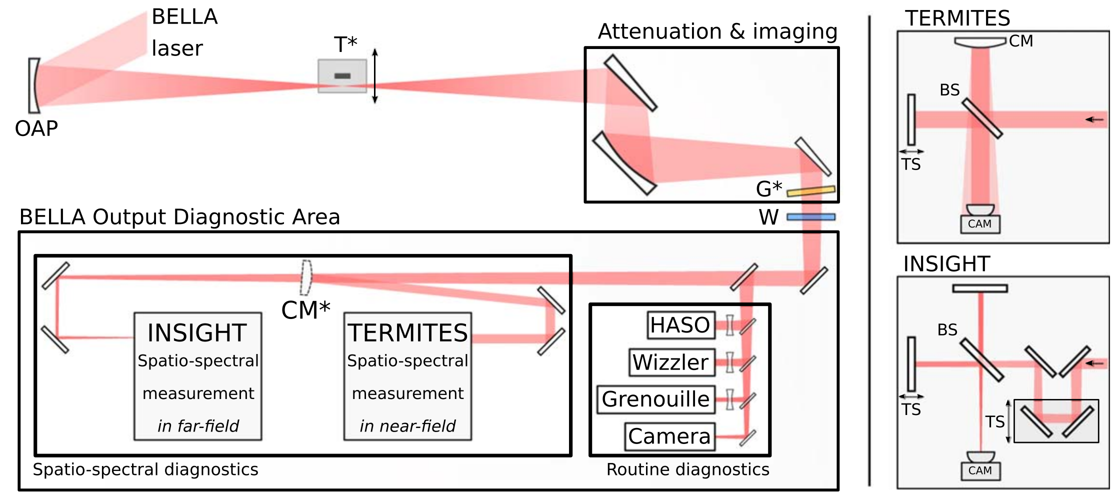

**Figure 1.** Sketch of the experimental set-up. The left panel shows the path of the BELLA laser beam from the compressor output to the experimental chamber, attenuation and imaging chamber, and finally to the diagnostic area. Here the INSIGHT and TERMITES devices have been installed, together with traditional space-only or time-only diagnostics used for such lasers. The right panels display sketches of the INSIGHT and TERMITES devices, which for practical reasons had to be used successively on two different weeks. The * symbol indicates retractable elements. OAP = off-axis parabola, T = target, G = gold foil, W = Vacuum window, CM = convex mirror, BS = beam splitter, TS = translation stage.

function. The design details of TERMITES are described in [18] and its associated supplementary material. In order to fit the device to the experimental conditions of this particular measurement, we chose the reference size to be half the diameter of the incident beam.

INSIGHT also relies on a Michelson interferometer, now with a flat mirror in each arm. This is used to measure the spatially-resolved first order autocorrelation function of the beam at each point of the detector (standard Fourier-transform spectroscopy), from which one can deduce the frequency-resolved spatial intensity profile of the beam. As detailed in [19], any pointing fluctuations must be compensated for in order to calculate the correct spectrum at the positions around focus. This was implemented in these measurements where the fluctuations on the BELLA focus were approximately 16 and 24 $\mu$m RMS for the horizontal and vertical axis respectively. This measurement is performed for multiple planes at and around best focus (here, around the image plane of the best focus). These data are then injected into an iterative phase-retrieval algorithm of the Gerchberg-Saxton type, to determine the spatial phase profile of the beam *at each frequency*.

The temporal scans of both techniques were designed so that the whole output spectrum of BELLA (43 nm FWHM centered around 800 nm [1]) could be retrieved with a satisfying resolution. This implied choosing a step size of 150 nm and a scan range of at least 50 $\mu$m.

Once the spatial amplitude and phase profiles at each frequency have been determined in a given plane (different for TERMITES and INSIGHT), the beam can be numerically propagated to any arbitrary longitudinal position, using plane wave decomposition [20] at each wavelength. All results presented in this article correspond to the front focal plane of the focusing parabola, i.e. to the plane located at a distance $f = 13.5$ m *before* this optic.

Like most of their relatives, these two techniques should actually be considered as spatio-spectral techniques, which determine $\tilde{E}(x, y, \omega) = \tilde{A}(x, y, \omega)\exp[i\phi(x, y, \omega)]$ up to an unknown spatially-homogeneous spectral phase. An additional measurement of the spectral phase at a single point of the beam is then required to lift this unknown, after which the spatio-temporal field $E(x, y, t)$ can be calculated by a Fourier-transform with respect to frequency. In the present case, this complementary information was provided by the GRENOUILLE device located in the output diagnostic area.

Both techniques require from a few hundreds to a thousand laser shots for each measurement, and all measurements were performed with the laser operated at 1 Hz. Three operation modes of the laser were used: 'low' power mode (225 mJ per pulse, 5.8 TW peak power) with the last amplifier turned off and wedge attenuation in the chain, moderate power mode (8.4 J per pulse, 215 TW peak power) in the same conditions but without attenuation, and full power (43 J per pulse, 1.1 PW peak power) with all amplifiers on and no attenuation before target.

We performed a set of tests with both techniques to verify that the attenuation and transport system does not lead to spatio-temporal distortions of the laser beam. First, to test the potential influence of nonlinear optical effects occurring along this system, we checked that the results of measurements performed at full power with Fourier-transform limited (FTL) pulses were identical to those obtained with pulses of the same energy, but

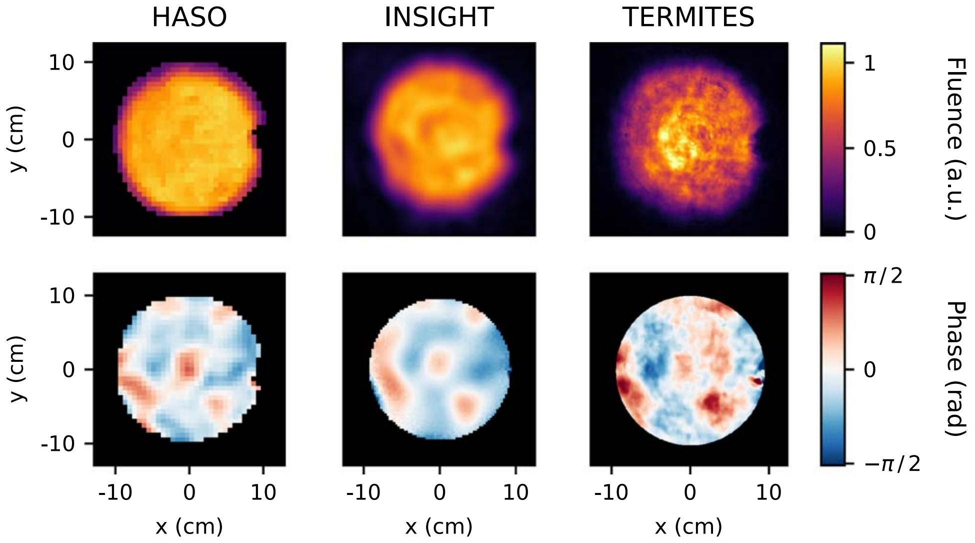

**Figure 2.** Validation test of TERMITES and INSIGHT on the BELLA laser. Results derived from these two techniques (second and third columns, obtained after frequency-averaging of the spectrally-resolved measurement outputs) are compared to the ones provided by a standard Shack–Hartmann wavefront sensor (HASO by Imagine Optics, left column). The top row shows the frequency-averaged spatial intensity profile of the collimated BELLA beam, and the bottom row its frequency-averaged spatial phase profile. Note the small clip on the right edge of the beam: this is due to a small hole in the first wedge of the attenuation line, normally used to collect the accelerated electron beam in laser-wakefield experiments. This hole is usually placed at the center of the laser beam, but was moved to its edge for this measurement campaign. The resulting clip is well retrieved by TERMITES and INSIGHT.

chirped in time to 1.2 ps by moving one of the compressor gratings (see supplementary document). For the consistency of this test, we also verified that chirping the pulse does not modify the spatio-temporal structure of the beam (due e.g. to undesired angular motion of the compressor grating), by comparing measurement results obtained at low power (thus safely avoiding any nonlinear effect in the attenuation system) for FTL and chirped pulses. Finally, at moderate power, we compared the results of measurements carried out with and without the gold foil, which showed that this foil does not introduce any additional coupling on the transmitted beam, but only a smooth spatially-homogeneous modification of the spectral envelope, corresponding to its theoretical transmission curve. With the support of all these tests, all results presented in this article correspond to the optimally-compressed BELLA beam at full power.

Validation tests of the measurement techniques themselves have already been presented, in [18] and [19] for TERMITES and INSIGHT respectively. The measurement configuration used in the present work offered an opportunity for a new type of test, which had not been possible before for practical reasons: with the spatio-temporal measurement devices separated from the Shack–Hartmann wavefront sensor (HASO by Imagine Optic) by only a few plane mirrors of small diameter, it is a safe assumption that the different beams arriving on these devices all have a similar wavefront. Therefore, we can safely compare the spatial intensity and phase profiles provided by this well-established instrument to the information provided by TERMITES and INSIGHT. Since this sensor has no spectral resolution, this is achieved by frequency-averaging the spectrally-resolved spatial profiles determined by these new techniques. This comparison, presented in figure 2, reveals a very good agreement, especially for the phase profiles, which is quite remarkable given the very different principles underlying these three techniques.

## Results and discussion

Spectrally-resolved spatial intensity and phase profiles of the BELLA laser at four different frequencies, measured at full power with INSIGHT, are displayed in figure 3. The complete evolution of these profiles as a function of frequency is displayed in supplementary movie 1, which is available online at stacks.iop.org/JPPHOTON/1/035001/mmedia.

The first important conclusion is that BELLA does not suffer from major low-order chromatic phase aberration. Such aberrations can be particularly detrimental for ultrashort lasers, and are expected to be of two main types for collimated laser beams: (i) angular dispersion, typically resulting from stretcher or compressor misalignment, associated in the time domain to pulse front tilt (PFT), (ii) frequency-dependent wavefront curvature, typically induced by chromatic lenses, associated in the time domain to pulse front curvature (PFC).

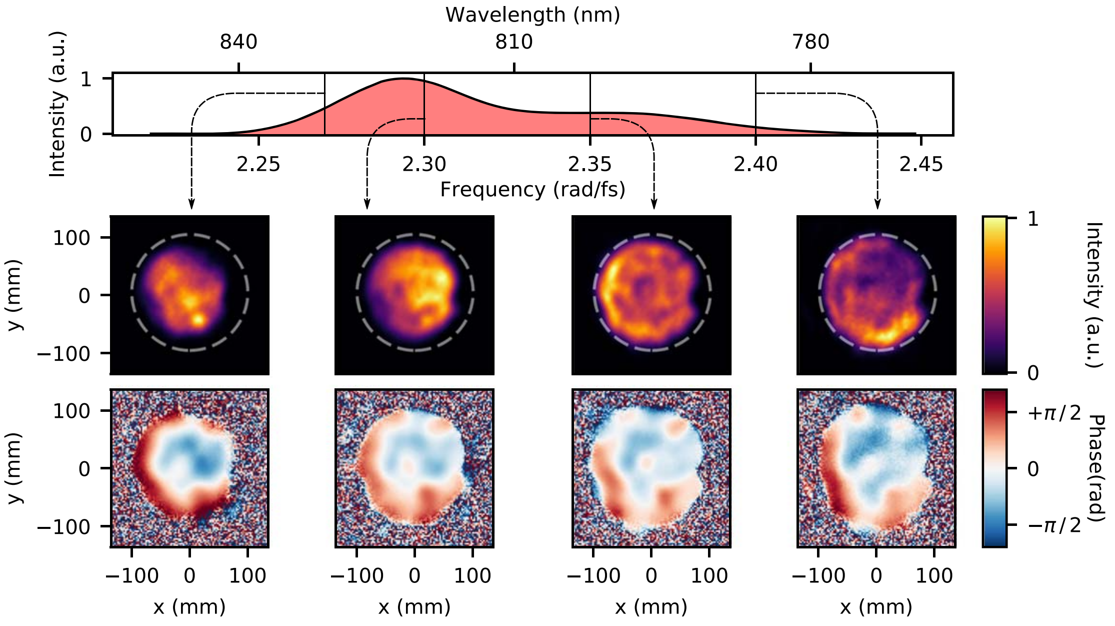

**Figure 3.** Frequency-resolved spatial properties of the collimated BELLA beam. Four frequencies $\omega_i$ are selected in the spatially-integrated spectrum (upper panel) and the corresponding spatial intensities $\tilde{A}^2(x, y, \omega_i)$ and phases $\phi(x, y, \omega_i)$ (lower row) are shown. These results have been obtained with INSIGHT.

The magnitude of these couplings is observed to be very weak on BELLA, as clearly appears by considering the coefficients of the frequency-resolved Zernike decomposition of the spatial phase, displayed in figure 4. At focus, the variation of the lateral position of the focal spot, due to frequency-dependent horizontal and vertical wavefront tilts, is less than 10% of the beam waist across the laser spectrum. The wavefront curvature does exhibit a variation with frequency, slightly increasing on the red side of the spectrum (see also figure 3). Yet, at focus, this curvature results in a longitudinal focus shift that never exceeds 6% of the BELLA Rayleigh range. This variation is not linear with frequency, indicating a higher-order spatio-spectral aberration, as opposed to a simple PFC.

Figure 4 also shows that the results obtained with TERMITES for the low-order chromatic phase aberrations are qualitatively consistent with those provided by INSIGHT, especially when considering the fact that these measurements were carried out on different weeks. But TERMITES actually provides finer information on higher-order chromatic aberrations affecting the beam. This clearly appears in supplementary movie 2 (stacks.iop.org/JPPHOTON/1/035001/mmedia), which shows the complete evolution with frequency of the beam spatial phase, provided by TERMITES: on these phase plots, spatial patterns of higher-frequency are observed, which drift along the horizontal direction as frequency varies. This effect is illustrated more quantitatively in figure 5, which displays $(x, \omega)$ and $(y, \omega)$ slices of this spatio-spectral phase, in the horizontal and vertical planes, at the center of the beam $(x = y = 0)$. The horizontal plane ($x$ axis) corresponds to the dispersion plane of the compressor. At each wavelength, 'high-frequency' (5–6 periods across the full beam) modulations of the spatial phase are observed along $x$. These modulations linearly shift in space as frequency changes, creating an oblique spatio-spectral pattern in the $(x, \omega)$ space (figure 5(a)). By contrast, such an oblique spatio-spectral pattern is not observed at all in the $(y, \omega)$ space, i.e. in the plane normal to the compressor dispersion direction (figure 5(b)).

A simple interpretation of this feature has been recently analyzed in detail in [21]. In between the first and the last gratings of the compressor the laser beam is laterally chirped, i.e. the central position of the 'beamlet' associated to each frequency shifts approximately linearly with frequency. When this occurs, any modulation of the spatial phase induced on the beam, e.g. due to defects of a mirror or a grating, is imprinted at a different position relative to the center of each beamlet. After the compressor, this lateral chirp is removed, and all beamlets are again centered on the same axis. The spatial modulations induced within the compressor are then expected to shift approximately linearly with frequency, precisely as observed in figure 5. The expected slope of the pattern induced in this way can be deduced from the geometry of the compressor and the characteristics of its gratings, and is consistent with the observed effect (red dashed line in figure 5), thus strongly supporting this interpretation.

A simple analytical calculation (see supplementary document) shows that, if the corresponding spatial phase modulation is assumed to be perfectly sinusoidal at each frequency and of weak amplitude, then the scattered energy at focus forms two satellite spots located at a distance of $\lambda_0 f/\Lambda$ ($\Lambda$ is the spatial period of the modulations)

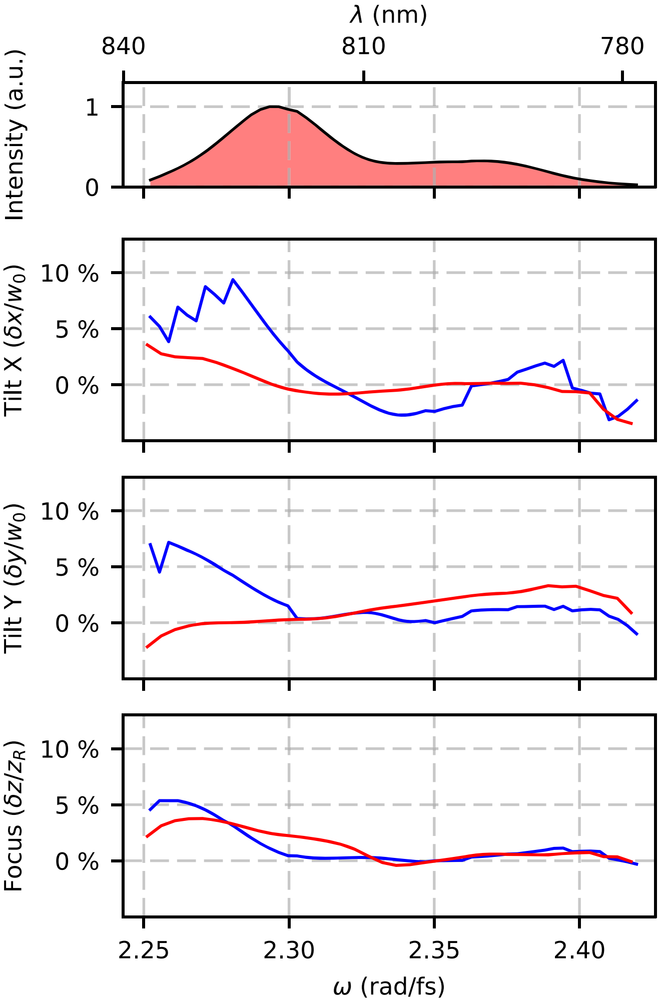

**Figure 4.** Low-order coefficients (tilt and curvature) of the Zernike polynomials decomposition of the spectrally-resolved spatial phase retrieved with TERMITES (red) and INSIGHT (blue). Tilt values are converted to lateral displacement of the focal spot, relative to the beam waist. Equivalently, curvature values are expressed in longitudinal displacement of the focal spot, relative to the Rayleigh range of the focused beam. The displacements are calculated relative to the ideal transverse and longitudinal focal positions, i.e. the intersection of the optical axis with the focal plane of the parabola.

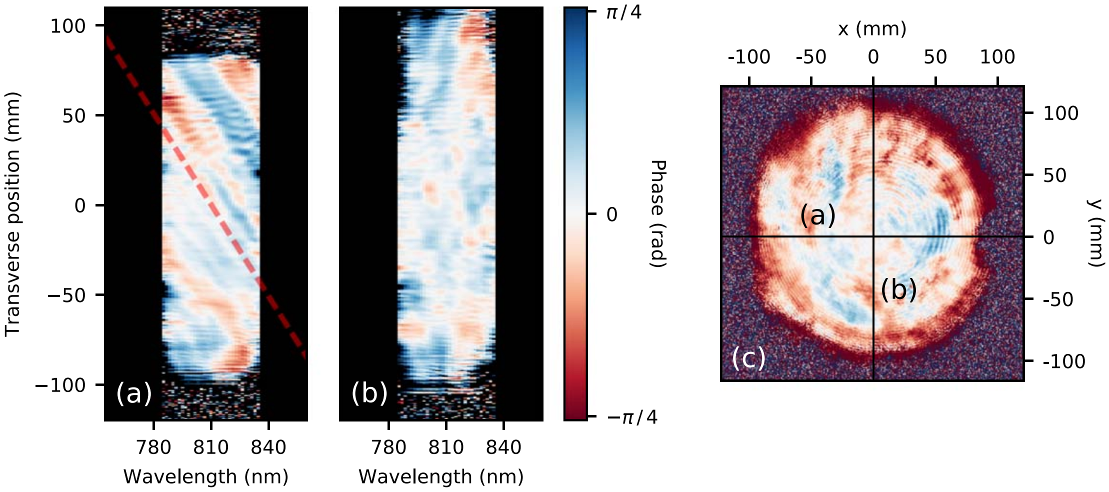

**Figure 5.** Spatio-spectral phase of the collimated BELLA beam, measured with TERMITES. Plots (a) and (b) respectively display $(x, \omega)$ and $(y, \omega)$ slices of this spatio-spectral phase, across the horizontal and vertical planes, at the center of the beam (see lines in image (c) showing a 2D phase profile at one frequency, with the spectrally-averaged wavefront subtracted). The red dashed line in (a) shows the estimated slope of the oblique spatio-spectral pattern that would be induced by spatial defects of optical elements located within the compressor, where the beam is laterally chirped. The origin of this line is arbitrary.

on each side of the main focal spot, with one satellite pulse advanced in time and the other delayed with respect to the main pulse by $\pm 2\pi s/\Lambda$ ($s$ is the slope of the modulation). For the parameters seen in the measurements presented here ($\lambda_0 = 810$ nm, $f = 13.5$ m, $\Lambda \approx 4$ cm, $s = 0.445$ m fs rad$^{-1}$ or 1.31 mm nm$^{-1}$ as in the figure) this results in an offset of 273 $\mu$m and 71 fs in space and time respectively. With an amplitude of 0.4 rad peak-to-valley over most of the beam, the satellite foci only contain 2% of the beam energy, and are at least 100× less intense than the main pulse.

Because of the relatively low amplitude of these modulations, most of the associated signal falls within the background of images acquired around focus. As a result, they are not retrieved in the near-field when using the INSIGHT measurements, although this might in principle be possible by using a camera with an increased dynamic range. More generally, TERMITES tends to have a much higher spatial resolution than other techniques for reconstruction of collimated beams: this clearly appears when comparing the different profiles in figure 2. This is because resolving the spatial interference fringes generated by the TERMITES interferometer requires a very high spatial sampling of the collimated beam (above 2000 × 2000 pixels within the beam profile here), which is preserved in the final reconstruction of the beam. Use of a larger camera chip for INSIGHT measurements would also increase the resolution in the calculated near-field data, but this is generally impractical when small pixels are also necessary to resolve the focal spot.

To quantify the impact of these various phase aberrations on the laser performance at focus, we define and calculate two different spatio-temporal Strehl ratios of the beam (see the supplementary document for details). The first one, $\mathrm{SR_{Full}}$, is the full spatio-temporal Strehl ratio: it is defined as the ratio of the actual peak intensity at focus, derived from the measured $E$-field, to the peak intensity that would be obtained for a beam with the same spatio-spectral amplitude, but with a perfectly constant spatio-spectral phase. This accounts for all phase aberrations present on the beam, both chromatic (i.e. frequency-dependent) and achromatic. We find $\mathrm{SR_{Full}} = 0.62$ from TERMITES data, and $\mathrm{SR_{Full}} = 0.88$ from the INSIGHT data. We note that the contribution of the oblique spatio-spectral pattern induced by the compressor (detected by TERMITES and not by INSIGHT) to this intensity reduction is actually very weak, so this cannot account for the different values of $\mathrm{SR_{Full}}$ predicted by the two techniques.

The second Strehl ratio of interest, $\mathrm{SR_{STC}}$, is defined as the ratio of the peak intensity at focus now calculated with the frequency-averaged wavefront distortions removed, to the peak intensity that would be obtained with a perfectly constant spatio-spectral phase. This corresponds to the Strehl ratio that would be achieved if the laser beam wavefront was corrected by a *perfect* adaptive optical system, removing all achromatic phase aberrations—while the deformable mirror actually used in the experiment still leaves some residual frequency-independent wavefront distortions (displayed in figure 2). This optimally-corrected beam would then still suffer from chromatic aberrations, which we detect in the present work. We find $\mathrm{SR_{STC}} = 0.85$ for TERMITES, and $\mathrm{SR_{STC}} = 0.92$ for INSIGHT. This shows that in the case of BELLA, the intensity reduction induced by purely chromatic effects is limited.

These calculations indicate that the significant difference in values of $\mathrm{SR_{Full}}$ derived from the two techniques, mostly originates from differences in the frequency-averaged beam properties, rather than from chromatic effects. The TERMITES and INSIGHT measurements were conducted one week apart, and indeed measurements with a standard wavefront sensor (HASO) indicate a lower frequency-averaged Strehl ratio in the week of the TERMITES measurements (see supplementary document). However, this difference is too weak to fully account for the one found on $\mathrm{SR_{Full}}$ between the TERMITES and INSIGHT results. This could be due to differences in the additional aberrations introduced in the transport line or measurement devices themselves, or to a more accurate calculation of the Strehl ratios from the TERMITES data due to the very high spatial resolution of this technique. More systematic and thorough measurement campaigns on smaller laser systems will be required to elucidate this point. In any case, along with the introduction of these calculations, the relatively good agreement and low severity of the $\mathrm{SR_{STC}}$ values are key results of this work.

We have so far concentrated on the phase properties of the BELLA beam, but our measurements actually also reveal interesting effects on the spatio-spectral intensity: as observed in figure 3, the beam mode size and shape significantly vary with frequency. As the frequency increases, the beam diameter increases, and the beam profile turns to a ring shape. The fact that the clip imprinted on the right edge of the beam (see figure 2 and explanations in its caption) is observed on the blue side of the spectrum but not on the red one clearly indicates that this is not a measurement artifact. We also emphasize that the reconstruction of such fine features in the near-field beam profile from INSIGHT data is quite remarkable, since the measurement was actually performed around focus, and the beam was then numerically propagated to a plane far from focus. This provides a strong validation of the spatial phase retrieved at focus with INSIGHT.

We can use simple numerical modeling to show that this frequency-dependent intensity profile is an intrinsic feature of high-power CPA lasers, which had not been clearly identified so far, to the best of our knowledge. To this end, we have modeled the amplification of the BELLA beam in the successive amplifiers, using the Frantz–Nodvik equations and considering a positively chirped laser beam (i.e. lower frequencies arrive

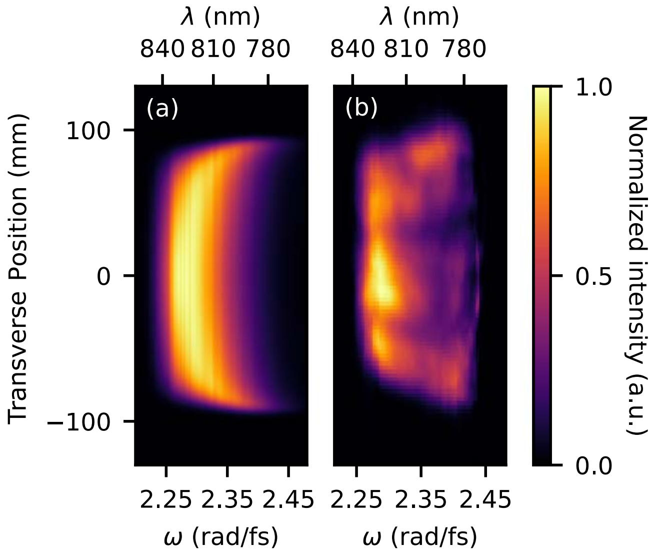

**Figure 6.** Spatio-spectral intensity of the BELLA beam. The left image displays the $(x, \omega)$ slice of this spatio-spectral intensity, across the horizontal plane, at the center of the beam $(x = y = 0)$, deduced from simulations of the CPA process based on the Frantz–Nodvik equations. The right image shows the same quantity, now derived from INSIGHT measurements at full power. To clearly highlight the spectral evolution of the beam spatial profile in these plots, the total energy in the beam at each frequency has been normalized to 1 (i.e. $\int dxdy\tilde{A}^2(x, y, \omega) = 1$ for all $\omega$ within the laser spectrum).

first). Details of these simulations are provided in the supplementary document, and essentially start with a measured spectrum after the XPW stage (where the spectral phase is flat), and the spectral phase imparted by the stretcher immediately after. This beam is then amplified in the successive five amplifier stages, with the pump and seed modeled in space, and the full spectral gain cross-section taken in to account. In figure 6, the $(x, \omega)$ spatio-spectral intensity profile of the beam predicted by these simulations for full power operating conditions (panel a) is compared to the one deduced from our INSIGHT measurements (panel b, same data as in figure 3), revealing a good qualitative agreement.

These simulations can then be exploited to get a simple interpretation of this effect: in the CPA scheme, the lower frequencies arrive first in the amplification medium, and are more efficiently amplified in the center of the beam. These frequencies deplete the amplification medium before the whole chirped pulse has been amplified. As a result, higher frequencies, which arrive later, are more efficiently amplified on the beam edges than at its center. This qualitatively explains the spectral evolution of the beam size, and the ring shape observed at high frequencies.

## Conclusion

In conclusion, we have reported the first spatio-temporal characterization of a PW femtosecond laser, carried out with two independent measurement techniques, with the laser focused at full power in the experimental chamber. These measurements show that the BELLA laser does not suffer from major chromatic aberrations that would severely degrade its performance. We estimate the reduction in peak intensity resulting merely from spatio-temporal couplings to about 10%, thus demonstrating that the CPA technique is still suitable and manageable at these extreme scales. We note however that significant chromatic effects start appearing on the red edge of the spectrum, suggesting that the beam optimization would possibly get more challenging for lasers with broader spectra, such as PW lasers now under construction in different laboratories worldwide.

These measurements provide very fine information on the beam properties and the laser system operation. In particular, we have observed small spatio-spectral modulations that have recently been predicted [21] to result from defects of optics within the grating compressor, as well as effects resulting from the temporal dynamics of the gain during the amplification of the chirped laser pulses. As ultrahigh intensity laser-plasma interaction experiments put more and more stringent requirements on the control of the laser parameters, such information could be used in the future for extremely fine optimization of high-power laser systems.

Laser-matter interaction experiments should ultimately greatly benefit from this new degree of knowledge of ultrashort laser beams. For instance, in the case of BELLA, the full spatio-temporal profile of the laser beam can be calculated in any arbitrary plane (see supplementary movie 3), and this can be used as an input for a realistic description of the laser field in 3D Particle-In-Cell simulations. This opens the way to a deeper understanding of laser-wakefield electron acceleration experiments on this system, which require guiding of the beam in plasma channels of many centimeters in length. This could ultimately contribute to an unprecedented optimization of laser-plasma accelerators.

## Acknowledgments

The authors gratefully acknowledge Amplitude Laser Group for their support. We also thank Chris Pieronek for helping with the experiment, Donald Syversrud, Zachary Eisentraut, David Evans, Nathan Ybarrolaza and Greg Mannino for technical support.

## Funding information

The research leading to this work has been funded by the ERC (grant ExCoMet number 694596), by Investissements d'Avenir LabEx PALM (projects EXYT and IMAPS), by the CEA's DFR Impulsion program, and has received financial support from Amplitude Laser Group. The work at the BELLA facility was supported by the Director, Office of Science, Office of High Energy Physics of the U.S. Department of Energy under Contract No. DE-AC02-05CH11231.

## ORCID iDs

Antoine Jeandet https://orcid.org/0000-0003-4549-3067
Kei Nakamura https://orcid.org/0000-0001-9842-7114
Spencer W Jolly https://orcid.org/0000-0002-5783-2081
Fabien Quéré https://orcid.org/0000-0002-4343-9780

## References

[1] Nakamura K, Mao H S, Gonsalves A J, Vincenti H, Mittelberger D E, Daniels J, Magana A, Toth C and Leemans W P 2017 *IEEE J. Quantum Electron.* **53** 1200121
[2] Sung J H, Lee H W, Yoo J Y, Yoon J W, Lee C W, Yang J M, Son Y J, Jang Y H, Lee S K and Nam C H 2017 *Opt. Lett.* **42** 2058–61
[3] Zeng X *et al* 2017 *Opt. Lett.* **42** 2014–7
[4] Clayton C E *et al* 2010 *Phys. Rev. Lett.* **105** 105003
[5] Wang X *et al* 2013 *Nat. Commun.* **4** 1988
[6] Leemans W P *et al* 2014 *Phys. Rev. Lett.* **113** 245002
[7] Kim H T *et al* 2017 *Sci. Rep.* **7** 10203
[8] Gonsalves A J *et al* 2019 *Phys. Rev. Lett.* **122** 084801
[9] Marklund M and Shukla P K 2006 *Rev. Mod. Phys.* **78** 591–640
[10] Strickland D and Mourou G 1985 *Opt. Commun.* **56** 219–21
[11] Bor Z 1989 *Opt. Lett.* **14** 119
[12] Bowlan P, Gabolde P, Shreenath A, McGresham K, Trebino R and Akturk S 2006 *Opt. Express* **14** 11892–900
[13] Cousin S L, Bueno J M, Forget N, Austin D R and Biegert J 2012 *Opt. Lett.* **37** 3291
[14] Wyatt A S, Walmsley I A, Stibenz G and Steinmeyer G 2006 *Opt. Lett.* **31** 1914
[15] Gabolde P and Trebino R 2006 *Opt. Express* **14** 11460–7
[16] Dorrer C and Bahk S W 2018 *Opt. Express* **26** 33387
[17] Miranda M, Kotur M, Rudawski P, Guo C, Harth A, L'Huillier A and Arnold C L 2014 *Opt. Lett.* **39** 5142–4
[18] Pariente G, Gallet V, Borot A, Gobert O and Quéré F 2016 *Nat. Photon.* **10** 547–53
[19] Borot A and Quéré F 2018 *Opt. Express* **26** 26444–61
[20] Goodman J W 2005 *Introduction To Fourier Optics* 3rd edn (Englewood, CO: Roberts & Company)
[21] Li Z, Tsubakimoto K, Yoshida H, Nakata Y and Miyanaga N 2017 *Appl. Phys. Express* **10** 102702

# Bibliography

[1] J. Hecht. 'Short History of Laser Development'. In: *Opt. Eng* 49.9 (2010), p. 091002. DOI: 10.1117/1.3483597 (cited on page 1).

[2] A. H. Zewail. 'Femtochemistry: Atomic-Scale Dynamics of the Chemical Bond $^\dagger$'. In: *J. Phys. Chem. A* 104.24 (2000), pp. 5660–5694. DOI: 10.1021/jp001460h (cited on page 1).

[3] S. Nolte et al. 'Ablation of Metals by Ultrashort Laser Pulses'. In: *J. Opt. Soc. Am. B* 14.10 (1997), p. 2716. DOI: 10.1364/JOSAB.14.002716 (cited on page 1).

[4] A. Vogel et al. 'Mechanisms of Femtosecond Laser Nanosurgery of Cells and Tissues'. In: *Appl. Phys. B* 81.8 (2005), pp. 1015–1047. DOI: 10.1007/s00340-005-2036-6 (cited on page 1).

[5] M. Lewenstein et al. 'Theory of High-Harmonic Generation by Low-Frequency Laser Fields'. In: *Phys. Rev. A* 49.3 (1994), pp. 2117–2132. DOI: 10.1103/PhysRevA.49.2117 (cited on page 1).

[6] R. Lichters, J. Meyer-ter-Vehn and A. Pukhov. 'Short-pulse Laser Harmonics from Oscillating Plasma Surfaces Driven at Relativistic Intensity'. In: *Physics of Plasmas* 3.9 (1996), pp. 3425–3437. DOI: 10.1063/1.871619 (cited on page 1).

[7] F. Quéré et al. 'Coherent Wake Emission of High-Order Harmonics from Overdense Plasmas'. In: *Phys. Rev. Lett.* 96.12 (2006), p. 125004. DOI: 10.1103/PhysRevLett.96.125004 (cited on page 1).

[8] M. Hentschel et al. 'Attosecond Metrology'. In: *Nature* 414.6863 (2001), pp. 509–513. DOI: 10.1038/35107000 (cited on page 1).

[9] J. Faure et al. 'A Laser–Plasma Accelerator Producing Monoenergetic Electron Beams'. In: *Nature* 431.7008 (2004), pp. 541–544. DOI: 10.1038/nature02963 (cited on page 1).

[10] C. G. R. Geddes et al. 'High-Quality Electron Beams from a Laser Wakefield Accelerator Using Plasma-Channel Guiding'. In: *Nature* 431.7008 (2004), pp. 538–541. DOI: 10.1038/nature02900 (cited on page 1).

[11] S. P. D. Mangles et al. 'Monoenergetic Beams of Relativistic Electrons from Intense Laser–Plasma Interactions'. In: *Nature* 431.7008 (2004), pp. 535–538. DOI: 10.1038/nature02939 (cited on page 1).

[12] A. J. Gonsalves et al. 'Petawatt Laser Guiding and Electron Beam Acceleration to 8 GeV in a Laser-Heated Capillary Discharge Waveguide'. In: *Phys. Rev. Lett.* 122.8 (2019), p. 084801. DOI: 10.1103/PhysRevLett.122.084801 (cited on page 1).

[13] R. A. Snavely et al. 'Intense High-Energy Proton Beams from Petawatt-Laser Irradiation of Solids'. In: *Phys. Rev. Lett.* 85.14 (2000), pp. 2945–2948. DOI: `10.1103/PhysRevLett.85.2945` (cited on page 1).

[14] H. Schwoerer et al. 'Laser-Plasma Acceleration of Quasi-Monoenergetic Protons from Microstructured Targets'. In: *Nature* 439.7075 (2006), pp. 445–448. DOI: `10.1038/nature04492` (cited on page 1).

[15] S. Steinke et al. 'Acceleration of High Charge Ion Beams with Achromatic Divergence by Petawatt Laser Pulses'. In: *Phys. Rev. Accel. Beams* 23.2 (2020), p. 021302. DOI: `10.1103/PhysRevAccelBeams.23.021302` (cited on page 1).

[16] A. R. Bell and J. G. Kirk. 'Possibility of Prolific Pair Production with High-Power Lasers'. In: *Phys. Rev. Lett.* 101.20 (2008), p. 200403. DOI: `10.1103/PhysRevLett.101.200403` (cited on page 1).

[17] H. Vincenti. 'Achieving Extreme Light Intensities Using Optically Curved Relativistic Plasma Mirrors'. In: *Phys. Rev. Lett.* 123.10 (2019), p. 105001. DOI: `10.1103/PhysRevLett.123.105001` (cited on page 1).

[18] S. Backus et al. 'High Power Ultrafast Lasers'. In: *Review of Scientific Instruments* 69.3 (1998), pp. 1207–1223. DOI: `10.1063/1.1148795` (cited on pages 1, 11).

[19] C. N. Danson et al. 'Petawatt and Exawatt Class Lasers Worldwide'. In: *High Pow Laser Sci Eng* 7 (2019), e54. DOI: `10.1017/hpl.2019.36` (cited on pages 1, 11).

[20] D. Papadopoulos et al. 'The Apollon 10 PW Laser: Experimental and Theoretical Investigation of the Temporal Characteristics'. In: *High Pow Laser Sci Eng* 4 (2016), e34. DOI: `10.1017/hpl.2016.34` (cited on page 1).

[21] D. Strickland and G. Mourou. 'Compression of Amplified Chirped Optical Pulses'. In: *Optics Communications* 56.3 (1985), pp. 219–221. DOI: `10.1016/0030-4018(85)90120-8` (cited on pages 2, 10).

[22] O. Martinez. 'Design of High-Power Ultrashort Pulse Amplifiers by Expansion and Recompression'. In: *IEEE J. Quantum Electron.* 23.8 (1987), pp. 1385–1387. DOI: `10.1109/JQE.1987.1073518` (cited on pages 2, 10).

[23] P. Maine et al. 'Generation of Ultrahigh Peak Power Pulses by Chirped Pulse Amplification'. In: *IEEE J. Quantum Electron.* 24.2 (1988), pp. 398–403. DOI: `10.1109/3.137` (cited on pages 2, 10).

[24] W. Thomson. *Popular Lectures and Addresses.* Cambridge University Press, 1891. DOI: `10.1017/CBO9780511997235` (cited on page 2).

[25] R. Trebino. *Frequency-Resolved Optical Gating: The Measurement of Ultrashort Laser Pulses.* Boston: Kluwer Academic, 2000. 425 pp. DOI: `10.1007/978-1-4615-1181-6` (cited on pages 2, 16, 18, 67).

[26] I. A. Walmsley and C. Dorrer. ‘Characterization of Ultrashort Electromagnetic Pulses’. In: *Advances in Optics and Photonics* 1.2 (2009), p. 308. DOI: `10.1364/AOP.1.000308` (cited on pages 2, 16).

[27] J. Primot. ‘Theoretical Description of Shack–Hartmann Wave-Front Sensor’. In: *Optics Communications* 222.1-6 (2003), pp. 81–92. DOI: `10.1016/S0030-4018(03)01565-7` (cited on pages 3, 15).

[28] B. C. Platt and R. Shack. ‘History and Principles of Shack-Hartmann Wavefront Sensing’. In: *Journal of Refractive Surgery* 17.5 (2001), S573–S577. DOI: `10.3928/1081-597X-20010901-13` (cited on pages 3, 15).

[29] J. Primot and L. Sogno. ‘Achromatic Three-Wave (or More) Lateral Shearing Interferometer’. In: *J. Opt. Soc. Am. A* 12.12 (1995), p. 2679. DOI: `10.1364/JOSAA.12.002679` (cited on pages 3, 15).

[30] J.-C. Chanteloup. ‘Multiple-Wave Lateral Shearing Interferometry for Wave-Front Sensing’. In: *Applied Optics* 44.9 (2005), p. 1559. DOI: `10.1364/AO.44.001559` (cited on pages 3, 15, 121).

[31] H. Vincenti and F. Quéré. ‘Attosecond Lighthouses: How To Use Spatiotemporally Coupled Light Fields To Generate Isolated Attosecond Pulses’. In: *Physical Review Letters* 108.11 (2012). DOI: `10.1103/PhysRevLett.108.113904` (cited on pages 3, 25).

[32] E. Balogh et al. ‘Dynamic Wavefront Rotation in the Attosecond Lighthouse’. In: *Optica* 4.1 (2017), p. 48. DOI: `10.1364/OPTICA.4.000048` (cited on pages 3, 25).

[33] A. Sainte-Marie, O. Gobert and F. Quéré. ‘Controlling the Velocity of Ultrashort Light Pulses in Vacuum through Spatio-Temporal Couplings’. In: *Optica* 4.10 (2017), p. 1298. DOI: `10.1364/OPTICA.4.001298` (cited on pages 3, 27, 94).

[34] D. Turnbull et al. ‘Ionization Waves of Arbitrary Velocity’. In: *Physical Review Letters* 120.22 (2018). DOI: `10.1103/PhysRevLett.120.225001` (cited on pages 3, 27, 94).

[35] D. Turnbull et al. ‘Raman Amplification with a Flying Focus’. In: *Physical Review Letters* 120.2 (2018). DOI: `10.1103/PhysRevLett.120.024801` (cited on pages 3, 27, 94).

[36] D. H. Froula et al. ‘Spatiotemporal Control of Laser Intensity’. In: *Nature Photonics* 12.5 (2018), pp. 262–265. DOI: `10.1038/s41566-018-0121-8` (cited on pages 3, 27, 94).

[37] S. Jolly et al. ‘Controlling the Velocity of a Femtosecond Laser Pulse Using Refractive Lenses’. In: *Opt. Express* (2020). DOI: `10.1364/OE.384512` (cited on pages 3, 27, 94, 143).

[38] F. Courvoisier et al. ‘Sending Femtosecond Pulses in Circles: Highly Nonparaxial Accelerating Beams’. In: *Opt. Lett.* 37.10 (2012), p. 1736. DOI: `10.1364/OL.37.001736` (cited on page 3).

[39] G. Zhu et al. ‘Simultaneous Spatial and Temporal Focusing of Femtosecond Pulses’. In: (2005), p. 7 (cited on page 3).

[40] C. Dorrer. ‘Spatiotemporal Metrology of Broadband Optical Pulses’. In: *IEEE Journal of Selected Topics in Quantum Electronics* 25.4 (2019), pp. 1–16. DOI: `10.1109/JSTQE.2019.2899019` (cited on pages 3, 31).

[41] V. Gallet. ‘Dispositifs expérimentaux pour la caractérisation spatio-temporelle de chaines laser femtosecondes haute-puissance’. PhD thesis. Université Paris Sud, 2014. URL: `https://hal.archives-ouvertes.fr/tel-01084002/document` (cited on pages 4, 49, 129).

[42] G. Pariente. ‘Caractérisation spatio-temporelle d’impulsions laser de haute puissance’. PhD thesis. Université Paris-Saclay, 2017. URL: `https://hal.archives-ouvertes.fr/tel-01487697/document` (cited on pages 4, 23, 53, 54, 68, 73, 120, 129, 138).

[43] G. Pariente et al. ‘Space–Time Characterization of Ultra-Intense Femtosecond Laser Beams’. In: *Nature Photonics* 10.8 (2016), pp. 547–553. DOI: `10.1038/nphoton.2016.140` (cited on pages 4, 56, 73, 120, 123, 129, 138).

[44] F. Quéré, V. Gallet and G. Pariente. ‘Device and Method for Characterization of a Light Beam’. Pat. WO 2015/193253. CEA. 2015 (cited on page 4).

[45] Robert H. Dicke. ‘Object Detection System’. U.S. pat. 2624876. 1945 (cited on page 10).

[46] C. Cook. ‘Pulse Compression-Key to More Efficient Radar Transmission’. In: *Proc. IRE* 48.3 (1960), pp. 310–316. DOI: `10.1109/JRPROC.1960.287599` (cited on page 10).

[47] J. Itatani et al. ‘Generation of 13-TW, 26-Fs Pulses in a Ti:Sapphire Laser’. In: *Optics Communications* 134.1-6 (1997), pp. 134–138. DOI: `10.1016/S0030-4018(96)00588-3` (cited on page 10).

[48] A. Offner. ‘Unit Power Imaging Catoptric Anastigmat’. U.S. pat. 3748015 (A). Perkin Elmer Corp. 1973 (cited on page 10).

[49] A. Suzuki. ‘Complete Analysis of a Two-Mirror Unit Magnification System. Part’. In: (), p. 7 (cited on page 10).

[50] J. Zhou et al. ‘Amplification of 26-Fs, 2-TW Pulses near the Gain-Narrowing Limit in Ti:Sapphire’. In: *Opt. Lett.* 20.1 (1995), p. 64. DOI: `10.1364/OL.20.000064` (cited on page 10).

[51] G. Cheriaux et al. ‘Aberration-Free Stretcher Design for Ultrashort-Pulse Amplification’. In: *Opt. Lett.* 21.6 (1996), p. 414. DOI: `10.1364/OL.21.000414` (cited on page 10).

[52] C. P. J. Barty, C. L. Gordon and B. E. Lemoff. ‘Multiterawatt 30-Fs Ti:Sapphire Laser System’. In: *Opt. Lett.* 19.18 (1994), p. 1442. DOI: `10.1364/OL.19.001442` (cited on page 11).

[53] E. Cartlidge. ‘The Light Fantastic’. In: *Science* 359.6374 (2018), pp. 382–385. DOI: `10.1126/science.359.6374.382` (cited on page 11).

[54] E. Treacy. ‘Optical Pulse Compression with Diffraction Gratings’. In: *IEEE J. Quantum Electron.* 5.9 (1969), pp. 454–458. DOI: `10.1109/JQE.1969.1076303` (cited on page 11).

[55] O. Svelto and D. C. Hanna. *Principles of Lasers.* 5th ed. New York: Springer, 2010. 620 pp. (cited on page 11).

[56] M. Nisoli, S. De Silvestri and O. Svelto. ‘Generation of High Energy 10 Fs Pulses by a New Pulse Compression Technique’. In: *Appl. Phys. Lett.* 68.20 (1996), pp. 2793–2795. DOI: `10.1063/1.116609` (cited on page 11).

[57] S. Sartania et al. ‘Generation of 0.1 TW 5 Fs Optical Pulses at a 1 kHz Repetition Rate’. In: *Opt. Lett.* 22.20 (1997), p. 1562. DOI: `10.1364/OL.22.001562` (cited on page 11).

[58] ISO 11146. ‘Test Methods for Laser Beam Widths, Divergence Angles and Beam Propagation Ratios’. In: *ISO Standards Catalog 31.260* (2005) (cited on page 14).

[59] ISO 13694. ‘Test Methods for Laser Beam Power (Energy) Density Distribution’. In: *ISO Standards Catalog 31.260* (2018) (cited on page 14).

[60] ISO 15367. ‘Test Methods for Determination of the Shape of a Laser Beam Wavefront’. In: *ISO Standards Catalog 31.260* (2003) (cited on page 14).

[61] A. E. Siegman. ‘How to (Maybe) Measure Laser Beam Quality’. In: *DPSS (Diode Pumped Solid State) Lasers: Applications and Issues.* Diode Pumped Solid State Lasers: Applications and Issues. Washington, D.C.: OSA, 1998, MQ1. DOI: `10.1364/DLAI.1998.MQ1` (cited on page 15).

[62] U. Schnars et al. *Digital Holography and Wavefront Sensing.* Berlin, Heidelberg: Springer Berlin Heidelberg, 2015. DOI: `10.1007/978-3-662-44693-5` (cited on page 15).

[63] R. W. Gerchberg and W. O. Saxton. ‘A Practical Algorithm for the Determination of Phase from Image and Diffraction Plane Pictures’. In: 35 (1972), p. 6 (cited on page 15).

[64] J. A. Snyman and D. N. Wilke. *Practical Mathematical Optimization.* Vol. 133. Springer Optimization and Its Applications. Cham: Springer International Publishing, 2018. DOI: `10.1007/978-3-319-77586-9` (cited on page 15).

[65] Strehl, Karl. ‘Aplanatische Und Fehlerhafte Abbildung Im Fernrohr’. In: *Zeitschrift für Instrumentenkunde* (1895), pp. 362–370 (cited on page 16).

[66] ISO 13695. ‘Test Methods for the Spectral Characteristics of Lasers’. In: *ISO Standards Catalog 31.260* (2004) (cited on page 16).

[67] ISO 11554. ‘Test Methods for Laser Beam Power, Energy and Temporal Characteristics’. In: *ISO Standards Catalog 31.260* (2017) (cited on page 16).

[68] G. Steinmeyer. 'A Review of Ultrafast Optics and Optoelectronics'. In: *J. Opt. A: Pure Appl. Opt.* 5.1 (2003), R1–R15. DOI: `10.1088/1464-4258/5/1/201` (cited on pages 16–18).

[69] J.-C. Diels and W. Rudolph. *Ultrashort Laser Pulse Phenomena: Fundamentals, Techniques, and Applications on a Femtosecond Time Scale.* 2nd ed. Optics and Photonics. Amsterdam ; Boston: Elsevier / Academic Press, 2006. 652 pp. (cited on page 17).

[70] R. Trebino et al. 'Measuring Ultrashort Laser Pulses in the Time-Frequency Domain Using Frequency-Resolved Optical Gating'. In: *Review of Scientific Instruments* 68.9 (1997), pp. 3277–3295. DOI: `10.1063/1.1148286` (cited on pages 17, 60).

[71] C. Iaconis and I. A. Walmsley. 'Spectral Phase Interferometry for Direct Electric-Field Reconstruction of Ultrashort Optical Pulses'. In: *Optics Letters* 23.10 (1998), p. 792. DOI: `10.1364/OL.23.000792` (cited on page 18).

[72] J. W. Goodman. *Introduction To Fourier Optics.* 3rd Revised edition. Englewood, Colo: Roberts & Company Publishers, 2005. 528 pp. (cited on page 22).

[73] S. Akturk et al. 'The General Theory of First-Order Spatio-Temporal Distortions of Gaussian Pulses and Beams'. In: *Optics Express* 13.21 (2005) (cited on page 23).

[74] A. G. Kostenbauder. 'Ray-Pulse Matrices: A Rational Treatment for Dispersive Optical Systems'. In: *IEEE Journal of Quantum Electronics* 26.6 (1990), pp. 1148–1157. DOI: `10.1109/3.108113` (cited on page 23).

[75] S. Akturk et al. 'Pulse-Front Tilt Caused by Spatial and Temporal Chirp'. In: *Opt. Express* 12.19 (2004), p. 4399. DOI: `10.1364/OPEX.12.004399` (cited on page 26).

[76] Z. Bor. 'Distortion of Femtosecond Laser Pulses in Lenses and Lens Systems'. In: *Journal of Modern Optics* 35.12 (1988), pp. 1907–1918. DOI: `10.1080/713822325` (cited on pages 26, 105, 117).

[77] Z. Li et al. 'Degradation of Femtosecond Petawatt Laser Beams: Spatio-Temporal/Spectral Coupling Induced by Wavefront Errors of Compression Gratings'. In: *Applied Physics Express* 10.10 (2017), p. 102702. DOI: `10.7567/APEX.10.102702` (cited on pages 29, 97).

[78] J. Bromage, C. Dorrer and R. K. Jungquist. 'Temporal Contrast Degradation at the Focus of Ultrafast Pulses from High-Frequency Spectral Phase Modulation'. In: *J. Opt. Soc. Am. B* 29.5 (2012), p. 1125. DOI: `10.1364/JOSAB.29.001125` (cited on page 30).

[79] C. Hooker et al. 'Improving Coherent Contrast of Petawatt Laser Pulses'. In: *Opt. Express* 19.3 (2011), p. 2193. DOI: `10.1364/OE.19.002193` (cited on page 30).

[80] D. N. Papadopoulos et al. 'High-Contrast 10 Fs OPCPA-Based Front End for Multi-PW Laser Chains'. In: *Opt. Lett.* 42.18 (2017), p. 3530. DOI: `10.1364/OL.42.003530` (cited on page 30).

[81] C. Froehly, A. Lacourt and J. C. Viénot. 'Time Impulse Response and Time Frequency Response of Optical Pupils.:Experimental Confirmations and Applications'. In: *Nouvelle Revue d'Optique* 4.4 (1973), pp. 183–196. DOI: `10.1088/0335-7368/4/4/301` (cited on page 31).

[82] B. Alonso et al. 'Spatiotemporal Amplitude-and-Phase Reconstruction by Fourier-Transform of Interference Spectra of High-Complex-Beams'. In: *JOSA B* 27.5 (2010), pp. 933–940. URL: `https://www.osapublishing.org/abstract.cfm?uri=josab-27-5-933` (cited on pages 31, 32).

[83] B. Alonso et al. 'Spatiotemporal Characterization of Few-Cycle Laser Pulses'. In: *Opt. Express* 20.16 (2012), p. 17880. DOI: `10.1364/OE.20.017880` (cited on page 31).

[84] P. Bowlan et al. 'Crossed-Beam Spectral Interferometry: A Simple, High-Spectral-Resolution Method for Completely Characterizing Complex Ultrashort Pulses in Real Time'. In: *Optics Express* 14.24 (2006), pp. 11892–11900. URL: `https://www.osapublishing.org/abstract.cfm?uri=oe-14-24-11892` (cited on page 32).

[85] C. Dorrer, E. Kosik and I. Walmsley. 'Spatio-Temporal Characterization of the Electric Field of Ultrashort Optical Pulses Using Two-Dimensional Shearing Interferometry'. In: *Appl Phys B* 74.S1 (2002), s209–s217. DOI: `10.1007/s00340-002-0912-x` (cited on page 32).

[86] S. L. Cousin et al. 'Three-Dimensional Spatiotemporal Pulse Characterization with an Acousto-Optic Pulse Shaper and a Hartmann–Shack Wavefront Sensor'. In: *Optics Letters* 37.15 (2012), p. 3291. DOI: `10.1364/OL.37.003291` (cited on page 33).

[87] A. Borot and F. Quéré. 'Spatio-Spectral Metrology at Focus of Ultrashort Lasers: A Phase-Retrieval Approach'. In: *Opt. Express* 26.20 (2018), p. 26444. DOI: `10.1364/OE.26.026444` (cited on pages 33, 34).

[88] R. J. Noll. 'Zernike Polynomials and Atmospheric Turbulence'. In: *J. Opt. Soc. Am.* 66.3 (1976), p. 207. DOI: `10.1364/JOSA.66.000207` (cited on page 36).

[89] A. E. Potter Jr. 'Multispectral Imaging System'. U.S. pat. 3702735A. National Aeronautics and Space Administration (NASA) (cited on pages 44, 50).

[90] R. D. Alcock and J. M. Coupland. 'A Compact, High Numerical Aperture Imaging Fourier Transform Spectrometer and Its Application'. In: *Meas. Sci. Technol.* 17.11 (2006), pp. 2861–2868. DOI: `10.1088/0957-0233/17/11/001` (cited on pages 44, 50).

[91] R. Bhargava. 'Infrared Spectroscopic Imaging: The Next Generation'. In: *Appl Spectrosc* 66.10 (2012), pp. 1091–1120. DOI: `10.1366/12-06801` (cited on pages 44, 50).

[92] G. B. Arfken and H.-J. Weber. *Mathematical Methods for Physicists*. 6th ed. Boston: Elsevier, 2005. 1182 pp. (cited on page 45).

[93] R. N. Smartt and W. H. Steel. 'Theory and Application of Point-Diffraction Interferometers'. In: *Japanese Journal of Applied Physics* 14.S1 (1975), p. 351. DOI: `10.7567/JJAPS.14S1.351` (cited on page 45).

[94] M. Miranda et al. 'Spatiotemporal Characterization of Ultrashort Laser Pulses Using Spatially Resolved Fourier Transform Spectrometry'. In: *Opt. Lett., OL* 39.17 (2014), pp. 5142–5145. DOI: `10.1364/OL.39.005142` (cited on page 46).

[95] P. Hariharan and D. Sen. 'Radial Shearing Interferometer'. In: *J. Sci. Instrum.* 38.11 (1961), pp. 428–432. DOI: `10.1088/0950-7671/38/11/305` (cited on page 46).

[96] D. S. Brown. 'Radial Shear Interferometry'. In: *J. Sci. Instrum.* 39.2 (1962), pp. 71–72. DOI: `10.1088/0950-7671/39/2/314` (cited on page 46).

[97] N. Abramson. 'Light-in-Flight Recording: High-Speed Holographic Motion Pictures of Ultrafast Phenomena'. In: *Appl. Opt., AO* 22.2 (1983), pp. 215–232. DOI: `10.1364/AO.22.000215` (cited on page 49).

[98] Z. Bor, Z. Gogolak and G. Szabo. 'Femtosecond-Resolution Pulse-Front Distortion Measurement by Time-of-Flight Interferometry'. In: *Optics letters* 14.16 (1989), pp. 862–864. DOI: `10.1364/OL.14.000862` (cited on pages 49, 105, 117).

[99] J. W. Cooley and J. W. Tukey. 'An Algorithm for the Machine Calculation of Complex Fourier Series'. In: *Math. Comp.* 19.90 (1965), pp. 297–301. DOI: `10.1090/S0025-5718-1965-0178586-1` (cited on page 51).

[100] S. van der Walt, S. C. Colbert and G. Varoquaux. 'The NumPy Array: A Structure for Efficient Numerical Computation'. In: *Computing in Science & Engineering* 13.2 (2011), pp. 22–30. DOI: `10.1109/MCSE.2011.37` (cited on page 51).

[101] K. Turkowski. 'Filters for Common Resampling Tasks'. In: *Graphics Gems*. Elsevier, 1990, pp. 147–165. DOI: `10.1016/B978-0-08-050753-8.50042-5` (cited on page 53).

[102] V. S. Chakravarthi, ed. *Proceedings of International Conference on VLSI, Communication, Advanced Devices, Signals & Systems and Networking (VCASAN-2013) / Veena S. Chakravarthi, Yasha Jyothi M. Shirur, Rekha P., Editors.* Lecture Notes in Electrical Engineering Volume 258. New Delhi: Springer, 2013. 472 pp. DOI: `10.1007/978-81-322-1524-0` (cited on page 53).

[103] M. A. Herráez et al. 'Fast Two-Dimensional Phase-Unwrapping Algorithm Based on Sorting by Reliability Following a Noncontinuous Path'. In: *Applied Optics* 41.35 (2002), pp. 7437–7444. DOI: `10.1364/AO.41.007437` (cited on page 54).

[104] S. van der Walt et al. 'Scikit-Image: Image Processing in Python'. In: *PeerJ* 2 (2014), e453. DOI: `10.7717/peerj.453` (cited on page 54).

[105] D. R. Kohler and V. L. Gamiz. 'Interferogram Reduction for Radial-Shear and Local-Reference-Holographic Interferograms'. In: *Appl. Opt.* 25.10 (1986), p. 1650. DOI: `10.1364/AO.25.001650` (cited on page 55).

[106] D. Li. 'Simple Algorithms of Wavefront Reconstruction for Cyclic Radial Shearing Interferometer'. In: *Opt. Eng* 41.8 (2002), p. 1893. DOI: `10.1117/1.1487854` (cited on page 55).

[107] E. L. Lago and R. de La Fuente. 'Amplitude and Phase Reconstruction by Radial Shearing Interferometry'. In: *Applied optics* 47.3 (2008), pp. 372–376. DOI: `10.1364/AO.47.000372` (cited on pages 55, 57).

[108] T. Oksenhendler et al. 'Self-Referenced Spectral Interferometry'. In: *Applied Physics B* 99.1-2 (2010), pp. 7–12. DOI: `10.1007/s00340-010-3916-y` (cited on page 60).

[109] R. N. Bracewell. *The Fourier Transform and Its Applications*. 3rd ed. McGraw-Hill Series in Electrical and Computer Engineering. Boston: McGraw Hill, 2000. 616 pp. (cited on page 67).

[110] K. Nakamura et al. 'Diagnostics, Control and Performance Parameters for the BELLA High Repetition Rate Petawatt Class Laser'. In: *IEEE Journal of Quantum Electronics* 53.4 (2017), pp. 1–21. DOI: `10.1109/JQE.2017.2708601` (cited on pages 86, 91).

[111] A. Jeandet et al. 'Spatio-Temporal Structure of a Petawatt Femtosecond Laser Beam'. In: *J. Phys. Photonics* (2019). DOI: `10.1088/2515-7647/ab250d` (cited on pages 91, 114, 121, 143).

[112] H.-M. Heuck et al. 'Chromatic Aberration in Petawatt-Class Lasers'. In: *Appl. Phys. B* 84.3 (2006), pp. 421–428. DOI: `10.1007/s00340-006-2230-1` (cited on pages 105, 117).

[113] M. Kempe et al. 'Spatial and Temporal Transformation of Femtosecond Laser Pulses by Lenses and Lens Systems'. In: *Journal of the Optical Society of America B* 9.7 (1992), p. 1158. DOI: `10.1364/JOSAB.9.001158` (cited on pages 105, 117).

[114] X. Gu, S. Akturk and R. Trebino. 'Spatial Chirp in Ultrafast Optics'. In: *Optics Communications* 242.4 (2004), pp. 599–604. DOI: `10.1016/j.optcom.2004.09.004` (cited on page 112).

[115] L. M. Frantz and J. S. Nodvik. 'Theory of Pulse Propagation in a Laser Amplifier'. In: *Journal of Applied Physics* 34.8 (1963), pp. 2346–2349. DOI: `10.1063/1.1702744` (cited on page 115).

[116] C. Durfee et al. 'Design and Implementation of a TW-Class High-Average Power Laser System'. In: *IEEE J. Select. Topics Quantum Electron.* 4.2 (1998), pp. 395–406. DOI: `10.1109/2944.686747` (cited on page 116).

[117] F. Giambruno et al. 'Design of a 10 PW (150 J/15 Fs) Peak Power Laser System with Ti:Sapphire Medium through Spectral Control'. In: *Applied Optics* 50.17 (2011), p. 2617. DOI: `10.1364/AO.50.002617` (cited on page 116).

[118] C. Tan. 'Determination of Refractive Index of Silica Glass for Infrared Wavelengths by IR Spectroscopy'. In: *Journal of Non-Crystalline Solids* 223.1-2 (1998), pp. 158–163. DOI: `10.1016/S0022-3093(97)00438-9` (cited on page 118).

[119] X. Chen et al. ‘Efficient Hollow Fiber Compression Scheme for Generating Multi-mJ, Carrier-Envelope Phase Stable, Sub-5 Fs Pulses’. In: *Laser Phys.* 21.1 (2011), pp. 198–201. DOI: `10.1134/S1054660X11010063` (cited on page 124).

[120] B. Alonso et al. ‘Characterization of Sub-Two-Cycle Pulses from a Hollow-Core Fiber Compressor in the Spatiotemporal and Spatiospectral Domains’. In: *Appl. Phys. B* 112.1 (2013), pp. 105–114. DOI: `10.1007/s00340-013-5406-5` (cited on page 124).

[121] T. Witting et al. ‘Characterization of High-Intensity Sub-4-Fs Laser Pulses Using Spatially Encoded Spectral Shearing Interferometry’. In: *Opt. Lett.* 36.9 (2011), p. 1680. DOI: `10.1364/OL.36.001680` (cited on page 124).

[122] T. Witting et al. ‘Sub-4-Fs Laser Pulse Characterization by Spatially Resolved Spectral Shearing Interferometry and Attosecond Streaking’. In: *J. Phys. B: At. Mol. Opt. Phys.* 45.7 (2012), p. 074014. DOI: `10.1088/0953-4075/45/7/074014` (cited on page 124).

[123] P. Tournois. ‘New Diffraction Grating Pair with Very Linear Dispersion for Laser Pulse Compression’. In: *Electron. Lett.* 29.16 (1993), p. 1414. DOI: `10.1049/el:19930947` (cited on page 126).

université PARIS-SACLAY
ÉCOLE DOCTORALE
Ondes et matière
(EDOM)

**Titre:** Caractérisation Spatio-Temporelle d'Impulsions Laser Femtoseconde par Spectroscopie à Transformée de Fourier auto-référencée

**Mots clés:** métrologie, interférométrie, laser femtoseconde, couplages spatio-temporels

**Résumé :** La technologie actuelle des lasers ultrabrefs permet de délivrer des impulsions d'une énergie de quelques dizaines de joules dont la durée est de l'ordre de la dizaine de femtosecondes. Focaliser fortement de telles impulsions permet d'obtenir des valeurs d'éclairement considérables, qui sont notamment utilisées pour générer des faisceaux de particules relativistes. Le bon fonctionnement des lasers de ultra-haute intensité nécessite un excellent contrôle des propriétés du faisceau en tout point de la chaîne d'amplification. Développer un tel niveau de contrôle exige de pouvoir mesurer les imperfections temporelles et spatiales des impulsions avec une très grande précision. Cependant, les instruments de mesure utilisés jusqu'à présent négligent un aspect important de la structure des impulsions lasers, qui est lié aux couplages spatio-temporels. Ces derniers représentent une classe particulière d'imperfections, dont l'influence sur les expériences d'ultra-haute intensité a longtemps été négligée. Les rares instruments capables de mesurer ces défauts spécifiques sont pour la plupart inadaptés à la caractérisation de faisceaux de haute énergie. Le travail présenté dans cette thèse a porté sur l'instrument TERMITES, qui permet la caractérisation totale d'impulsions ultrabrèves, ainsi que leur restitution en trois dimensions. TERMITES est une technique auto-référencée qui est basée sur la spectroscopie par transformée de Fourier résolue spatialement. Une première partie de la thèse présente l'étude détaillée et l'optimisation de l'instrument TERMITES. Dans un deuxième temps, différents systèmes laser sont caractérisés grâce à cet instrument, permettant ainsi d'établir la première revue expérimentale des différentes origines de couplages spatio-temporels dans les lasers ultrabrefs.

**Title:** Spatio-Temporal Characterization of Femtosecond Laser Pulses Using Self-Referenced Fourier Transform Spectroscopy

**Keywords:** metrology, interferometry, femtosecond laser, spatio-temporal couplings

**Abstract:** Current ultrashort laser technology makes it possible to generate pulses lasting a few tens of femtoseconds, with energies of up to tens of joules. Strongly focusing such pulses produces ultra-intense fields that are notably used to generate relativistic particle beams. Proper operation of ultra-intense laser facilities requires to control the temporal and spatial properties of ultrashort pulses. Until now, measurement devices used for this purpose have neglected an important aspect of ultrashort pulses structure, which is linked to spatio-temporal couplings. Spatio-temporal couplings are a particular kind of defects in ultrashort pulses, of which the influence on ultra-intense experiments has been largely overlooked until recently. The rare instruments capable of measuring spatio-temporal couplings are hardly scalable to high-energy laser beams. This thesis is dedicated to TERMITES, a device for the full characterization of ultrashort laser beam, which is used to provide their three dimensional shape in space and time. TERMITES is a self-referenced technique based on spatially-resolved Fourier-Transform Spectroscopy. The first part of this work presents the detailed study of TERMITES, as well as the optimization of its design. Multiple laser systems are then characterized using the instrument. The obtained results are used to establish the first experimental review of spatio-temporal couplings origins in ultrashort lasers.

Université Paris-Saclay
Espace Technologique / Immeuble Discovery
Route de l'Orme aux Merisiers RD 128 / 91190 Saint-Aubin, France